



UNIVERSITÀ DEGLI STUDI DELL' AQUILA
DIPARTIMENTO DI INGEGNERIA INDUSTRIALE E DELL'INFORMAZIONE E DI
ECONOMIA

Dottorato di ricerca in
INGEGNERIA INDUSTRIALE E DELL'INFORMAZIONE E DI ECONOMIA
XXX ciclo

Titolo della tesi

Nanoscale sensors based on 2D TMDs and nanostructured Metal Oxides for gas sensing applications

SSD ING-IND/22

Dottorando

Seyed Mahmoud Emamjomeh

Coordinatore del corso

Prof. Roberto Cipollone

Tutore

Prof. Carlo Cantalini

A.A 2017-2018

Abstract

Chemical gas sensor is an electronic functional device to warn us about dangerous gases in human environment. Its function and reliability can save human health, lives and environment from diseases and disasters and control the air pollution. Thus, it can be said the human generation is closely related to the function ability and properties of gas sensors that could be counted sensitivity, selectivity and stability.

To improve these features, in recent decades there has been an increased attention for the development of nanomaterials which provide high structural and morphological control, high efficiency and miniaturization of gas sensors.

The work presented in this thesis is focused on the synthesis of mono-few layered 2D TMDs semiconductors and metal oxide nanomaterials for manufacturing gas sensors for toxic gas sensing measurements. A wide range of gas sensors have been realized, starting from the synthesis of various semiconductors such as metal oxides and Transition Metal Dichalcogenides and using various deposition techniques. In particular, electrospinning, spin coating and ball milling assisted ultra sound probe sonication were utilized to obtain one-dimensional (1D) nanofiber metal oxides and two-dimensional (2D) TMDs respectively.

Morphological characterization of materials was carried out by means Scanning Electron Microscope (SEM), Atomic Force Microscopy (AFM), Transmission Electron Microscope (TEM), High Resolution Transmission Electron Microscopy (HRTEM), X-ray Diffraction (XRD) and X-ray Photoelectron Spectroscopy (XPS). The electrical characterizations were carried out by a laboratory equipment. Target gases such as H₂, CO, NO₂ with concentrations like those found in polluted environments were investigated. Fabricated gas sensors have shown excellent results and performances suggesting the use of nanomaterials-based devices for commercial purposes.

This PhD work has developed through relationships with various research groups including the Departments of Physics and Industrial Engineering of the University of L'Aquila, the Department of Industrial Engineering of the University of Padova, the Department of Chemistry of the University of Pavia, School of Chemical Sciences of the University of Auckland in New Zealand; and School of Chemical and Physical Sciences of Victoria University of Wellington in New Zealand.

Thesis Objectives

The work presented in this thesis is focused on the synthesis of metal oxide (MOS) nanofibers (NF) and mono-few layered 2D Transitional Metal Dichalcogenides (TMDs) to be employed as gas sensors for gas sensing applications. In particular, this research has been aimed to:

- The preparation of Metal Oxide Semiconductors (MOS) nanofibers by electrospinning techniques and optimization of nanofibers manufacturing processes by Electrospinning technique and studying their gas response under light illumination and thermal activation modes at room temperature;
- The preparation of mono-few layered 2D Transitional Metal Dichalcogenides (TMDs) by grinding assisted probe sonication technique and optimization of exfoliation process;
- Investigating the surface chemistry of exfoliated WS₂ during exfoliation;
- Investigating the thermal stability of exfoliated WS₂/WO₃ at elevated temperatures;
- The morphological, microstructural and electrical characterization of synthesized sensing materials to define factors influencing gas sensing properties;
- Investigating the gas sensing properties of above mentioned nanostructured semiconductors to target gases such NH₃, H₂S, H₂, NO₂, and humidity under simulated conditions.

Achieved results

The main achievements of this research program have been:

- The manufacturing of monodimensional (nanofibre) nanostructured devices by Electrospinning deposition processes by means WO_3 precursors and fabrication of room temperature NO_2 gas sensors;
- Controlled the surface oxidation and thermal stability of commercial few layered WS_2 as a very high sensitive sensor to 1 ppm NH_3 and 1 ppm H_2 target gases;
- Fabricated a reproducible and controllable exfoliation procedure to fabricate pristine mono-few layered WS_2 for gas sensing applications by means of grinding assisted probe sonication;
- Explored the oxidation sources during WS_2 exfoliation process and proposed a comparable-yield exfoliation process to fabricate pristine mono-few layered WS_2 .

Perface

During the Doctoral Program several publications were published as follows:

Journal publications:

- S.M. Emamjomeh, V. Paolucci, F. Perrozzi, S.J. Bradley, M. Nardone, L. Ottaviano, C. Cantalini, "Controlling microstructure and surface oxidation of WS₂ exfoliated by ball milling and sonication for gas sensing applications", under review by the journal of sensor and actuators.
- F. Perrozzi, S.M. Emamjomeh, V. Paolucci, G. Taglieri, L. Ottaviano, C. Cantalini, Thermal stability of WS₂ flakes and gas sensing properties of WS₂/WO₃ composite to H₂, NH₃ and NO₂, Sensors and Actuators B: Chemical, 2017.
- M. Sturaro, E.D. Gaspera, N. Michieli, C. Cantalini, S.M. Emamjomeh, M. Guglielmi, A. Martucci, Degenerately Doped Metal Oxide Nanocrystals as Plasmonic and Chemoresistive Gas Sensors, ACS Applied Materials and Interfaces, 2016.
- A. Resmini, U. Anselmi-Tamburini, S. M. Emamjomeh, V. Paolucci, I. G. Tredici, C. Cantalini, The Influence of the Absolute Surface Area on the NO₂ and H₂ gas responses of ZnO Nanorods Prepared by Hydrothermal Growth", Thin Solid Films, 2016.
- L. Giancaterini, S.M. Emamjomeh, A. De Marcellis, E. Palangea, A. Resminib, U. Anselmi-Tamburini, C. Cantalini, The influence of thermal and visible light activation modes on the NO₂ response of WO₃ nanofibers prepared by electrospinning, Sensors and Actuators B: Chemical, 2016.

Conference and proceedings publications

- S.M. Emamjomeh, L. Lee, G.S. Henshaw, V. Paolucci, C. Cantalini, D.E. Williams, “Enhanced NO₂ response of surface decorated WO₃ low-cost gas sensors”, IMCS June 2018, Vienna.
- V. Paolucci, S.M. Emamjomeh, C. Cantalini, “WS₂-decorated rGO for Quasi Room-Temperature Gas Sensing Applications”, IMCS June 2018, Vienna.
- U. Anselmi-Tamburini, J.M. Tulliani, V. Paolucci, S.M. Emamjomeh, C. Cantalini, “Correlation between the NO₂ gas sensing properties and surface area of ZnO nanofibers, hierarchical and thin films structures”, IMCS June 2018, Vienna.
- L. Giancaterini, S.M. Emamjomeh, A. De Marcellis, E. Palange, C. Cantalini, NO₂ gas response of WO₃ nanofibers by light and thermal activation”, Procedia Engineering, 2015.
- C. Cantalini, L. Giancaterini, S.M. Emamjomeh, J.M. Tulliani, A. Resmini, U. Anselmi-Tamburini, Surface area effect on NO₂ gas sensing properties of nanofiber-nanowire brush-like ZnO nanostructures compared to thin films, 6th GOSPEL Workshop; Gas sensors based on semiconducting metal oxides-basic understanding & application fields, Tuebingen, Germany, 7th - 9th June 2015.

Acknowledgements

I wish to thank my supervisor, Prof. Carlo Cantalini for his consistent and warm guidance during my PhD course. Without his assistance and support I would not be able to finish. His academic arrangements regarding all my experiments and analysis for nano materials have provided me the opportunity of the contribution to diverse research works and the accumulation of a great deal of experiences. I also would like to thank Prof. Luca Ottaviano of department of physical and chemical sciences of the university of L'Aquila for his kind advice in my study and giving me the opportunity to work with AFM machine in his lab. I thank Dr. Francesco Perrozzi of department of physical and chemical sciences of the university of L'Aquila for his great assistance and kind advice on my study and I am very grateful that he made efforts spending time for training me AFM basics and analysis and finally helped me build expertise. I also thank Ms. Fabiola Ferrante for her kind assistance in performing my experiments in our lab.

I also want to express my great gratitude to Prof. David Williams of School of Chemical Sciences of the University of Auckland, New Zealand for hosting me in his group and his kind advice in my study and giving me the opportunity to work with variety of characterization instruments and commercial gas sensors. I also thank Dr. Geoff Henshaw and Dr. Lita Lee of Aeroqual Ltd., Auckland, New Zealand, for their assistance on preparing and testing commercial sensors. I thank Dr. Siobhan Bradley and Dr. Erin Service of School of Chemical Sciences of Victoria University of Wellington, New Zealand, for their great assistance and spending huge amount of time to help me with HRTEM investigation on layered materials.

Finally, I thank my father and grandparents that their supports have been my treasure and strength for my study at long distance. The thesis is the answer to your prayers. Most of all, I thank my wife Maryam Lohrasbi that her trust and love shown in difficult seasons encouraged me to continue and finalize PhD course.

Indice

1	Chapter 1: Nanostructured Metal Oxides (MOs) for gas sensing applications.....	1
1.1	MOS semiconductors and their surface reaction.....	2
1.1.1	Semiconducting metal oxide gas sensors	3
1.1.2	Chemoresistive gas sensors	3
1.1.3	Oxygen Absorption / Desorption Reactions.....	4
1.1.4	MOS Semiconductor surface reaction with oxidizing and reducing gases	8
1.2	Factors affecting the characteristics of a sensor.....	12
1.2.1	Working principles in MOS sensors.....	13
1.2.2	Effect of Particle size.....	16
1.2.3	Effect of microstructure.....	19
1.2.4	Effect of doping.....	20
1.3	Gas sensor characteristics.....	22
1.3.1	Sensitivity.....	22
1.3.2	Selectivity.....	23
1.3.3	Long-term stability	23
1.3.4	Response time/ Recovery time	23
1.4	Nanostructures based on metallic oxides	24
1.4.1	0D MOs nanostructures.....	25
1.4.2	1D MOs nanostructures	27
1.4.3	1D structure preparation techniques	31
1.4.4	2D structures preparation techniques	32
1.4.5	3D structures preparation techniques	33
1.4.6	Hierarchical structures.....	34
1.5	Sensing applications of nanomaterials	35
1.5.1	Introduction	35

1.5.2	Quantum confinement effects	36
1.5.3	Nano Effect of Small Size of Metal Oxide Nanoparticles	37
1.6	Manufacturing processes in nanotechnology	39
1.6.1	Production technologies single-dimensional (1D) and two-dimensional (2D)	39
1.6.2	Electrospinning	40
1.6.3	Production of Thin Film: Spin coating	47
2	Chapter 2: 2D Transition Metal Dichalcogenides (TMDs) for gas sensing applications	49
2.1	2D semiconductors for gas sensing applications	50
2.1.1	Oxygen ions surface adsorption mechanism in 2D materials	50
2.2	TMDs and their properties	53
2.2.1	Composition and crystal structure of TMDs	53
2.2.2	electronic structure	56
2.2.3	Band gap structure - From bulk to mono-few layered TMDs	58
2.3	Defects in 2D TMDs	60
2.3.1	Zero-dimensional defects in TMDs	62
2.3.2	One-dimensional defects in TMDs	63
2.3.3	Two-dimensional defects in TMDs	65
2.4	Chemical air stability and Ageing of 2D TMDs	67
2.5	Transition metal dichalcogenide sensors	71
2.5.1	MoS ₂ sensors	71
2.5.2	WS ₂ sensors	74
2.6	Classification of TMDs nanostructures	75
2.7	Preparation of TMD Nanostructures	76
2.7.1	Top-Down Approaches	77
2.7.1.1	Preparation of 2D TMDs	77
2.7.2	Bottom-Up Approaches	84

3	Chapter 3: Materials Characterization and Electrical Measurement Techniques .	86
3.1	Introduction	87
3.2	Material Characterization techniques.....	88
3.2.1	X-Ray Diffraction (XRD) measurements.....	88
3.2.2	SEM.....	88
3.2.3	TEM and high resolution TEM and STEM.....	89
3.2.4	FT-IR	90
3.2.5	Thermal analysis.....	90
3.2.6	XPS measurements.....	90
3.2.7	AFM measurements.....	91
3.2.8	Raman Spectroscopy	91
3.2.9	DLS measurements.....	92
3.3	Electrical characterization of sensors.....	93
3.3.1	Introduction	93
3.3.2	Sensor substrate.....	96
3.3.3	Substrate welding and housing in measuring cell	98
3.3.4	Gas fluxing system	100
3.3.5	Power supply, control and data acquisition.....	102
3.3.6	Electrical response and data processing	103
4	Chapter 4: WO ₃ nanofibers fabrication for gas sensing measurement	107
4.1	Fabrication of WO ₃ nanofibers	108
4.1.1	Reagents, mixing and refluxing.....	111
4.1.1.1	W–O precursor-gel FTIR characterization	112
4.1.1.2	Thermogravimetric characterization.....	114
4.1.2	Final Solution preparation and Electrospinning	115
4.1.2.1	Electrospinning: Influential Parameters.....	117
4.1.3	Heattreatment.....	121
4.1.4	SEM characterization of annealed nanofibers.....	122
4.1.5	Electrical and optical characterization of WO ₃ nanofibers	124
4.2	Discussion of the electrical responses.....	129

	4.2.1	Response in dry air.....	129
	4.2.2	Response to NO ₂	131
	4.2.3	Gas sensing conclusion.....	133
5		Chapter 5: Mono-few layer WS ₂ fabrication for gas sensing measurements	134
	5.1	Fabrication of mono-few layers WS ₂	135
	5.1.1	Reagents Mixing, Milling and Evaporation.....	140
	5.1.1.1	Operating principles of ball milling	141
	5.1.1.2	Ball milling: Influential Parameters	142
	5.1.2	Mixing, Probe Sonication and Centrifugation	145
	5.1.2.1	Sonication: Influential Parameters	146
	5.1.3	Spin Coating and heat treatment.....	152
	5.2	WS ₂ microstructure and oxidation during exfoliation.....	153
	5.2.1	Microstructural properties of exfoliated WS ₂	153
	5.2.2	Chemical composition of exfoliated WS ₂	160
	5.3	Gas sensing response	165
	5.4	Chapter summery and conclusion.....	170
6		Chapter 6: Thermal stability of WS ₂ flakes for gas sensing applications.....	171
	6.1	Introduction.....	172
	6.2	Materials and sensor fabrication.....	174
	6.3	Thermal stability of WS ₂ flakes.....	174
	6.4	WS ₂ /WO ₃ composite growth mechanism.....	182
	6.5	Electrical response of WS ₂ films- Results.....	184
	6.6	Electrical response of WS ₂ films– discussion	195
	6.6.1	H ₂ gas	195
	6.6.2	NH ₃ gas	196
	6.6.3	NO ₂ gas	197
	6.7	Chapter summary and conclusion.....	198
7		References.....	200
8		Annexes	210

8.1	A1: Operating instructions: material preparations	211
8.2	A2: Operating instructions: preparation processes.....	213
8.3	A3: Interdigitated substrate: technical specifications and characterization 216	
8.4	A4: Characteristic parameters for a semiconductor oxide sensor	220
8.5	A5: Testing protocol for electrical tests	221

***1 Chapter 1: Nanostructured
Metal Oxides (MOs) for gas
sensing applications***

1.1 MOS semiconductors and their surface reaction

Introduction

The first gas sensor was commercialized in 1923. It was comprised of hot platinum wire working at several hundred degrees, utilizing the catalyst to detect combustible gases in an atmosphere. The operating process is to measure the resistance changes resulting from the elevated temperature on gas sensing. The signal output was only few millivolts at 1000 ppm of isobutene. An improved catalytic combustion sensor using a catalyst such as palladium was fabricated in the shape of a bead. This type of gas sensor was being used in limited fields and operated by skilled experts. In the 1960s, extensive need for better gas sensors was raised in Japan owing to gas bottle explosion accidents involving liquefied petroleum (LP) gas. LP gas was popular for domestic applications in heating and cooking. Therefore, there was a demand for research on low cost, sensitive gas sensors.

Since 1962 Tagushi delivered the first patent on SnO₂ metal oxide based chemoresistive gas sensors. Semiconducting metal oxide gas sensors have been widely used and studied in the sensing of diverse gases. Investigations have shown that the gas sensing mechanism is strongly related to surface reactions, so one of the important parameters of gas sensors, the sensitivity of the metal oxide based materials, will change with the factors influencing the surface reactions, such as chemical components, surface-modification and microstructures of sensing layers, temperature and humidity [1].

The operating mechanism of semiconductor metal oxide sensors (MOS) is based on the variation of the electrical resistance of the material due to oxidation/reduction reaction caused by adsorption/desorption of interfering gases on the surface of the material. An electronic device measures the variation of resistance through a well-defined transfer function and determines the true value of the gas concentration by transmitting the output signal. Gas selectivity and reactions caused by interference from other gases or by humidity are partially attenuated by careful formulation of the composition and chemical nature of the basic oxides using catalysts and through selecting a suitable working temperature by means of a heating circuit.

1.1.1 Semiconducting metal oxide gas sensors

The semiconducting metal oxide gas sensor is a chemiresistive type gas sensor. It is normally constructed from a semiconducting material on a heated insulating substrate and connected by metal wires. The sensing signals are obtained in the form of resistance changes. This gas sensor has a wide range of gas detection capability that covers the market needs for detecting oxygen, inflammable gases, toxic gases and air pollutants. However, since the invention of SnO₂ chemo-resistive metal oxide gas sensors until now, the semiconducting metal oxide type suffers from lack of selectivity. However, the potential advantages, such as the low cost, reliable performance that metal oxide presents, makes it the fastest growing type of material for gas sensors which have been commercially expanded.

1.1.2 Chemoresistive gas sensors

Chemiresistor constitutes one of the most investigated groups of gas sensor devices; its operating mechanism is that the gas molecules adsorbed on the surfaces of the gas sensing material induce a change of its electrical resistance, and by measuring this resistance change, the target gases can be effectively detected. Chemiresistors have their own advantages, such as ease in fabrication, simplicity of operation, cost effectiveness, long term stability, low power consumption, ability to reuse and are also easy in miniaturization [2].

Chemiresistors contain the sensing materials supported by an inert substrate and two metallic electrodes or interdigitated electrodes. It can be used to detect O₂, CO, H₂, NO_x, SO_x, Cl₂ and some organic vapors [3, 4]. Figure 1-1 shows a chemiresistor sensor substrate comprising Pt finger type electrodes on Si₃N₄ substrate and 4x3 mm² area for depositing semiconductor materials. The chemoresistive sensors are included with a back-side heating circuit. The deposited sensor will be connected to a volt-amperometric system to measure the resistance changes of deposited semiconductor when exposed to air and different oxidizing and reducing gases [4].

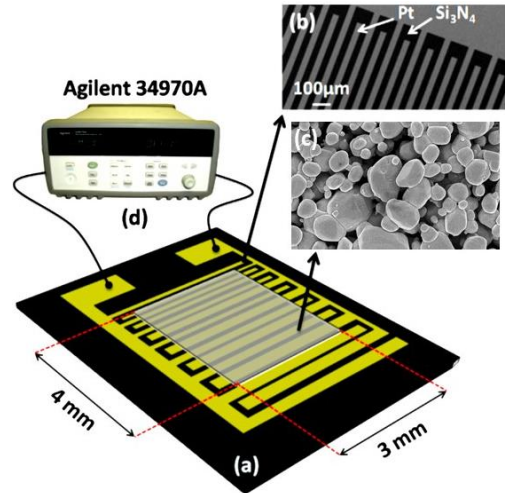


Figure 1-1- Main features of a chemoresistive gas sensor substrate with the deposited WO_3 film: (a) Substrate front sideshowing the 4×3 mm deposited area (light grey); (b) SEM image of the Pt finger-type electrodes on Si_3N_4 substrate; (c) SEM image of the printed WO_3 film on the Pt electrode (light grey) and on the substrate (dark grey); (d) electrical connections to measure the resistance of the film by the volt-amperometric technique [4].

1.1.3 Oxygen Absorption / Desorption Reactions

The ability of a sensor to detect traces of a gas is related to its ability to vary its surface electrical conductivity. The basic concept is that oxygen adsorbs on the gas-solid interface at the active adsorption sites, represented by superficial oxygen atoms, V_{O} . During this adsorption, the conducting electrons of the solid are consumed to allow the formation of ionic species adsorbed according to the reaction 1-1:



Where $\text{O}_{2\text{ gas}}$ represents gaseous oxygen while $\text{O}_{2\text{ ads}}^-$ represents the adsorbed oxygen ion on the surface vacancy of material, V_{O} . The reaction confirms that oxygen adsorption causes an electron consumption (e), this translates, in physical terms, into a gradual depletion of charge in the grain zone adjacent to the depletion Layer. Such emptying causes a decrease in the concentration of charge near the surface and a potential barrier of the Schottky barrier is formed.

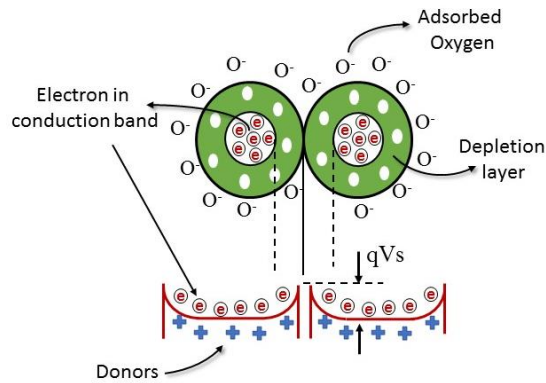


Figure 1-2-Structural and band models of conductive mechanism upon exposure to reference gas. (a) with or (b) without CO [5].

Semiconducting materials

A semiconductor material has an electrical conductivity value falling between that of a conductor, such as copper, and an insulator, such as glass. Their resistance decreases as their temperature increases, which is behavior opposite to that of a metal and their valence band is fully occupied, but unlike insulators, the energy gap between valence band and conductor band in semiconductors is much smaller than 1eV. This makes it easier to energize valence electrons and send them to the conduction band.

Semiconductors are divided in two main groups depending on the impurity in their crystalline lattice:

- n-type semiconductors
- p-type semiconductors

In n-type semiconductors, free electrons are the majority carriers and holes are minority carriers. To better understand this, for example, if the silicon that has 4 electrons in its valence band is doped with antimony atoms that have 5 electrons in their valence band, 4 electrons of antimony make covalent band with 4 electrons of valence band of silicon and an extra free electron of antimony will be introduced to the valence band. At room temperature, these loosely attached fifth valence electrons of impurity atoms can easily come out from their position due to thermal excitation. Due to this phenomenon there will be a huge number of free electrons but still there are breakdowns of covalent bonds in the

crystal due thermal excitation at room temperature. The free electrons in addition to free electrons created due to breakdown of a semiconductor to semiconductor and semiconductor to impurities covalent bonds cause total of free electrons in the crystal. Although whenever a free electron is created during breakdown of a semiconductor to semiconductor covalent bond there is a vacancy created in the broken bond. These vacancies are referred as holes. Each of these holes is considered as positive equivalent of negative electron as it is created due to lack of one electron. Here electrons are main mobile charge carriers. In an n-type semiconductor there will be both free electrons and holes, but number of holes are quite smaller than that of electrons because holes are created only due to breakdown of semiconductor to semiconductor covalent bond whereas free electrons are created both due to loosely bounded non-bonded fifth valence electron of impurity atoms and break down of semiconductor to semiconductor covalent bonds. Hence, number of free electrons is much higher than the number of holes in n-type semiconductor. That is why free electrons are called majority carriers and holes are called minority carriers in the n-type semiconductor. As the negatively charged electrons are mainly involved in charge transferring through this semiconductor it is referred as negative type or n-type semiconductor. Figure 1-3 clearly show a n-type semiconductor.

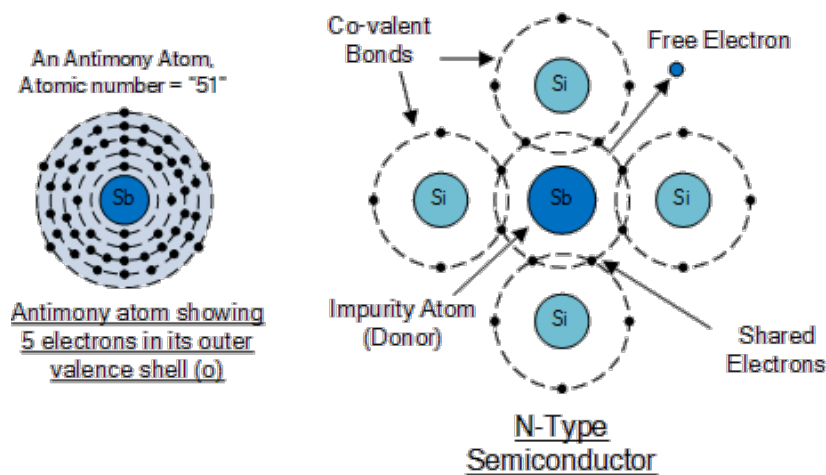


Figure 1-3 Schematic of a n-type semiconductor

In the same way, if the silicon that has four electrons in its valence band is doped with boron atoms that have 3 electrons in their valence band, as Figure 1-4 shows, three complete covalent band will be formed but one covalent bond will be left incomplete with

one electron. Therefore, there is one electron for one electron and this vacancy is referred as hole. In this case, impurity generates empty energy levels in the valence band and there are many holes in the absence of thermal excitation. Thus, there is an excess of positive charge carriers and the level of Fermi moves down.

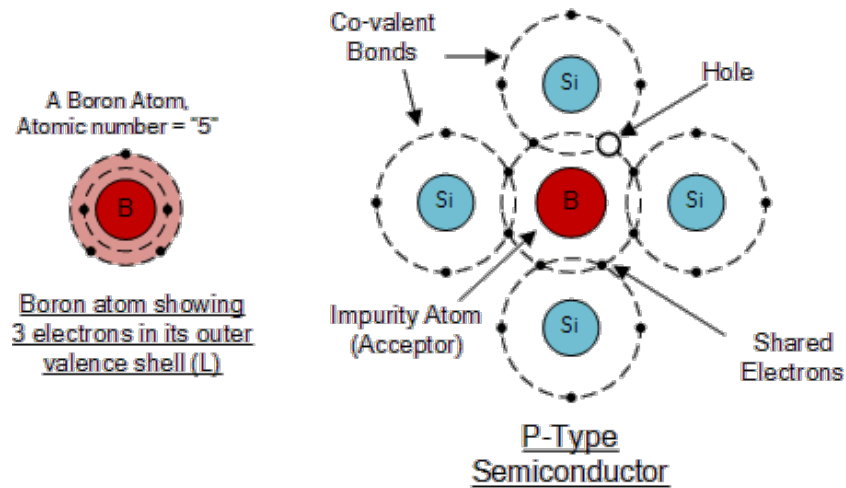


Figure 1-4- Schematic of p-type semiconductor

Each hole is created from one impurity atom. Beside electron mobility, in a semiconductor crystal, holes can also move like electrons, but the mechanism of their movement is different from that of electrons. When one hole is formed from an incomplete covalent bond, it will not remain incomplete lifelong. Very soon electron of other neighboring covalent bonds breaks out and fills the hole and makes a new covalent bond. In this case, we can say that the hole is moved from its previous position to a new position. The same mechanism will happen for the rest of holes and each hole will further move to another new position. This is how the holes move in a semiconductor crystal. Finally, we can say that a p-type semiconductor has plenty of holes that move randomly inside the crystal. Besides the holes generated from trivalent impurity atoms in the p-type semiconductor crystal, there will also be thermally generated electron-hole pairs that refers to those electron-hole pairs that are generated due to the breakdown of covalent bond due to thermal excitations at room temperature. These thermally generated electrons contribute free electrons in the p-type semiconductor crystal. Hence, the total number of holes in a p-type semiconductor is a sum of holes due to trivalent impurity atoms and

holes generated due to thermal excitation whereas free electrons are only due to thermal excitation. Hence, number of free electrons in a p-type semiconductor is much smaller than number of holes in it and therefore holes are considered as majority carriers and electrons are called minority carriers in a p-type semiconductor [6].

1.1.4 MOS Semiconductor surface reaction with oxidizing and reducing gases

For an assigned configuration of the ion-adsorbed oxygen species, when interfering gases interact with the surface of the semiconductor, the base line resistance (R_a at equilibrium) will change. Based on the type of semiconductor (n-type or p-type) and interfering gas (oxidizing or reducing), such variation in resistance may be an increase or a decrease. For n-type semiconductors the interfering gases can be classified as reducing gases or as oxidizing gases, depending on whether they cause a decrease or an increase of R_a respectively. Following the interactions of reducing and oxidizing gases at the surface of a n-type semiconductor are discussed [6].

Reducing gas adsorption

When carbon monoxide (CO) interacts with the surface of a n-type semiconductor at a temperature of around 300 ° C, CO is oxidized and delivers electrons in the conduction band of the semiconductor and the semiconductor is reduced according to the equation 1-2:

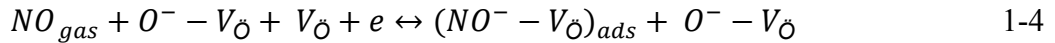
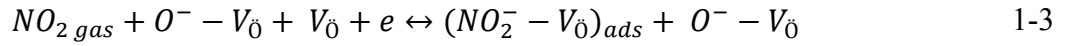


In this reaction CO directly reacts with the adsorbed oxygen molecules, $O^- - V_{\dot{O}}$, the CO_2 will be released, and the electron is injected in the material and according to Figure 1-5, the thickness of the depletion layer decreases, the concentration of the charge carriers (electrons) increase, and the potential barrier (ΔE) decrease.

As a result, R_g that is defined as the resistance of the semiconductor at equilibrium when exposed to CO gas, decrease as compared with the resistance when exposed to air R_a ($R_g < R_a$).

Oxidizing gas adsorption

NO/NO₂ are defined as oxidizing gases as they tend to be adsorbed and oxidized on the surface of semiconductor through the reactions 1-3 and 1-4:



From these reactions, it is noticed that NO and NO₂ gases tend to react with oxygen vacancies $V_{\dot{O}}$ rather than adsorbed oxygen species, $O^- - V_{\dot{O}}$. According to this mechanism, the conducting electrons of the material are consumed.

According to the Figure 1-5 and above-mentioned reactions, equations 1-3 and 1-4, of NO/NO₂ at the surface of semiconductor, we can conclude that when the thickness of the depletion layer increases, the concentration of the charge carrier (electrons) decreases, and the potential barrier (ΔE) increases and therefore, as a result, R_g decreases as compared with the resistance when exposed to air R_a , ($R_g < R_a$).

Table 1-1 shows the reactions and the variation of resistance of type n and type p oxides according to the type of gas under examination, depending on whether it is oxidizing or reducing.

GAS	Gas reaction with the surface	Resistance	
		n-type (WO ₃ , TiO ₂ , SnO ₂ , ZnO)	p-type (NiO, Co ₃ O ₄ , CNT, GO)
Oxidizing	$NO_2 + \square + e^- \leftrightarrow NO_2^- + \square$	R ↑	R ↓
Reducing	$CO + O^- - \square \leftrightarrow CO_2 + \square + e^-$ $H_2 + O^- - \square \leftrightarrow H_2O + \square + e^-$	R ↓	R ↑

Table 1-1- Response mechanism of p and type n sensors with relative adsorption of gas on the surface. $\square + e^-$ in represents as electron hole pair.

The schematic of oxygen, CO, NO and NO₂ adsorption on the surface of a n-type semiconductor illustrated in Figure 1-5.

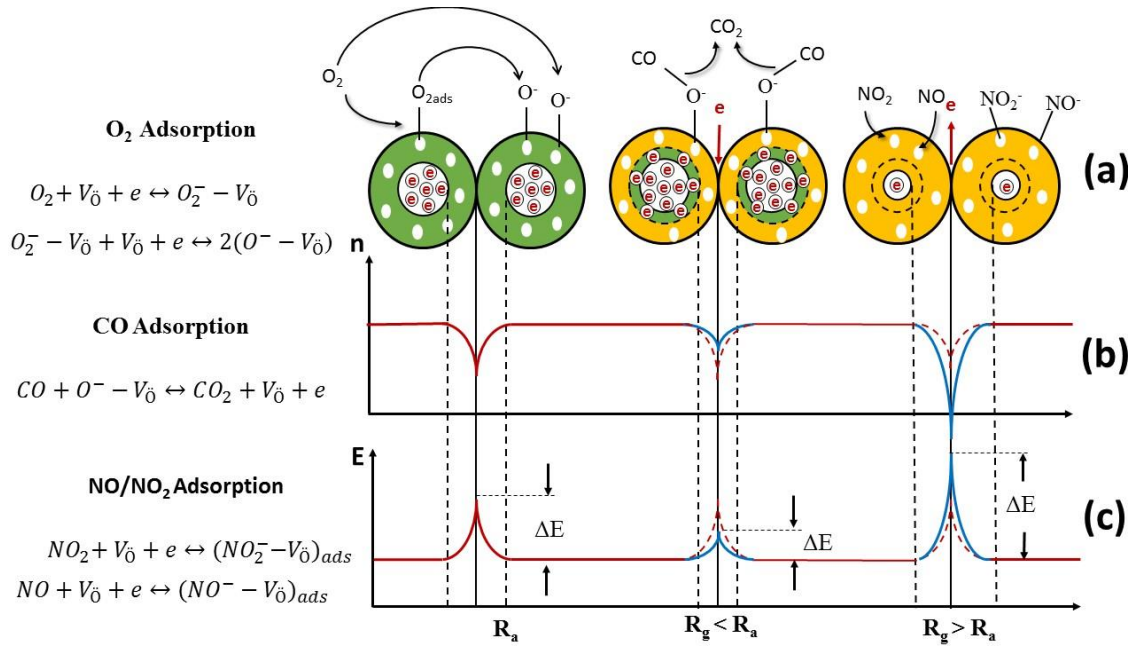


Figure 1-5- n-type semiconductor operation mechanism: (a) Depletion layers of the grains when exposed to oxygen, CO and NO/NO₂, (b) Electron density profiles, (c) Evolution of the electrical potential.

The thickness of the depletion layer (d_{SC}) can be calculated through Debye's equation as follows;

$$d_{SC} = \frac{Q_S}{N_d e} \quad 1-5$$

$$Q_S = \left(\sum_j N_{S,j} q_j \theta_j \right) \quad 1-6$$

where $N_d e$ is the number of donors per volume of the material, $N_{S,j}$ is the number of surface states of j type with unitary electronic charge, q_j , per unit of surface, θ_j is the fraction of adsorbed area corresponding to the states surface type j , and is the electric charge of the electron. The surface potential and the height of the Schottky barrier, can be calculated by equation 1-7:

$$\Delta\phi_S = \frac{(Q_S)^2}{2\varepsilon\varepsilon_0 N_d e} \quad 1-7$$

where Q_S is the charge associated with surface oxygen coverage, ε is the dielectric constant of the material, ε_0 is the dielectric constant relative to the vacancy. It should be noted that if $\varepsilon\varepsilon_0 = 10^{-12} F/cm$, $N_d \approx 10^{18} cm^{-3}$, $\Delta\phi_S \approx 1V$ would have a surface $\sum_j N_{S,j} \theta_j \approx 10^{13} cm^{-2}$ which implies a depletion layer thickness of d_{SC} between 1-100 nm.

According to the reaction 1-8 the oxygen adsorption on the surface of the semiconductor is a function of both environmental O_2 partial pressure and the presence of active sites ($V_{\bar{O}}$) on the surface of semiconductor.



On the junction between the grains, the depletion layer and the associated potential barrier (ΔE in Figure 1-5) create contacts on which strength increases and takes on a controlling aspect. Resistance is a function of the coverage degree by adsorbed oxygen ions and varies only by varying the surface concentration of the latter. Previous studies on O_2 adsorption on the surface of the semiconductor materials have shown that the adsorbed O_2 can be in forms of O_2^- , O^- and O^{2-} at different operating temperatures. The different nature of these species is a function of the working temperature of the semiconductor materials as follows:



As can be seen, at the temperatures below $150^\circ C$, $O_2^- - V_{\bar{O}}$ species are stable, while at temperatures above $150^\circ C$, the $O^- - V_{\bar{O}}$ species are stable. The two equilibrium reactions reported above, from the point of view of the material resistance, result in a variation in the concentration of charge carriers. It might be concluded that at an assigned working temperature, at equilibrium, a given value of the electrical resistance of the

material corresponds to a given concentration of oxygen gas. In normal operating conditions, if the balance between atmospheric and material oxygen reached, R_a is defined as the value of the resistance that the material reaches at the equilibrium state [7-9].

Gas desorption

When the reducing or oxidizing gases such as CO, NO and NO₂ are removed from the working environment of the sensor, the surface of the semiconductor tends to desorb the oxidized and/or reduced species and restore the equilibrium conditions of the adsorbed oxygen species.

When CO is removed from the sensor working environment, the atmospheric oxygen tends to be adsorbed and to restore the balance concentration of the species $O^- - V_O$. The equilibrium moves to the left side of the equation 1-2 (electron consumption), and the resistance of the material raises up. This resistance is reported to the equilibrium value R_a (where $R_a > R_{gCO}$).

When NO/NO₂ gases are removed from the sensor working environment, the system tends to restore the oxygen concentration V_O . The equilibria in reactions 1-3 and 1-4 move to the left and the material resistance decreases (due to electron injection) and returns to the equilibrium value R_{aNO/NO_2} (where $R_a < R_{gNO/NO_2}$) [9].

1.2 Factors affecting the characteristics of a sensor

The process of gas sensing by a semiconductor device involves two key functions as illustrated in Figure 1-6. (i) Recognition of a target gas through a gas–solid interaction which induces an electronic change of the oxide surface (receptor function) and (ii) transduction of the surface phenomenon into an electrical resistance change of the sensor (transducer function) [10]. Accordingly, for a given type of base material, the sensor sensitivity depends on some issues such as the structural features, the presence and state of catalytically active surface dopants, and the working temperature.

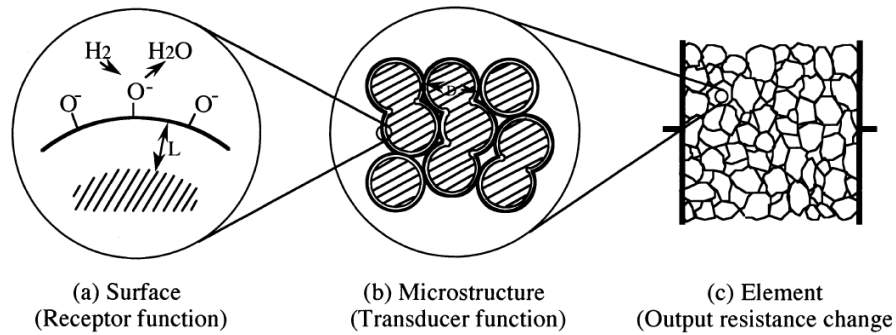


Figure 1-6- Receptor and transducer function of a semiconductor gas sensor: a) surface, providing the receptor function, b) microstructure of the sensing layer, providing the transducer function, and c) element, enabling the detection of the change in output resistance of the sensing layer, here deposited on an interdigital microelectrode [7].

After briefly introducing the general working principle of the pure metal oxide, the influence of particle size on sensor performance will be discussed.

1.2.1 Working principles in MOS sensors

The working principle of a chemoresistive MOS gas sensor like WO_3 or SnO_2 is based on the shift of the state of equilibrium of surface oxygen reaction due to the presence of the target analyte that is defined as receptor function. The resulting change in chemisorbed oxygen is recorded as a change in resistance of the MOS material that is defined as transducer function [10]. As an example, reducing gases lead to an increase of the conductivity for n-type semiconductors and a decrease for p-type materials, whereas the effect of oxidizing gases is vice versa. The mechanism is discussed in the following example for SnO_2 , which is a wide-bandgap n-type semiconductor and used in various sensor applications. In the absence of any humidity and the presence of oxygen (e.g., in synthetic air), oxygen is ionosorbed on the metal oxide surface. The ionosorbed species act as electron acceptors due to their relative energetic position with respect to the Fermi level E_F (Figure 1-7).

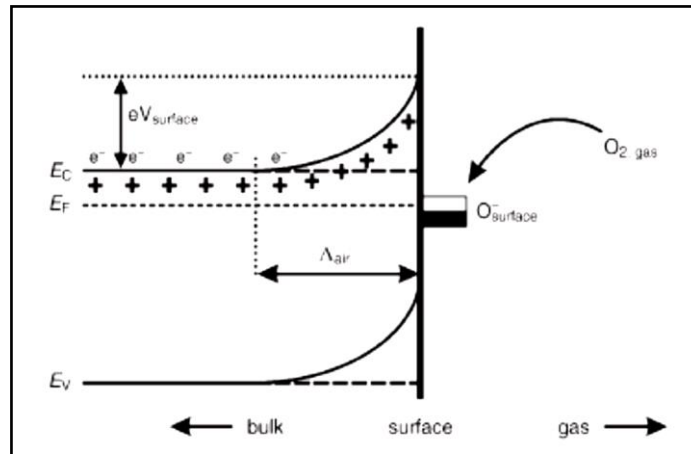


Figure 1-7- Simplified model illustrating band bending in a widebandgap semiconductor after chemisorption of charged species (here the ionosorption of oxygen) on surface sites. E_C , E_V , and E_F denote the energy of the conduction band, valence band, and the Fermi level, respectively, while Λ_{air} denotes the thickness of the space-charge layer, and $eV_{surface}$ the potential barrier. The conducting electrons are represented by e^- and $+$ represents the donor sites [11].

As explained above, depending on the temperature, oxygen is predominantly ionosorbed on the surface as O^{2-} ions (below 420 K) or as O^- ions (between 420-670 K, that is, the general operating temperature range). Above 670 K, the parallel formation of O^{2-} occurs, which is then directly incorporated into the lattice above 870 K [8]. The required electrons for this process (that is originating from donor sites and is intrinsic oxygen vacancies) are extracted from the conduction band (E_C) and are trapped at the surface, leading to an electron-depleted surface region, the so-called space-charge layer Λ_{air} [12-15]. The maximum surface coverage of about 10^{-3} to 10^{-2} cm^{-1} ions is dictated by the Weisz limitation, which describes the equilibrium between the Fermi level and the energy of surface-adsorbed sites. The presence of the negative surface charge leads to band bending (Figure 1-7), which generates a surface potential barrier $eV_{Surface}$ of 0.5 to 1.0 eV. The height ($eV_{Surface}$) and depth (Λ_{air}) of the band bending depend on the surface charge [13], which is determined by the amount and type of adsorbed oxygen. At the same time, Λ_{air} depends on the Debye length L_D , which is a characteristic of the semiconductor material for a particular concentration of donors according to equation 1-11:

$$L_D = \sqrt{\frac{\epsilon_0 \epsilon k T}{e^2 \eta_d}} \quad 1-11$$

where K is Boltzmann's constant, ϵ is the dielectric constant, ϵ_0 is the permittivity of free space, T is the operating temperature, e is the electron charge, and η_d is the carrier concentration, which corresponds to the donor concentration assuming full ionization. As an example, L_D for SnO_2 at 523 K is about 3 nm, with $\epsilon=13.5$, $\epsilon_0=8.85 \times 10^{-12} \text{ Fm}^{-1}$, and $\eta_d = 3.6 \times 10^{24} \text{ m}^{-3}$. This situation describes the idealized case where humidity is not involved in the surface chemistry. However, any real system under ambient conditions is under the influence of water-forming hydroxyl groups, which may affect the sensor performance. In polycrystalline sensing materials, electronic conductivity occurs along percolation paths via grain-to-grain contacts and therefore depends on the value of eV_{Surface} of the adjacent grains. eV_{Surface} represents the Schottky barrier. In this case, the conductance of the sensing material (G) can be calculated by the equation 1-12 [16]:

$$G \approx \exp\left(\frac{-eV_{\text{surface}}}{kT}\right) \quad 1-12$$

Reducing gases, such as CO, react with the ionosorbed oxygen species via the formation of unidentately and/or bidentately bound carbonate groups and desorb finally as CO_2 [17]. Thus, even traces of reducing gas decrease the amount of adsorbed oxygen significantly and the surface trapped electrons are released back to the bulk. Consequently, the height of the Schottky barrier is reduced, which results in an increase of the conductance of the whole sensing layer (Figure 1-8).

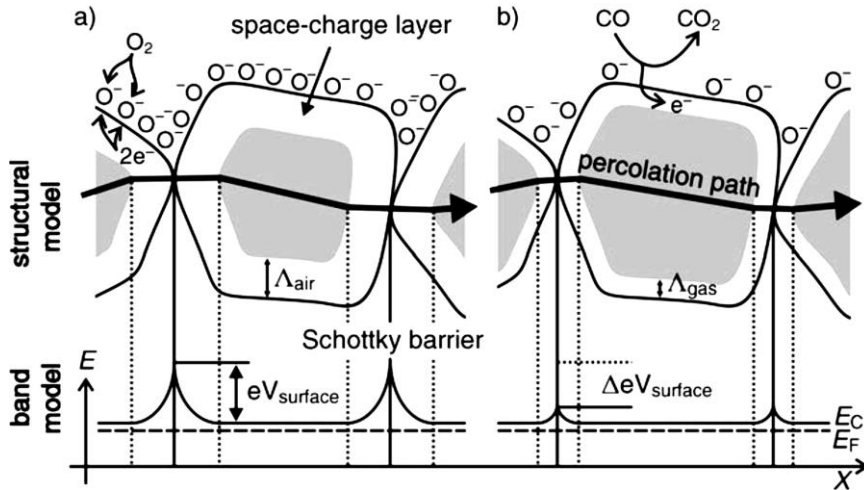


Figure 1-8- Structural and band model showing the role of intergranular contact regions in determining the conductance over a polycrystalline metal oxide semiconductor: a) initial state, and b) effect of CO on Λ_{air} and eV_{Surface} for large grains [18].

1.2.2 Effect of Particle size

The huge change in electrical resistance can be explained by assuming the formation of double Schottky barriers for transport of electrons through grain boundaries. The depletion layer thickness (L_s) is expressed by equation 1-13:

$$L_s = L_D \sqrt{\frac{eV_s^2}{kT}} \quad 1-13$$

where k is the Boltzmann constant, T is the temperature, V_s is the Schottky potential, and L_D is the Debye length. The Schottky barrier (potential), V_s , and L_D are given by equations 1-14 and 1-15:

$$V_s = \frac{2\pi q^2 N_s^2}{\epsilon N_d} \quad 1-14$$

$$L_D = \sqrt{\frac{\epsilon kT}{2\pi e^2 N_d}} \quad 1-15$$

where ϵ is the dielectric constant, N_d is the concentration of the donor impurity, q is the

surface state charge, and N_s is the concentration of the surface charge states.

Typical values of the depletion layer thickness (L_s) are in the range of 1-100 nm. Its dependency on grain size (diameter, D) has been observed empirically [19]. The gas sensitivity of sintered SnO_2 changed with a change in D . For $D > 20$ nm the sensor response barely changed along with the grain size; for $D < 20$ nm it increased with decreasing grain size; for $D < 10$ nm, the increase was huge. Some studies revealed that D has a critical value (D_c), 6 nm for SnO_2 , and corresponds to twice the thickness (L_s) of the surface charge layer [20, 21].

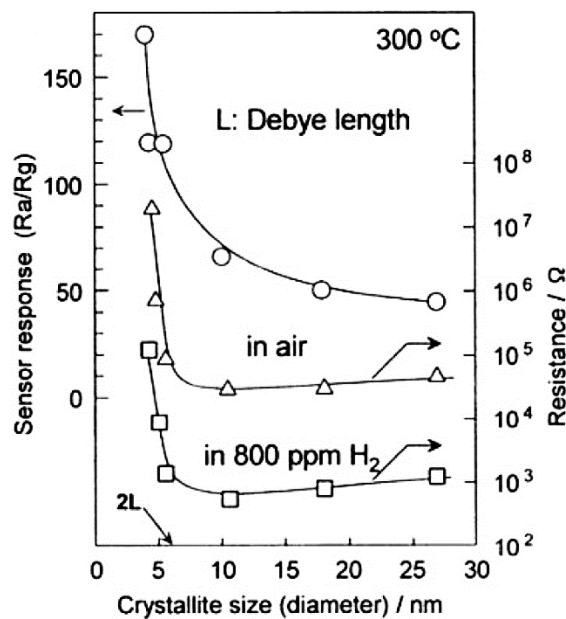


Figure 1-9- Grain size effect on resistance and sensor response of SnO_2 to H_2 [20].

For $D \gg 2L_s$: a small portion of the volume of grains has surface interactions with the analyte gas. The effect on the sensor conductivity is dominated by the grain boundary (GB) barriers to intergrain charge transport from one grain to another. The electrical resistance of a sample with large grains is controlled by Schottky barriers and changes with them exponentially, see Figure 1-11(a).

For $D \geq 2L_s$: in this case, the grain is somewhat larger or similar in size to the thickness of the depletion layer. The unaffected volume (core region) becomes smaller. When D is approaching $2L_s$, but still larger, the depletion region in each neck of each aggregate makes the conduction channel constricted, see Figure 1-11(a). Consequently, changes in

the total conduction is affected by the GB barriers and the cross-sectional area of constricted channels. From these two factors, the gas sensitivity increases with decreasing grain diameter.

For $D < 2L_s$: In this case, the conductivity decreases steeply because the crystallites are almost depleted of mobile charge carriers throughout the entire grain and the conduction channels between the grains have vanished, see Figure 1-11(b). The energy bands are nearly flat, since intercrystallite charge transfer is not interrupted by GB barriers and the GB barrier effect is negligible, see Figure 1-10(b). However, the sensing mechanism of particles in this range is not clear.

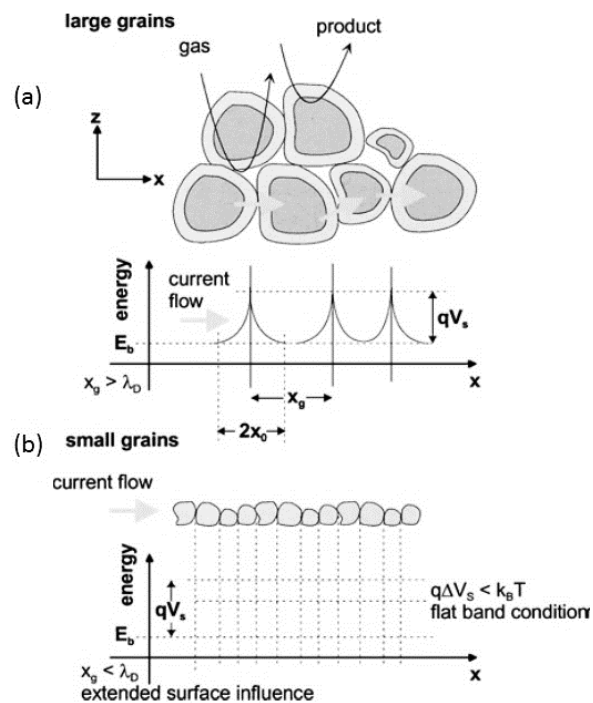


Figure 1-10- Schematic representation of a porous sensing layer with geometry and energy band. λ_D Debye length, x_g grain size [11].

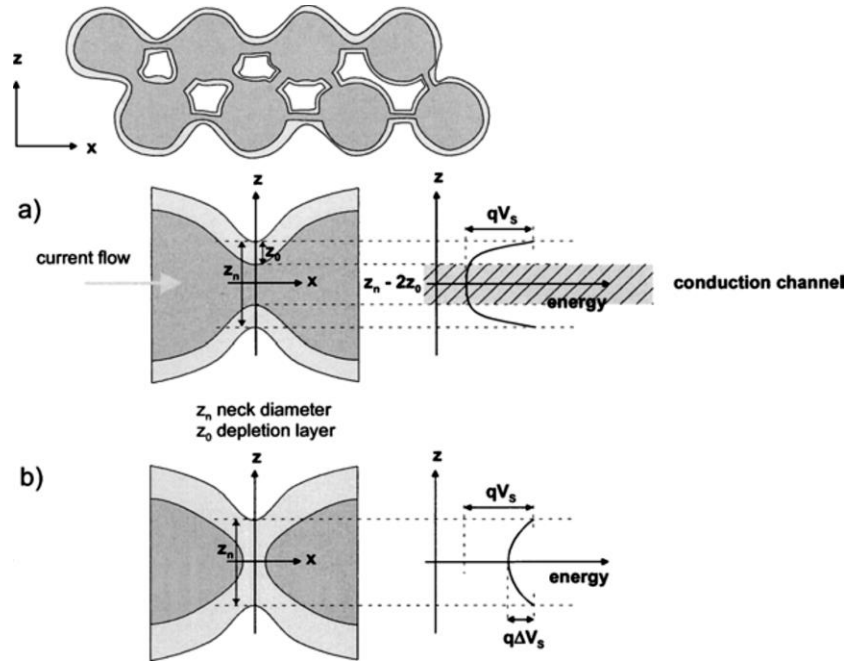


Figure 1-11- Schematic representation of a porous sensing layer with geometry and surface energy band-case with necks between grains. Z_n is the neck diameter; Z_0 is the thickness of the depletion layer. a) represents the case of only partly depleted necks whereas b) represents large grains where the neck contact is completely depleted [11].

1.2.3 Effect of microstructure

Beside the particle size, the influence of the microstructure, that includes the film thickness and its porosity, is an important issue that plays a critical factor on the response time and the sensitivity of sensor and is needed to be discussed. Sensing layers are penetrated by oxygen and analyte molecules so that a concentration gradient is formed, which depends on the equilibrium between the diffusion rates of the reactants and their surface reaction. The rate of reaching the equilibrium condition determines the response time (τ_{ads}) and recovery time (τ_{des}). Therefore, a fast diffusion rate of the analyte and oxygen into the body of sensing material, which depends on its mean pore size and the working temperature, is fundamental. Moreover, maximum sensitivity will be achieved when all percolation paths contribute to the overall change of resistance and are all accessible to the analyte molecules in the ambient. Thus a thinner film together with a higher porosity results in a higher sensitivity and enhanced response time [22, 23]. This was verified experimentally by Yamazoe et al., investigating the gas response on H_2 and

H₂S of thin films of monodisperse SnO₂ with particle diameters ranging from 6–16 nm [24, 25]. It was found that the sensor response was greatly enhanced with decreasing film thickness but with increasing grain size up to 16 nm. The latter appears to be unexpected but can be understood in terms of an increased porosity, which cannot be achieved with the smallest particles studied. Thus, by controlling the nano and microstructure of the sensing layer, for example, by arranging the primary particles into larger secondary particles, analyte diffusion is facilitated via the larger micropores, whereas the grain size effect on the sensitivity can be maintained.

1.2.4 Effect of doping

Pure metal oxides are not able to comply with all the demands of a perfect chemiresistor, to overcome the inherent limitations of the pure base material, doping with metals and/or oxides has a profound impact on the sensor performance. It should be noted that this kind of doping is not comparable with the bulk doping of semiconductors for microelectronic applications. In this case, doping is in fact the addition of catalytically active sites to the surface of the base material. Ideally, the doping process improves sensor performance by increasing the sensitivity, favoring the selective interaction with the target analyte and thus increasing the selectivity and decreasing the response and recovery time, respectively, which is then accompanied by a reduction of the working temperature. Furthermore, surface doping may enhance the thermal and long-term stability. The control parameters are composition, size, habit, and redox state of the surface modifiers, as well as their dispersion on and/or into the metal oxide surface. As is known from the size-dependent properties of catalytically active nanoparticles, the particle size can effectively control the temperature range as well as the efficiency of a catalytic reaction. To explain the influence of surface additives, two different mechanisms are applied, one electronic sensitization and the other is chemical sensitization. In the case of electronic sensitization, the additive in its oxidized state acts as a strong acceptor for electrons of the host semiconductor. This induces an electron-depleted space-charge layer near the interface. By reacting with a reducing analyte, for example H₂, the additive is reduced releasing the electrons back to the semiconductor (Figure 1-12) [10].

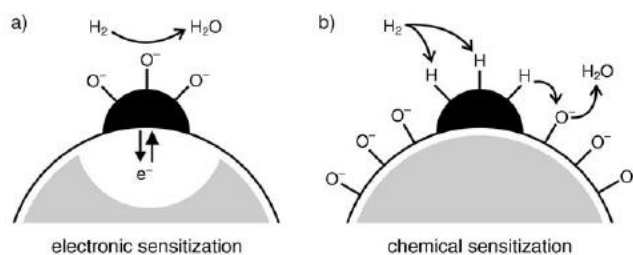


Figure 1-12- Mechanism of sensitization by metal or metal oxide additives: a) electronic sensitization, where the additive is an acceptor for electrons and the redox state/chemical potential is changed by reaction with the analyte; b) chemical sensitization by activation of the analyte (H_2) followed by spill over and change of the surface oxygen concentration [10].

This type of sensitization has been observed for AgO/Ag , PdO/Pd , and CuO/Cu systems. In the same sense the high sensitivity of CuO -cluster-doped SnO_2 towards H_2S can be understood. Here the conversion of CuO into CuS is accompanied by a change in the chemical potential, thus affecting the state of charge at the semiconductor/dopant interface [26]. The second case refers to chemical sensitization, which results from a catalytic surface reaction. Thereby, it is assumed that deposited clusters of noble metals (typically Pt or Au) provide preferred adsorption and activation sites for the target analyte from which activated pieces are spilled over onto the semiconductor to react with the ionosorbed oxygen (Figure 1-12(b)). As a result, the surface coverage with oxygen, and therefore $eV_{Surface}$, is reduced and accompanied by a change in conductance according to Equation 1-12, while the cluster itself remains unchanged. However, the real situation is far more complicated and searching for sensor materials with tailored properties still requires a purely empirical approach. This is illustrated in Figure 1-13, which shows the multitude of parameters that are affected by introducing a doping element to a base metal oxide. If a doping element is already added (even in small amounts) during the preparation process of the semiconductor, the morphology, the electronic properties of the base material, as well as the overall catalytic activity will be affected. And even in cases where the doping element is added by post-treatment to the preformed base material, different methods of dispersion and segregation will be observed, depending on the mutual solubility.

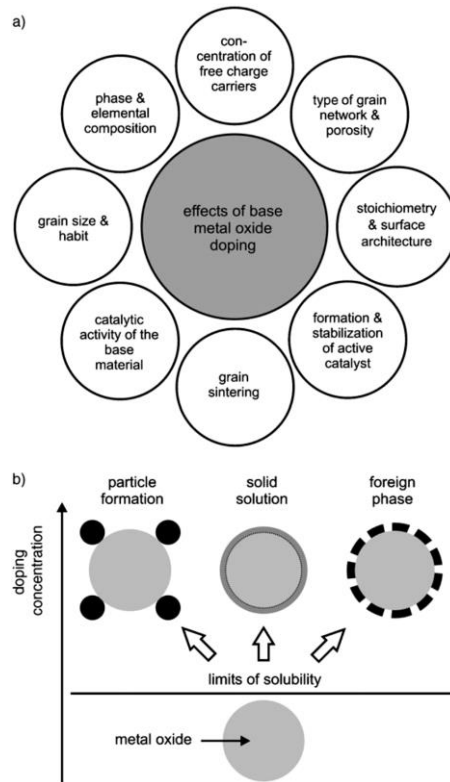


Figure 1-13- a) Parameters that may be affected by the addition of doping elements during the preparation of a metal oxide; b) formation of a segregation layer and mixed phases on the surface of a semiconductor is dependent on the nature of doping elements [27]

1.3 Gas sensor characteristics

1.3.1 Sensitivity

The resistance of a chemiresistive gas sensor changes when it is exposed to the target gas. As explained under “reception and transducer functions”, the interaction of the gas sensor surface with the analyte gas produces variations in the electronic state, see section 1.1.4. The sensor response, S , for n-type and p-type semiconductors are presented by equations 1-16 and 1-17 respectively as follows:

$$S = \frac{R_{air}}{R_{gas}} \quad (\text{for n-type semiconductor}) \quad 1-16$$

$$S = \frac{R_{gas}}{R_{air}} \quad (\text{for p-type semiconductor}) \quad 1-17$$

A high value of S means high sensitivity. A percentage value for a n-type semiconductor is also expressed under the following equation:

$$S\% = 100 \times \left(\frac{R_{air} - R_{gas}}{R_{air}} \right) \quad (\text{for n-type semiconductor}) \quad 1-18$$

1.3.2 Selectivity

A chemiresistive gas sensor exhibits characteristic sensitivity toward a designated gas. Normally one gas sensor can detect several gases. More sensitivity is usually desired for a particular one under similar operating conditions, if possible, exclusively, even when there is coexistence of interfering gases. So, the selectivity is expressed by:

$$Selectivity = \frac{\text{Sensitivity of the sensor for interfering gas}}{\text{Sensitivity towards to desired gas}} \quad 1-19$$

1.3.3 Long-term stability

Stability is an important criterion required for gas sensors. This is because gas sensors should operate consistently under repeated conditions, experiencing response and recovery by detecting a gas at various concentrations and sometimes in harsh environments. Stable performance without showing a drift is another important measure to evaluate the performance of gas sensors.

1.3.4 Response time/ Recovery time

Response time is defined as a time taken to reach 90% of the saturation value of resistance when the sensor is exposed to the gas and is shown by τ_{ads} . A small value of time implies a good sensor. Recovery time is defined as a time taken to drop back to 10% of the saturation value of resistance when the sensor is placed in clean air and is shown by τ_{des} . This value also should be small for a good sensor.

1.4 Nanostructures based on metallic oxides

Introduction

The term “nanotechnology” refers to a multidisciplinary approach to the realization of materials, devices and systems in which at least one of the three spatial dimensions of the components has a measure of the order of nanometers (nm, $1 \text{ nm} = 10^{-9} \text{ m}$).

Materials that their structural and functional properties depend on at least one of the three dimensions on a nanometer scale are called nanostructured materials and such nanometric components are called nanostructures. The physics of nanostructures as a new and well-known scientific discipline is commonly traced back to the intuition of Richard Feynman, who explained the possibility of controlling matter and making devices on a scale atomic atom for the first time in a conference held in December 1959 at the California Institute of Technology. At that conference, remembered also for his title *There's plenty of room at the bottom*, Feynman noted that "the principles of physics do not oppose the possibility of manipulating atomic objects per atom", anticipating a broad spectrum of scientific research fields technical application that at the end of the 20th century already appear well-established. Among these are manufacturing methods based on electron beams or atoms, molecular beam epitax, nanometric lithography, electronic microscopy, atom atom manipulation, quantum and spin-based electronics (today called spintronic), to micro and nano-electromechanical systems (MEMS, Micro-Electro-Mechanical Systems, and NEMS, Nano-Electro-Mechanical Systems, respectively).

Possible applications of nanotechnologies are expanding very rapidly and directly or indirectly affect all sectors of economic activity. The ability to produce materials precisely assembling nanostructured blocks with a composite and controlled size to obtain structures of desired shape and size represents a radical change in both production processes and materials properties, other than those so far known. These changes make the application potential of nanostructured materials very high, either in the form of dust, artifacts or thin films, or in special shapes such as dwarf fibers, unworkable with traditional textile materials.

Depending on dimensionality, some typical types of nanomaterials are defined (Table 1-2) such as:

- nanocrystals;
- filament structures;
- laminated (single or multilayer) or lamellar structures;
- Nanostructured materials (materials whose constituent elements such as particles, aggregates or cavities have at least a dimension smaller than 100 nm).

Type of Nanomaterial	Dimension	Material
(0-D) nanocrystals and clusters (quantum dot)	Diameter 1-10 nm	Metals, semiconductors, magnetic materials
(0-D) Other Nanoparticles	Diameter 1-100 nm	Ceramic Oxides
(1-D) Nanowire	Diameter 1-100 nm	Metals, semiconductors, oxides
(1-D) Nanotube	Diameter 1-100 nm	Carbon
(2-D) Nanoparticles matrix	Several nm ² to several μm ²	Metals, Semiconductors, Magnetic Materials
(2-D) Thin films	Thicknesses 1-1000 nm	Various materials (organic and inorganic)
(3-D) Three-dimensional structures	Several nm in 3 dimensions	Metals, semiconductors, magnetic materials

Table 1-2- Classification of nanomaterials by varying dimensionality

1.4.1 0D MOs nanostructures

The term "structure 0D" normally identifies the set of particles formed by atomic or molecular aggregates with a diameter of between 2 and 200 nm. Nanoparticles have the feature of having all nanometer size. The term is currently used to denote nanoaggregates, that is, molecular or atomic aggregates with interesting chemical-physical properties that can also be produced and used in nanotechnologies [28].

Special equipment, electronic microscopes (scanning and transmission) or soft and hard

X-rays, should be used for their study. Nanoparticles are of great scientific interest as they are in fact a bridge between coarse materials and atomic or molecular structures. Large material had physical properties consistent with its size, but nanometer scale size dependent properties are often observed. Material properties change as soon as they approach the nanometer scale when the percentage of atoms in the surface of the material becomes significant. For materials of more than one micrometre size, the percentage of atoms at the surface level is insignificant in relation to the number of atoms included in the total mass of the material.

The interesting and sometimes unexpected properties of nanoparticles are due more to the large surface area of the material which prevails over the contributions made by the small mass of the material.

An excellent example of this is the absorption of solar radiation by photovoltaic cells, much higher in nanoparticulate composites than in thin layers that constitute continuous pieces of material. In this case, the smaller particles are the larger the solar absorption.

Other size-dependent property changes include quantum confinement in semiconductor particles, surface plasmon resonance in some metal particles, and super-magnetism in magnetic materials.

Nanoparticles have a very large surface area in relation to volume, thus provide a high propelling force for diffusion, especially at high temperatures. Sintering can take place at lower temperatures, on shorter time scales than with larger particles; this theoretically does not affect the density of the final product, although the difficulty of flow and the tendency of nanoparticles to agglomerate complicates the phenomenon. The large surface area in volume ratio also reduces the incipient melting point of dwarf particles [29]. Figure 1-14 shows the images of different types of 0D NSMs.

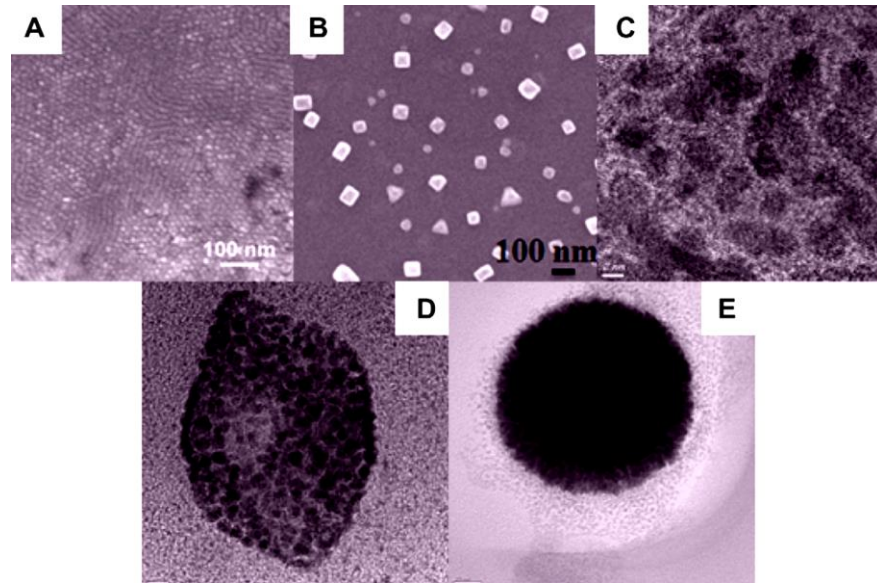


Figure 1-14- Typical scanning electron microscope (SEM) and transmission electron microscope (TEM) image of different types of 0D NSMs, synthesized by several research groups. (A) Quantum dots, (B) nanoparticles arrays, (C) core-shell nanoparticles, (D) hollow cubes, and (E) nanospheres [28].

1.4.2 1D MOs nanostructures

One-dimensional (1D) nanostructures, such as nanotubes, nanofibers and nanowires, have been the focus of intense research activity in the recent years, for their unique application in mesoscopic physics and nanoscale devices. It is also proved that 1-D nanostructures provide good electrical and thermal transport or mechanical properties by dimensionality and size reduction.

Although 1D nanostructures can be manufactured using many advanced nanolithographic techniques such as electron beam or ion beam lithography, probe scan lithography and X-ray or UV lithography, the further development of these nanostructures and techniques for implementing 1D nanostructures with a diverse range of materials and reasonably low costs still require great effort. Unconventional methods based on chemical synthesis could provide an alternative and intriguing strategy for the generation of 1D nanostructures in terms of material diversity, cost, and high-volume productivity.

Chemistry plays a particularly important role in the synthesis and characterization of nanoconductive units such as nanocrystals of metals, oxides and semiconductors, nano

particles and composites involving ceramics, carbon nanotubes and polymers involving dendrimers and block copolymers. The assembly of these units also involves chemistry [30].

Figure 1-15 shows the 1D NSMs, such as nanowires, nanorods, nanotubes, nanobelts, nanoribbons, and hierarchical nanostructures

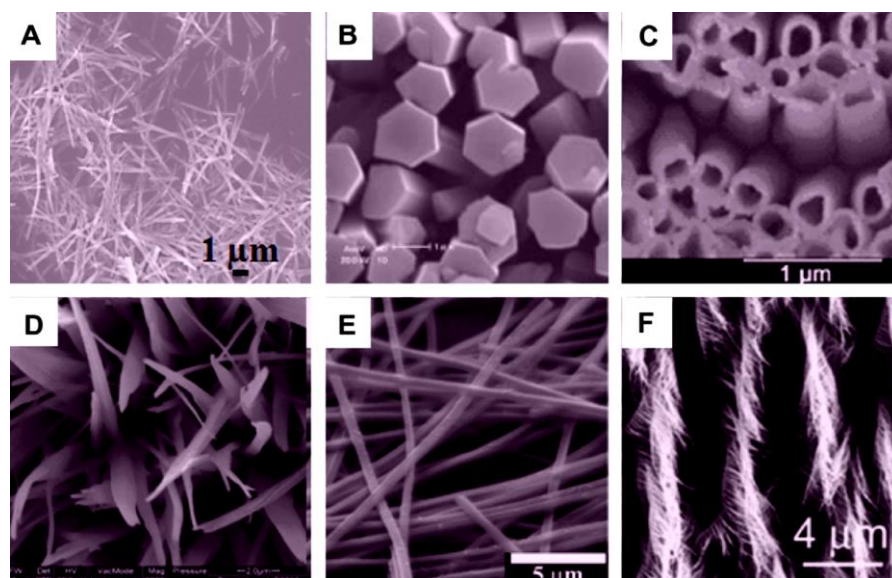


Figure 1-15- Typical SEM image of different types of 1D NSMs, synthesized by several research groups. (A) Nanowires, (B) nanorods, (C) nanotubes, (D) nanobelts, (E) nanoribbons, and (F) hierarchical nanostructures [31].

Nanotubes

The carbon nanotubes (CNTs) were discovered in 1991 by S. Iijima in Japan. Since that time, there has been intense research activity related to the synthesis, structure, properties and applications of CNTs. The discovery of carbon nanotubes has also led to many research into unidimensional nanostructures such as nanotubes both organic and inorganic [32]. It is extremely difficult to give a precise definition of carbon nanotubes, especially because of the huge variety of sizes and conformations they may have. The CNTs have an elongated cylindrical structure with diameters of the order of the nanometers and the lengths of the micron order; they are made up of one or more sheets of graphite coiled on themselves to form a tube. Generally, their terminal part is closed by a fullerene hemispherical structure [33]. In general, nanotubes can be divided into two large families: single-walled nanotubes (SWNTs) and multi-walled nanotubes (MWNTs).

SWNTs can be considered for conformation and structure as belonging to the fulleren family, while MWNTs are closer to the nanofilament family, which they represent a particular case. MWNTs are nanotubes formed by several concentric SWNTs and are therefore called "multi-walled nanotubes". There may be lip-lip interactions that seem to stabilize the growth of these nanotubes (Figure 1-16).

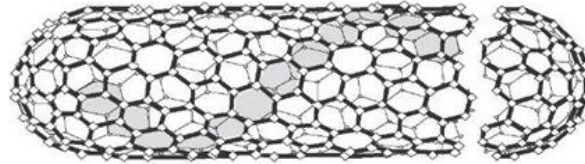


Figure 1-16- Ideal SWNT, closed at the ends of two semi-fullerenes.

Nanofibers

Nanofibers are defined as fibers having a diameter of the order of the nanometers. It is important to point out that while the academic community has approved the criterion of taking nanotechnology less than 100 nm, the business sector has allowed greater flexibility while also accepting values up to 500 nm.

It is obvious that nanofibres geometrically fall into the category 1D which also includes nanotubes and nanorods. Nanofibre production techniques are diverse and include both top-down and bottom-up. Specifically, polymeric nanofibres can be elaborated by a number of techniques such as interfacial polymerization, phase separation, self assembly and electrospinning.

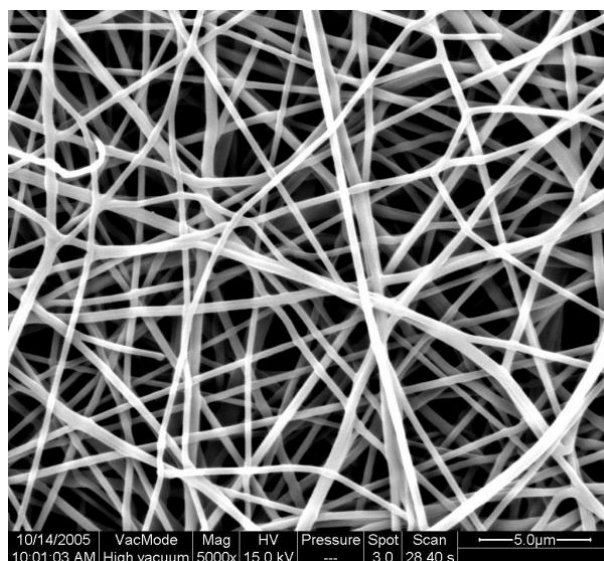


Figure 1-17- SEM image of nanofibres.

Inorganic nanofibers (sometimes called ceramic nanofibers) can be prepared with various types of inorganic substances by means of the electrospinning technique. The most frequently mentioned ceramic materials with nanofibrillar morphology are titanium dioxide (TiO_2), silicon dioxide (SiO_2), zirconium dioxide (ZrO_2), aluminum oxide (Al_2O_3), titanium titanate ($\text{Li}_4\text{Ti}_5\text{O}_{12}$), titanium nitride (TiN) or platinum (Pt). Synthesis usually consists of two main phases: in the first phase, the nanofibers of the polymer (organic) are created by the conventional electrospinning technique; in the second phase, the polymeric nanofibers formed of inorganic salts or organometallic compounds are stratified into ceramics by heat treatment. In the formation of nanofibers from the solution, a very high surface/volume ratio is obtained which in a few tens of milliseconds allows complete evaporation of the solvent [34].

Nanorods

In the field of nanotechnologies, nanorods are a morphology of nanometric objects. Each of them varies from 1-100 nm. They can be synthesized by metals or semiconductor materials. Standard proportions (length / width) are 3-5. Nanorods are produced by direct chemical synthesis, a combination of ligands acts as a form control agent and as a bond of different facets of the nanorod with different strength. This allows the different nanorod faces to grow in a different way, producing an elongated object.

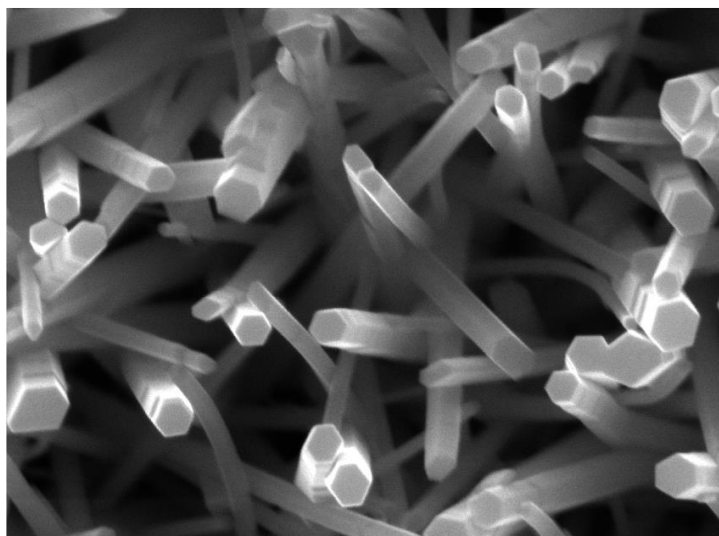


Figure 1-18- SEM image of ZnO nanorods

1.4.3 1D structure preparation techniques

In recent years, a wide variety of 1D structures of organic and inorganic materials have been synthesized and characterized. These structures have been realized using various techniques. One of the most important factors in the synthesis of 1D structures is controlling the composition, size and crystallinity.

The formation of a solid starting from a liquid, steam or solid phase involves two fundamental steps: nucleation and growth. Since the concentration of the constituent elements (atoms, ions, molecules) of a solid becomes sufficiently high, they aggregate into small clusters (or nuclei) through homogeneous nucleation. With the continuous supply of constituent elements, these nuclei can serve as seeds for further growth in order to form larger structures. Various strategies for 1D structures have been developed with different levels of control over growth parameters: these include the use of solid anisotropic crystal structure to facilitate the growth of single-dimensional structures, the introduction of a solid liquid interface to reduce the precursor symmetry, the use of different models with 1D morphologies to direct the formation of single-dimensional structures, the use of an over-saturation controller to modify the growth of the structure, using appropriate reagents for kinetically controlling the growth rate of the various precursor facets, the self-assembly of 0D nanostructures, and finally the reduction in the

size of 1D microstructures (Figure 1-19) [35, 36].

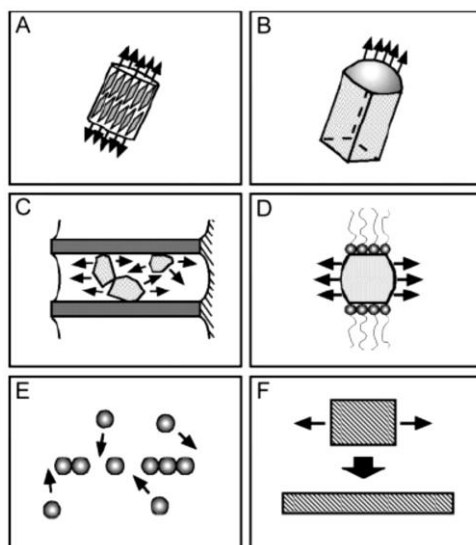


Figure 1-19- Schematic representation of six different strategies that have been developed to achieve one-dimensional growth (1D): a) the anisotropic crystallographic structure of a solid constrains growth; b) confinement from a liquid droplet as in steam-liquid-solid process; c) imposing a direction through the use of a pattern; d) kinetic control provided by a capping reagent; e) self-assembly of 0-D nanostructures; f) reducing the size of 1-D microstructures [31].

In particular, the most used methods for preparation are: drawing, template synthesis, phase separation, self assembly, melt blown, separation of multicomponent fibers and electrospinning. The electrospinning process will be further explained in detail.

1.4.4 2D structures preparation techniques

Bi-dimensional structures are structures that have two macroscopic and one nanoscopic dimensions, so commonly referred to as thin films, which are often used as protective layers for optical and electrical applications and also for sensing applications.

The most popular processes for thin film preparation can be divided into two categories: physical methods and chemical methods.

Physical methods are those that a material is physically transferred from a medium to a substrate to form the film and on the other hand, chemical methods are those which suitable chemical precursors are carried on a substrate where a chemical reaction with

thin film formation occurs [31].

In Figure 1-20 represents the most common preparation processes of thin films:

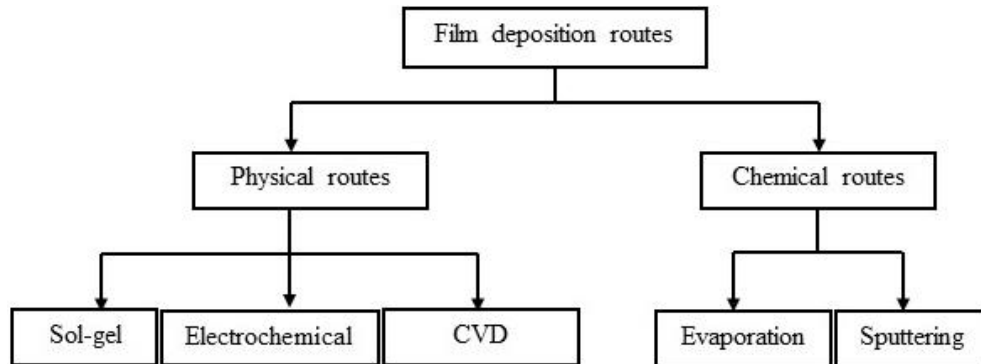


Figure 1-20- The main thin film preparation routes

1.4.5 3D structures preparation techniques

Owing to the large specific surface area and other superior properties over their bulk counterparts arising from quantum size effect, 3D NSMs have attracted considerable research interest and many 3D NSMs have been synthesized in the past 10 years. It is well known that the behaviors of NSMs strongly depend on the sizes, shapes, dimensionality and morphologies, which are thus the key factors to their ultimate performance and applications. Therefore, it is of great interest to synthesize 3D NSMs with a controlled structure and morphology. In addition, 3D nanostructures are important materials due to their wide range of applications in the area of catalysis, magnetic material and electrode material for batteries. Moreover, the 3D NSMs have recently attracted intensive research interests because the nanostructures have higher surface area and supply enough adsorption sites for all involved molecules in a small space. On the other hand, such materials with porosity in three dimensions could lead to a better transport of the molecules. In Figure 1-21, we show the typical 3D NSMs, such as nanoballs (dendritic structures), nanocoils, nanocones, nanopillars and nanoflowers [31].

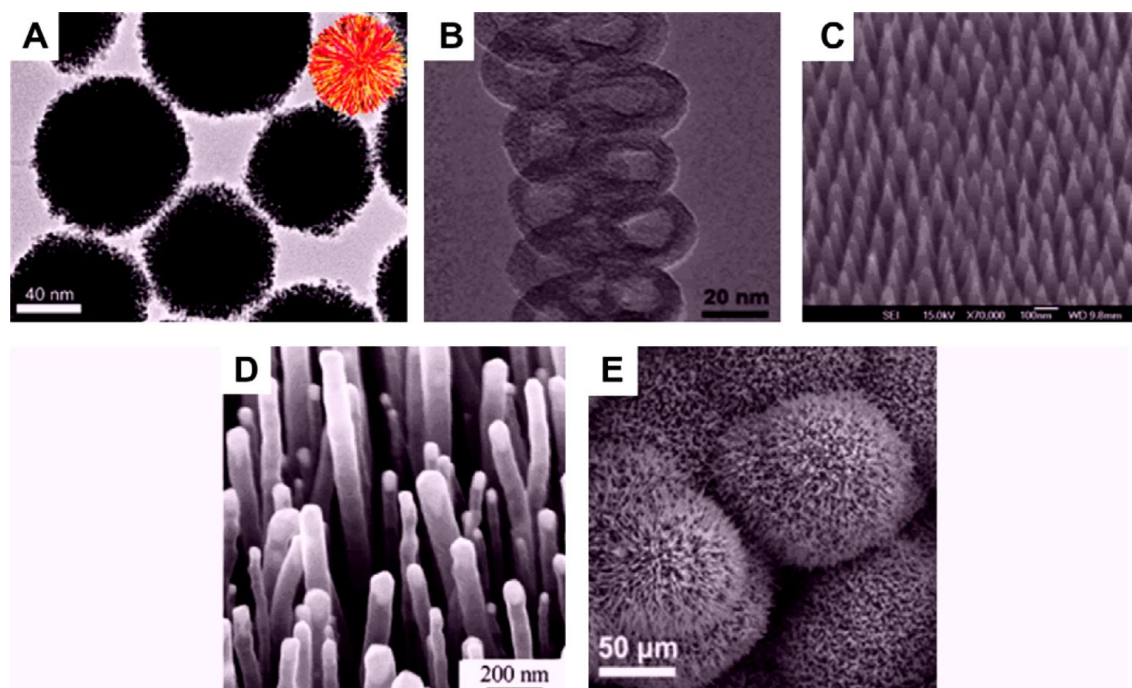


Figure 1-21- Typical SEM and TEM image of different kinds of 3D NSMs, which is synthesized by our and several research groups. (A) Nanoballs (dendritic structures), (B) nanocoils, (C) nanocones, (D) nanopillars, and (E) nanoflowers [31].

1.4.6 Hierarchical structures

Hierarchical nanostructures are top-of-the-range structures that are constructed from nano-sized constructs such as nanoparticles (0D), nanowires, nanocubes and nanotubes (1D) and nanosheets (2D). Hierarchical nanostructures show well-aligned porous structures without sacrificing the high surface area and are extremely difficult to achieve due to agglomeration tendency of oxide nanoparticles. Various hierarchical structures are classified considering the size of the nano-building blocks and the resulting hierarchical structures, referring to the dimensions of the nano-building blocks and assembled hierarchical structures respectively (Figure 1-22).

Nano Building Blocks	Hierarchical nanostructures
0-D nanoparticles	0-3 hollow
1-D nanowires, nanorods	1-1 comb 1-1 comb 1-1 Brush
	1-2 dendrite
	1-3 urchin 1-3 thread 1-3 hollow urchin
2-D nanosheets	2-3 flower 2-3 hollow flower
3-D nanocubes	3-3 hollow

Figure 1-22- Schematic of diverse 0D, 1D, 2D and 3D hierarchical structures.

For example, “1-3 urchin” describes a structure that includes nanowires / nanorods (1D) with a secondary construction to form a spherical spider (3D) curve and “2-3 flower” indicates a flower type 3D structure consisting of a hierarchical structure assembled from nanosheets (2D). Under this picture, the spherical spheres can be considered as assembling nanoparticles (1D) in a spherical spherical shape (3D). Therefore, based on what has been said, “0-3 hollow spheres” should be considered as a type of hierarchical structure [37].

1.5 Sensing applications of nanomaterials

1.5.1 Introduction

A revolutionary area using nanostructured materials is the sensor one. Sensors are devices

for detecting and measuring different features (eg temperature, pressure, lengths, electrical potential, speed, concentration of certain elements or chemical compounds, etc.) and their variations depending on time or other variables of interest for particular purposes. The sensors are therefore used for a wide variety of functions, including, for example, the monitoring and control of mechanical and electromechanical systems and the monitoring of relevant safety parameters.

1.5.2 Quantum confinement effects

Nanostructuring of materials results in changes in the conduction, magnetic, optical, thermal, mechanical properties of issues related to scale phenomena. On the other hand, nanostructuring has a significant effect on sensors performance and increases the sensitivity and selectivity of sensors through reduction in dimensions.

As previously pointed out, an important parameter of a semiconductor material is the width of the "energy gap" that separates the conduction and valence bands. In macroscopic semiconductors, the width of this gap is a fixed parameter determined by the nature of the material. However, the situation changes in the case of nanostructured semiconductor particles, smaller than 10 nm (Figure 1-23).

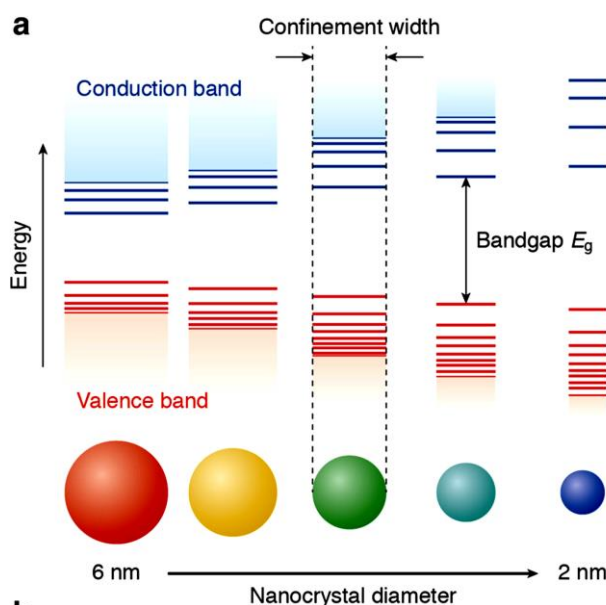


Figure 1-23- a Schematic representation of the quantum confinement effects: the bandgap (or HOMO–LUMO gap) of the semiconductor nanocrystal increases with decreasing size, while

discrete energy levels arise at the band-edges. The energy separation between the band-edge levels also increases with decreasing size [38].

This range of dimensions corresponds to the quantum confinement regime, where electronic excitations "feel" the presence of particle bounds and respond to changes in grain size by adjusting their energy spectrum. This phenomenon is known as quantum size effect, while the nanometric particles that exhibit it are often referred to as quantum dots (QD).

As the QD size decreases, the energy gap increases, leading, in particular, to a blue shift in the emission spectrum. At first approximation, this effect can be described by a simple quantum box model. For a spherical R-ray QD, this model assumes that the dependence on the energy gap dimension is simply proportional to $1 / R^2$. In addition to the growing energy gap, quantum confinement leads to a collapse of massive energy bands of massive material in discrete, or 'atomic' energy levels [38].

1.5.3 Nano Effect of Small Size of Metal Oxide Nanoparticles

In addition to the quantum size effect, the reduction in the size of nano crystals results in a so-called "small size effect": when the grain size (D) is twice as small as the thickness of the electronic emptying layer (L) then the resistance of the sensor can be quickly modulated by changing the extent of the impoverishment, obtainable through interactions with the sample gas.

As shown in Figure 1-24, a sensor is considered to be composed of partially sintered crystallites that are connected to their neighbors by necks. Those interconnected grains form larger aggregates that are connected to their neighbors by grain boundaries. On the surface of the grains, adsorbed oxygen molecules extract electrons from the conduction band and trap the electrons at the surface in the form of ions, which produces a band bending and an electron depleted region called the space-charge layer. When the particle size of the sensing film is close to or less than double the thickness of the space-charge layer, the sensitivity of the sensor will increase remarkably. Xu et al. [39] explained the phenomena by a semiquantitative model. Three different cases can be distinguished according to the relationship between the particle size (D) and the width of the space-charge layer (L) that is produced around the surface of the crystallites due to chemisorbed

ions and the size of L is about 3 nm for pure SnO_2 material in literatures. When $D \gg 2L$, the conductivity of the whole structure depends on the inner mobile charge carriers and the electrical conductivity depends exponentially on the barrier height. It is not so sensitive to the charges acquired from surface reactions. When $D \geq 2L$, the space-charge layer region around each neck forms a constricted conduction channel within each aggregate. Consequently, the conductivity not only depends on the particle boundaries barriers, but also on the cross-section area of those channels and so it is sensitive to reaction charges. Therefore, the particles are sensitive to the ambient gas composition. When $D < 2L$, the space-charge layer region dominates the whole particle and the crystallites are almost fully depleted of mobile charge carriers. The energy bands are nearly flat throughout the whole structure of the interconnected grains and there are no significant barriers for intercrystallite charge transport and then the conductivity is essentially controlled by the intercrystallite conductivity [39]. Few charges acquired from surface reactions will cause large changes of conductivity of the whole structure, so the crystalline SnO_2 becomes highly sensitive to ambient gas molecules when its particle size is small enough.

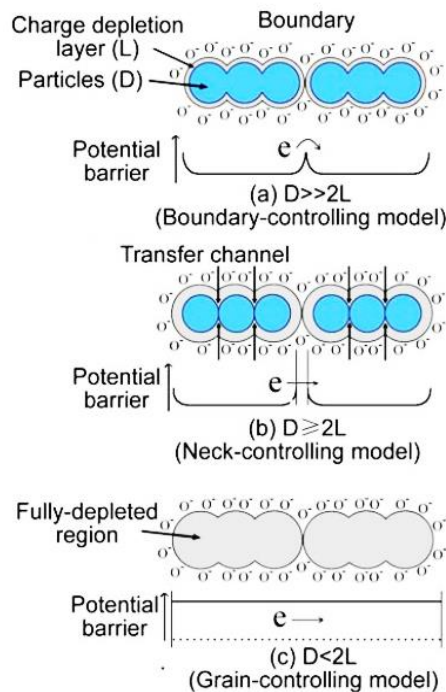


Figure 1-24- Schematic model of the effect of the crystallite size on the sensitivity of metal-oxide gas sensors: (a) $D \gg 2L$; (b) $D \geq 2L$; (c) $D < 2L$ [39].

Based on Xu's model, many new sensing materials are developed to achieve high gas sensing properties. Typically, the nanocomposite of SnO₂ and multiwall carbon nanotube (MWCNT) was exploited to detect persistent organic pollutants (POPs) which possess stable chemical properties and are ordinarily difficult to detected with metal oxides. The preparation of materials with size and porosity in the nanometer range is of technological importance for a wide range of sensing applications.

In addition to those just described, another great variety of physical properties such as mechanical strength, plasticity, sintering and alloy capacity, diffusivity and chemical reactivity, as well as crystal growth patterns (self-assembling), are dependent on the particle size. Among the modulating properties there are also thermodynamic properties (critical temperatures for phase transitions such as liquefaction, evaporation), reticular dynamics (optical and acoustic vibration modes of the lattice), optics (photoemission and absorption), electronic (work function, positions of energy levels, electron-phonon coupling), magnetic (magnetization enhancement) and dielectric performance [39].

1.6 Manufacturing processes in nanotechnology

Manufacturing processes in nanotechnology are typically divided into two general approaches: the top-down and the bottom-up manufacturing. The top-down process is that classically associated with the electronics industry. According to this approach, nanoscale devices are manufactured from larger objects, whose dimensions are gradually reduced using the lithography techniques proper to microelectronics.

The second bottom-up approach is based on the idea of assembling physical systems and devices on a nanometric scale, using appropriate mechanisms of self-organization at the atomic/molecular level. It starts from small constituent elements, normally aggregated with molecules, and attempts to control their assembly into nanostructures, using them as building blocks [39].

1.6.1 Production technologies single-dimensional (1D) and two-dimensional (2D)

A wide variety of 1D and 2D structures have been synthesized and characterized by

organic and inorganic materials. These structures have been fabricated utilizing various techniques in which one of the most important factors in the synthesis of 1D structures is controlling the composition, size and crystallinity of nanostructures.

Following, two fabrication techniques that have been widely used, specially in this thesis, will be outlined: electrospinning to fabricate 1D nanofibers and spin coating for 2D 2-dimensional structures.

1.6.2 Electrospinning

The basic principle of electrospinning technique is that, when an electrically charged solution is feed through a small opening such as nozzle, needle or pipette tip then due to its charge the solution is drawn as a jet towards an oppositely charged conducting collector plate. The solvent evaporates gradually during jet travel towards the collecting plate and a charged solid fiber is laid to accumulate at the collector. Such a simple synthesis technique was evolved in late 1930 when scientist patented the spinning of cellulose acetate fibers. But this technique suffered from some disadvantages like incomplete drying of fibers resulting in less aggregated web structure. Further, in 1940, Formhals patented another method for producing composite fiber webs from multiple polymer and fiber substrates by electrostatically spinning polymer fibers on a moving base substrate. The fundamental studies on the jet formation were carried out by Taylor in the 1960s. The shape of the polymer droplet is produced at the tip of the needle when an electric field is applied and showed that it is a cone and the jets are ejected from the vertices of the cone.

Electrospinning is based on the application of an electric field to the composite polymeric solution contained within a syringe. The loaded solution exits the needle under the thrust of a volumetric pump and forms a fluid jet which, by virtue of the electric charges, is stretched and thinned to form a fiber, due to evaporation of the solvent and repulsion between the charges. The fibers that are formed are deposited on a suitable manifold in the form of non-woven fabric (disordered deposition), obtaining micro or nanofibrose (mat) structures. ES technique is a simple and low-cost method for producing NFs in the range of nanometer (nm) to few micrometers with a large variety of materials includes such as TiO₂, ZnO, MnO₂, SnO₂, CuO, V₂O₅, WO₃, NiO and HfO₂ metal oxides [40].

The basic equipment structure of ES technique is shown in Figure 1-25.

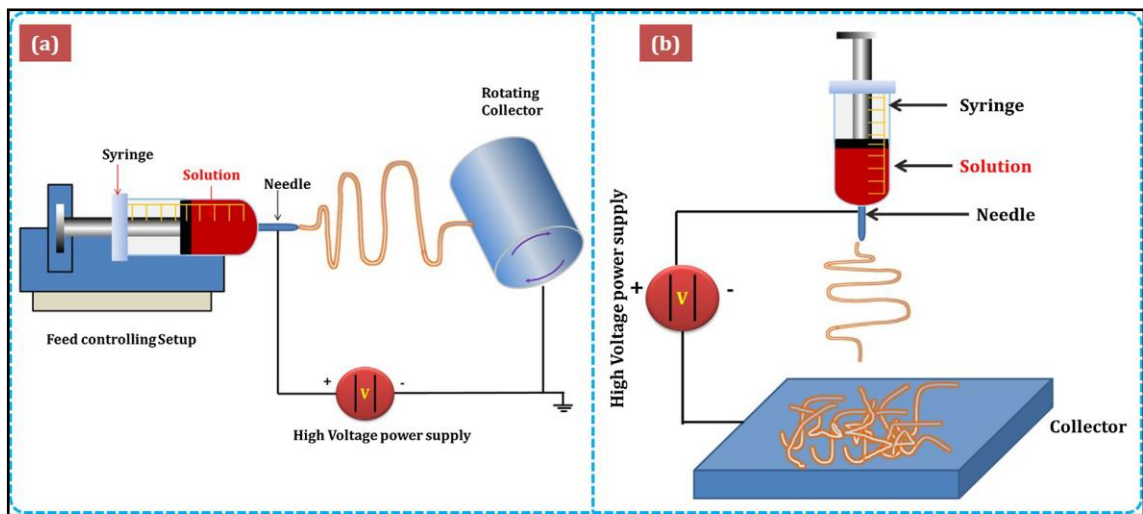


Figure 1-25- a) Horizontal electrospinning (left side) b) vertical electrospinning technique (right side).

The ES consists of several simple parts,

- polymeric solution;
- syringe pump;
- electrode in contact with solution;
- high voltage generator connected to the electrode;
- collector grounded where the fibers are collected.

The solution is contained within a syringe (a few mL); the electrode is connected to the needle of the syringe, so that the solution is loaded. At a certain distance from the needle, the earthing manifold is positioned, with nanofibers deposited on it. A syringe type pump (for very low flow rates) allows setting the flow of the solution out of the syringe. Once the generator is switched on and the desired voltage (usually between 10 kV and 20 kV) is set, one drop of the solution leaving the needle tip is deformed until it is conical due to the electric field effect, then from the cone the same part of a jet, consisting of a nanofibre, directed towards the collector (the direction of the jet is determined by the direction of the electric field). The high charge density on the jet surface causes a strong charge instability and causes the electrophilic fiber to oscillate quickly (movement is similar to that of a whip). The whiskers are so fast that they give the impression that many

nanofibers come from the single drop; in fact, jet photographs show that fiber is one and the rapidity with which the fiber moves creates an optical effect for the fibers to appear to be multiple. The nanofibre network deposited on the manifold consists of a single nanofibre that is completely random on it. The solvent (typically in solution in excess of 80%) evaporates from the needle to the collector. It would be desirable to choose a solvent, a distance between the needle and the collector and temperature to ensure that the threaded fiber is completely dry when it reaches the manifold and that the solvent is completely evaporated. Any residual charge on the nanofiber is discharged to the contact with the collector (connected to the ground) and the nanofibre membrane can be detached from the manifold. The detailed study of the ES technique depends on properties presented in table Table 1-3 and these parameters are being widely studied and optimized to fabricate nanofibers with appropriate properties [40-42].

Solution	Process	Ambient parameter
Viscosity	Applied Voltage	Temperature
Solution concentration	Distance between tip and collector	Humidity
Molecular weight	Flow rate	
Surface tension conductivity	Collector	

Table 1-3- Conditions for electrospinning techniques.

The electrophilic process is divided into several key passages, shown in Figure 1-26: casting; cast elongation; instability region (whiplash movement); fiber deposition.

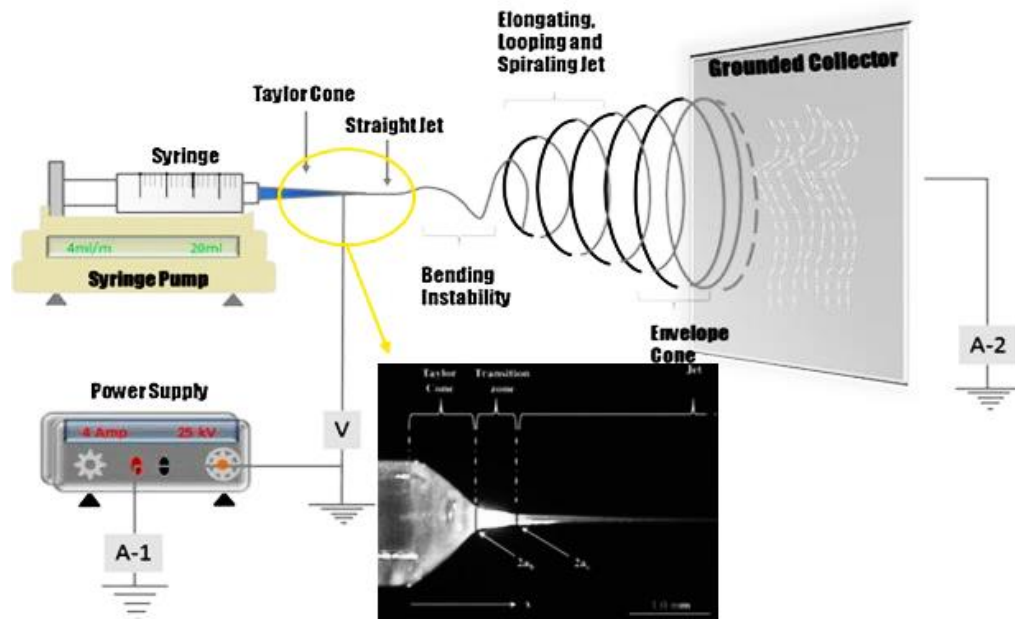


Figure 1-26- electrospinning Process Steps: jet Start; cast elongation; instability region; fiber deposition.

Starting the jet

This first step is in turn divided into two intermediate stages: the generation of the drop and the formation of the Taylor cone. During the generation of the drop the polymer solution is pumped through the needle of the syringe with very low flow rates. In the absence of an electric field, the drop on the tip of the needle will assume a shape controlled only by the gravitational force and the surface tension of the liquid; however, the stability of the drop is strongly modified under the electric field. The interaction between the loaded fluid and the external electric field causes deformations of the shape of the drop. With the increase of the outer field the shape of the drop becomes progressively longer and then, very close to the critical potential, assumes a conical shape with a characteristic semiangle of about 30° . Once a sufficiently high voltage (critical voltage) is reached, the electric force and the force of gravity are opposed to the surface tension and at this point the formation of the jet is observed [43] (Figure 1-27).

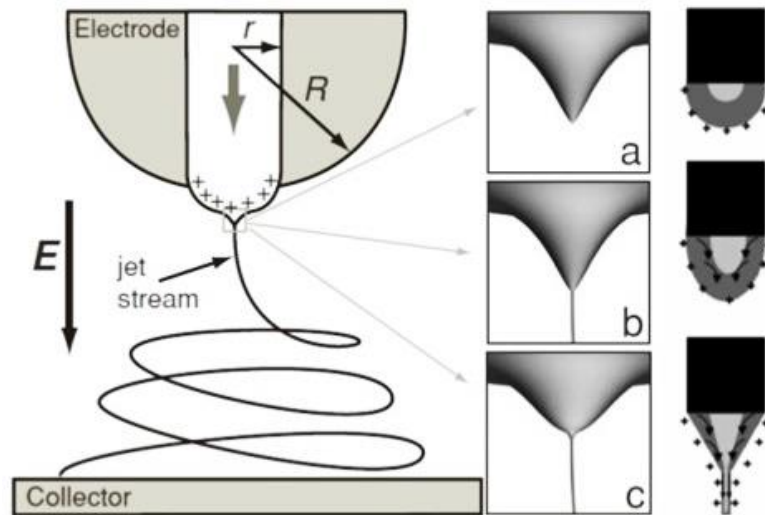


Figure 1-27- Deformation of a drop due to the introduction of an electric field. They are shown several times following the application of a high electrical potential close to the critical one [43].

In Taylor's cone formation step, at critical potential, the so-stretched drop takes the form of a cone, leaving a thin liquid jet. This cone takes its name from the one who discovered it and is referred to as Taylor's cone. It is concluded that liquids with high surface tension require higher values of critical voltage; The same applies to liquids with high viscosity and low conductivity. One important observation is that the shape of the cone is strongly modified to high electric fields, in fact it becomes more concave near the tip and tends to disappear to even larger fields, or because it moves within the needle or because strong circulation removes the fluid from the inside of the drop [44], See Figure 1-28.

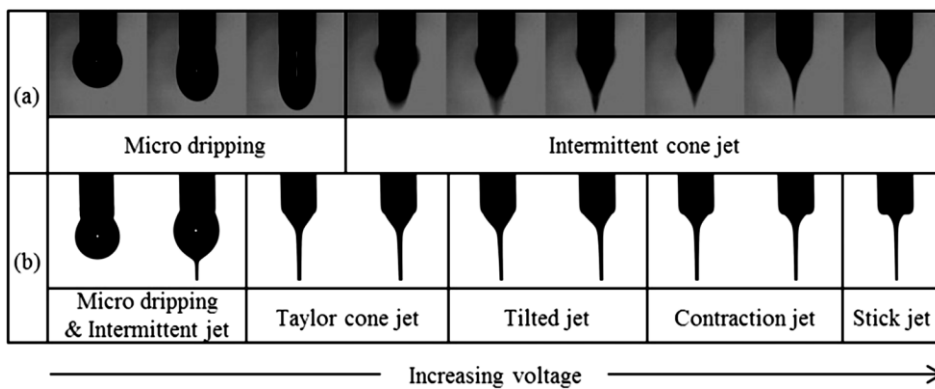


Figure 1-28- Deformation of Taylor's cone at high electrical fields [44].

Jet elongation

The jet forms almost instantly as soon as it exceeds the critical voltage value. The force of repulsion of the surface charges accumulated in the jet, since the electric field has a specific direction, itself has a direction: in particular it has an axial component that causes the elongation of the jet in its path to the collector (the direction of the electric field is in fact the needle of the syringe towards the manifold). A study conducted by Buer et al. [45] demonstrates that jet speed increases as it moves away from Taylor's cone; as a result, the diameter of the jet decreases either due to the stretching of the jet and the effect of the evaporation of the solvent. The jet therefore, increasingly accelerates towards the manifold, tapering more and more. In this first phase, the jet is stable, and its stability is due to polymer chains: the motion regime is of a laminar type.

Instability region

The jet, which for the starting line is straight, becomes unstable and in its transit to the collector begins to show a circular pattern, which is called the whipping instability. At each turn the jet becomes thinner and elongated, forming a spiral that opens like a cone towards the manifold. Figure 1-29a,b show the principle of the formation and propagation of whiplash instability: at the point where instability begins, the jet segment (shown in dotted lines) grows in response to the repulsive electrical forces between the evenly distributed charges within the cast. The charge brought by the disturbed segment is forced to move (FDO) downward and outwardly from the charges located above the disturbed region, while the same disturbed segment is pushed (FUO) upwards and outward from the charges below it. The resultant of these FR forces lies in a radial direction with respect to the straight jet and grows exponentially over time as the radial displacement of the segment increases. At the same time the repulsion of the adjacent charges in the jet causes all the curved and straight lines of the jet to continue stretching along their local axes. The elongation grows faster in the bent segments. Whiplash instability is similar to itself as the jet goes to the collector and this contributes to a sharp reduction in the diameter. The phase of friction instability, therefore, is the one most responsible for reducing the size of nanofibers during the electrospinning process. Figure 1-29c shows the straight line length of the jet and the area of instability [46].

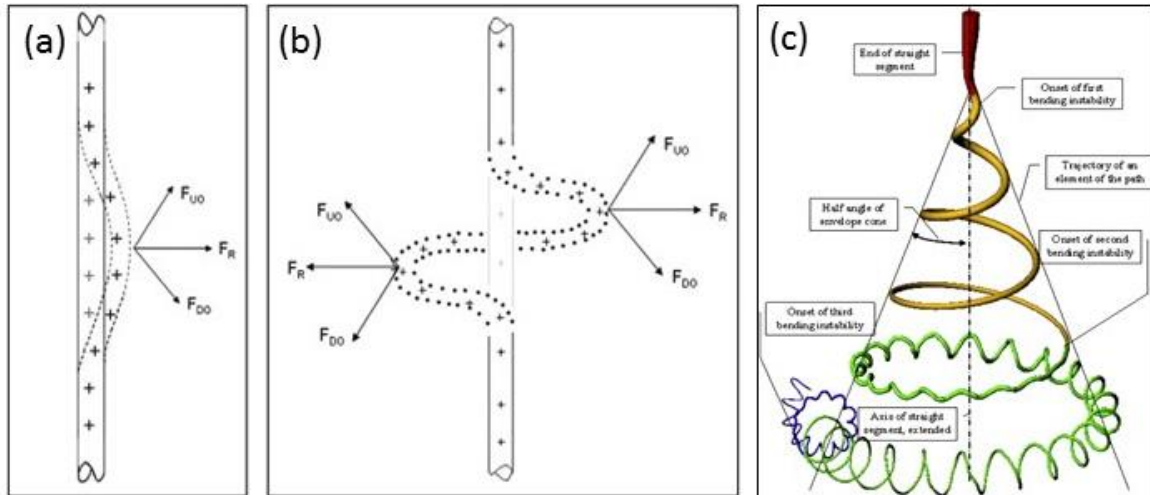


Figure 1-29- (a,b) Whipping instability propagation mechanism, (c) Schematic representation of a sequence of whiplash instability [46].

Deposition of fibers

During the passage of the jet towards the collector the solvent evaporates; what is left is composite polymer nanofibers. Ideally, there should be no trace of solvent when the jet touches the manifold, otherwise the newly formed polymeric nanofibers are again dissolved in the residual solvent. The evaporation speed of the solvent depends on several factors, including, for example, the distance between tip and collector that were previously mentioned in table Table 1-3. This phase is very important for controlling the value of fiber diameters: in fact, it is also from the evaporation rate of the solvent and the time it takes to evaporate that depends on the final size of the obtained nanofibers. In some cases, that depends on the relative humidity of the environment, the use of high concentrations of solvent or the use of polymeric materials with a glass transition temperature close to or below the environment temperature, soft fibers are deposited, which give rise to partial coalescence phenomena. Coalescence processes occur whenever two soft fibers come in contact or cross, leading to a mechanical fabric cross-linking when the solvent is evaporated [27].

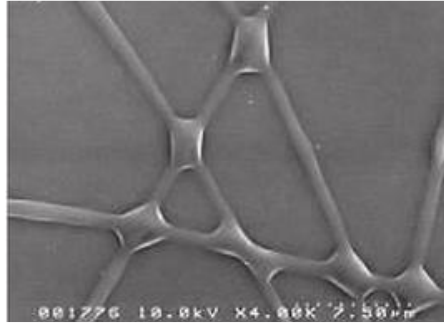


Figure 1-30- Examples of nanofibre coalescence in PLLA Fiber [27].

1.6.3 Production of Thin Film: Spin coating

The spinning process has been developed for materials used in microelectronics and is applicable on small substrates such as sensor substrates.

It is a technique of depositing an excess amount of salt prepared on a substrate, which is subsequently rapidly rotated by means of a special rotating coating (rotor); during rotation, the liquid distributes on the substrate due to centrifugal force, giving rise to a coating whose thickness depends on the balance between the centrifugal force and the viscosity of the precursor solution. The spin coating process is generally divided into four main phases:

- deposition of the solution on the substrate;
- spin-up;
- spin off;
- evaporation.

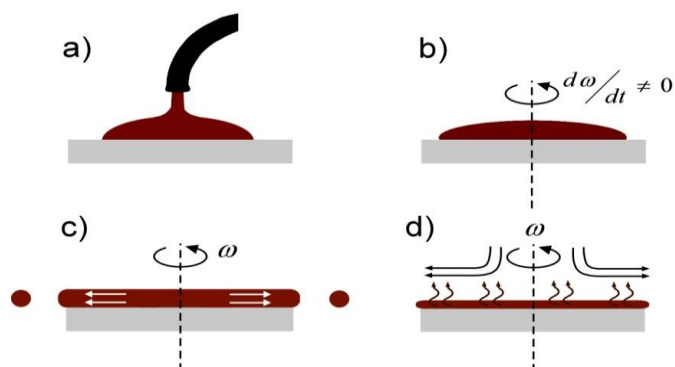


Figure 1-31- The four main types of spin coating, a) Deposition, b) Spin-up, c) Spin-off d) Evaporation.

In the first phase Figure 1-31a, a few drops of the solution are deposited on the surface of the substrate that is attached to the rotating disc of the spin coater; usually an excess of solution is deposited, compared to the amount actually requested (this is because a part of the solution is projected out of the disk). In the spin-up phase, the liquid flows radially towards the edge of the substrate, driven by the centrifugal force.

In the spin-off phase, the excess liquid exits the substrate perimeter and is ejected in the form of droplets. As the film thins, the excess amount of expelled solution decreases because the thinner the layer, the more the sliding resistance and the concentration of the non-volatile components (and therefore the viscosity) will be greater.

Evaporation is the primary cause of the screening of the film. One advantage of spin coating is that the liquid film tends to become uniform during spin-off. This trend arises from the balance between the two main forces: the centrifugal force, which drives the flow radially outward, and the friction, which acts inwardly. During spin-up, the centrifugal force exceeds the force of gravity and rapid thinning represses all inertia forces other than centrifugal force. An integral part of the deposition process is the drying phase of the film, which in the case of spin coating is done by simply evaporating the solvents at ambient temperature and pressure, leading to the formation of the so-called xerogel. If the solvent is removed from the gel under supercritical conditions and without deposition, there will be formation of an aerogel [47]. A quantitative estimate of the thickness of films produced by spinning can be calculated by following equation:

$$h = \left(1 - \frac{\delta_A^0}{\delta_A}\right) \left(\frac{3\eta e}{2 \delta_A^0 \omega^2}\right) \quad 1-20$$

where h is the final thickness of the film, δ_A is the volumetric volumetric mass per unit, δ_A^0 its initial value, and the solvent evaporation rate, η the viscosity and ω the angular velocity.

***2 Chapter 2: 2D Transition Metal
Dichalcogenides (TMDs) for
gas sensing applications***

2.1 2D semiconductors for gas sensing applications

Introduction

Among the sensing materials, metal oxides have generally advantages of high sensitivities and low cost; however, high operating temperature (OT), large power requirement, and low selectivity have been their serious drawbacks. Thus, this is important to explore novel sensing materials with high sensitivity and low operating temperature. Graphene is one of those 2-dimensional type of materials which is highly studied for gas sensing applications. Graphene is an atomic-thin layered carbon nanomaterial with a large surface-to-volume ratio, that provides large adsorbing capacity of gas molecules and strong surface activities.

In recent years, the layered inorganic analogues of graphene, such as transition metal dichalcogenides (TMDs) including MoS₂, WS₂, MoSe₂, WSe₂, ReS₂, and ReSe₂, as well as layered metal oxides (MoO₃ and SnO₂), layered group III–VI semiconductors (GaS, GaSe, and SnS₂), phosphorene, h-BN, etc., have also raised attention due to their thickness-dependent physical and chemical properties. In addition to having a large surface-to-volume ratio like graphene, these layered inorganic analogues also have semiconducting properties with an appropriate bandgap, which is attractive for modulating the transport characteristics to enhance the sensing performance.

2.1.1 Oxygen ions surface adsorption mechanism in 2D materials

As previously explained in detail in Chapter 1, in conventional metal oxide based gas sensors like SnO₂, the sensing mechanism is related adsorbed oxygen ions on their surface. In the normal operating temperature range (200 °C-500 °C), oxygen negative ions such as O₂⁻, O⁻ and O²⁻ are adsorbed on the surface of metal oxides and charge them negatively. Different gases adsorbing on metal oxides will interact with the oxygen negative ions, and change the conductivity of the metal oxides. After exposing to a reducing gas, it releases a negative charge due to the oxidation, and results in increasing the conductivity of metal oxides.

Apart from the conventional metal oxides, the gas sensing of graphene and related layered

inorganic analogues like Transition Metal Dichalcogenides (TMDs) is mainly based on the charge transfer processes, in which the sensing materials act as charge acceptors or donors. When layered materials are exposed to various gases, the charge transfer reaction happens between the sensing materials and the adsorbed gases, accompanied by different charge transfer directions and quantities, which results in different changes of the material resistance. If the sensing materials are re-exposed to air, desorption of gas molecules occurs, that cause the resistance of the sensing material to return to the initial state. Taking n-type MoS₂ as an example, Yue et al. reported the charge transfer between different gas molecules and monolayer MoS₂, and the adsorbed gas molecules include O₂, H₂O, NH₃, NO, NO₂. Figure 2-1 shows the charge density difference for the above gases interacting with monolayer MoS₂, where the red region shows the charge accumulation, while the green region shows the charge depletion.

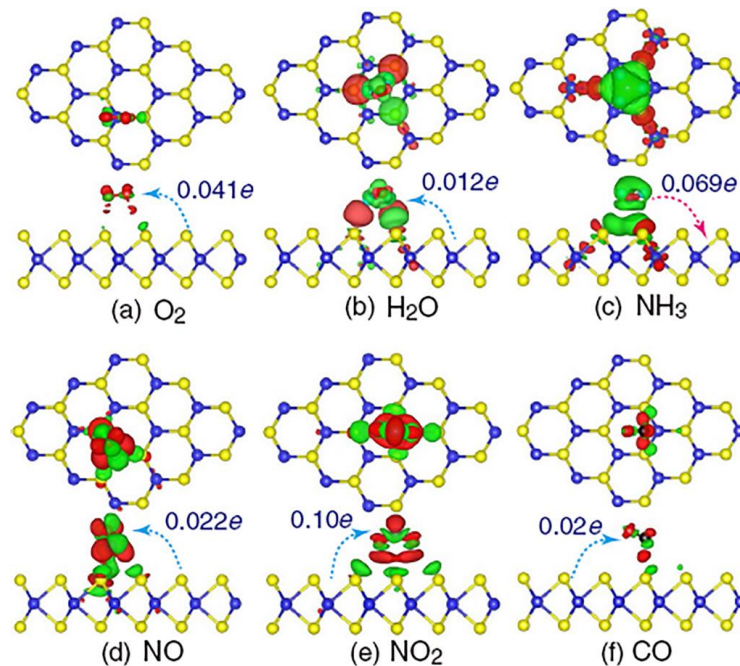


Figure 2-1- Charge transfer process and density difference plots for (a) O₂, (b) H₂O, (c) NH₃, (d) NO, (e) NO₂, and (f) CO interacting with monolayer MoS₂ [48].

Before gas adsorption, some electrons have already present in the conduction band (CB) of the n-type MoS₂ monolayer. When n-type MoS₂ exposes to these electron-accepted gases such as O₂, H₂O, NO, NO₂, and CO, the electron charges transfer from MoS₂ to the

sensitive gases, resulting in a decrease of carrier density in MoS₂. Therefore, the resistance of n-type MoS₂ increases. On the other hand, NH₃ molecules adsorbed on the MoS₂ act as charge donors and transfer electrons to the MoS₂ monolayer, and result in increasing the electron carrier density of the n-type MoS₂ monolayer, reducing its resistance [48]. The charge transfer process can be proved by observing the photoluminescence (PL) change of sensing materials before and after adsorbing of gases. Tongay et al. explored the modulation of light emission efficiency by physisorption of gases, where O₂ and H₂O acted as "molecule gating" controlling carrier density and light emission of MoS₂, MoSe₂, and WSe₂. Physisorbed O₂ and H₂O induced electron charge transfer from n-type MoS₂ and MoSe₂ to gases, and this process reduced the original carrier density of the sensing materials and depleted n-type materials (Figure 2-2(a)). As shown in Figure 2-2(b), for n-type MoS₂ and MoSe₂, neutral exciton (X⁰) was destabilized but negatively charged exciton (X⁻) recombination was relatively high, and total radiation intensity was low. After adsorbing O₂ and H₂O, X⁰ was stabilized while X⁻ was depleted due to the charge transfer, accompanied by the drastic enhancement in PL. However, the physisorption of O₂ and H₂O resulted in the opposite effect of PL for p-type WSe₂ [49].

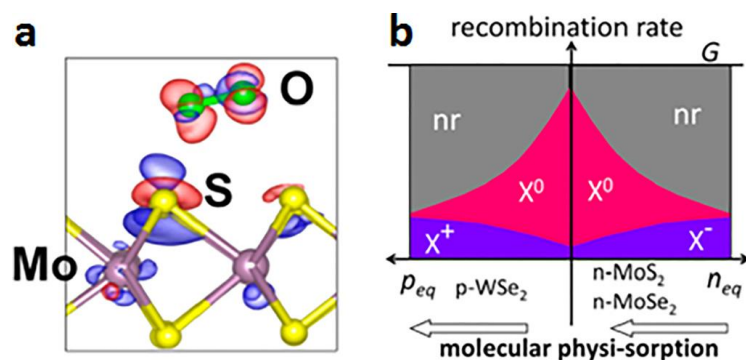


Figure 2-2- (a) Charge density difference between pristine MoS₂ and O₂⁻ adsorbed MoS₂. Red and blue represent charge accumulation and charge depletion, respectively. (b) Rate of X⁰, X⁻ and X⁺ as a function of equilibrium electron density in n-type MoS₂, MoSe₂ and p-type WSe₂ [49].

2.2 TMDs and their properties

Graphene, while being fundamentally and technologically interesting for a variety of applications, is chemically inert and can only be made active by functionalization with desired molecules [50], which in turn results in the loss of some of its exotic properties. In contrast, single-layered 2D TMDs whose generalized formula is MX_2 , where M is a transition metal of groups 4-10 and X is a chalcogen (Figure 2-3) exhibit versatile chemistry. This offers opportunities for fundamental and technological research in a variety of fields including catalysis, energy storage, sensing and electronic devices such as field-effect transistors and logic circuits.

The properties of bulk TMDs are diverse, ranging from insulators such as HfS_2 , semiconductors such as MoS_2 and WS_2 , semimetals such as WTe_2 and TiSe_2 , to true metals such as NbS_2 and VSe_2 . A few bulk TMDs such as NbSe_2 and TaS_2 exhibit low-temperature phenomena including superconductivity, charge density wave (CDW, a periodic distortion of the crystal lattice) and Mott transition (metal to non-metal transition). Exfoliation of these materials into mono- or few-layers largely preserves their properties, and leads to additional characteristics due to confinement effects. The chemistry of MX_2 compounds thus offers opportunities for going beyond graphene and opening up new fundamental and technological pathways for inorganic 2D materials [51].

2.2.1 Composition and crystal structure of TMDs

Many TMDs crystallize in a graphite-like layered structure that leads to strong anisotropy in their electrical, chemical, mechanical and thermal properties. Group 4-7 TMDs in Figure 2-3(a) are predominantly layered, whereas some of group 8-10 TMDs are commonly found in non-layered structures. In layered structures, each layer typically has a thickness of 6~7 Å, which consists of a hexagonally packed layer of metal atoms sandwiched between two layers of chalcogen atoms. The intra-layer M-X bonds are predominantly covalent in nature, whereas the sandwich layers are coupled by weak van der Waals forces thus allowing the crystal to readily cleave along the layer surface. Several studies have shown that the single layers are stabilized by development of a ripple structure as in the case of graphene [52, 53]. The metal atoms provide four electrons to

fill the bonding states of TMDs such that the oxidation states of the metal (M) and chalcogen (X) atoms are +4 and -2, respectively. The lone-pair electrons of the chalcogen atoms terminate the surfaces of the layers, and the absence of dangling bonds renders those layers stable against reactions with environmental species. The M-M bond length varies between 3.15 Å and 4.03 Å, depending on the size of the metal and chalcogen ions. These values are 15-25% greater than the bond lengths found in elemental transition metal solids, indicating limited energetic and spatial overlap of the d orbitals in TMD compounds. The metal coordination of layered TMDs can be either trigonal prismatic or octahedral (typically distorted and sometimes referred to as trigonal-antiprismatic) as shown in Figure 2-3 b and c, respectively. Depending on the combination of the metal and chalcogen elements, one of the two coordination modes is thermodynamically preferred. In contrast to graphite, bulk TMDs exhibit a wide variety of polymorphs and stacking polytypes (a specific case of polymorphism) because an individual MX₂ monolayer, which itself contains three layers of atoms (X-M-X), can be in either one of the two phases. Most commonly encountered polymorphs are 1T, 2H and 3R where the letters stand for trigonal, hexagonal and rhombohedral, respectively, and the digit indicates the number of X-M-X units in the unit cell (that is, the number of layers in the stacking sequence).

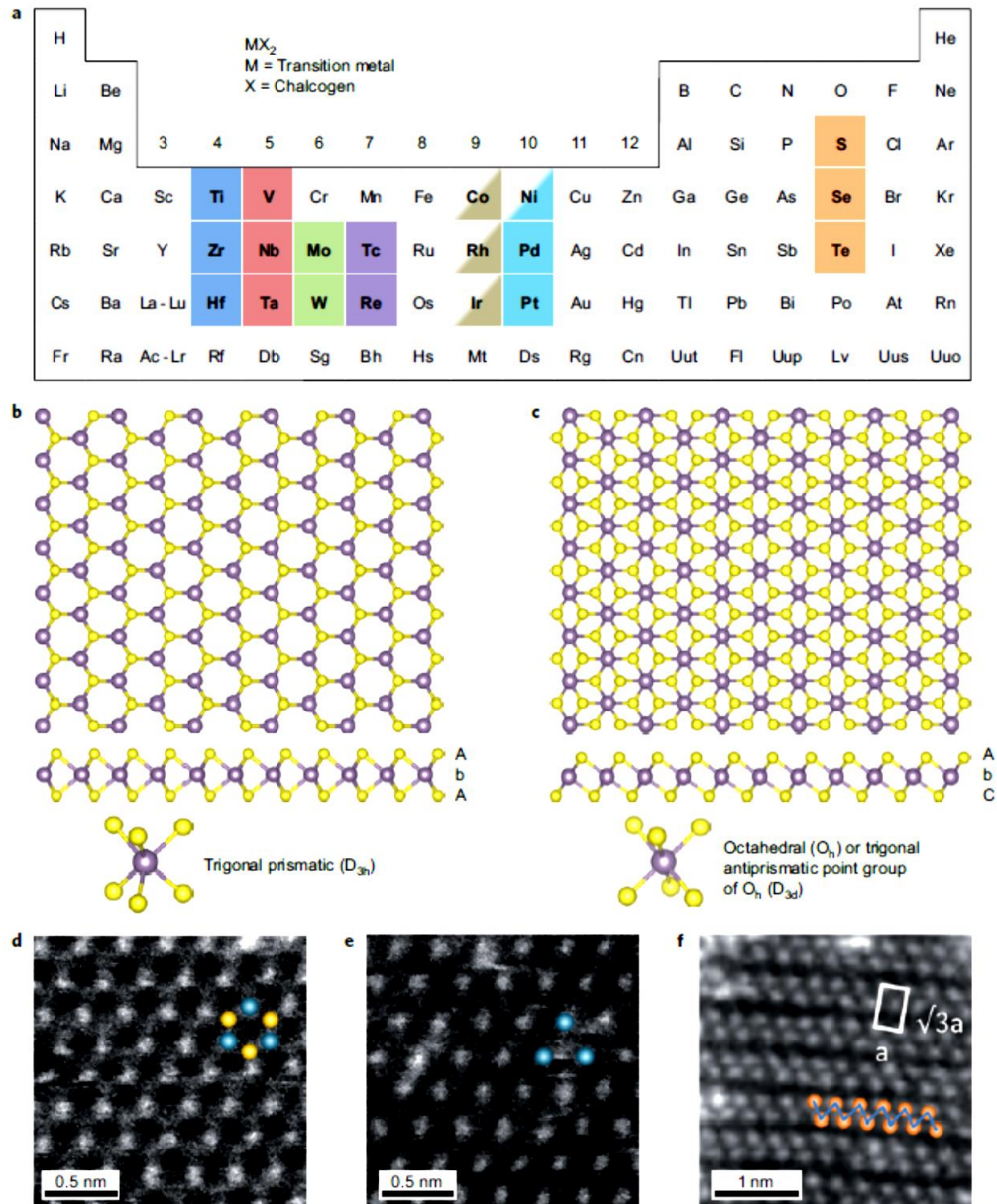


Figure 2-3- Structure of monolayered TMDs.

a) Partial highlights for Co, Rh, Ir and Ni indicate that only some of the dichalcogenides form layered structures. For example, NiS₂ is found to have pyrite structure but NiTe₂ is a layered compound.

b and c) c-Axis and section view of single-layer TMD with trigonal prismatic (b) and octahedral (c) coordinations. Atom colour code: purple, metal; yellow, chalcogen. The labels AbA and AbC represent the stacking sequence where the upper- and lower-case letters represent chalcogen and metal elements, respectively.

d and e) Dark-field scanning transmission electron microscopy image of single-layer MoS₂ showing the contrast variation of 1H (d) and 1T (e) phases. Blue and yellow balls indicate Mo and S atoms, respectively.

f) Zigzag chain clusterization of W atoms due to Jahn–Teller distortion in single layer WS₂. The

clustered W atoms are represented by orange balls. The $\sqrt{3}a \times a$ unit cell of the superstructure is indicated with a white rectangle [54].

There are three different polytypes (that is, three different stacking sequences) for 2H polymorphs. A single TMD can be found in multiple polymorphs or polytypes, depending on the history of its formation. For example, natural MoS₂ is commonly found in the ‘2H phase’ where the stacking sequence is AbA BaB (The capital and lower-case letters denote chalcogen and metal atoms, respectively). Synthetic MoS₂, however, often contains the 3R phase where the stacking sequence is AbA CaC BcB [55]. In both cases, the metal coordination is trigonal prismatic. Group 4 TMDs such as TiS₂ assume the 1T phase where the stacking sequence is AbC AbC and the coordination of the metal is octahedral. For the sake of simplicity, we will focus our attention on monolayer TMDs in the discussions below.

It should be highlighted that monolayer TMDs exhibit only two polymorphs: trigonal prismatic and octahedral phases. The former belongs to the D_{3h} point group whereas the latter belongs to the D_{3d} group. In the following discussion, they are referred to as monolayer 1H (or D_{3h})- and 1T (or D_{3d})- MX₂, respectively. These crystal phases can be differentiated using several techniques including high-resolution scanning transmission electron microscopy in annular dark field mode, as shown in Figure 2-3d and e.

Recent studies have shown that due to the lattice match of the 1H and 1T phases of MoS₂ and WS₂, coherent interfaces between domains of the two phases can also form. Additional clustering can occur owing to distortions (for example the zig-zag chain-like patterns shown in Figure 2-3f, and discussed at the end of section 2.2).

2.2.2 electronic structure

The electronic structure of TMDs strongly depends on the coordination environment of the transition metal and its d-electron count; this gives rise to an array of electronic and magnetic properties as summarized in Table 2-1. In both 1H and 1T phases, the non-bonding d bands of the TMDs are located within the gap between the bonding (σ) and antibonding (σ^*) bands of M-X bonds as illustrated in Figure 2-4a. Octahedrally coordinated transition metal centres (D_{3d}) of TMDs form degenerate d_{z^2, x^2-y^2} (e_g) and $d_{yz, xz, xy}$ (t_{2g}) orbitals that can together accommodate the TMDs’ d electrons (a maximum

of 6, for group 10 TMDs). On the other hand, the d orbitals of transition metals with trigonal prismatic coordination (D_{3h}) split into three groups, d_{z^2} (a_1), $d_{x^2-y^2,xy}$ (e), and $d_{xz,yz}$ (e'), with a sizeable gap (~ 1 eV) between the first two groups of orbitals. The diverse electronic properties of TMDs (see Table 2-1) arise from the progressive filling of the non-bonding d bands from group 4 to group 10 species.

Group	M	X	Properties
4	Ti, Hf, Zr	S, Se, Te	Semiconducting ($E_g = 0.2 \sim 2$ eV).
5	V, Nb, Ta	S, Se, Te	Narrow band metals ($\rho \sim 10^{-4}$ $\Omega \cdot \text{cm}$) or semimetals. Superconducting. Charge density wave (CDW). Paramagnetic, antiferromagnetic, or diamagnetic.
6	Mo, W	S, Se, Te	Sulfides and selenides are semiconducting ($E_g = 1$ eV). Tellurides are semimetallic ($\rho \sim 10^{-3}$ $\Omega \cdot \text{cm}$). Diamagnetic
7	Tc, Re	S, Se, Te	Small-Gap semiconductors. Diamagnetic.
10	Pd, Pt	S, Se, Te	Sulfides and selenides are semiconducting ($E_g = 0.4$ eV) and diamagnetic. Tellurides are metallic and paramagnetic. PdTe ₂ is superconducting

Table 2-1- Electronic character of different layered TMDs [55]

When the orbitals are partially filled, as in the case of 2H-NbSe₂ and 1T-ReS₂, TMDs exhibit metallic conductivity. When the orbitals are fully occupied, such as in 1T-HfS₂, 2H-MoS₂ and 1T-PtS₂, the materials are semiconductors. The effect of chalcogen atoms on the electronic structure is minor compared with that of the metal atoms, but a trend can still be observed: the broadening of the d bands and corresponding decrease in bandgap with increasing atomic number of the chalcogen. For example, the bandgap of 2H-MoS₂, 2H-MoSe₂ and 2H-MoTe₂ decreases gradually from 1.3 to 1.0 eV [55].

The preferred phase adopted by a TMD depends primarily on the d-electron count of the transition metal. Group 4 TMDs (featuring d_0 transition metal centres) are all in the octahedral structure whereas both octahedral and trigonal prismatic phases are seen in group 5 TMDs (d_1). Group 6 TMDs (d_2) are primarily found in trigonal prismatic geometry and group 7 TMDs (d_3) are typically in a distorted octahedral structure. Group 10 TMDs (d_6) are all in an octahedral structure.

It is well known that intercalation with alkali metals induces phase changes in some

TMDs. For example, lithium intercalation in 2H-MoS₂ results in transformation to the 1T polymorph [55-58]. The reverse scenario of 1T to 2H transition has also been observed in TaS₂ on Li intercalation [59]. Destabilization of the original phase may be attributed to the effective change in the d-electron count through transfer of an electron from the valence s orbital of the alkali metal to the d orbital of the transition metal centre as well as the relative change in the free energy of the two phases. Recent studies have shown that the phase transformation can be partial, producing a 2H-1T hybrid structure [54, 60]. Seifert et. Al., reported that phase stabilization of 1T through substitutional doping may be a viable route to controlled local phase transformation, in turn achieving metal-semiconductor hybrid structures [61]. As 1T-MoS₂ and 1T-Ws₂ exhibit metallic character, 1H-1T interfaces represent unique electronic heterojunctions across a chemically homogeneous layer, indicating a potential route to molecular electronics devices.

In addition to phase transformation, several TMDs develop a periodic distortion of crystal lattice (reminiscent of a CDW) under certain conditions owing to instability in their electronic structure. Typically, CDW phases are stable at low temperatures (<120 K for TaSe₂ and <40 K for NbSe₂) but this CDW-like lattice distortion has been observed at room temperature in some intercalated TMDs. The driving force for such distortions in TMDs is believed to be the ‘Jahn-Teller instability’ in which the splitting of partially filled degenerate orbitals causes a reduction of the free energy [62]. The formation of a superlattice by chain clusterization of metal atoms has been observed at room temperature in Li-intercalated MoS₂ and WS₂; an example is shown in Figure 2-3f [54]. Instead of the hexagonal arrangement with a ‘a × a’ unit cell (where a is the lattice parameter), a $\sqrt{3}a \times a$ (or $2a \times a$), $\sqrt{3}a \times \sqrt{3}a$, or $2\sqrt{3}a \times 2\sqrt{3}a$ superlattice is formed by shifting the atoms from their equilibrium position. Interestingly, the distorted phase can be metastable even after the intercalant is removed. The properties of such distorted TMDs are expected to be significantly different from that of their undistorted counterparts [63].

2.2.3 Band gap structure - From bulk to mono-few layered TMDs

Although a lot of study on bulk and chemically exfoliated TMDs have been conducted since the 1960s, a focused effort on deposition and isolation of high-quality single-layer nanosheets was re-initiated after the discovery of graphene [62]. Changes in interlayer

coupling, degree of quantum confinement, and symmetry elements lead to dramatic differences in the electronic structure of single-layer TMDs compared with the bulk counterparts. The effect is particularly pronounced for semiconducting TMDs [64, 65]. The band structures of TMDs can be calculated from first principles density functional theory (DFT). Figure 2-4b shows the band structures obtained for bulk and few- to mono-layer MoS₂, a group 6 TMD in trigonal prismatic structure. The bulk material is an indirect-gap semiconductor having a bandgap of ~1 eV with a valence band maximum (VBM) at the Γ point and a conduction band minimum (CBM) at the midpoint along Γ -K symmetry lines. In contrast, an isolated monolayer of the same material is a direct-gap semiconductor with VBM and CBM coinciding at the K-point. This indirect-to-direct bandgap transition on going from a bulk to a monolayer material arises from quantum confinement effects. The transition is manifested as enhanced photoluminescence in monolayers of MoS₂, MoSe₂, WS₂ and WSe₂, whereas only weak emission is observed in multilayered form [60, 65-68]. In the case of group 6 TMDs, the size of the monolayer bandgap is typically ~50% larger than that of bulk materials [65, 69].

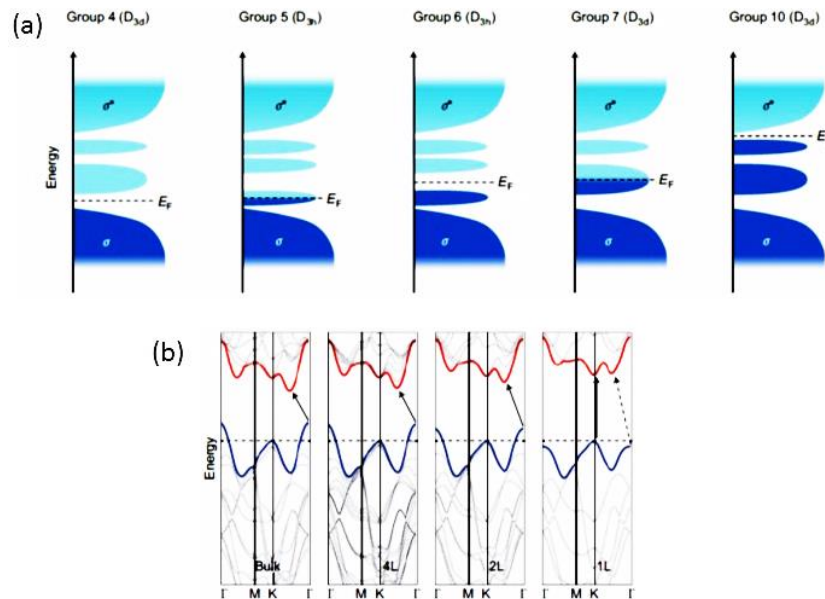


Figure 2-4- d-Orbital filling and electronic character of various TMDs.

a) Qualitative schematic illustration showing progressive filling of d orbitals that are located within the bandgap of bonding (σ) and anti-bonding states (σ^*) in group 4, 5, 6, 7 and 10 TMDs. D_{3h} and D_{3d} refer to the point group associated with the trigonal prismatic and the octahedral coordination of the transition. It should be noted that this simple model assumes ideal coordination; structural distortion often seen in many tellurides and group 7 TMDs lead to

deviation in the electronic structure. The filled and unfilled states are shaded with dark and light blue, respectively. According to ligand field theory, D_{3d} compounds form two non-bonding d orbitals, $d_{yz,xz,xy}$ (bottom) and d_{z^2, x^2-y^2} (top), while D_{3h} (or O_h) compounds exhibit three d orbitals whose character is predominantly d_{z^2} , $d_{x^2-y^2,xy}$, and $d_{xz,yz}$ (from bottom to top). When an orbital is partially filled (such as in the case of group 5 and 7 TMDs), the Fermi level (E_F) is within the band and the compound exhibits a metallic character. When an orbital is fully filled (such as in group 6 TMDs), the Fermi level is in the energy gap and a semiconducting character is observed. **b)** Energy dispersion (energy versus wavevector k) in bulk, quadrilayer (4L), bilayer (2L) and monolayer (1L) MoS_2 from left to right. The horizontal dashed line represents the energy of a band maximum at the K point. The red and blue lines represent the conduction and valence band edges, respectively. The lowest energy transition (indicated by the solid arrows) is direct (vertical) only in the case of a single layer. Indirect transition in monolayer (dashed arrow in 1L plot) is greater in energy than the direct band edge transition (solid arrow). [65, 69].

2.3 Defects in 2D TMDs

Classification of defects in 2D mono-few layered TMDs

Before discussing structural defects, the polytype structure of defect-free (or pristine) TMDs crystals will be introduced (see Figure 2-5) [70]. A single molecular layer of MX_2 is formed by an atomic trilayer which consists of two adjacent layers of chalcogen atoms (X) covalently bonded by a layer of transition metal atoms (M) forming an X-M-X layer configuration. Two possible structural polytypes have been reported for a monolayer MX_2 : the semiconducting trigonal prismatic phase (we adopt the notation 1H for monolayers; see Figure 2-5a; the 2H phase refers to bulk crystals), and the metallic octahedral prismatic phase (the 1T phase; see Figure 2-5b) [55]. In certain cases, the 1T phase is not thermodynamically stable, and its structurally distorted derivative, denominated as 1T' can be observed instead (see Figure 2-5c). When TMD crystals have more than one atomic chalcogen–metal–chalcogen (X-M-X) layer of the 1H phase bonded by van der Waals (vdW) forces, additional polytypes appear in account for variations in stacking orders. A Bernal stacking (AbA BaB) yields the 2H phase (see Figure 2-5d), while an AbA CaC BcB stacking yields a rhombohedral phase denominated as the 3R phase (see Figure 2-5 e).

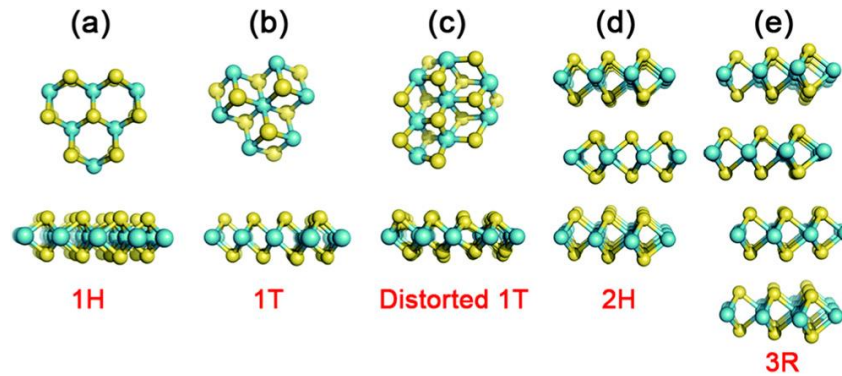


Figure 2-5- Structural polytypes of pristine TMD layers. Chalcogen atoms are shown in yellow, and transition metal atoms are shown in blue. (a) The 1H phase, (b) the 1T phase, (c) the distorted 1T, or 1T' phase, (d) the 2H phase, (e) the 3R phase. [70].

After introducing pristine crystal structures, the structural defects in mono-few layered TMDs (intrinsic and extrinsic defects in CVD grown and mechanically exfoliated nanosheets) are classified as follows. By definition, 2D TMDs could be infinitely large within their basal planes, but are only atomically thin perpendicular to the planes. Consequently, defects residing in these 2D crystals could be classified according to their dimensionality as zero-dimensional (point defects, dopants or non-hexagonal rings; see Figure 2-6a), one-dimensional (grain boundaries, edges, and in-plane heterojunctions; see Figure 2-6b) and two-dimensional (layer stacking of different layers or vdW solids, wrinkling, folding, and scrolling; see Figure 2-6c).

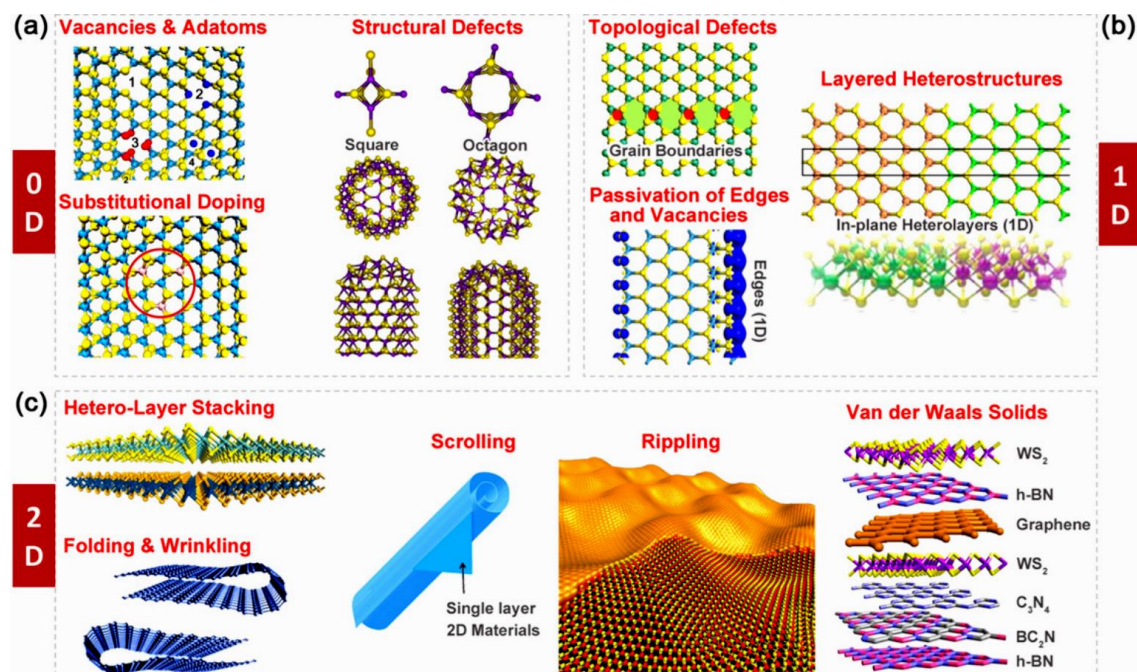


Figure 2-6- An overview of defects in 2D TMDs. (a) Typical zero-dimensional defects such as vacancies, adatoms, dopants, squares, and octagons. [71, 72] (b) Typical one-dimensional defects such as grain boundaries, edges, and phase interfaces. (c) Typical two-dimensional defects such as folding, wrinkling, scrolling, rippling, and vertically stacked hetero-layers [73-75]

2.3.1 Zero-dimensional defects in TMDs

The simplest and most abundant defects in TMDs are vacancies, and the anti-sites that form on them (see Figure 2-6a). In synthetic TMD samples, six varieties of intrinsic point defects are observed with regularity (see Figure 2-7a): single sulfur vacancies (V_S), double sulfur vacancies (V_{S_2}), a vacancy of a Mo atom and a triad of its bonded S within one plane (V_{MoS_3}), a vacancy of a Mo atom and all six of its nearest neighbors (V_{MoS_6}), an antisite, with Mo occupying a V_{S_2} (MoS_2), and a pair of S atoms occupying a Mo position (S_{2Mo}). The notable absence of V_{Mo} from this list is likely due to its tendency to complex with sulfur vacancies. With the exception of MoS_2 , reconstruction of the structure is minimal upon forming vacancies, and the defects retain trigonal symmetries [76, 77]. It is also possible for other atomic species to replace lattice atoms by substituting elements. When considering the extent to which a foreign atom may substitute onto a crystal lattice,

the ion's relative size, electronegativity, valence, and end member crystal structure are all relevant factors. The lanthanide contraction is a fortuitous periodic trend, which results in comparable radii for the 4d and 5d transition metals. This makes possible a wide variety of dopants from across the transition metal block. Notably, the similarity of W and Mo based on the criteria enumerated above allows for the formation of complete solid solutions in monolayer crystals [78].

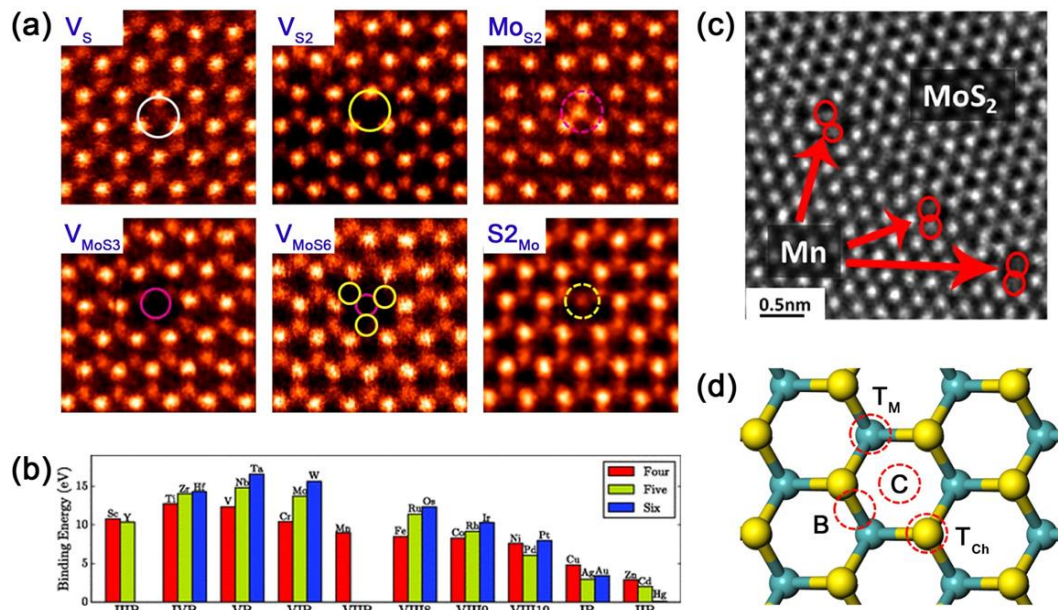


Figure 2-7- Zero-dimensional defects. (a) Atomic-resolution annular dark field (ADF) images showing different types of vacancy and vacancy complexes in MoS_2 monolayers. (b) Comparison of binding energies for MoS_2 monolayers doped with transition metal atoms. Red, green and blue symbols correspond to dopants in group four, five and six, respectively. (c) TEM image showing MoS_2 monolayers substitutionally doped by Mn atoms, (d) A schematic diagram showing four sites of adatoms adsorbed onto TMD lattices [80].

2.3.2 One-dimensional defects in TMDs

Extrinsic sulfur line vacancies result from the agglomeration of sulfur vacancies which are usually produced by electron bombardment. Single- and double line vacancies are observed experimentally, both aligned along the zig-zag direction (see Figure 2-8a and b). This experimental result agrees with calculations which determine the formation energy of sulfur line vacancies in the zig-zag direction exhibit lower formation energies than those along the armchair direction. In all cases, the formation energies of line

vacancies are a function of the number of vacancies, in the range of 5-6 eV per vacancy for lengths of 6-16. When the freestanding edge regions are imaged by TEM, the orientation of line defects also depends on the strain. Thus, strain may serve as a means to select line vacancy orientations for tuning electronic properties [81] [82].

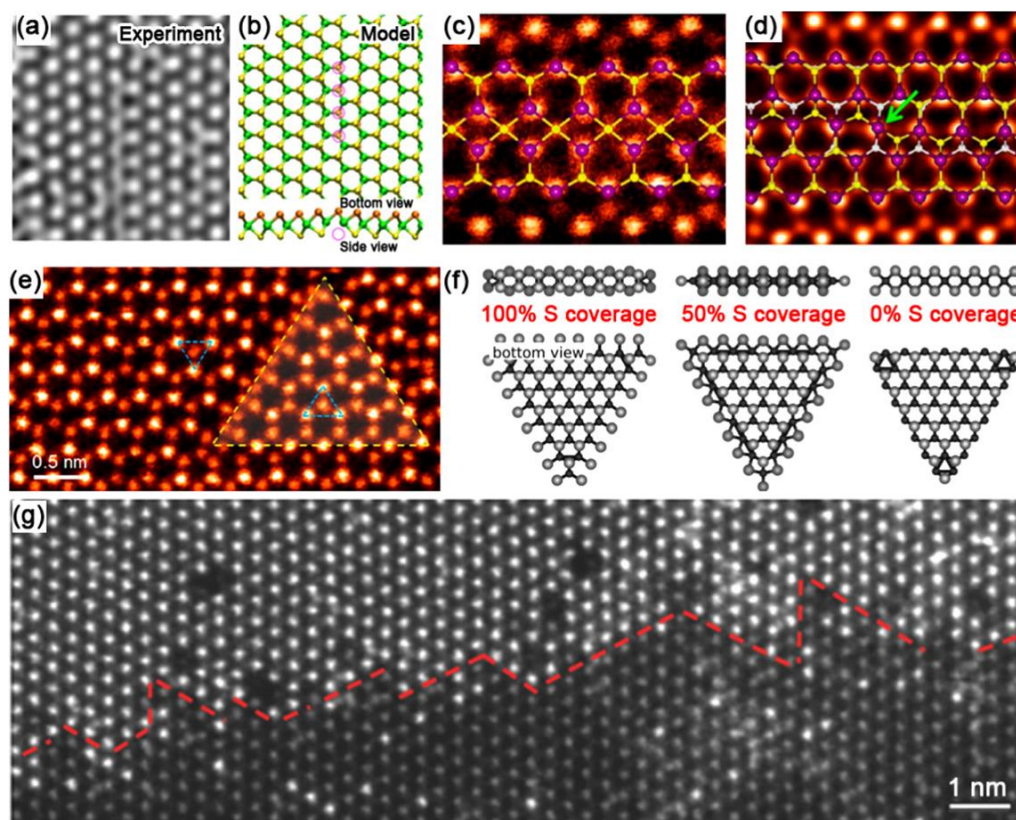


Figure 2-8- One-dimensional defects. (a) High-resolution transmission electron microscopy (HRTEM) image and (b) structural model showing a single vacancy line in MoS₂ monolayers.

(c) and (d) ADF images of 4|4P and 4|4E 60° grain boundaries in CVD MoS₂ monolayers. Structural models are overlaid on ADF images. (e) ADF image showing an inversion domain in monolayer MoSe₂. (f) Structural models showing Mo-terminated MoS₂ domains edges with different percentages of sulfur coverage. (g) ADF image showing a 1D interface between monolayer MoS₂ and WS₂ [72].

In addition to sulfur line vacancies, grain boundaries are often observed in TMD monolayers. In comparison to one-atom-thick materials, TMD grain boundaries and the dislocation cores they are comprised of are quite complex. This is because three atomic layers compose TMD monolayers (i.e. chalcogen-metal-chalcogen). As atoms are removed, the structure relaxes in three dimensions, to form dreidel shaped dislocations

with a variety of ringed motifs that are dependent on the grain boundary angle [79].

5 Patterns of two point-sharing four member rings (4|4P) form mirror twin grain boundaries in synthetic MoS₂ and MoSe₂, when grains meet at 60° angles along the zig-zag direction (see Figure 2-8c and d). 4|4E metallic edge-sharing line defects are another possible 60° grain boundary morphology, which can result in triangular inversion domains with metallic edges (see Figure 2-8e). The situation becomes more complex for smaller angles, with 4|6, 4|8, 5|7, and 6|8 motifs appearing. HAADF-STEM shows that on these low angle, and high strain (up to 58%) grain boundaries, sulfur atoms are quite mobile, even under low accelerating voltages, resulting in dislocation movement [76, 83, 85].

We now turn our attention to the most prominent defects in TMD flakes, their edges. Synthetic TMD single-crystalline islands most often adopt triangular shapes with edges that appear sharp in microscopic images. The triangular morphology of these flakes can be explained through the 2D application of the Wulff construction, which simply states that low energy edges will be preferred. These surface energies are a function of the μ_S , or the sulfur vapor potential. When μ_S is low (i.e., under low sulfur vapor pressures), MoS₂ will adopt distorted hexagonal shapes rather than triangles. Nanoscale calculations predict that under the sulfur rich conditions prevalent during TMD growth, (1010) Mo edges with either 50% or 100% S (see Figure 2-8f) are the most thermodynamically stable. Nevertheless, in CVD grown samples the Mo-terminated edges with both 0% and 50% S coverage have been observed, suggesting that CVD is a process away from equilibrium. Lateral hetero-interfaces constitute another form of 1D defect. Lateral (inner/outer) heterostructures of MoS₂/WS₂, MoSe₂/WSe₂, MoS₂/MoSe₂, and WS₂/WSe₂ have been reported recently. Structurally coherent sharp interfaces (see Figure 2-8g) have been observed as a result of covalent epitaxy between two dissimilar TMD layers with similar lattice constants [72, 76, 84].

2.3.3 Two-dimensional defects in TMDs

Perfect 2D materials have been predicted by theories as unstable upon thermal fluctuation, but after the discovery of graphene, it has gradually become clear that suspended graphene could be stabilized by the formation of ripples, i.e., finite surface roughness and

deformation. Similarly, ripples with a typical height on the order of nm have been observed in as-synthesized MoS₂ monolayers (see Figure 2-6c) and can be generated deliberately by scanning a laser beam over MoS₂ monolayers. Ripples introduce strain into the materials and could well affect their electronic properties. In few-layered TMDs, adjacent layers are coupled by vdW forces. The magnitude of vdW forces depends sensitively on the interlayer spacing, which is correlated to stacking configuration. Most synthetic few-layered TMDs exhibit a Bernal stacking (AbA BaBK), but derivations from this stacking configuration are also possible, especially when TMD layers are stacked manually via transfer techniques. Due to the handling of TMDs, it is also possible for flakes to fold over onto themselves. For those that assume the 1H phase, folding produces a structure distinct from the 2H phase. The vdW interface has strong impact on the electronic and optical properties of few-layered TMDs, therefore the interface associated with a stacking and layer orientation can be viewed as a 2D defect (see Figure 2-6c) [52, 86-89].

There is a large family of known 2D materials, such as graphene, hBN, TMDs, and layered oxides. Given the similarity in their interlayer ‘bonding’, 2D materials of different kinds can be placed one on top of another, forming vertical heterostructures or vdW solids (see Figure 2-9a). When the top layer (e.g. MoS₂) has a crystal structure similar to the bottom layer (e.g. graphene) (see Figure 2-9b), their stacking occurs via vdW epitaxy. Compared to covalent epitaxy where adjacent layers are covalently bonded, vdW epitaxy is more tolerant to lattice mismatch between layers, thereby allowing a variety of 2D materials to be stacked in this way. The interfaces between vertical hetero-layers can also be viewed as 2D defects which generate new properties in the materials (see Figure 2-6c). The structure and electronic properties of TMD have been predicted for a wide number of TMD materials: the semiconducting TMDs of Mo and W become semi-metallic, while metallic NbS₂ and NbSe₂ become small gap semiconductors. Therefore, achieving defect control in these 2D systems is very important in order to tailor their electronic properties [90-92].

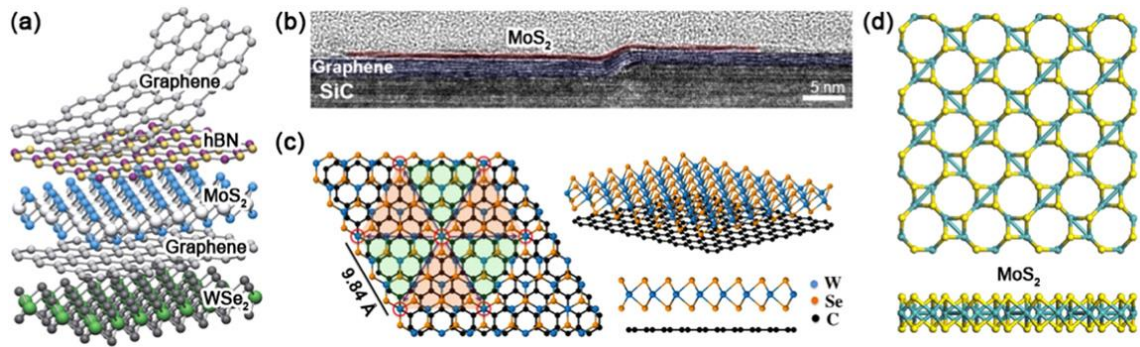


Figure 2-9- Two-dimensional defects. a) Schematic representation of vdW heterostructures made by stacking different 2D materials. b) Cross-sectional transmission electron microscopy (TEM) image showing a 2D interface between MoS₂ and graphene layers. (c) Structural model showing a Moiré pattern in vertically stacked monolayer WSe₂ and graphene. (d) Relaxed structural models showing 8–4 MoS₂ Haeckelites [92].

2.4 Chemical air stability and Ageing of 2D TMDs

It is well understood that a monolayer of trigonal prismatic semiconducting TMDs exhibits a direct band gap (in the range 1.52 eV) that it is not present in few-layered systems. This direct band gap is what differentiates monolayer TMDs from other 2D materials such as graphene, which is a zero band gap semimetal.

Oxidation and degradation can alter the electronic properties of MX₂ TMD monolayers, with the corresponding impact on the electrical performance of any TMD-based device. Studies show the degradation of TMDs at elevated temperatures higher than 250 °C, or under UV and heat and moisture. Unlike the fast degradation of black phosphorus in air, TMDs have been considered as air-stable semiconductors under ambient conditions. but Koratkar and his group investigated the long-time air stability of mono layer WS₂ and MoS₂ and showed the susceptibility and large scale structural and morphological changes to the sheets and intense degradation of TMDs to ambient degradation. Their study indicates that the generally accepted view that monolayer TMDs are air-stable materials under ambient conditions is incorrect and adsorption of organic materials from the ambient and the gradual oxidation of TMDs occur along grain boundaries over a period of months.

Figure 2-10b shows WS₂ monolayer after being stored at room temperature (~25°C) in a container with desiccant for 1 year, that cracks formed in all the WS₂ sheets, especially along the grain boundaries. WS₂ monolayers that were exposed to moisture-rich conditions (i.e., without drying desiccant) at room temperature went through even more severe structural and morphological changes over the 1-year period, as shown in Figure 2-10c (almost the entire WS₂ sheet exhibits visible degradation). Figure 2-10b and c indicate that high-humidity conditions severely accelerate the degradation of WS₂. Additionally, MoS₂ showed similar graduation deterioration, with the grain boundaries and edges first being oxidized in 6 months and almost the whole crystal in 1 year (Figure 2-10d–f) [94].

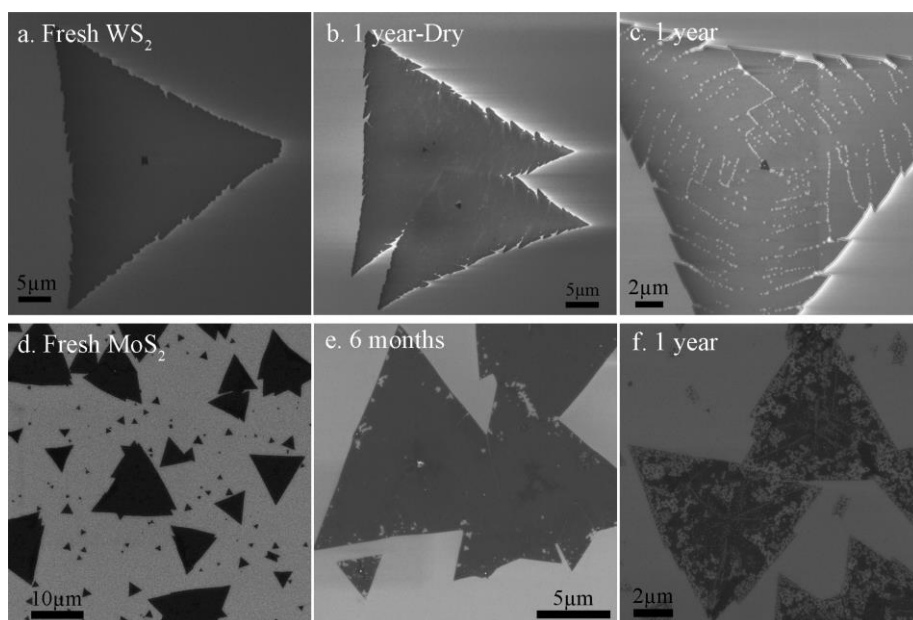


Figure 2-10- Scanning electron microscopy (SEM) images of (a) fresh WS₂, aged WS₂ after 1 year in a container (b) with and (c) without desiccant, (d) fresh MoS₂, and (e) aged MoS₂ after 6 months without desiccant and (f) after 1 year without desiccant. All the samples were stored in Class 100 cleanroom conditions [94].

Figure 2-11 illustrate the integrated PL intensity map of a typical fresh WS₂ sheet (the optical image of the flake is shown in the inset image). Figure 2-11b shows the corresponding PL mapping and the optical image (inset) of typical 1-year-old WS₂ sheets. There is significant spatial variation in the PL intensities in Figure 2-11b, with certain regions exhibiting severe PL quenching indicative of extensive damage to the samples.

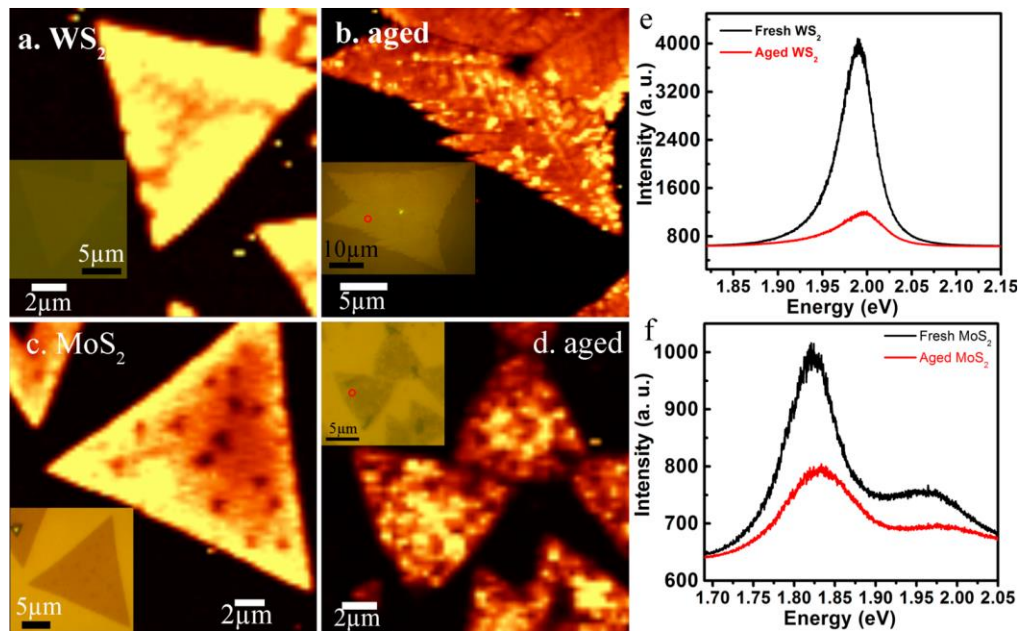


Figure 2-11- Photoluminescence spectra of fresh and aged TMDs. PL intensity map (centered at the A exciton) of fresh WS₂ (a), WS₂ aged for 1 year under ambient conditions (b), fresh MoS₂ (c), and MoS₂ aged for 1 year under ambient conditions (d). The inset optical images show the WS₂ and MoS₂ flakes from which the data were taken. (e, f) Representative PL spectra of the fresh and 1-year-aged WS₂ (e) and fresh and 1-year-aged MoS₂ (f). Both the monolayer WS₂ and MoS₂ films were aged for 1 year under ambient conditions (i.e., room temperature and atmospheric pressure).

An important observation from the measured PL spectra (Figure 2-11e) is that the PL intensity of the 1-year-aged WS₂ sample is almost 6 times smaller than the fresh WS₂, that indicates intensive PL quenching due to the oxidation of the WS₂ nanosheet.

Figure 2-11c shows PL mapping and the optical image (inset) of a typical freshly grown MoS₂ sheet, while Figure 2-11d shows the PL mapping of a typical 1-year-old MoS₂ sample showing significant PL quenching and spatial variation in the PL intensity. The PL spectrum (Figure 2-11f) of MoS₂ is mainly dominated by neutral A-exciton emission, along with B-exciton emission arising from the spin-orbital splitting of the valence band, ~150 meV away from the A peak.

To study the chemical nature of the aging process, J. Gao et al., studied the room temperature XPS measurement of fresh and 1-year aged WS₂ and MoS₂, see Figure 2-12.

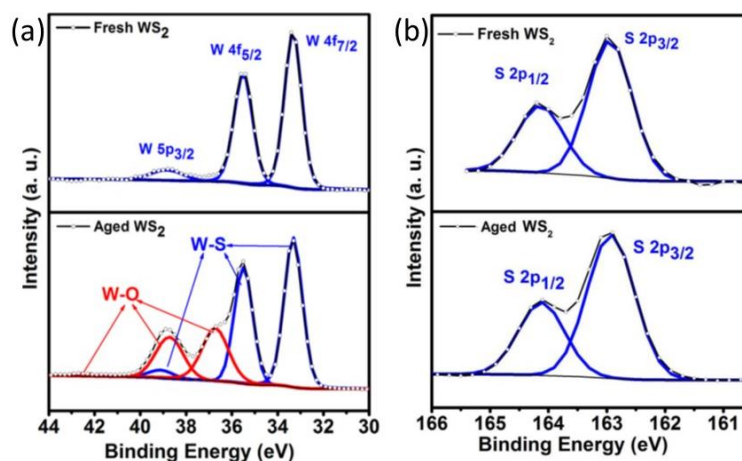


Figure 2-12- XPS spectra (calibrated using the adventitious carbon C 1s peak) of fresh and 1-year-aged WS₂ (a) and fresh and 1-year aged MoS₂ (b) showing W 4f (a), Mo 3d (b), with Gaussian-Lorentzian fitting of each peak. The W 4f (Mo 3d) contributions exhibit two distinct sets of peaks after 1 year.

In fresh WS₂, the W:S ratio is $\sim 1:2$, with only one chemical state doublet in the W 4f core-level spectra (with W 4f_{7/2} at 33.4 eV and W 4f_{5/2} at 35.5 eV). However, the W:S ratio after one year is reduced to 1:1 in the aged WS₂, indicating intense sulfur loss (Figure 2-12a). Furthermore, the W 4f core-level spectra recorded from the aged WS₂ samples show an additional doublet feature at higher binding energies (~ 3.1 eV), indicating the presence of tungsten in a higher oxidation state than pristine WS₂. The three new peaks (red curves) with higher binding energy originate from the oxidized W (W-O), and the remaining three peaks (blue curves) are corresponding to the S-bound W (W-S). It should be noted that the sulfur is still bound exclusively to W without exhibiting any extra chemical states, as shown in the Figure 2-12 b.

This result suggests that, in addition to the “oxidation” of the transition metal, oxygen is also present in the aged sample in the form of “organic contaminants” that are adsorbed onto the aged sheets. The XPS analysis did not indicate the formation of any sulfur oxide (SO_x) under ambient conditions for the aged TMD samples, which indicates that S atoms are being displaced by oxygen in these films.

J. Gao et al., concluded that the S loss mechanism during aging is not clear and suggested that one possibility for S loss is that O is first bonded to S, followed by breaking of the S-metal bond, followed by substitution of the S by O or OH radicals. Such processes are

likely initiated or catalyzed at regions with S deficiency (such as defects and grain boundaries) and then gradually propagated throughout the entire TMD sheet [94].

2.5 Transition metal dichalcogenide sensors

In the recent years the isolation of 2D TMDs has raised the interest in this field. 2D layered TMDs consist of a plane of metal atoms covalently bonded to the chalcogen atoms. 2D TMDs have superior molecular sensing capability due to their unique physical and chemical properties as mentioned above, such as semiconducting property, high surface-to volume ratio (impact ratio), sizable bandgaps, high absorption coefficient, and availability of reactive sites for redox reactions. Following the gas sensing of two of most studied TMDs, MoS₂ and WS₂ will be discussed.

2.5.1 MoS₂ sensors

The bulk MoS₂ possesses an indirect bandgap (1.2 eV), while the bandgap of monolayer MoS₂ becomes direct and wider (1.8 eV). The MoS₂ monolayer consists of one layer of Mo atoms sandwiched between two layers of S atoms, and the adjacent S-Mo-S sheets are held together by van der Waals interactions. Micromechanically exfoliated MoS₂ flakes have been used to fabricate gas sensors, which demonstrate excellent sensing characteristics. Zhang et al. fabricated MoS₂ films with different thicknesses using the micromechanical exfoliation, and the obtained single- and multilayer MoS₂ films were used in field-effect transistors (FETs) for the detection of NO the obtained sensor was an n-type semiconductor. On the contrary, the FET sensors based on bilayer (2L), trilayer (3L), and quadrilayer (4L) MoS₂ films exhibited both stable and sensitive responses to NO with a detection limit of 0.8 ppm.

Figure 2-13 c and d show the sensing behavior of the two FETs upon exposure to NH₃ and NO₂. It can be seen that the resistance of both FETs decreases when exposed to NH₃ but increases upon exposure to NO₂. For n-type semiconducting MoS₂, NH₃ acts as an electron donor while NO₂ acts as an electron donor, which confirms the charge transfer mechanism. The five-layer MoS₂ sensor shows better sensitivity than that of the two-layer

device, due to the different electronic structure in samples with dissimilar thickness [95].

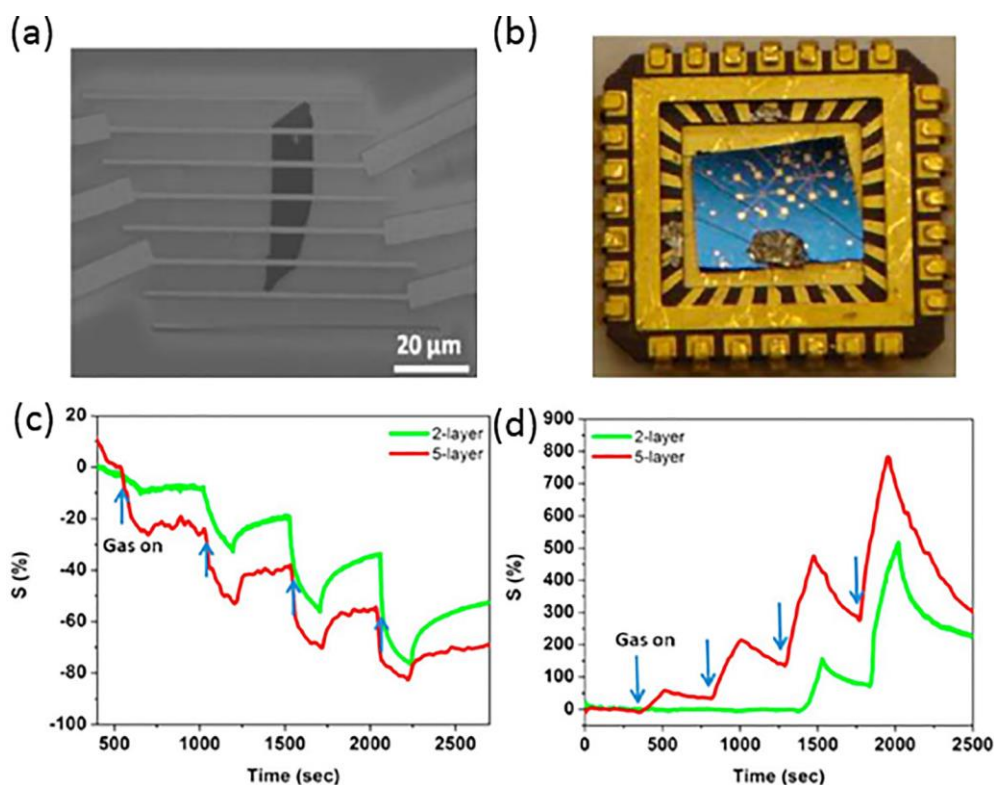


Figure 2-13- (a) SEM image of a two-layer MoS₂ transistor. (b) Optical image of the MoS₂ sensor on the chip. Comparison of cyclic sensing performances between two-layer and five-layer MoS₂ devices to (c) NH₃ and (d) NO₂ (for 100, 200, 500, 1000 ppm).

Donarelli et al. reported on MoS₂-based resistive-type gas sensors which exhibited sensing response to both oxidative (NO₂) and reducing (relative humidity and H₂) gases. Two types of gas sensors were fabricated by depositing liquid-chemically exfoliated MoS₂ flakes on prepatterned Si₃N₄ substrates and then annealing in air at 150°C and 250°C, respectively. The "150°C annealed" MoS₂-based device showed a p-type conductivity in the whole 25-200°C operating temperature (OT) range when exposing to NO₂ and 50% relative humidity, ascribing to nitrogen substitutional doping of S vacancies on the MoS₂ surface. This device was not sensitive to 1 ppm NO₂ at room temperature, while it showed significant resistive changes at higher OTs; in particular, it exhibited good NO₂ response at 150°C or 200°C. Alternatively, the 250°C annealed" MoS₂-based device showed an n-type behavior to NO₂, H₂, as well as relative humidity, attributing to the increase in S vacancy concentrations and the occurrence of partial surface oxidation of MoS₂ into

MoO₃. This device showed outstanding sensing performances to NO₂ at 200°C, with a detection limit of 20 ppb and response intensity equal to 5.80 at 1 ppm concentration. Also, it showed good electrical response to H₂. In addition, both p- and n-type sensors were sensitive to relative humidity [96].

MoS₂ is usually used as a good gas-sensing material due to its various active sites (sulfur defect, vacancy, and edge sites of MoS₂) for selective molecular adsorption, together with the semiconducting behaviors and large surface- to-volume ratio. For example, Jung et al. synthesized three distinct MoS₂ films with different alignment directions to compare the effect of the MoS₂ alignments on their gas adsorption properties. Various MoS₂ alignments were prepared by using rapid sulfurization of predeposited Mo seed layers with different thicknesses during CVD process, including (1) horizontally aligned MoS₂, (2) mixture of horizontally and vertically aligned MoS₂ layers, and (3) vertically aligned MoS₂. The vertically aligned MoS₂ had superior sensing performance to NO₂ gas molecules (about 5-fold enhanced sensitivity) compared to the horizontally aligned MoS₂ (Figure 2-14). The electrical response to NO₂ molecules correlated directly with the density of exposed edge sites of MoS₂, due to the high gas adsorption onto the edge sites of vertically aligned MoS₂. DFT calculations showed that multiple configurations were along the edge sites of MoS₂ with stronger NO₂ binding energies, verifying the experimental results. These results provided clear comparison of gas adsorption properties between the edge and the terrace sites of MoS₂ and significantly enhanced MoS₂ based gas-sensing performance [95].

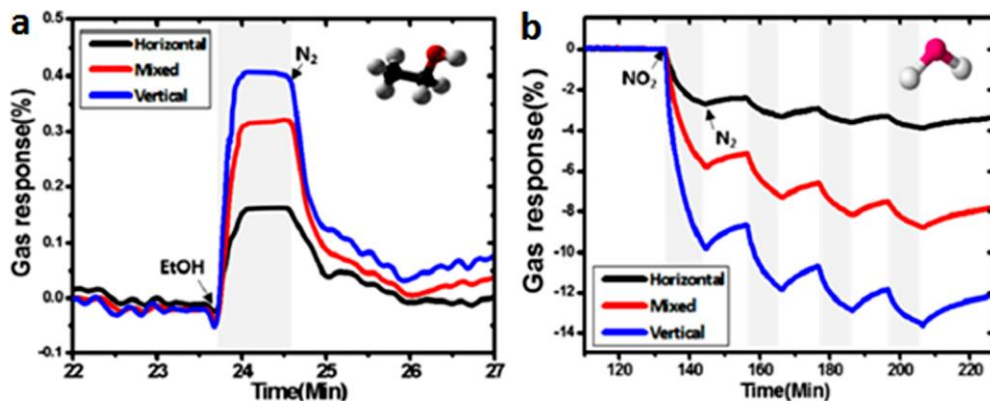


Figure 2-14- Resistance changes of distinct MoS₂ films upon adsorption of (a) 1000 ppm ethanol (C₂H₅OH) and (b) 100 ppm of NO₂.

The large surface-to-volume ratio of the layered MoS₂ film offers unique opportunities for surface functionalization to enable efficient charge transfer between MoS₂ and gas molecules. In particular, the incorporation of functional nanomaterials, such as noble metals, and metal oxides can be an effective way of enhancing the sensing performances of MoS₂ [95].

2.5.2 WS₂ sensors

Monolayer WS₂ comprises a tungsten layer sandwiched between two sulfur layers in a trigonal prismatic arrangement forming a S-W-S structure. Due to its excellent optical, electrical, and mechanical properties, combined with appreciable bandgap and high surface-to-volume ratio, WS₂ has been reported in various applications including field emission, FETs, sensors, etc. The multilayer WS₂ FETs could respond to various gas molecules, including reducing gas of ethanol and NH₃, as well as oxidizing gas of O₂. When exposed to ethanol and NH₃, the source-drain current of the FET increased, whereas it decreased in O₂ and air, attributing to the different charge transfer between multilayer WS₂ and the adsorbed gas molecules. Moreover, this FET was more sensitive to the reducing NH₃ molecules rather than other gases (Figure 2-15 b). NH₃ served as electron donors, increasing the electron concentration of n-type WS₂ nanoflakes; however, O₂ acted as electron acceptors to withdraw electrons from the WS₂ nanoflakes, thus reducing their conductivity. However, O₂ acted as electron acceptors to withdraw electrons from the WS₂ nanoflakes, thus reducing their conductivity. As shown in Figure 2-15c, more gas molecules would be adsorbed under light illumination, and then the sensitivity of multilayer WS₂FET was increased for O₂ but decreased for ethanol and NH₃. However, ethanol and NH₃ molecules acting as “n-dopants” significantly enhanced the photo-responsivity (R_k) and external quantum efficiency (EQE) of the FET, while the O₂ molecules acting as “p-dopants” reduced the R_k and EQE. Importantly, the maximum R_k and EQE of the WS₂FETs were 884A/W and 1.73%, respectively, in the NH₃ atmosphere under light illumination (Figure 2-15d) [95].

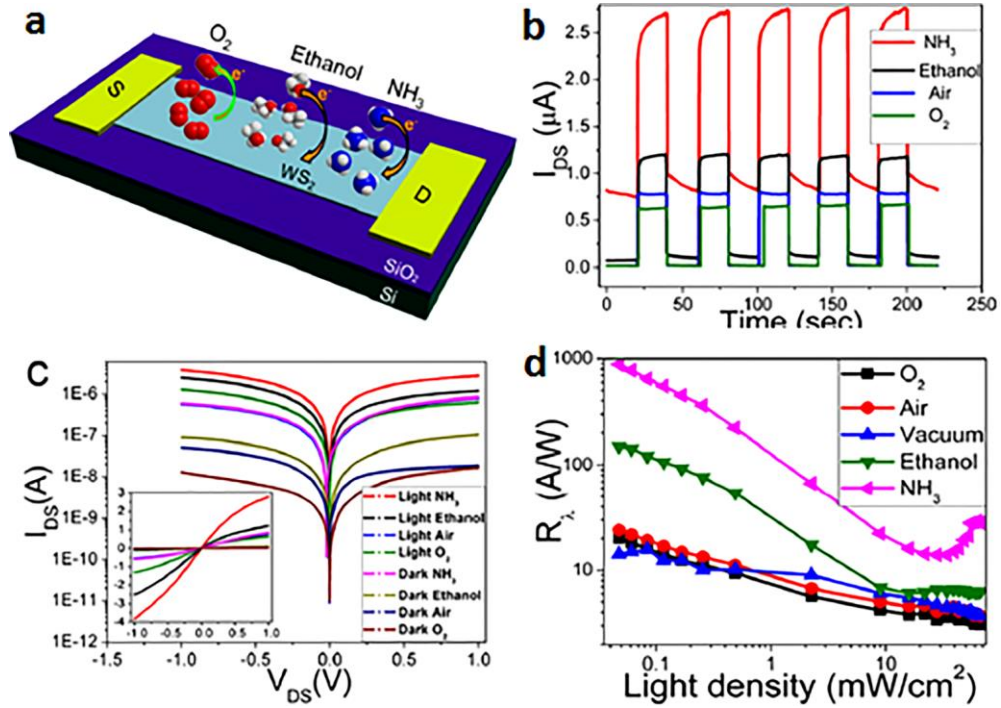


Figure 2-15- (a) Schematic diagram of the multilayer WS₂ nanoflakes transistor.
(b) Time-dependent photocurrent response under various gas atmospheres.

2.6 Classification of TMDs nanostructures

the intrinsic and great properties of 2D TMDs nanostructures make their counterparts of different dimensionalities, such as zero-dimensional (0D) and one-dimensional (1D) TMDs structures, highly attractive. 0D TMDs including the dot structures with the sizes below 100 nm in all dimensions, such as TMDs quantum dots (QDs), small nanoflakes, and nanoparticles, have been prepared and widely applied in the sensing field. In addition, the unique 1D morphologies of TMDs nanostructures, such as nanoribbon, nanotubes, and nanobelts are also presented with a range of great applications. Classification and application of nanostructured TMDs is briefly illustrated in Figure 2-16 [97].

2.7.1 Top-Down Approaches

2.7.1.1 Preparation of 2D TMDs

Mechanical exfoliation

Mechanical exfoliation is one of the earliest and most common top-down approach to obtain ultrathin 2D TMD nanosheets. The resistance in the exfoliation of layered materials like TMDs is the van der Waals attraction between the adjacent layers. The process to overcome this force and obtain mono-few layers from the bulk TMD is a mechanical phenomenon. In general, there are two kinds of mechanical routes to exfoliate bulk TMDs into mono-few layered TMDs, normal force and lateral force. One applies normal force to overcome the van der Waals forces when peeling two layers apart, and the other one can also exert lateral force to promote the relative motion between the two layers. These two mechanical routes are illustrated in Figure 2-17. In the following sections, in terms of the above two mechanical routes, ball milling and sonication mechanical exfoliation routes are discussed [98].

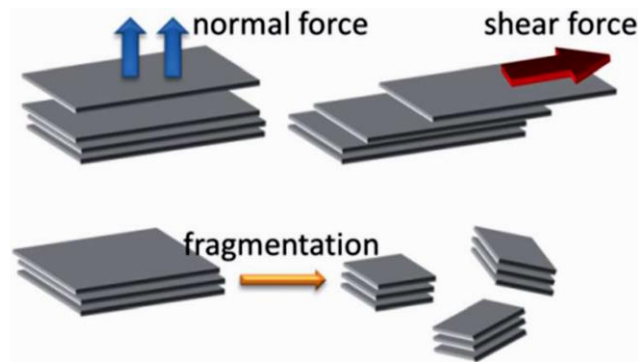


Figure 2-17- Two kinds of mechanical routes for mechanical exfoliation of van der Waals layered material into mono-few layers and the auxiliary route for fragmentation.

Mechanical exfoliation: Micromechanical cleavage

The general idea of this method is the cleavage of graphene or TMD layers from the bulk HOPG surface. The procedure is presented in Figure 2-18. The exfoliation mechanics of this method are that the Scotch tape is applied to the HOPG surface and thus exerts a normal force. If one takes great pains to repeat this normal force numerous times, the

TMD layer becomes thinner and thinner and finally it will become single-layer TMD. The exfoliation mechanics are dominated by a normal force. This method can be used to prepare high-quality and large-area TMD flakes. However, this method is extremely labour-intensive and time-consuming. It is limited to laboratory research and seems impossible to scale up for industrial production [98].

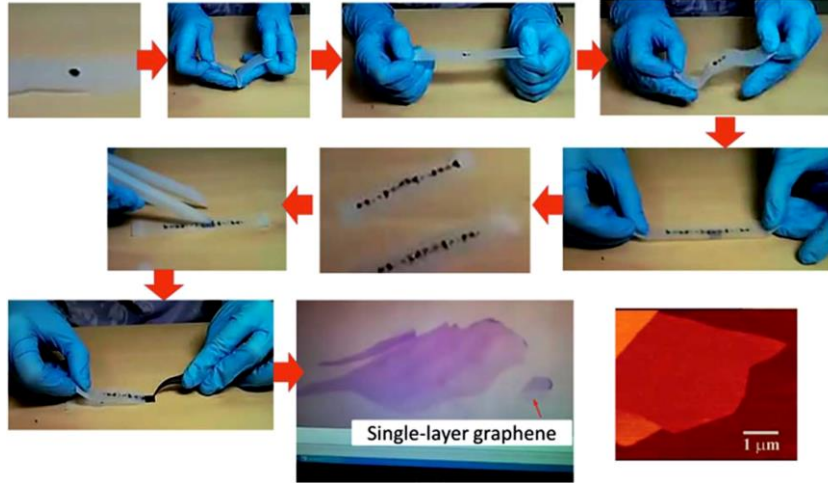


Figure 2-18- An illustrative procedure of the Scotch-tape based micromechanical cleavage of HOPG.

Mechanical exfoliation: Sonication

Sonication assisted liquid-phase exfoliation is known as large-scale production technique to fabricate mono-few layer TMDs from their bulk form. Coleman's group first reported the high-yield production of graphene by the sonication assisted liquid-phase exfoliation of graphite in 2008. In their work, graphite powder was dispersed in specific organic solvents, followed by sonication and centrifugation.

It has been demonstrated that such a kind of liquid-phase exfoliation of graphite is attributed to the small net energetic cost during the exfoliation process. This energy balance for the graphene and solvent system can be expressed as the enthalpy of mixing per unit volume in equation 2-1.

$$\frac{\Delta H_{mix}}{V_{mix}} = \frac{2}{T_{flake}} (\delta_G - \delta_{sol})^2 \phi \quad 2-1$$

in which T_{flake} is the thickness of a TMD flake, ϕ is the TMD volume fraction, and δ_i is the square root of the surface energy of phase i (i denotes TMD or solvent) which is denoted as the energy per unit area required to overcome the van der Waals forces when peeling two sheets apart. It is obvious that when the graphene and solvent surface energies are close, the mixing enthalpy will be smaller, and the exfoliation occurs more easily. Therefore, the surface energy of a solvent is imperative for such a kind of exfoliation. By using a range of solvents with different surface energies and measuring the corresponding concentration of the resultant graphene dispersions, the optimal surface energy of the solvents can be roughly estimated. The good solvents tend to have a surface energy of 70-80 mJm⁻², or a surface tension energy of 40-50 mJ m⁻² at room temperature.

If the sonication time is long or sonication is intensive, the solvents would suffer from degradation and their properties will also be changed. These may make the large-scale production of graphene by sonication fail. Therefore, in these conditions, the above-mentioned model should be modified. In the sonication method, the exfoliation mechanics originate from the liquid cavitation, as illustrated in Figure 2-19. The cavitation-induced bubbles distribute around the layered TMDs.

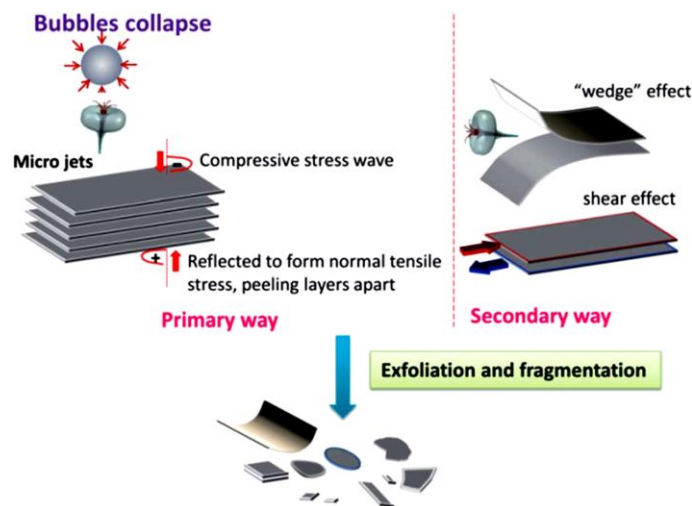


Figure 2-19- Illustration of the mechanical mechanism for exfoliation via sonication.

When these bubbles collapse, micro-jets and shock waves will act on the TMD surfaces instantly, resulting in compressive stress waves which propagate throughout the TMD body. According to the theory of stress waves, once the compressive wave spreads to the

free interface of TMD, a tensile stress wave will be reflected back to the body. As such, collapses of numerous micro-bubbles will lead to intensive tensile stress in the TMD flakes; just as intensive “sucking discs” exfoliate the flakes. In addition, a secondary process is possible in that the unbalanced lateral compressive stress can also separate two adjacent flakes by a shear effect. Also, the micro-jets may split the TMD flakes just as a wedge is driven into the interlayer. In a word, it is the tensile stress that effectively exfoliates TMDs into mono-few layers TMD flakes, resulting in a normal force dominated way [98].

Mechanical exfoliation: Ball milling

Besides the sonication-based exfoliation method which is a normal-force-dominated way, shear force can also be utilized to laterally exfoliate bulk TMD into mono-few layers TMD flakes, as schematized in Figure 2-17. Ball milling, a common technique in the powder production industry, is a good candidate for generating shear force. The mechanical mechanism of ball milling in exfoliating mono-few layers TMDs can be illustrated in Figure 2-20.

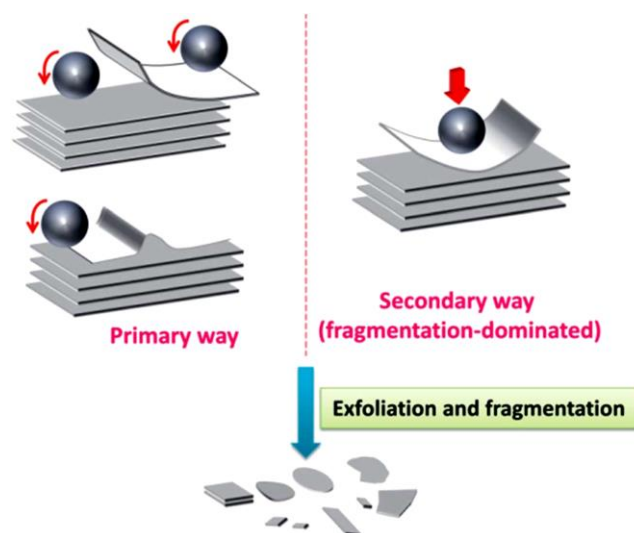


Figure 2-20- Illustration of the mechanical mechanism for exfoliation via ball milling.

In most ball milling apparatus, there are two possible ways responsible for the exfoliation and fragmentation effects. The primary one is the shear force, which is thought to be an

excellent mechanical route for exfoliation. This way is highly desired for achieving large-sized TMD flakes. The secondary one is the collisions or vertical impacts applied by the balls during rolling actions. In this way, large flakes can fragment into small ones, and some-times even destroy the crystalline nature of structures to form amorphous or non-equilibrium phases. Therefore, it is expected that to attain high-quality and large-sized graphene, the secondary effect should be minimized.

Generally, two types of ball milling techniques, i.e. planetary ball mills and stirred media mills, are widely used. Besides, ball milling techniques are being used in wet and dry modes. Initially, ball milling was adopted to reduce the size of graphite, and it was found that graphitic flakes with a thickness down to 10 nm could be obtained. But this milling scheme was not further continued to obtain graphene. Until 2010, following the same idea as the sonication-based liquid-phase exfoliation of graphene, Knieke et al., Zhao et al., modified the milling technique to produce graphene. So far variety of studies has done to investigate the effect of different solvents with diverse surface tension energy during wet ballmiling such DMF, NMP, tethramethylura etc [98].

Chemical exfoliation

Chemical exfoliation of TMDs bulk crystals is an attractive alternative to obtain large scale synthesis of 2D nanostructures. Layers within bulk TMDs crystals were first intercalated with *n*-butyl lithium in hexane. Subsequently, water is added and the reaction with *n*-butyl lithium produced H₂ gases, which expand and exert internal pressure to push the layers apart. Zhang's group developed another simple yet high yield and efficient strategy to obtain TMDs nanosheets based on a controlled electrochemical lithiation process (Figure 2-21). Liquid-phase exfoliation, first proposed by Coleman and co-workers, is another great top-down approach for 2D TMDs preparation, using sonication to exfoliate the bulk crystals in liquid solvents (Figure 2-21b). This approach is very simple and scalable to obtain quantities of TMDs exfoliates. In addition, liquid-phase exfoliation of TMDs crystals can also be achieved by exposing those materials to shear treatments [97].

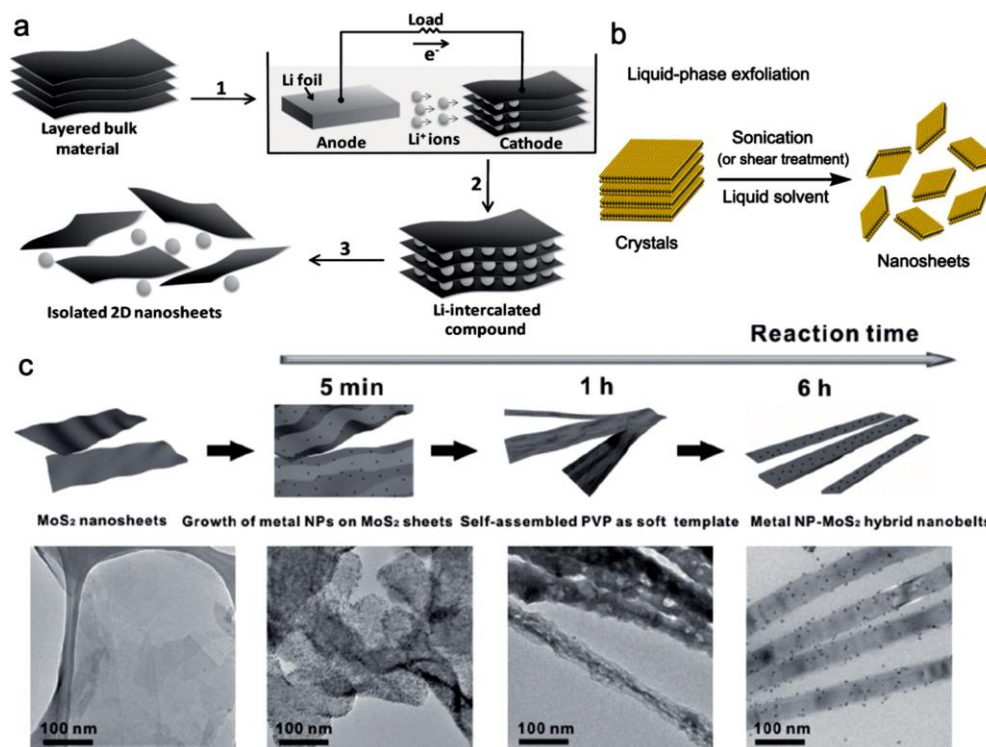


Figure 2-21- Top-down approaches for the preparation of 2D and 1D TMDs nanostructures.

a) Electrochemical lithiation process for preparing 2D MoS₂ nanosheets. b) Liquid-phase exfoliation route for the preparation of 2D TMDs nanosheets from their bulk crystals.

c) Schematic illustration of the synthesis process of 1D MoS₂ nanobelts from their 2D-related morphologies [97].

Preparation of 1D TMDs

Due to the top-down approaches, 1D TMDs nanostructures can be obtained through the morphological changes of the nanosheet structures with the consequence of a series of chemical reactions. The uniform and robust semiconductive MoS₂ nanoribbons can be obtained from a MoS₂ nanosheet under electron beam irradiation. Meanwhile, a general method for 1D TMDs nanobelts was developed by the etching of TMDs nanosheets (Figure 2-21), and thus 1D MoS₂, TaS₂, TiS₂, WSe₂, and TaSe₂ nanomaterials were successfully synthesized. However, in addition to the nanosheets structures, recently, it was found that nanotubes were also good materials to generate 1D WS₂ and MoS₂ nanoribbons through laser irradiation-induced unzipping.

Preparation of 0D TMDs

The top-down approaches of 0D TMDs preparation can be classified as chemical exfoliation and sonication-induced treatment methods. Due to a range of chemical reactions, chemical exfoliation is introduced for the preparation of 0D nanostructures from the bulk crystals, nanoparticles, and nanosheets morphologies. Firstly, an assay based on the effective exfoliation and disintegration of bulk TMDs crystals was designed. K atoms were firstly intercalated into covalently bonded WS₂ sheets in bulk WS₂ crystals. Subsequently, the reaction between K atoms and ethanol/H₂O mixture produce H₂ which exfoliated 0D WS₂ QDs (Figure 2-22a). Interestingly, starting bulk TMDs ultimately determines the eventual morphologies of TMDs nanostructures. For example, MoS₂ nanoparticles was used to produce uniform MoS₂ QDs based on traditional Li intercalation-exfoliation method (Figure 2-22b). In order to achieve the controllable preparation of TMDs QDs, a series of chemical reactions, including Fenton reaction, electrochemical etching process, and H₂SO₄ intercalation method, were introduced. Sonication-assisted exfoliation in the liquid phase is also a good technique for 0D TMDs preparation. For example, a sulfuric acid-assisted ultrasonic route was introduced for the preparation of MoS₂ QDs by exfoliating and cutting bulk MoS₂ powders. Furthermore, combining the sonication and solvothermal treatment, MoS₂ and WS₂ QDs possessing monolayer thickness were also synthesized from their bulk crystals (Figure 2-22c). By using an universal and facile preparation method for 0D TMDs nanostructures with a combination of sonication and grinding techniques, one can prepare TMDs quantum dots (MoS₂, ReS₂, TaS₂, WS₂, MoSe₂, and WSe₂) and NbSe₂ nanodots [97].

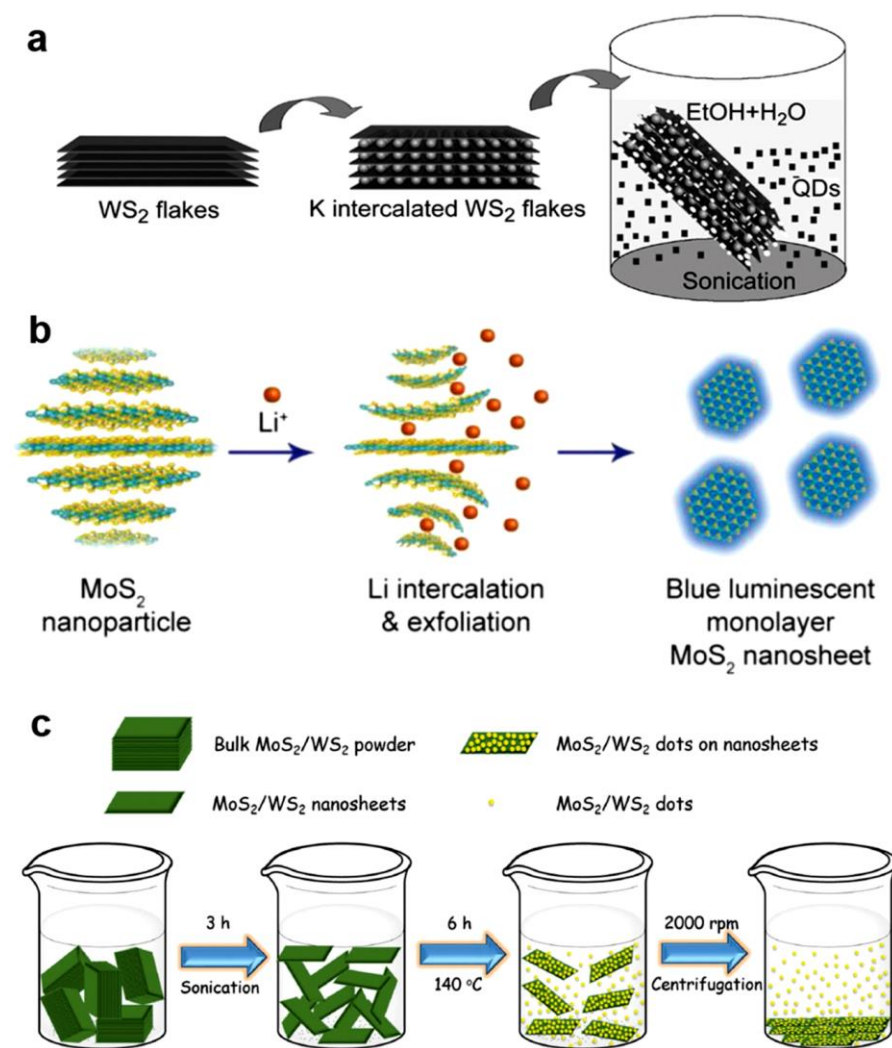


Figure 2-22- Top-down approaches for the preparation of 0D TMDs nanostructures. a) Scheme of the preparation of monolayered WS₂ quantum dots using K-intercalation and sonication method. b) Schematic illustration of fabrication of blue luminescent MoS₂ quantum dots from the Li intercalation and exfoliation of MoS₂ nanoparticles. c) Schematic representation of the synthesis process to prepare MoS₂/WS₂ quantum dots by using a liquid exfoliation and solvothermal treatment approach in DMF, NMP, and DMEU [97].

2.7.2 Bottom-Up Approaches

Preparation of 2D TMDs

Bottom-up approaches can be used to prepare uniform single- and few-layered TMDs nanosheets with large area size. Chemical vapor deposition (CVD) technique is a common bottom-up approach to synthesize 2D nanomaterials with comparatively large

dimensions. Several reports have demonstrated that the CVD approach can produce high-quality TMDs films with controlled size range and thickness. Moreover, bottom-up wet chemistry techniques also offer a powerful alternative to the earlier exfoliation routes in synthesizing TMDs nanosheets. The nanosheets were prepared in high yield directly and those parameters used to modulate nanomaterial size, shape, and uniformity, including judicious choice of surface stabilizing ligands and reaction conditions, may also be applicable to TMDs, which intrinsically form nanosheets due to their layered crystal structures [97].

Preparation of 1D TMDs

the direct growth of 1D TMDs nanostructures seem hard to control. Therefore, most of bottom-up approaches, relying on the use of templates, are developed for the 1D TMDs preparation. According to the previous reports, 1D TMDs nanoribbons, such as WS₂ and WSe₂ nanotubes, and MoS₂ nanoribbons could be synthesized with the matrix of 1D metal oxides nanostructures in the presence of S or Se precursor.

Preparation of 0D TMDs

0D TMDs nanostructures could be obtained through the typical synthesis reactions of Mo and S precursors and thus several routes, including CVD approaches, solvothermal reactions, and laser technique, have been presented. In 2000, MoSe₂ and WSe₂ nanoclusters were synthesized through dissolving the metal (IV) chloride in an anhydrous inverse micelle and adding H₂Se. Subsequently, a metal-organic CVD approach was adopted for large-scale synthesis of MoSe₂ nanoparticles and hollow fullerene-like MoS₂ nanoparticles from reaction between Mo(CO)₆ and elemental sulfur or selenium, respectively. Additionally, a range of solvothermal approaches from various precursors were utilized for 0D TMDs preparation [97].

***3 Chapter 3: Materials
Characterization and Electrical
Measurement Techniques***

3.1 Introduction

As the purpose of this thesis is focused on synthesis and characterization of semiconductor nanostructures for gas sensing applications. Various semiconductors such as MOS nanofibers and mono-few layered 2D WS₂ were prepared utilizing different synthesis methods for gas sensing applications.

Variety of characterization techniques were employed to characterize the obtained nanostructures and evaluate the synthesis methods.

As-prepared and annealed semiconductors nanostructures were characterized by X-ray diffraction (XRD) to evaluate the crystal structure at different annealing temperatures.

Fourier Transform Infra Red (FT-IR) spectroscopy was used to characterize the polymer and alkoxide bonds in the preparation steps of WO₃ precursor for electrospinning.

Thermogravimetric and Differential Thermal Analysis (TG-DTA) was utilized to obtain the crystallization and best annealing temperature of WO₃.

Scanning Electron Microscopy (SEM) was used to study the microstructure of synthesized and annealed nanostructures, X-Ray photoelectron microscopy was utilized to study the surface chemistry of exfoliated 2D TMDs.

Atomic Force Microscopy (AFM) was widely used to optimize the grinding and sonication processes, step by step.

Transmission Electron Microscopy (TEM), High Resolution Transmission Electron Microscopy (HRTEM), Scanning Transmission Electron Microscopy (STEM) and Fast Fourier Transform (FFT) was widely used to study the surface chemistry and quality of exfoliated mono-few layered WS₂, optimize the grinding assisted sonication process.

All the obtained nanostructures were deposited on a sensor substrate and the gas sensing properties of synthesized nanostructures were studied in-depth exposed to different reducing and oxidizing gases.

Besides, electrical and gas sensing measurement and characterization of fabricated semiconductors will be explained in this chapter.

3.2 Material Characterization techniques

3.2.1 X-Ray Diffraction (XRD) measurements

X-ray diffraction is the most widely used powerful technique to identify the crystal structure and the atomic array of materials. It is based on constructive interference of monochromatic X-rays and a crystalline sample. The interaction of the incident X rays with the sample produces constructive interference when conditions satisfy Bragg's Law (Equation 3-1). This law relates the wavelength of electromagnetic radiation to the diffraction angle and the lattice spacing in a crystalline sample.

$$n\lambda = 2d \cdot \sin \theta \quad 3-1$$

In this thesis, crystalline phases evolution of WO₃ nanofiber samples as well as mono-few layer exfoliated WS₂ and WS₂ commercial powder, annealed at different temperatures was monitored by grazing incidence XRD (PAN Analytical X'PERT Pro) using Cu K_{α1} radiation ($\lambda = 0.154$ nm) and 0.02° angle step.

Analysis of the spectra was carried out using the Traces (GBC Co.) software package with the database of the Joint Committee on Powder Diffraction Standards of the International Centre for Diffraction Data (JCPDS-ICDD; 2001, 2003 versions). The crystallite size was calculated using the Scherrer equation, 3-3.

$$\tau = \frac{k\lambda \cos \theta}{\beta} \quad 3-2$$

where τ is the mean crystallite dimension, K is the shape factor (0.89), λ is the X-ray wavelength (Cu K_α = 1.5418Å), β is the line broadening at full width half maximum intensity (FWHM) in radians, and θ is the Bragg angle.

3.2.2 SEM

The morphology of synthesized sensing materials in this work were observed using

scanning electron microscopy (SEM). The equipment used in the works presented in this thesis include Scanning Electron Microscope (SEM) TESCAN MIRA 3 XMU Microscope, and Field Emission Gun-Scanning Electron Microscope (FEG-SEM) Mira3 XMU Tescan.

Nanostructured semiconductors (WO_3 nanofibers and mono-few layer TMDs) were all deposited on an interdigitated sensor substrate shown in Figure 1-1 (see section 3.3.2) and studied under SEM.

The oxide materials investigated in this thesis are semiconductors. Electron charge was induced by an incident electron beam from time to time. So, in case of electron charge, the observations were performed after coating the sample with a platinum layer of less than 5 nm.

3.2.3 TEM and high resolution TEM and STEM

The most powerful tool for the structure analysis is transmission electronic microscopy (TEM). An electron beam from a gun penetrates materials, creating images and patterns on a fluorescent screen or a digital screen. These are used to identify the internal structure of materials or determine unknown materials or structural modifications. By this tool, we identified and confirmed the structures of mono-few layered WS_2 .

Specially, High Resolution Transmission Electronic microscope (HRTEM) and Fast Fourier Electron microscopy (FFT) are extensively used in this thesis to evaluate the exfoliation process and exfoliated mono-few layered WS_2 and optimize the process parameters. Besides, Scanning Transmission Electron Microscopy (STEM) was used to evaluate the purity of and surface chemistry of exfoliated mono-few layer WS_2 nanosheets.

The HRTEM machine used in this work was HRTEM - JEOL 2100 Field Emission electron microscope operated at 200 kV.

Two types of grids; carbon grids and grids with hole were used to deposit dispersions containing nanomaterials. In most of depositions, a dilouted dispersion of exfoliated WS_2 were drop deposited onto the grids. In some cases, few grids were dip coated into the dispersion to compare with drop deposited samples were drop diposition showed better results since it was possible to increase the amount of nanostrcutured material by adding more drops.

3.2.4 FT-IR

Fourier-Transform Infrared Spectroscopy (FTIR) was used in this work to evaluate the formation of Tungsten trioxide precursor for electrospinning. The evolution of the precursor solution was monitored by THERMO NICOLET NEXUS870 machine.

3.2.5 Thermal analysis

Thermogravimetric analysis/differential thermal analysis (TGA/DTA) is a qualitative and quantitative analyzing method to evaluate the crystallization temperature thermal stability of heated samples. The thermogravimetric analysis (TGA) estimates the weight loss or weight gain of a material when heated to a specific temperature over time. The differential thermal analysis (DTA) identifies the temperature regions and the magnitude of a change in energy.

Thermal analysis was carried out using a LINSEIS L81-I. It consists of a computer (to control the instrument), an isolated oven which contains a high-precision balance and a thermocouple to precisely measure mass change and temperature difference against the temperature, and a gas purge system to control the atmosphere. The thermal analysis was undertaken to determine the decomposition temperature and to identify the reaction of a precursor, tungsten alkoxide mixed with polymer, during an experiment. The test was done in an inert atmosphere to prevent oxidation.

3.2.6 XPS measurements

Surface chemistry, surface oxidation and sulfur oxygen replacing of WS₂ sheets over annealing as well as the amount of defects was evaluated by X-ray photoelectron microscopy (XPS).

X-Ray Photoemission Spectroscopy (XPS) that is used in this thesis is a PHI 1257 spectrometer equipped with a monochromatic Al K α source ($h\nu=1486.6$ eV) with a pass energy of 11.75 eV (93.9eV survey), corresponding to an overall experimental resolution of 0.25 eV.

3.2.7 AFM measurements

Atomic Force Microscopy (AFM) was used in this work to evaluate the yield of exfoliation process by measuring the thickness and lateral dimensions of exfoliated WS₂ flakes. Air tapping mode AFM was performed with a Veeco Digital D5000 system. Using silicon tips with spring constant of 3 N/m and resonance frequencies between 51 and 94 kHz. Samples for AFM investigations were prepared via spinning (at 2000 rpm for 30s) 10 μ l of centrifuged WS₂/Eth solution on a Si₃N₄ substrate. The substrates have been previously cleaned in a piranha base solution (3:1:3 mixture of ammonium hydroxide NH₄OH with hydrogen peroxide and milli-Q water) to enhance their wettability. Gwyddoin software was used to analyze the AFM results.

3.2.8 Raman Spectroscopy

Raman spectroscopy was employed to investigate the oxidation of exfoliated WS₂ nanosheets. The Raman Effect occurs when light impinges upon a molecule and interacts with the electron cloud and the bonds of that molecule: the incident photon excites the molecule into a virtual state. When the molecules relax to ground state, most of the photons scatter elastically (Rayleigh scattering), while inelastic scattering occurs in a very small fraction (1 in 10⁷ of incident photons). The energy of the scattered radiation is less than the incident radiation for the Stokes line and the energy of the scattered radiation is more than the incident radiation for the anti-Stokes line (Figure 3-1).

Raman spectra were acquired using a Micro Raman Spectrometer (μ RS) (LABRAM spectrometer, Horiba-Jobin Yvon, $\lambda = 633$ nm, 1 μ m spatial resolution, and ≈ 2 cm⁻¹ spectral resolution) equipped with a confocal optical microscope (100 \times MPLAN objective with 0.9 numerical aperture and 0.15 mm work distance). 10 μ L of the WS₂/Eth solution was deposited on a 270 nm SiO₂ substrate.

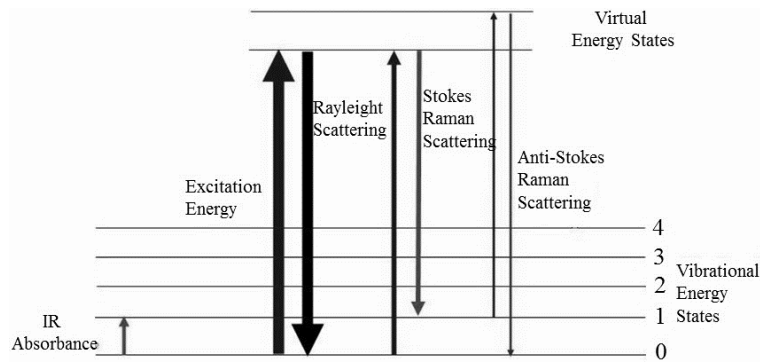


Figure 3-1- Energy level diagram showing the states involved in the Raman effect.

3.2.9 DLS measurements

Particle size distribution was determined by Dynamic Light Scattering (DLS) Malvern Mastersizer 2000. DLS was used to elucidate the overall dimension exfoliated WS_2 within a dispersion and evaluate the exfoliation yield and optimize the exfoliation process parameters. Different parts of DLS machine is shown in Figure 3-2. To prepare samples for DLS measurement, 0.005 g WS_2 powder was dispersed in 100 ml of pure ethanol previously probe sonicated for 30 seconds. The dispersion was sonicated for few seconds to make homogenous WS_2 /Ethanol dispersion. After few seconds of sonication, the sample will be inserted into the light scattering cell (wet cell) and the overall dimensions of exfoliated sheets will be measured by light scattering technique.

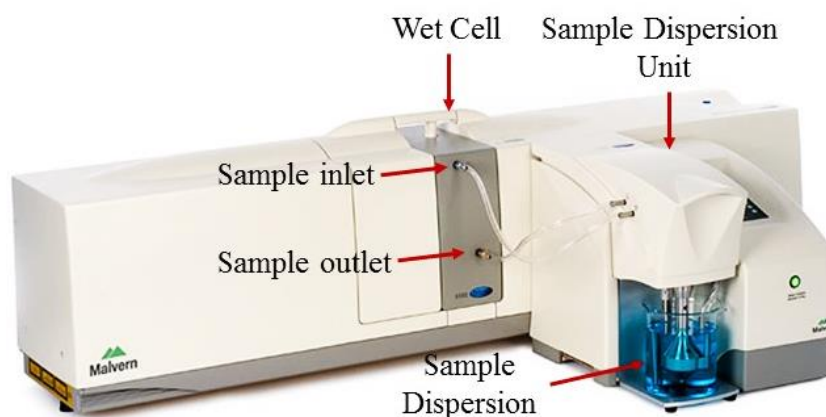


Figure 3-2- Dynamic Light Scattering machine, Malvern Mastersizer 2000

3.3 Electrical characterization of sensors

3.3.1 Introduction

After synthesizing the nanostructured semiconducting sensing materials that will be further explained in detail, the sensing material will be deposited onto the sensing electrodes and will be subjected to electrical tests to investigate their electrical properties in presence of certain target gases and then evaluate their performance in terms of sensitivity, selectivity and stability.

Below is a flow chart that describes the electrical characterization. The process consists of the following phases and blocks:

- deposition of the material on special interdigitated substrates;
- welding of the substrate on T0-12 pins and housing in the measuring cell;
- gas fluxing system;
- power supply, control and data acquisition system.

Figure 3-3 shows the global scheme for the electrical characterization of the manufactured devices.

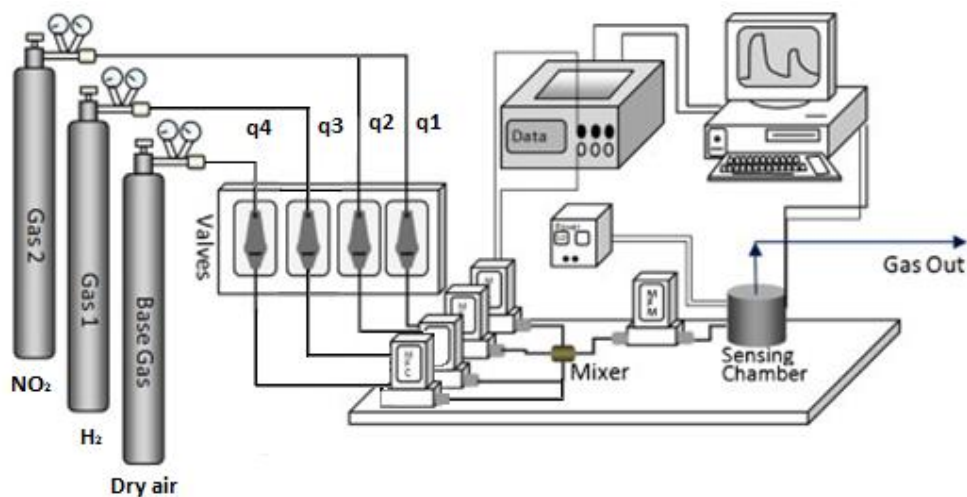
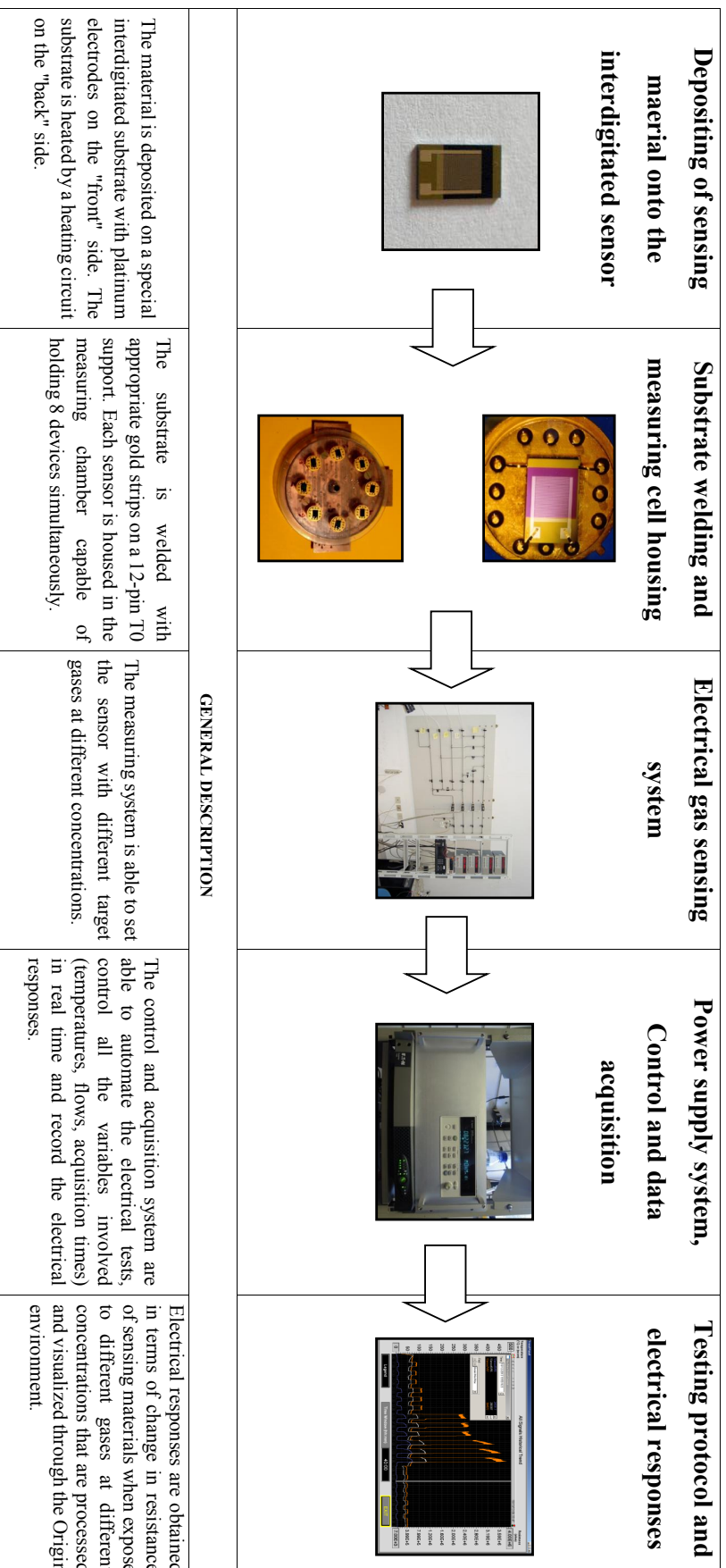
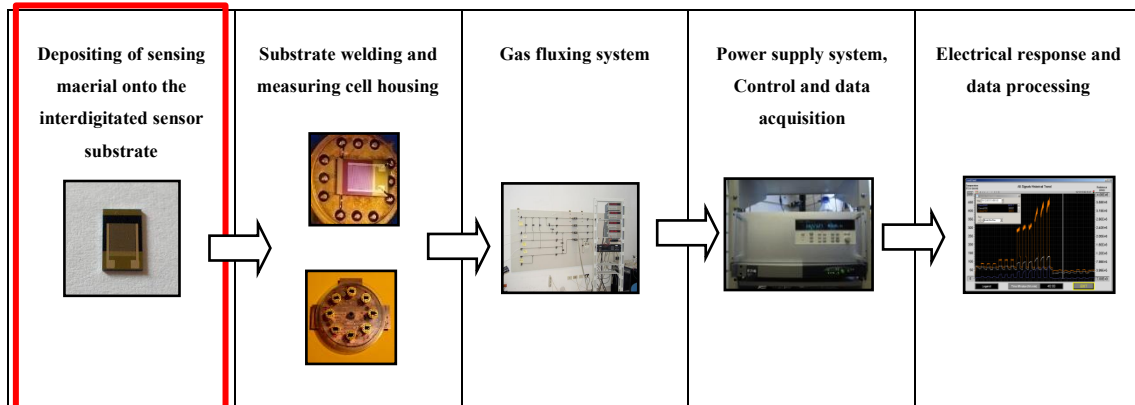


Figure 3-3- Electrical characterization of the sensors: overall scheme.

FLOW CHART OF THE ELECTRICAL CHARACTERIZATION PROCESS



3.3.2 Sensor substrate



The substrates used for the deposition of sensing material and for the subsequent electrical characterization are rectangular supports made of polycrystalline silicon (Si). A very thin amorphous layer of Si_3N_4 (200 nm) is deposited on the surface of this support by Chemical Vapor Deposition (CVD) technique.

The system of electrodes on the front side and the back side of the substrate shown in Figure 3-4 b is obtained by the photolithographic technique

The sensing material will be deposited on the “front side” that two overlapping metallic platinum finger combs make up the electric signal circuit.

The “Back side” consists of a heating circuit that is used to heat up the sensing material to the defined operating temperature of sensor, and the thermistor circuit is used to control the temperature of the substrate, see Figure 3-4.

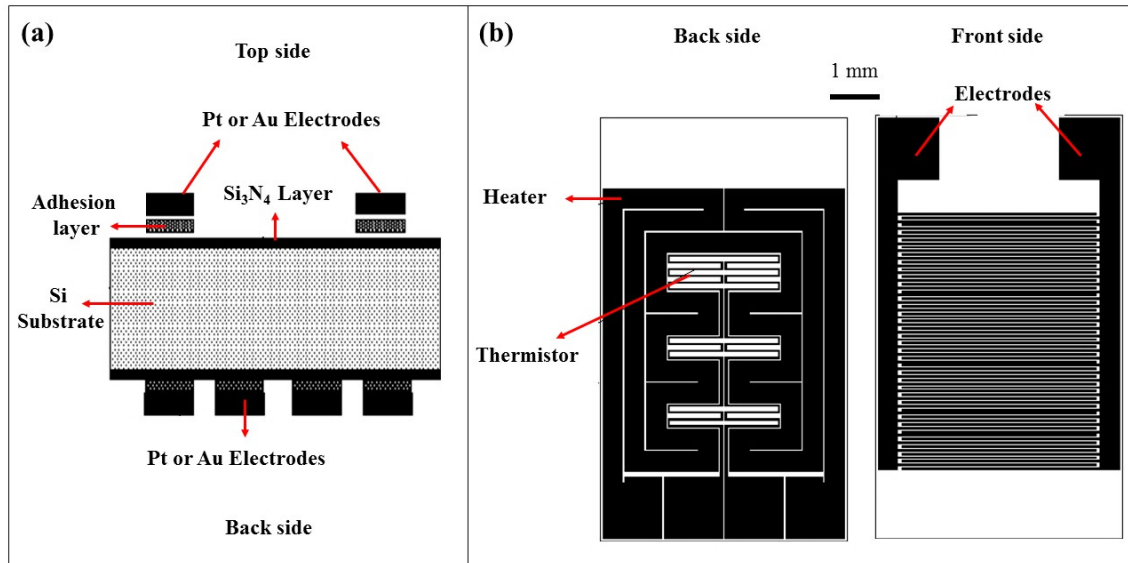


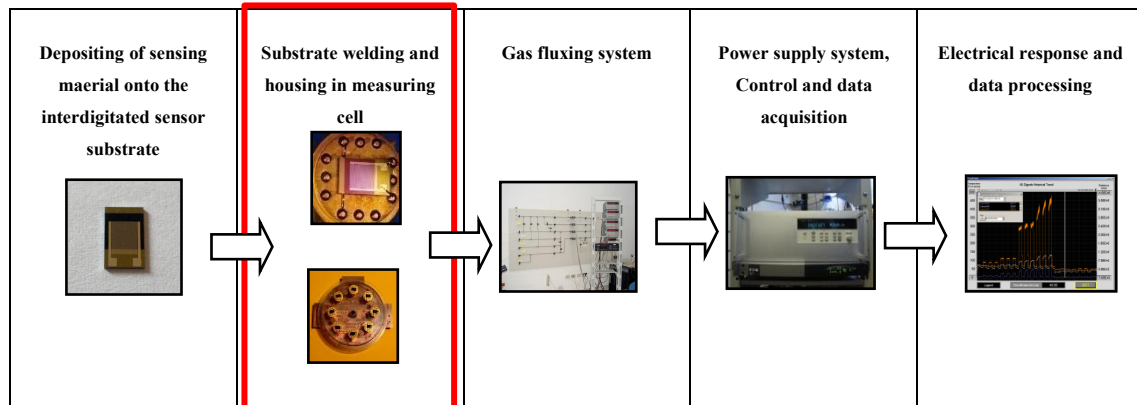
Figure 3-4- Schematic illustration of interdigitated sensor substrate a) cross section of sensor substrate, b) front and back side circuits of sensor substrate

These substrates represent the second generation of supports family, called "Eurochip", that were previously designed and manufactured in Holland by the group of prof. De Roj on sapphire substrates.

This generation of substrates differs from the previous one as regards only the nature of the support materials (in this case Si₃N₄). The geometry, the size of the electrodes and the circuits present is the original one.

Silicon Nitride substrates were made on 4 "wafers with photolithographic technology at the company MICROSENS, world leader in the field of thin film commercial sensors manufacturing. The specifications and the complete characterization of this type of substrate are reported in detail in ANNEX 3.

3.3.3 Substrate welding and housing in measuring cell



After depositing the sensing material onto the two-overlapping metallic platinum finger combs electrodes, the front side electrodes and the back-side electrodes will be welded to the 12-pin support (T0-12) by means of gold strips to ensure the electrical contact of the substrate to the support, see Figure 3-5. These contacts provide the continuity of the signal between the substrate and the supply and acquisition and control system.

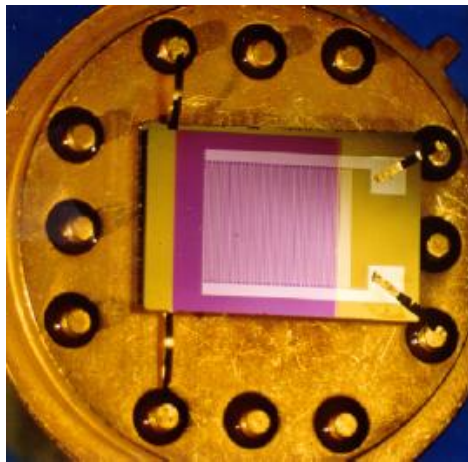


Figure 3-5- Detail of a sensor welded on a T0-12 support.

The devices connected to the T0-12 are housed inside the measuring cell that contains up to 8 sensors simultaneously with the possibility of independent current supply of the substrates. During the sensing measurements, sensors and sensing materials could be activated by two different modes, one is thermal activation modes that is provided by the heating circuit on the back side of the sensor substrates, and the other is light illumination

mode that is provided by the four-color LED lamps placed on top of the sensors at an specific distance, see Figure 3-6.

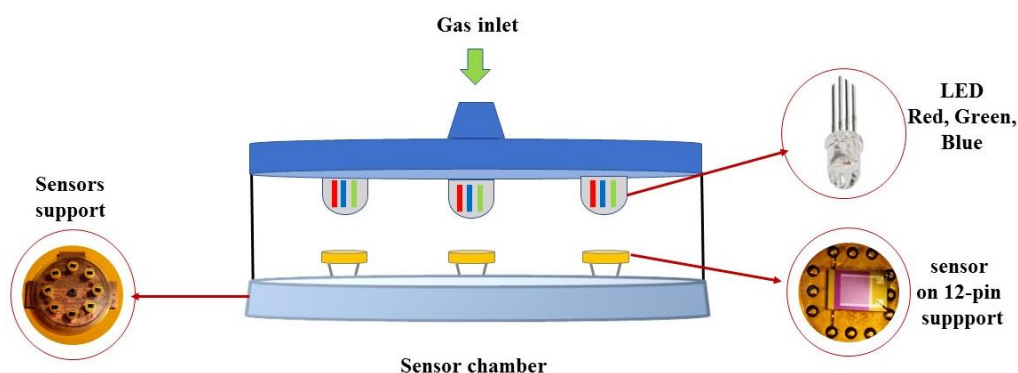


Figure 3-6- Measurement chamber with details of the plate on which the eight sensor supports are housed.

Each LED that is placed right on top of each sensor consists of three different colors; Red (RD), Green (GR) and Purple Blue (PB). The gas response of semiconductor gas sensors activated by visible light sources is known to be dependent from both the emission wavelengths and the irradiance. The characterization of the LED sources has been carried out before any gas response evaluation. Figure 3-7 reports the LED emission spectrum showing the normalized lightpower as a function of the wavelength. The measurements identify the peak wavelengths located at $\lambda = 430$ nm (PB), at $\lambda = 570$ nm (GR) and at $\lambda = 630$ nm (RD) and the resulting emission spectra present negligible overlapping. The evaluation of the light irradiance has been obtained by integrating each spectral response curve of Figure 3-7 at four different distances (0.5 cm, 1 cm, 2 cm and 3 cm) between the LED and the photodetector of the power-meter. The corresponding LEDs light irradiance conditions are reported in Table 3-1.

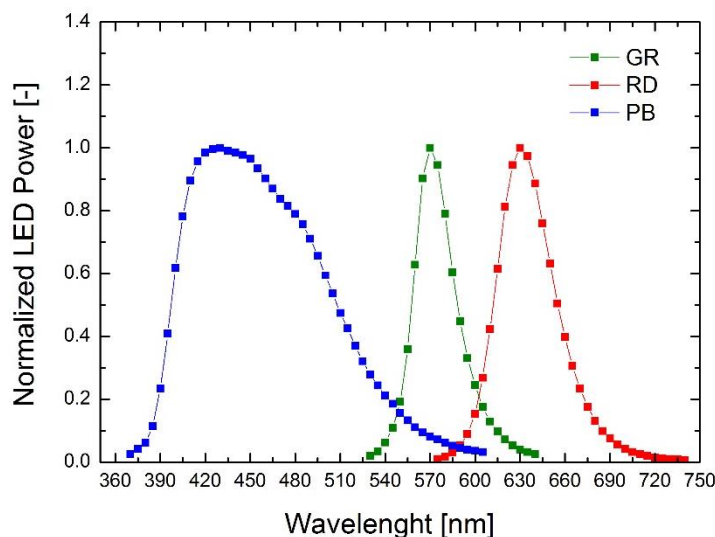
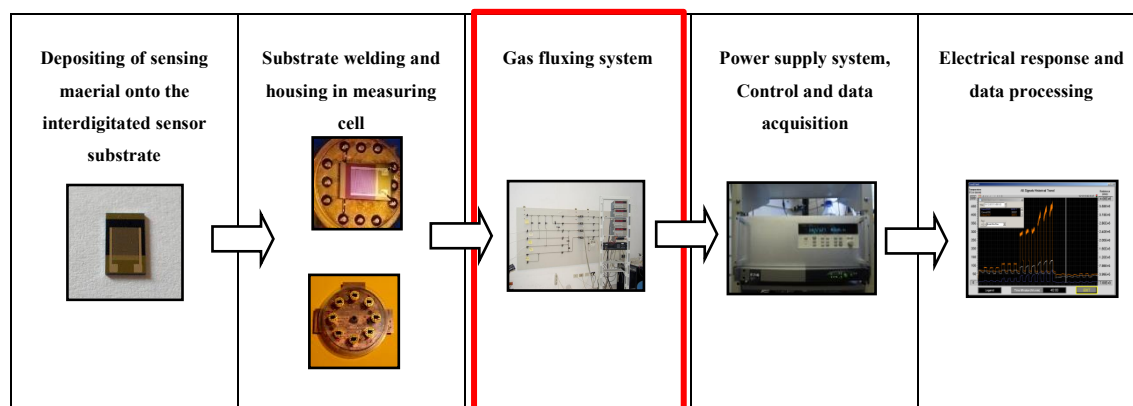


Figure 3-7- Light emission spectra of the employed LED: normalised light power as a function of the wavelength.

LED colour	Light intensity at 0.5cm [$\mu\text{W}/\text{cm}^2$]	Light intensity at 1cm [$\mu\text{W}/\text{cm}^2$]	Light intensity at 2cm [$\mu\text{W}/\text{cm}^2$]	Light intensity at 3cm [$\mu\text{W}/\text{cm}^2$]
RD ($\lambda=630\text{nm}$)	95	89	59	30
GR ($\lambda=570\text{nm}$)	40	38	27	15
PB ($\lambda=430\text{nm}$)	770	668	468	270

Table 3-1- LED light intensity as a function of the distance from the power-meter photodetector.

3.3.4 Gas fluxing system



The system shown in Figure 3-8 shows the test bench used for gas flushing.

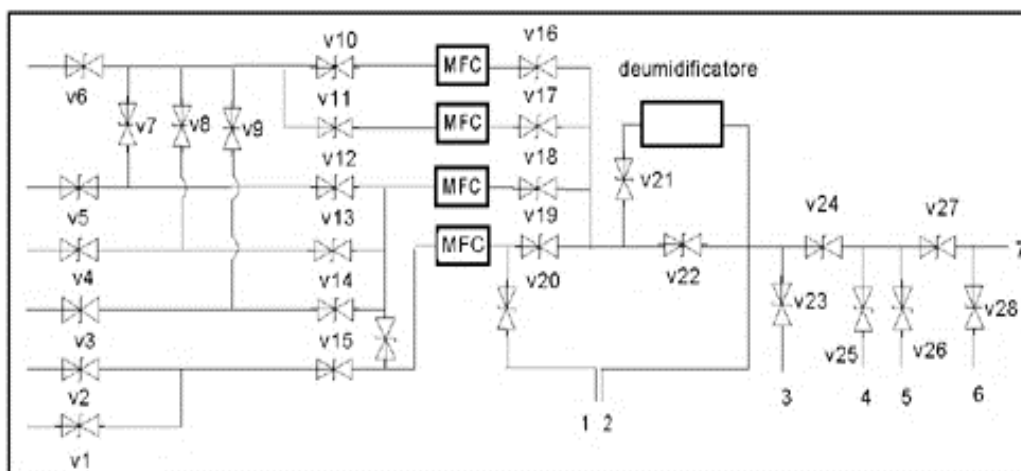


Figure 3-8- Schematic of the gas fluxing system.

The system is able to flow up to 4 different gases at different flow rates into the measuring cell. The system is provided with the certified storage cylinders for gaseous mixtures with specific concentration. The system is also equipped with a calibrated dehumidifier capable of supplying specific relative humidity deriving from the humidification of the incoming dry air.

The following gases or gas mixtures were used in this thesis:

- Dry air;
- Wet air (0-95% U.R.);
- Mixture of NO₂ in dry air (10 ppm);
- Mixture of H₂S in dry air (20 ppm);
- Mixture of H₂ in dry air (500 ppm);
- Mixtures of NH₃ in dry air (500 ppm)

The flow rates of the four output channels are regulated by four Texas Instruments solenoid valves connected to the control system. Below are the different full scale and therefore the maximum flow rates that can be provided by each of solenoid valves.

- Valve 1: 500 sccm

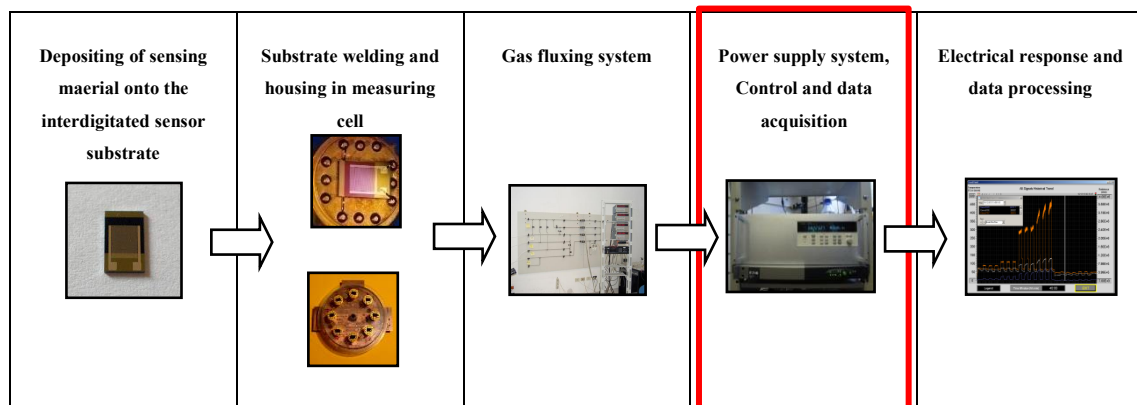
- Valve 2: 500 sccm
- Valve 3: 100 sccm
- Valve 4: 20 sccm

The concentration of the sample gas entering the chamber (C) is determined by the degree of dilution of the initial air/gas mixture (C₀), (characteristic or initial concentration of each cylinder), according to the equation 3-3:

$$C = \frac{C_0 \cdot (q_1 + q_2)}{Q} \quad 3-3$$

where q_1 and q_2 are the flow rates of the lines that feed the air/gas mixture, while Q is the resulting flow rate, which always assumes the value of 500 sccm (for standardization of the tests).

3.3.5 Power supply, control and data acquisition



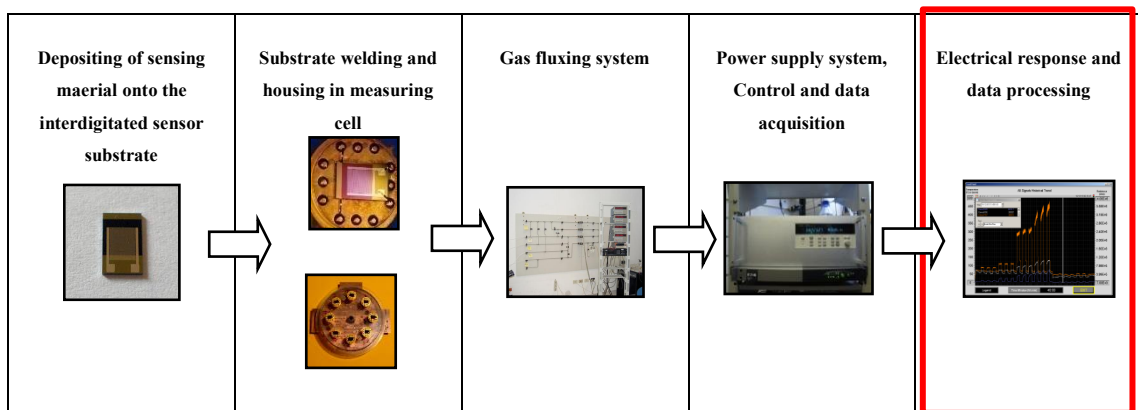
The power supply, control and data acquisition system consist of the following modules:

- "National Instruments NI 9472 8-Channel 24 V Logic, 100 μ s module, Sourcing Digital Output Module", which supplies the heating circuit in the "Back" side of the device with a certain current (see thermal characterization of the substrate - Annex 3).
- "Agilent 34970A Data Acquisition Unit. Modul 34901 Multiplexer", capable of displaying and recording 15 data channels in real time (resistances, temperatures, flows). It measures the passing current and then processes the data supplying of

resistance values through the Ohm's law.

- The software for the acquisition system is based on an Instrument Server architecture (developed with LabVIEW and resident in NI cRIO) connected to a supervision and control client (developed in WinXP with the SCADA NI Lookout package). Through a remote connection software, it is possible to manage and control the gas sensing tests in real time and to act on some important parameters during construction.

3.3.6 Electrical response and data processing



Electrical responses and characteristic parameters

During the electrical tests, the sensing material is subjected to different inputs and parameters such as temperatures, target gas concentrations and humidity that alter its conductance characteristics. If the change in conductivity derives from the presence of a target gas, changes in the electrical resistance are obtained from a base level in air (R_a) at a constant level in air + sample gas (R_g), as illustrated in Figure 3-9.

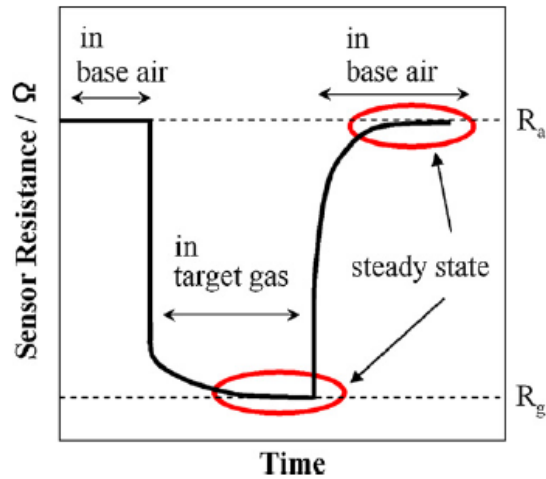


Figure 3-9- Schematic of the gas fluxing system.

Based on the kind of oxide being tested, ie p-type semiconductors, the gas response can be defined through the following equations:

- Oxidizing gas

$$S_{ox}^p = \frac{R_a}{R_g} \quad 3-4$$

- Reducing gas:

$$S_{rd}^p = \frac{R_g}{R_a} \quad 3-5$$

S_{rd} and S_{ox} , for a given Operating Temperature (OT) and concentration of the sample gas, take the name of Practical Sensitivity or Sensor Response. By plotting the practical sensitivity as a function of the relative concentration of the input gas in bi-logarithmic scale, a straight line is obtained. This slope is named the Sensitivity plot.

In addition to the two types of sensitivity, the gas-sensing characteristics of the metal oxide are characterized by the response time and the recovery time. The response time is defined as the required time to reach 90% of the stationary response signal at equilibrium, while the recovery time represents the required time to recover 90% of the original

baseline in equilibrium.

Other characteristics to be considered in the evaluation of the responses are the stability of the baseline, that is the ability to recover the baseline (in air) after desorption of the gas, and the selectivity, that is defined by the ability to discriminate the target gas (ex: NO₂) in the presence of an interfering gas (ex: H₂). This characteristic is evaluated through the so-called Cross-Sensitivity test.

Annex 4 shows a list of the definitions of the various parameters used to fully characterize a semiconductor gas sensor [99-101].

Testing protocol for electrical tests

Each of the manufactured sensor device (made of MOx or exfoliated TMD) has been subjected to a standard protocol for a better electrical and conductometric characterization of the sensing material.

The system can interrogate the devices by managing material working temperatures, gas flows in the measuring cell and, as previously described, the "Agilent" module, applies a specific voltage to the electrode/sensitive layer circuit, and measures the passing current and then, calculate the output resistance values by Ohm's law.

The standard characterization protocol consists of various tests which are subdivided into various sub-tests depending on the chosen parameters (temperatures, times, flow rates). Each test is performed to determine and derive some parameters or characteristics of the material. Table 4.7 shows the various tests and their characteristics that can be obtained from the answers obtained.

Type of Test	Obtained Characteristics and Parameters
Test at different temperatures with target gas step	<ul style="list-style-type: none"> - Ideal operating temperatures - Adsorption and desorption times at various temperatures
Test at different concentrations of target gas	<ul style="list-style-type: none"> - Detection limit of target gas - Recovery of the baseline - Sensitivity line - Adsorption and desorption times
Test at different concentrations of target gas - cumulative test	<ul style="list-style-type: none"> - Recovery of the baseline - Sensor stability - Sensitivity line
Cross sensitivity (Target gas - Humidity)	- Influence of humidity on the response to a target gas
Cross sensitivity (Target gas - interfering gas)	- Influence of an interfering gas on the response to a target gas.

Table 3-2- Type of tests carried out according to the testing protocol and various obtainable parameters and characteristics according to the obtained test results.

Detailed examples of input cycles (times, temperatures, flow rates of the flushing system) to obtain the listed tests are presented in ANNEX 5.

***4 Chapter 4: WO₃ nanofibers
frabrication for gas sensing
measurement***

4.1 Fabrication of WO₃ nanofibers

Introduction

The technique used in this thesis to fabricate nanofibers is electrospinning, and the metal oxide material is tungsten triOxide (WO₃) that is a n-type semiconductor.

Electrospining is mainly a process to fabricate nanofibers from synthetic polymers for technical applications such as textile and filter industry, and medical industry such as drug delivery and tissue engineering. So far, considerable attempts have been made not only in the theoretical understanding and modeling of this process, but also in the optimization of operational parameters to control the formation of fibers and to design a wide range of devices. These studies and results have led to the extension of electrospinning process to fabricate nanofibers beyond polymers made of metals, metal oxides, organic/inorganic and inorganic/inorganic materials.

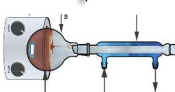
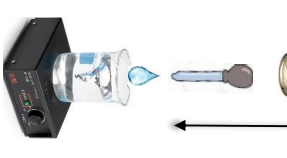
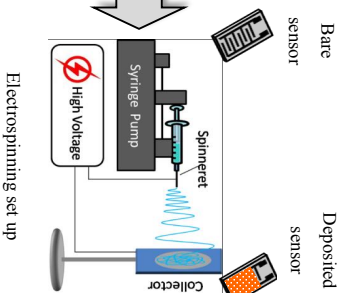
One of the application of nanofibers that are being widely studied is gas sensing applications. One of the specifications of nanofibers that makes them suitable sensing material is outlined as; their one-dimensional structure that increases the reacting and sensing surface area, the short electronic diffusion distances across the fiber diameter and the high porosity of the non-woven fabric obtained with electrospinning [102].

Following, the flow chart of the metal oxide nanofiber preparation process is illustrated that consists of the following steps:

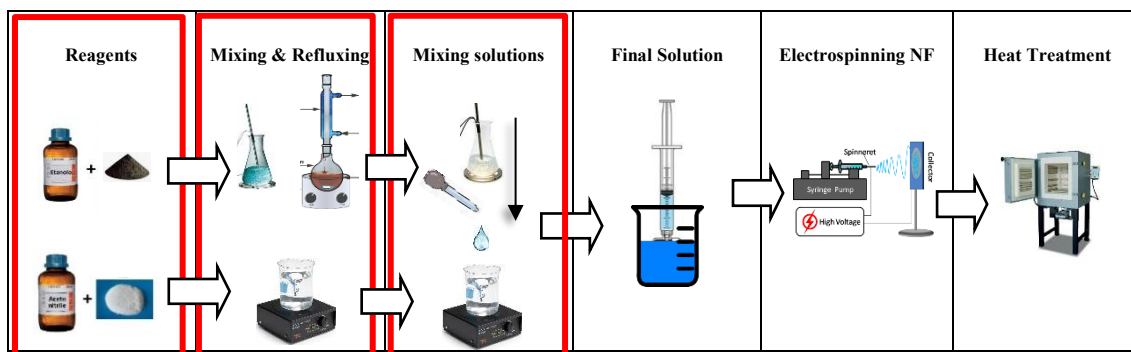
- Identification of reagents
- Mixing of reagents
- Refluxing and metal alkoxide preparation
- Polymer mixing and precursor preparation
- Electrospinning nanofibers
- Heat treatment

Following the flow chart, each of the above mentioned steps will be described and discussed.

FLOW CHART OF THE NANOFIBRE PREPARATION PROCESS

Reagents	Mixing and Refluxing	Drop by Drop Mixing	Final solution	Electrospinning NF	Heat Treatment
<p>Solvent Tungsten Chloride</p>  <p>DMF PVP</p> 	<p>Tungsten Chloroalkoxide</p>  <p>Refluxing</p>  <p>Polymer solution</p> 	<p>Precursor-Tungsten Chloroalkoxide</p>   <p>Polymer solution</p> 	<p>Final solution</p> 	<p>Electrospinning NF</p>  <p>Bare sensor</p> <p>Deposited sensor</p>	<p>Heat Treatment</p> 
General Description of Process Set up					
<p>Appropriate reagents (PVP, DMF, tungsten chloride, ethano) are selected as components of the composite polymeric solution for electrospinning.</p>	<p>Two solutions are prepared under nitrogen in glow-box: tungsten chloroalkoxide that is refluxed to form precursor tungsten alkoxide, and polymer solution.</p>	<p>After refluxing and extracting Chloride in glow-box, obtained tungsten alkoxide solution is added drop by drop to the polymer solution under stirring to form the final polymeric solution for electrospinning.</p>	<p>The final polymeric solution is pulled inside the syringe to be mounted on the electrospinning machine for spinning.</p>	<p>Final solution is spinned and deposited on the bare interdigitated sensor substrate by means of electrospinning technique.</p>	<p>The nanofibers are subjected to high temperature calcination to remove the polymer and ensure the formation of the desired oxide crystals.</p>
CRITICAL PARAMETERS AND CONTROL OF PROCESS STEPS					
<p>1. Chemical composition of powders</p>	<p>1. Concentration of W-O solution 2. Viscosity of polymer solution 3. Reactivity of W-O solution with oxygen</p>	<p>1. Refluxing/chlorine removal 2. Molecular weight of the polymer 3. Mixing of the solutions 4. Concentration 5. Surface tension</p>	<p>1. Viscosity of the final solution 2. W-O concentration in final solution</p>	<p>1. Process parameters 2. Parameters of the solution 3. Environmental parameters. 4. Diameter of the fibers 5. Shape of the fibers.</p>	<p>1. Temperature 2. Time 3. Heating speed /cooling down</p>

4.1.1 Reagents, mixing and refluxing

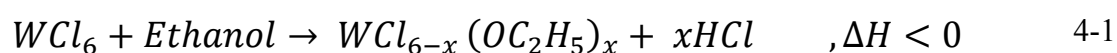


For the preparation of nanofibers based on metallic oxides, a colloidal final solution was prepared using two different solutions: one precursor based on inorganic metal salts dissolved in ethanol and the other based on polyvinyl phormamide dissolved (PVP) in Dimethyl Formamide (DMF).

The precursor salt solution provides the overall system with the right amount of material to form metallic oxide nanofiber after heat treatment; the polymeric solution has the function of carrier and makes the overall solution viscosity to the right point to allow the formation of nanofibers.

In order to prepare the precursor solution, tungsten chloride WCl₆ was dissolved in Ethanol. Since WCl₆ is very reactive in air, all the process steps from precursor preparation till electrospining and nanofiber deposition was done under nitrogen environment inside glove-Box at 25 °C and the relative humidity (RH) of 4.5% (±2%).

By dissolving 0.4 g of anhydrous tungsten(VI) chloride (WCl₆) in 5 mL of ethanol, under stirring at room temperature in a glove box under N₂ controlled atmosphere, a yellow color solution formed after 2 minutes which changed to dark blue and stayed stable, see Figure 4-1 a-e. Equation 4-1 shows the exothermic reaction in which the obtained stable dark blue solution is liquid tungsten chloro alkoxide with the pH of 1 and hydrogen chloride that evaporates;



To transform tungsten chloro alkoxide to tungsten alkoxide and remove the chlorine and form a pure W-O bond in solution, the obtained solution, was refluxed at 50°C under nitrogen environment, see Figure 4-1f. After 48 hours of refluxing a transparent solution was obtained, Figure 4-1 f-j.

The stability and the evolution of W-O bond in the obtained sol-gel precursor (SGP) was monitored over a period of 4 days by FT-IR.

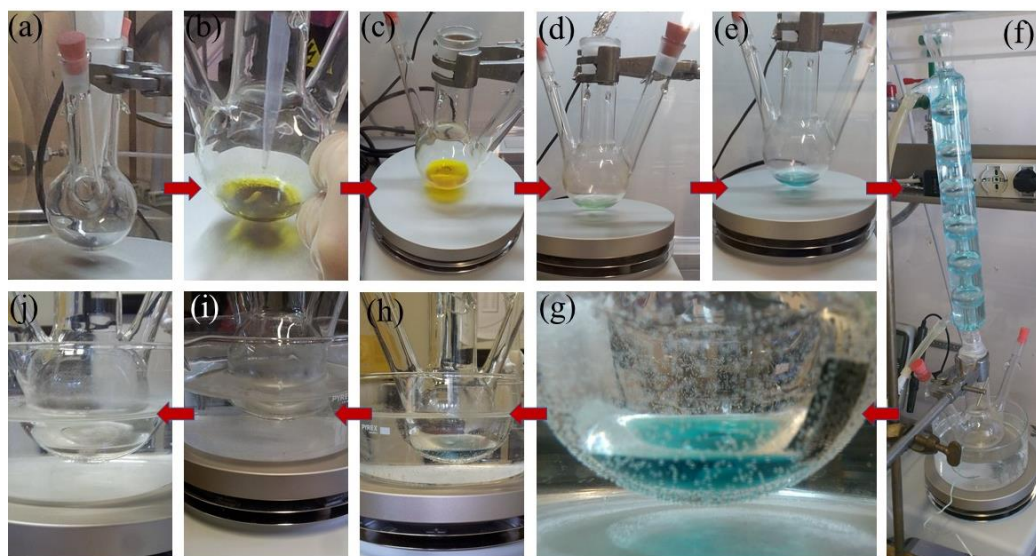


Figure 4-1- WO₃ precursor preparation steps; a) WCl₆ powder inside a beaker in glove-box under N₂ environment, b) adding ethanol to the WCl₆ powder, c) WCl₆ in ethanol after few seconds, d) WCl₆ and ethanol after 1 minute, e) WCl₆ and ethanol after 2 minutes, f) WCl₆/ethanol solution under refluxing, g) dark blue WCl₆/Ethanol solution at the beginning of refluxing, h) dark blue WCl₆/Ethanol solution after 1 hour of refluxing, i) transparent solution obtained after 2 days (48 hours) of refluxing, j) transparent solution after 4 days of refluxing

4.1.1.1 W-O precursor-gel FTIR characterization

In order to make the most effective use of the refluxing procedure to yield transparent SGP solution, we have monitored the evolution of W-O bonds inside the SGP solution by FTIR. Figure 4-2(a) shows the FTIR spectra of the SGP solution collected over a period of four days. The black curve has been collected after the first hour (solution in Figure 4-1h), whereas the red and blue curves refer to samples collected after 2 and 4 days of reflux, respectively (solutions shown in Figure 4-1 i&j respectively). From a qualitative point of view, no differences can be found between the red and blue curves. It turns out

that two days refluxing are at least needed to complete the stabilization of the chemical compounds inside the SGP transparent solution. On the other hand, the large differences between the black and the red curves provides a strong evidence that the sol gel process has not yet activated after 1 h. From a quantitative point of view, apart from the broad band centered around 3370 cm⁻¹ (OH stretching) and 1627 cm⁻¹ (OH bending) showing the occurrence of W-alkoxides formation, other peaks may be attributed to C=O and =CH₂ bonds [103]. Referring to Figure 4-2(b), the appearance of amorphous W-O bonds can be assigned, according to literature [103], to the shallow shoulder located around 600 cm⁻¹. This W-O peak shifts towards higher wave numbers, at 813 cm⁻¹ (see green curve in Figure 4-2(a)), in the WO₃ electrospun NFs annealed at 450°C. This blue shift can be assigned to the formation of W-O-W crystalline bonds [104].

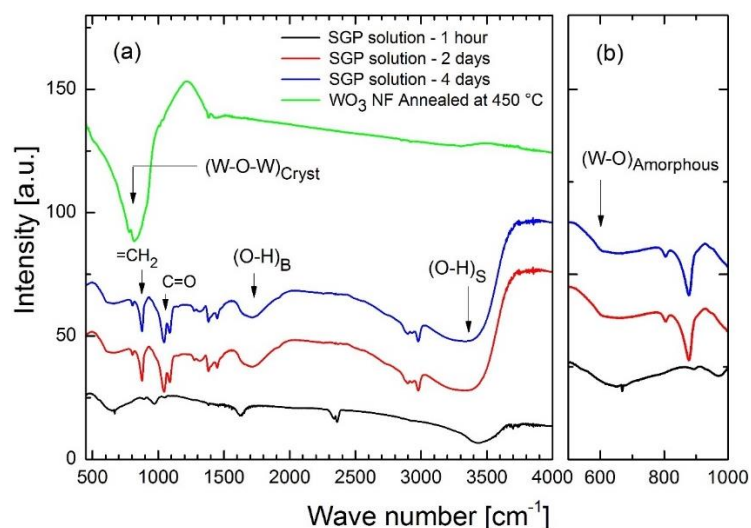


Figure 4-2- Panel (a): Survey FTIR spectra of the SGP solution collected after 1 h (black), 2 days (red) and 4 days (blue) together with the annealed WO₃ NF at 450°C (green). Panel (b): Close-up in the FTIR 500-1000 cm⁻¹ of the SGP solution.

The polymer solution (PMS) was prepared by desolving 0.17 g of PVP (molecular weight (MW) = 1,300,000) in 1 mL of DMF.

The final solution (PVP + DMF) + (WO₃-TR) was prepared in N₂ controlled atmosphere by adding drop by drop the polymeric precursor solution (WO₃-TR) to the polymer solution (PVP + DMF) inside a glove-box under N₂ at 29°C and relative humidity of 4.5% ±2%.

Table 4.1 shows the amounts of the various substances used to obtain the final solution.

WO ₃ TR	Precursor solution		Polymer solution	
	Salt	Solvent	Polymer	Solvent
	WCl ₆	Ethanol	PVP	DMF
Amount	0.4 g	5 mL	0.17 g	1 mL

Table 4-1- Quantity of the various substances used to obtain the final solution.

4.1.1.2 Thermogravimetric characterization

The spinning solution (SPS) prepared by mixing the SGP transparent solution with the PMS has been characterized by thermogravimetric technique in the temperature range 25-500°C in static air. Figure 4-3 shows the percentage of weight loss as function of the temperature of the PMS and the SPS, respectively. The burn out of the PMS is almost completed at 150°C yielding an associated weight loss of 80%. The 100% and 85% of entire weight losses of the PMS and of the SPS are respectively achieved in the temperature range 450-500°C. These results imply that, 15% of the SPS initial weight is still left at 500°C and this 15% agrees with the calculated weight percentage of the expected WO₃ in the spinning solution after complete reaction of the WCl₆ precursor and full crystallization. XRD diffraction measurements on the samples annealed at 400°C, 450°C and 500°C agree with the results confirming the formation of monoclinic WO₃ crystalline structure in the range 300-350°C [105, 106].

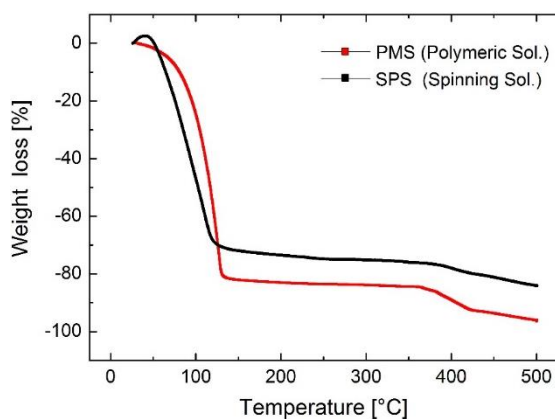
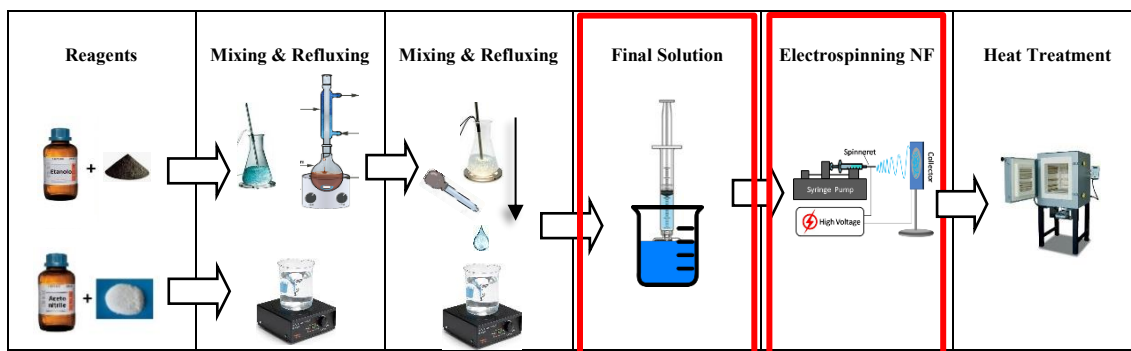


Figure 4-3- Thermogravimetric response displaying the percentages of weight loss as a function of the temperature of the polymeric solution (PMS, red curve) and the spinning solution (SPS, black curve).

4.1.2 Final Solution preparation and Electrospinning



After drop by drop adding of the precursor to the polymer solution under stirring, the mixture was left for a couple of hours under stirring to obtain a homogenous polymeric final solution. The obtained mixture was inserted inside a 5 mL syringe and was placed on an automatic pump with an appropriate flow rate.

Figure 4-4 represents the electrospinning machine used for depositing MOS nanofibers in this work. As can be seen this device is composed of the following parts:

- 5 mL syringe (ARTSANA) needle No. 14 - 23G x 1¼" - 0.60 x 30 mm;
- Silicon based DPN substrate with a layer of naturally occurring silicon oxide 2-3 nm and inclusions of nitrogen (Micron);
- High potential voltage generator ($V = 0-30\text{kV}$; $W = 20\text{Watt}$; $I_{\text{max}} = 13\text{A}$);
- Manually movable X-Y axels;
- Rotational Collector;
- Automatic pump that houses the syringe containing the solution and allows adjusting the flow rate.

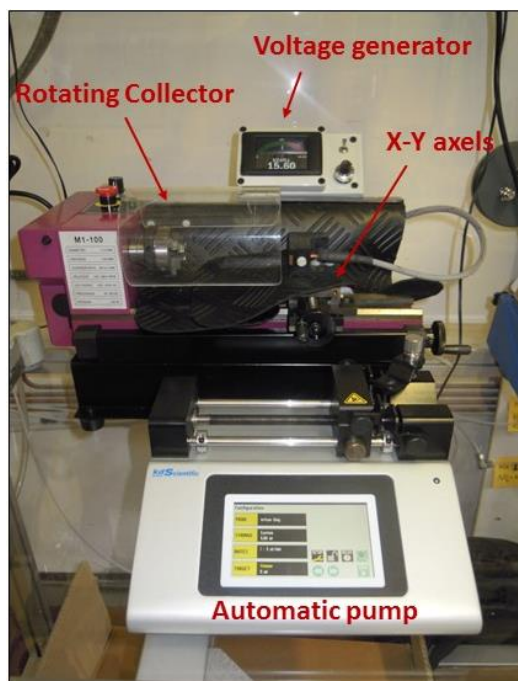


Figure 4-4- Experimental set-up for electrospinning deposition of nanofibers inside a glove-box

The general set up and working of this device is in this way that the final solution composed of M-O and polymer solutions is injected in a horizontal syringe and then the syringe and its piston is actuated by the dosing pump. The solution coming out of the syringe passes through a tube connected to the metallic needle, which in turn is connected to the positive electrode of a high voltage potential generator via a metal clamp. The bare interdigitated sensor substrate is placed on the rotational collector. Manually you can actuate the collector motor and change the rotational speed of the collector, which rotates on a plane perpendicular to the needle, and set the desired voltage value; if the set voltage value is higher than the critical value, a deformation of the drop on the tip of the needle will be observed with the naked eye and then the formation of the jet explained in section 1.6.2. The fibers that emerge from the cast are deposited on the manifold, thus completing the electrical circuit.

The purpose of the electrospinning process applied to the manufacture of metallic oxide sensors is the production of nanofibres that are uniform and continuous in their length and have a circular cross section with values of a diameter of several hundred nm. Nanofibre diameter is a key parameter for the non-woven fabric produced with them, as it influences structural characteristics such as the pore diameter and the specific surface, which

strongly influence the gas adsorption of the sensor; likewise, the nanofibre shape controls the specific inner surface of the fabric, the porosity, and also the gas flow around the fibers.

For this reason, it is important to evaluate which parameters are most influenced by the diameter of the fibers and their shape, but also how to modify them in order to obtain fibers with desired characteristics and reproducibility.

4.1.2.1 Electrospinning: Influential Parameters

Solution Parameters: Polymer concentration

A low polymer concentration in solution causes a sharp narrowing of the fiber diameter along the needle path/collector solely evaporation of the solvent. However, the effect of polymer concentration goes beyond this direct contribution, in fact it strongly influences viscous viscoelastic response and fluid flow. The fiber diameter tends to increase (non-linearly) with the polymer concentration, but it should be noted that all combinations of polymer/solvent concentrations can not be spun. Very low polymer concentrations solutions (<4%) form drops during spinning [107], on the other hand, solutions with excessive polymer concentrations are so viscous that cause electrospinning failure, as the drop dries or the solution flow rate through the needle is too low.

One of the conditions required for fiber formation is the appropriate viscosity of the solution. This condition can be obtained through two ways, one by using a high molecular weight polymer or another by increasing the polymer concentration. In this way the entanglements between the polymer chains keep the cast together and prevent it from breaking and increase the solution drops. The number of entanglements is closely related to the length of the polymer chains, the higher the molecular weight of the polymer in solution the more the entanglements, and also an increase in concentration means a greater number of polymer chains.

An inadequately viscous solution can lead to both breakage of the cast and the formation of droplets as well as the formation of beaded fibers (there are fibers with small drops arranged along them); in the latter case, when the viscosity of the solution is not such as to overcome the surface tension this will result in a structure called a necklace.

For particular polymer concentrations in the solvent it may happen that branched fibers are obtained as a smaller secondary casting developed from the main jet, or the jet breaks

into multiple jets. This is because during the stretching and evaporation of the solvent the form and amount of charge per unit surface present in the jet are changed; as a consequence that the balance between the electric forces and the surface tension is no longer respected and the jet becomes unstable. This type of secondary instability, which leads to the branch of one or more smaller jets from the main jet, may accompany the primary spasm-instability and is frequently observed in more viscous and concentrated solutions and subjected to a higher electrical field than the minimum required to produce a single jet, see Figure 4-5.

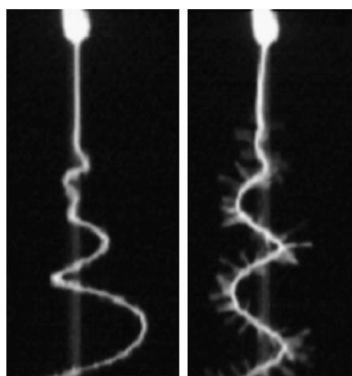


Figure 4-5- Spiral jet ramifications of a dissolved polycaprolactone solution in acetone. The ramifications grow in a radial direction with respect to the main jet segment from which they are distributed [8].

Solvent type of solution

For a given range of polymer concentrations, it can happen that rapid evaporation of the solvent leads to the formation of ribbon fibers, see Figure 4-6. Initially evaporation of the solvent affects the surface of the fluid jet, the phenomenon gives rise to a solid surface shell and the consequent further evaporation of the solvent into the core of the jet causes the formation of hollow fibers.



Figure 4-6- Schematic model for the formation of ribbon fibers [8].

Electrical Conductivity of solution

As mentioned above, the electrospinning involves stretching the solution due to the repulsion of the charges on the surface of solution. Consequently, at a higher conductivity there is more charge in the jet, therefore, the stretching effect will be more relevant, and leads to a reduction in the diameter of the fibers as well as a lesser tendency to form beads. The conductivity of the solution will be simply increased by adding a small amount of salt to the solution. Salt should be chosen, bearing in mind that the mobility of ions depends on their size; smaller ions in solution means greater mobility and a greater stretch of the jet [107].

Applied potential

The applied voltage and the resulting electrical field have a direct impact on the stretching and acceleration of the jet and fiber morphology. In general, higher voltages cause a stronger electric field and more important Coulomb forces: thus, increasing the stretching of the jet, resulting in a decrease in fiber diameters and an increase of solvent evaporation speed. Too high voltages, however, cause an acceleration of the jet to dramatically reduce the jet transit time to the collector; the fibers therefore do not have much time for stretching and elongation, that result in fibers with higher diameters.

Flow rate

As the flow of the syringe pump increases, the fiber diameter is expected to increase as the volume of solution to be spun in the unit of time is higher. But this is not always true; if the flow rate is equal to the speed at which the solution is "pulled" by the jet (determined by the force of the electric field and then by the voltage), enhancing the flow rate increases

the number of charges. In this case, the stretching of the jet is greater and the obtained fibers have smaller diameters, in contrast to what previously mentioned above. If you work with higher flow rates, because of the higher volume of solution to be treated, the time it takes for the solvent to evaporate completely is higher. If the velocity with which the jet moves towards the manifold is very high, and therefore the time taken to reach the collector is very small, the solvent does not have enough time to evaporate. The fibers therefore, when deposited on the collector and come into contact with the fibers already deposited, melt and stick together, precisely because of the residual solvent. For this reason, it is preferable to work with lower flow rates, so that the solvent evaporates completely.

Needle/collector distance

A decrease in the distance between needle and collector causes an increase in fiber diameter as it suppresses the last stages of the elongation process induced by whiplash instability. Increasing the distance, however, increases the electric field and therefore the acceleration of the jet and hence prevents the solvent from evaporating completely.

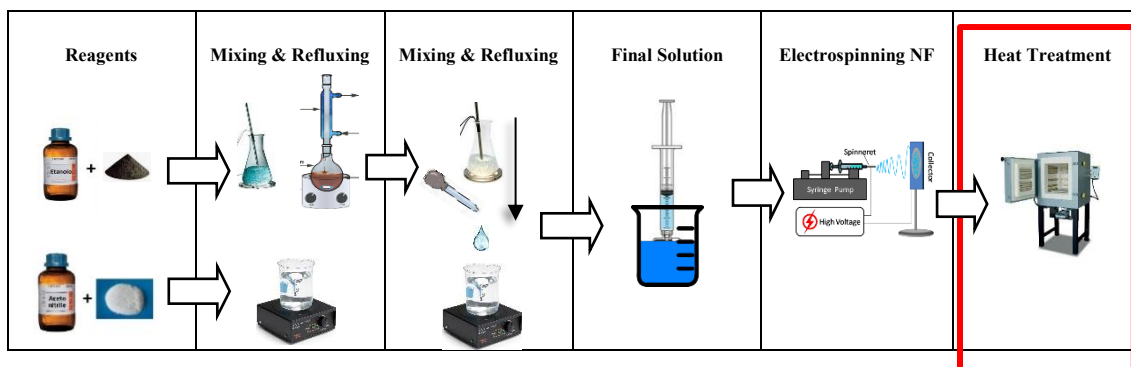
Depending on the characteristics of the solution, the distance may also affect the morphology of the obtained fibers; In fact, for high needle / collector distances, the deposition of wrinkled fibers results from the formation of curvature instability in the final part of the jet. Such instability appears to be due to longitudinal compression forces acting at the time of impact on the collector and is a phenomenon other than whiplash instability originating from electrical factors.

Considering the above mentioned influential parameters, the WO₃ nanofibers electrospinning parameters are presented in Table 4-2.

Electrospun nanofiber	Needle/Collector distance (Cm)	Pump capacity ($\mu\text{L}\cdot\text{min}^{-1}$)	Voltage (V)
WO ₃ nanofiber	10	1	14

Table 4-2- Electrospinning parameters for the WO₃ nanofiber preparaion.

4.1.3 Heat treatment



To evaporate the polymer and crystallize WO₃ in the spun nanofiber, samples should be fired at an appropriate temperature.

In particular, the formed WO₃ must have a well-defined structure, morphology, surface area and a well-defined pore volume, and must also exhibit good mechanical strength.

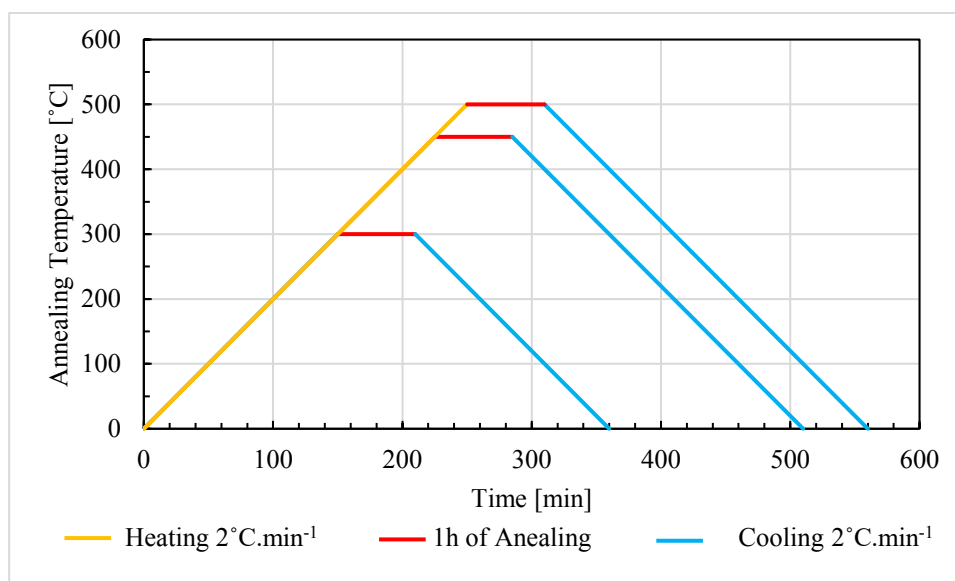
The oven used for annealing process is a programmable cycle furnace, Lenton, and the oven chamber consists of four heat-shrinkable radiant heat plates, which allow uniform temperature in each part of the heating chamber.

Among the various types of chemical or chemical-physical transformations that occur during calcination, polymer burning and evaporation forms a porous structure of nanofibers, also beside the evaporation of polymer, elevated temperature results in crystallisation of WO₃ grains along in the nanofiber shape.

The other important issue to consider is the grain size of the crystallized WO₃ by annealing. Smaller grains provide more surface area for gas adsorption on the other hand vigorous annealing may result in grain growth, decreasing the surface area and also rupture in the nanofibers and forming discontinuous nanofibers.

For these reasons it is of high importance to evaluate the right annealing temperature and duration of as electrospun nanofibers. According to the thermal analysis and literature results, electrospun nanofibers were oven-annealed in static for 1 h within the temperature range 300-500°C using a heating and cooling rate of 2°C/min. The annealing procedure and profile used in this work is presented in Table 4-3 and Figure 4-7 respectively.

Electrospun nanofiber	Annealing Temperature [°C]	Annealing duration [h]	Heating rate [°C.min ⁻¹]
WO ₃	300	1	2
	450	1	2
	500	1	2

Table 4-3- Annealing procedure of WO₃ electrospun nanofibersFigure 4-7- Annealing process of electrospun WO₃ nanofibers

4.1.4 SEM characterization of annealed nanofibers

Figure 4-8 compares the SEM images for the as deposited and annealed WO₃ NFs at low (left side) and high magnification (rightside), deposited on Si₃N₄ substrates. From a morphological point of view, there are not large differences comparing the as deposited NFs (Figure 4-8(a) and (b)) with the annealed at 300°C (Figure 4-8(c) and (d)). At 300°C the NFs still maintain a smooth appearance without any evidence of crystallization, confirming an incomplete removal of the polymer. Between 400°C and 450°C a sort of “spider web” structure is developed, with entangled NFs characterised by a rough surface made of loosely sintered grains, as displayed Figure 4-8(e) and (f). At 450°C NFs resulted to be shrunk as respect to those ones annealed at 300°C, with diameters ranging from 20 nm to 100 nm and composed by a fine texture of 20 nm in diameter micro-crystalline

grains. At 500°C excessive grain growth causes the fibers to crack with the subsequent formation of extended fibers discontinuity, as reported in Figure 4-8(g) and (h).

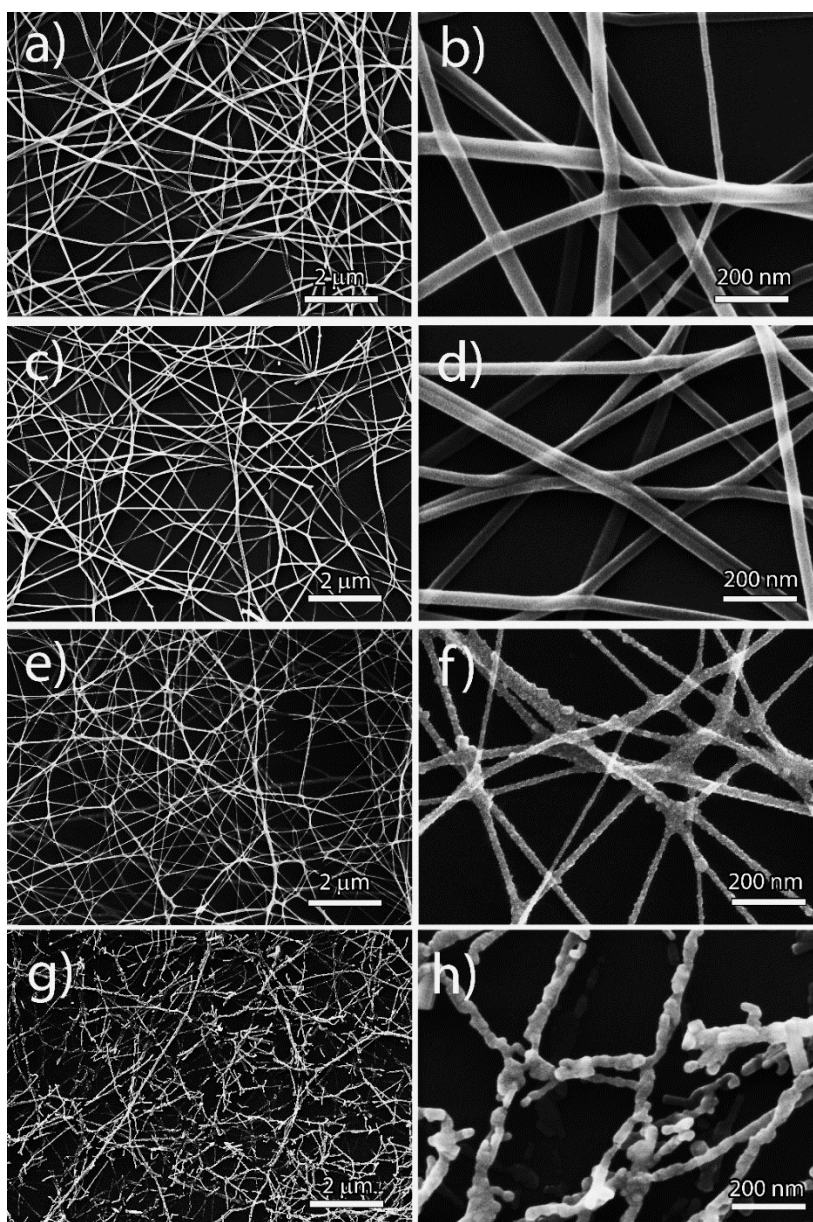


Figure 4-8- SEM images of electrospun NFs annealed at different temperatures for 1 h. Panels (a) and (b), as deposited; panels (c) and (d), after annealing at 300°C; panels (e) and (f), after annealing at 450°C; panels (g) and (h), after annealing at 500°C.

4.1.5 Electrical and optical characterization of WO₃ nanofibers

The gas response of MOX sensors activated by visible light sources is known to be dependent from both the emission wave-lengths and the irradiance. The characterization of the LED sources has been carried out before any gas response evaluation and previously explained in detail in section 3.3.3.

Electrical gas responses have been carried out by exposing the 450°C annealed WO₃NFs to different temperatures in the range 25-100°C and different illumination conditions. Preliminary tests have been performed at room temperature (25°C ± 2°C) to investigate the influence of the LED source characteristics on the “gas response properties”. The following figures of merit have been introduced to address these “gas response properties”:

- Base line resistance (BLR): the resistance in dry air at equilibrium before a gas exposure;
- Relative response (RR): the ratio (R_G/R_A) or (R_A/R_G) for a given concentration of oxidizing or reducing gas, respectively. R_A and R_G represent the resistance in dry Air and in Gas, respectively;
- Adsorption/desorption time (τ_{ads}/τ_{des}): the time required to reach 90% of the full response at equilibrium, during both gas adsorption and desorption;
- Recovery percentage (RP): the percentage ratio $(\Delta_D/\Delta_A) \times 100$, where Δ_D and Δ_A are the variations of the electrical resistance during gas adsorption and desorption, respectively, calculated within the time scale of the sensing cycle.

Regarding these points it must firstly be pointed out that, given the time scale of a sensing cycle, gas adsorption/desorption times can be eventually numerically quantified only if the equilibrium conditions are achieved. Secondly, the recovery percentage (RP) is a measure of the sensor ability to recover, after degassing, its BLR. Under these circumstances it could happen that by desorbing in air, equilibrium conditions are achieved (i.e., $\tau_{ads/des}$ can be quantified) but the sensor resistance fails to regain its original base line value. This occurs in the case of irreversible adsorption, when gas molecules are bound so strongly to the surface that they never desorb, regardless the time scale of a sensing cycle. Lastly, it may be the case that no equilibrium conditions are achieved during desorption so that neither base line recovery is achieved, nor $\tau_{ads/des}$ times can be

quantified.

Figure 4-9 shows the influence of light illumination at different wavelengths on the response to 400 ppb NO₂ at room temperature and dry air carrier gas. The time scale for each adsorption and desorption cycle has been set at 60 min. The distance of the LEDs sources from the sensor surface has been placed at its minimum value of 0.5 cm. Table 4-4 displays a quantitative description of the gas response for the NFs annealed at 450°C.

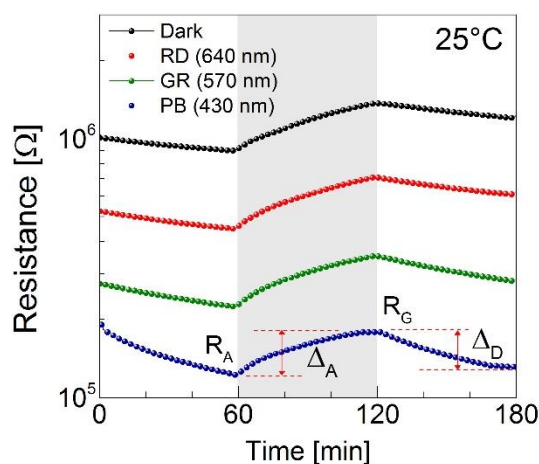


Figure 4-9- The influence of light illumination at different wavelengths to 400 ppb NO₂ at room temperature and dry air carrier gas, for a distance between the LEDs and the MOX surface equal to 0.5 cm.

Figure 4-9 and Table 4-4 show that, departing from dark conditions, decreasing the wavelength from RD to PB the BLR decreases of almost one decade. RRs are nearly constant under dark conditions and RD and GR illumination, whereas the PB illumination produces a slight decrease of RR with the increase of the light irradiance reaching a minimum value of 1.38 ± 0.2 for $770 \mu\text{W}/\text{cm}^2$. RP values remarkably increase from 9% (dark conditions) up to 92% (purple-blue). Considering the features and shapes of the curves displayed in Figure 4-9 no adsorption/desorption equilibrium conditions have been achieved within the time scale of the experiment. This is the reason why $\tau_{\text{ads/des}}$ times have not been shown (see the last two columns of Table 4-4).

Light source	Wavelength [nm]	Photon energy [eV]	Light intensity [$\mu\text{W}/\text{cm}^2$]	BLR [Ω]	RR [-]	RP [%]	τ_{ads} [min]	τ_{des} [min]
Dark	-	-	-	8.9×10^5	1.55 ± 0.2	9	-	-
RD	630	1.94	95	4.5×10^5	1.57 ± 0.3	38	-	-
GR	570	2.18	40	2.5×10^5	1.56 ± 0.2	55	-	-
PB	430	2.88	270	1.4×10^5	1.49 ± 0.2	83	-	-
			568	1.3×10^5	1.43 ± 0.2	86	-	-
			770	1.2×10^5	1.38 ± 0.2	92	-	-

Table 4-4- BLR, RR, RP and response times to 400 ppb NO₂ at room temperature for light illumination at different wavelengths. Also reported the sensor responses by changing the PB light intensities ranging from 270 to 770 $\mu\text{W}/\text{cm}^2$.

The influence of the PB light intensity obtained by changing the LED distances from sensor surface is shown in Figure 4-10. The numerical values are also reported in the last three lines of Table 4-4. Adsorption and desorption times have been extended to a time scale of 3 hours to reach the equilibrium. Moreover, the sensor surface temperature has been controlled by a thermocouple positioned on the back side of the substrate. No local heating of the substrate under the highest intensity of 770 $\mu\text{W}/\text{cm}^2$ of the PB illumination has been measured. Regardless its intensity, PB illumination decreases (increases) (RRs) (RPs) as compared to dark condition, RD and GR illumination. More in detail, by increasing the PB light intensity the RRs slightly but steadily decrease (from 1.49 to 1.38) whereas RPs improve (from 83% to 92%). Equilibrium conditions are almost achieved during adsorption after three hours exposure to 400ppb NO₂. On the other hand, no equilibrium conditions have been achieved during desorption in dry air within the time scale of the experiment.

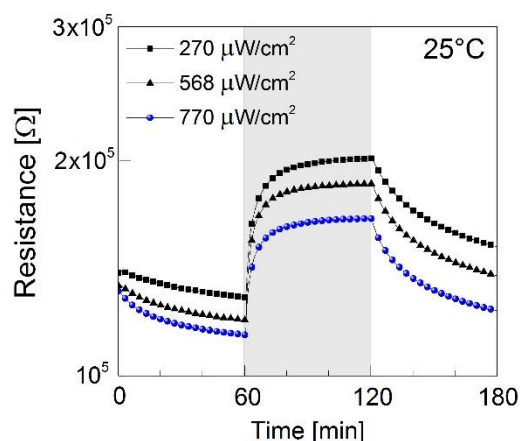


Figure 4-10- The influence of the PB light illumination for different intensities to 400 ppb NO₂ at room temperature and dry air carrier gas.

PB light at 770 $\mu\text{W}/\text{cm}^2$, although less responsive in terms of RRs, has been selected for further investigations, considering its greater recovery and faster response time, in view of its practical application. The influence of thermal and PB light activation to different NO₂ sub-ppm concentrations are compared in Figure 4-11. During the test PB light intensity was set at 770 $\mu\text{W}/\text{cm}^2$ and the OT changed from 25°C to 100°C. Table III compares RRs, Recovery RPs, τ_{ads} and τ_{des} as function of OT, in dark and light conditions, respectively. From Figure 4-11 it turns out that the slope of the BLRs (dotted lines in Figure 4-11a) tend to be horizontal as OT increases. This feature is well represented in Table 4-5 by the increase of the RPs. To this extend the positive effect of light illumination is remarkable considering that RPs values, under PB light, reach 92% at 25°C and 99% at 100°C, as compared to 9% and 96% in dark conditions, respectively. Equilibrium conditions during adsorption and desorption are hardly achieved at 75°C OT, considering 60 minutes the time scale of each cycle. Adsorption and desorption times at equilibrium are slightly shorter under PB light illumination, but with a tendency to be comparable with the values in dark conditions at 100°C. RRs under dark conditions are always greater than the one recorded under PB illumination within the OT range 25-100°C OT. The maximum value of RR is achieved at 75°C OT for both dark conditions and light illumination, whereas a pronounced reduction of the RRs is recorded at 100°C OT. It may be concluded that:

- 1- the NFs light activation decreases the BLR with decreasing the light wavelengths;

- 2- the PB illumination slightly decreases the RR as respect to the dark conditions, GR and RD illumination;
- 3- RR further decreases by increasing PB light intensity;
- 4- PB light source is the most effective to enhance the RP of the BLR and to reduce the adsorption/desorption times;
- 5- the combined action of OT and PB light illumination demonstrated that heating the NFs at 75°C with a PB light intensity of 770 $\mu\text{W}/\text{cm}^2$ allow achieving RR of 12.4 to 400 ppb NO₂ and RP of 97% of the BLR.

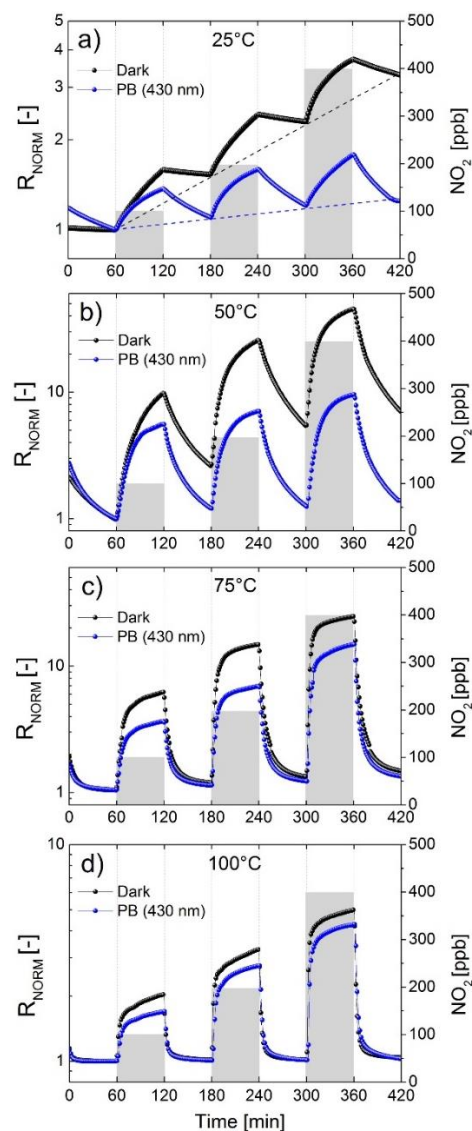


Figure 4-11- Dynamic normalized responses of WO₃ NFs annealed at 450°C to NO₂ gas (100-400ppb in dry air) in dark conditions (black line) and PB light ($\lambda=430\text{nm}$ at $770\mu\text{W}/\text{cm}^2$) at different OT (25-100°C).

OT [°C]	DARK CONDITIONS					PB LIGHT ILLUMINATION				
	BLR [Ω]	RR=R _G /R _A [-]	RP (Δ _D /Δ _A)*100 [%]	τ _{ads} [min]	τ _{des} [min]	BLR [Ω]	RR=R _G /R _A [-]	RP (Δ _D /Δ _A)*100 [%]	τ _{ads} [min]	τ _{des} [min]
25	8.9 x	1.55	9	-	-	1.2 x 10 ⁵	1.38	92	-	-
50	9.7 x	8.29	81	-	-	5.8 x 10 ⁴	7.62	95	-	-
75	3.2 x	18.42	93	38	42	9.3 x 10 ³	12.46	97	33	38
100	6.2 x	4.95	96	31	33	3.4 x 10 ³	4.32	99	30	32

Table 4-5- Comparison of RR, RP, τ_{ads} and τ_{des} to 400ppb NO₂ in dark conditions and PB light illumination (λ=430nm at 770μW/cm²) at different OT (25-100°C).

4.2 Discussion of the electrical responses

4.2.1 Response in dry air

WO₃ is a non-stoichiometric oxide presenting a slight deficiency of lattice oxygen ions [WO_{3-x}] giving to the structure its characteristic *n*-type behavior [105, 108]. In air at equilibrium the ambient oxygen adsorbs in the forms of O₂⁻, O⁻ or O²⁻, depending on the surface temperature [109]. In the temperature range 25-100°C, O₂⁻ is reported to be the most stable species, adsorbing primarily on lattice oxygen vacancies, according to the reaction 4-2.



where e_{CB}^- represents electrons from the conduction band, $V_O^{\bullet\bullet}$, according to the Kröger-Vink notation, represents a doubly charged positive oxygen vacancy and $(O_2^- - V_O^{\bullet\bullet})_{ADS}$ a chemisorbed oxygen coupled with $V_O^{\bullet\bullet}$. The equilibrium 4-2 corresponds to the initial state of the WO₃ NFs surface at equilibrium in air.

At room temperature, exposing to visible light the WO₃ NFs produces a behavior like the one previously reported for thick [110, 111] and mesoporous WO₃ films [112]. The decrease of the base line resistances of Figure Figure 4-9 and Figure 4-10 can be explained taking into consideration the photo-desorption of the adsorbed surface oxygen species $(O_2^- - V_O^{\bullet\bullet})_{ADS}$, induced by impinging photons with associated visible light energies ranging between 2.88eV (PB) and 1.94eV (RD). To this extend WO₃ with a band gap of 2.75eV [113], is a promising material since it is capable of desorbing O₂⁻ by both

electronic band-to-band transition at $\lambda \leq 430\text{nm}$ (first mechanism) and by direct adsorption of the incident photon by use of less energetic sources at $\lambda \leq 630\text{nm}$ (second mechanism). The first mechanism [110-112, 114, 115], as shown in the reactions which follow, occurs at $\lambda \leq 430\text{nm}$ (i.e., PB light with a photon energy of 2.88eV). Here the photo-induced electron-hole couple reaction 4-3 yields h^+ to desorb oxygen from $(O_2^- - V_O^{\bullet\bullet})_{ADS}$ reaction 4-4 providing, at the same time, photo-generated electrons (e_{hv}^-) with enough energy to overcome the band gap (located at 2.75eV), which quickly recombine with $O_{2(g)}$ reaction 4-5. A new equilibrium is thus displaced reaction 4-6, comprising the presence of strongly chemisorbed $(O_2^- - V_O^{\bullet\bullet})_{ADS}$ and less bound $(O_2^- - V_O^{\bullet\bullet})_{hv}$. Based on this, oxygen on the whole is not desorbed from the surface, but is actually, partially transformed, to a less electro-negative $(O_2^- - V_O^{\bullet\bullet})_{hv}$ species which is responsive for the thinning of the depletion layer and eventually for the decrease of the base line resistance as displayed in Figure 5.



To this extend, the slight decrease of the base line resistance of Figure 4-10 with the increase of the PB light intensity (from 270 to 770 $\mu\text{W}/\text{cm}^2$), may be attributed to a shift of the equilibrium of reaction 4-6 to the right, enabling the increase of the concentration of further less charged states.

The second mechanism takes place by direct impingement of photons (with energy $h\nu$) on the $(O_2^- - V_O^{\bullet\bullet})_{ADS}$, enabling direct desorption of adsorbed oxygen according to reaction 4-7.



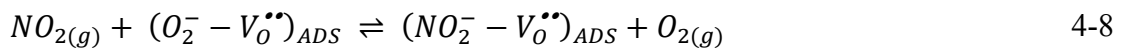
Less energy of the impinging photon is required for reaction 4-7 to occur, considering that the binding energy of chemically-adsorbed oxygen atoms on defective SnO₂, has been estimated to be 1.67eV [116]. To this extend, as shown in Figure 4-9, RD ($\lambda=630\text{nm}$)

and GR ($\lambda=570\text{nm}$) light with associated photon energies of 1.94eV and 2.18eV, respectively, appear to be able to activate the second mechanism, therefore contributing to the decrease of the base line resistance. Both mechanisms contribute to oxygen desorption, but with significant differences in terms of base line recovery and adsorption/desorption times. The bigger recovery percentages RPs achieved by using the PB light illumination, as respect to RD and GR light illuminations as shown in Table Table 4-4 and Figure 4-9, are explained considering that PB light might trigger interband fast electrons transition, whereas RD and GR lights activate only surface desorption processes, with longer timescales, that are characteristic of chemical desorption processes at room temperature.

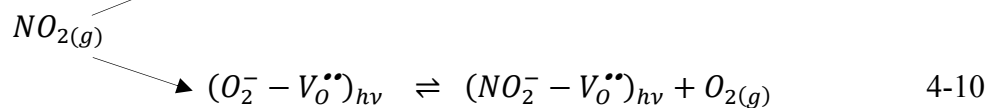
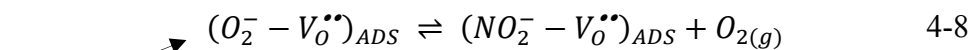
4.2.2 Response to NO₂

Studies on NO₂ gas molecules adsorption on SnO_{2-x} defective metal oxide surfaces highlighted that at temperatures $T < 200^\circ\text{C}$, NO₂ molecules primarily adsorbs on surface oxygen vacancies $V_O^{\bullet\bullet}$. Considering the stronger attitude of NO₂ as respect to O₂ to extract electrons, two adsorption mechanisms have been tentatively proposed which explain the increase of the electrical resistance of *n*-type materials like WO₃, when exposed to few ppm NO₂ [16].

At room temperature and dark conditions, a surface electron transfer mechanism takes place (reaction 4-8), whereas at higher temperatures a thermally-activated transition of bulk-generated conduction band electrons (e_{CB}^-) prevails (reaction 4-9).



At room temperature and PB light illuminations the oxide surface is characterized by the presence of $(O_2^- - V_O^{\bullet\bullet})_{ADS}$ in equilibrium with $(O_2^- - V_O^{\bullet\bullet})_{hv}$ (see reaction 4-6). In this case NO₂ molecules are expected to react as proposed by reactions 4-8 and 4-10.



According to reactions 4-8 and 4-10, the smaller increase of the resistance at room temperature of the PB illuminated WO₃ as respect to samples in the dark conditions (Table 4-4, Figure 4-9 and Figure 4-11a), may be explained considering that the depth of the depletion layer increases by NO₂ adsorption, but to different extents. Indeed, under light illumination, a pre-existing thinner depletion layer associated with the formation of less charged $(O_2^- - V_O^{\bullet\bullet})_{hv}$, might inhibit the formation of larger depleted zones after NO₂ adsorption. This has been represented by reaction 4-10 considering the formation of $(NO_2^- - V_O^{\bullet\bullet})_{hv}$ adsorbates, with associated reduced surface charge. In presence of NO₂ gas, PB illumination decreases the height of the Schottky barrier between the grains, giving rise to a smaller increase of the sensor resistance, thus explaining the smaller RRs of the illuminated samples as respect to the ones under dark conditions. Moreover, the reduced RRs to NO₂, by increasing PB light intensities (see Figure 4-10 and Table 4-4) could be also explained taking into consideration that the equilibrium of reaction 4-6 could shift to the right, giving rise to a larger amount of $(NO_2^- - V_O^{\bullet\bullet})_{hv}$ adsorbates when exposing the surface to NO₂. At room temperature, the RPs of the illuminated samples after degassing, may also account for an easier desorption process of less bounded $(NO_2^- - V_O^{\bullet\bullet})_{hv}$ species as respect to the more strongly charged $(NO_2^- - V_O^{\bullet\bullet})_{ADS}$.

Finally, by increasing the OT under dark conditions, the formation of thermally activated conduction electrons enables the reaction 4-9 to overcome reaction 4-8. The occurrence of reaction 4-9 alone, (since reactions 4-8 and 4-10 are excluded in the dark), explains the bigger resistance increase deriving from the NO₂ exposure, with a maximum of the relative response at 75°C. The poor recovery of the base line by degassing at temperatures less than 50°C (see black plot of Figure 4-11a and b) could also be explained considering that thermal desorption of the strongly charged $(NO_2^- - V_O^{\bullet\bullet})_{ADS}$ species is reported to starts at around 80°C [117].

By increasing the OT under PB light illumination, the adsorption of NO₂ molecules takes place by both reaction 4-9 and reaction 4-10. The latter, as previously discussed, partially inhibits the resistance increase, due to the formation of a thinner depletion layer. It derives that the NO₂ gas resistance changes, under PB light, illumination, are always smaller as respect the ones in dark conditions (compare dark and PB illuminated samples of Figure 4-11). It should also be pointed out that the thermal activation is more effective to boost electrical changes than light activation. It must also be considered that the thermal

activation is effective on the whole available surface, whereas under PB illumination, only the illuminated photon-impinged surfaces, participate to the overall response. This is particularly relevant considering the porous nature of the NFs, made of poorly sintered grains.

4.2.3 Gas sensing conclusion

The influence of thermal and visible light activation on electrospun WO₃ nanofibers annealed at 450°C has been presented with the aim of investigating the influence on the NO₂ gas responses (in the concentration range 100-400 ppb) by using light illumination in the visible at different wavelengths and intensities, different operating temperatures and their combined effects. Gas response at room temperature of electrospun WO₃ nanofibers annealed at 450°C has shown that with increasing both photon energy and light intensity, beside a slight decrease of the relative response, recovery of the base line and response times greatly improves as respect to dark conditions. Sensor relative responses to NO₂ gas in the dark conditions resulted always to over-perform the one recorded under PB light illumination, in the investigated temperature range 25-100°C. This behaviour has been explained considering the formation of less charged surface species arising from PB illumination on the WO₃ surfaces. Indeed, we found that light illumination allows for an almost full recovery of the base line and for faster response times at low operating temperatures. Moreover, the reported results demonstrate that it is possible to achieve a relative response of about 12.4 and a 97% of full recovery of the base line exposing the electrospun WO₃ nanofibers to 400ppb NO₂ by combining purple-blue light illumination ($\lambda=430\text{nm}$ with an intensity as low as $770 \mu\text{W}/\text{cm}^2$) and at mild operating temperatures of 75°C. Finally, this paper addresses the big opportunity for tuning the response of electrospun WO₃ nanofibers to NO₂ via combined photo and mild thermal activation means.

***5 Chapter 5: Mono-few layer WS₂
fabrication for gas sensing
measurements***

5.1 Fabrication of mono-few layers WS₂

Introduction

The exfoliation technique used in this thesis to fabricate mono-few layers WS₂ is sonication assisted ball milling. WS₂ is a 2D layered TMD and is an n-type semiconductor that has shown promising gas sensing applications.

In recent years layered materials such as, 2D transition metal dichalcogenides (TMDs) have attracted a high level of interest due to their peculiar properties, which make them appealing for potential applications in gas sensing [118], photo-electro-catalytic hydrogen evolution [119], optical and electronic devices [120] and energy storage [121].

Few layer 2D TMDs can be produced through different methodologies like mechanical and liquid phase exfoliation of bulk crystals, classified as top-down routes, or via direct bottom-up routes like chemical vapor deposition. High yield liquid exfoliation methods comprising ion intercalation and ultrasonic cleavage have also been widely employed to exfoliate bulk-layered materials. Besides liquid phase exfoliation, ball milling as a newly explored high yield mechanical exfoliation method has been utilized for scalable production of mono and few layer graphene and TMDs nano-sheets [122]. More recently, enhanced mixed methods comprising assisted grinding and sonication have been shown to produce higher concentrations of TMDs nano-sheets and reduced number of defects. All the above mentioned preparations are devoted to optimization of the exfoliation procedure, or have focused on morphological aspects, rather than investigating the influence of the preparation methods on the evolution of surface defects (i.e. sulphur vacancies) and/or the occurrence of oxidation phenomena [123]. Spontaneous oxidation in air represents, indeed, the “Achilles’ heel” of TMDs, which may strongly influence their properties over time. To this extent we demonstrated that both exfoliated MoS₂ and WS₂ easily oxidize to their metal oxides counterparts, and that temperature plays the

major role when controlling the surface oxidation phenomena.

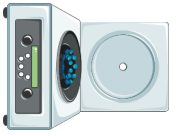
Regarding gas sensing applications, 2D single layer MoS₂ field effect transistor, 3D MoS₂ and 3D MoS₂/Graphene aerogel have been shown to be ideal substitutes for traditional metal oxides sensors. Considering that gas sensitivity and long-time electrical response is generally dependent on the reproducibility of the preparation with respect to both microstructure (i.e. number of layers, lateral size, surface area, etc.) and chemical composition (i.e. defects concentration and surface oxidation), we demonstrated a practical, high-reproducible, and easy way to fabricate chemoresistive thin films gas sensor, by drop casting suspensions of few flakes graphene oxide, phosphorene and more recently TMDs utilizing both liquid-exfoliated MoS₂ and commercially exfoliated suspensions of WS₂ [124]. Aim of this work is to apply a combined grinding and sonication method to achieve a reproducible and high yield exfoliation methodology and to investigate the influence of process conditions on the spontaneous oxidation of exfoliated WS₂. Starting from commercial WS₂ powders, we have firstly optimized the grinding and sonication times to yield controlled and reproducible morphology of few flakes WS₂. Secondly, we have determined that maintaining process temperatures below 180°C, spontaneous oxidation of WS₂ flakes in air to yield amorphous WO₃ can be easily controlled. Lastly, we investigated the gas responses to NO₂ and H₂ of drop casted mono to few flake WS₂ chemoresistive thin films, discussing the likely gas-response mechanism. Following, the flow chart of the mono-few layer WS₂ flakes exfoliation process is illustrated that consists of the following steps:

- Identification of reagents
- Mixing and milling
- Solvent evaporation
- Probe sonication
- Centrifugation

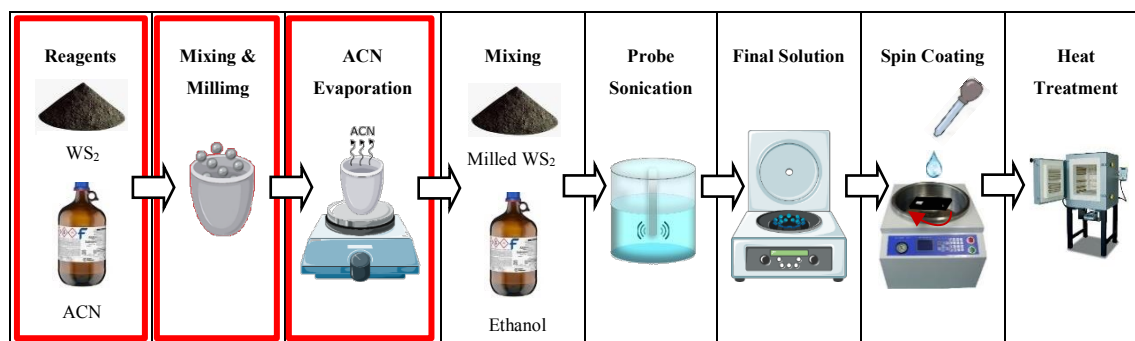
- Spin coating

Following the flow chart, each of the above mentioned steps will be described and discussed.

FLOW CHART OF THE EXFOLIATION PROCESS PROCESS

Reagents 	Mixing and Milling  2 hours 400 rpm Room Temp.	Acetonitrile Evaporation  At room temperature over night	Mixing 	Probe Sonication  Ball milled WS ₂ dispersed in Ethanol 90 min 250 W T ≤ 25°	Centrifugation  90 min 2500 rpm T ≤ 25°C	Spin Coating  1000 rpm 30 seconds Under air flow	Heat Treatment  Different annealing Temp.
General Description of Process Set up							
Appropriate solvent (Acetonitrile) with low evaporation temperature is chosen for ball milling.	WS ₂ dispersed in acetonitrile is ball milled for 2 hours at room temperature. The ball/powder weight ratio was 24.	After ball milling the ball milled WS ₂ was left at room temperature over night to evaporate the residual of Acetonitrile.	After evaporating ACN, dried WS ₂ were dispersed in pure ethanol and probe sonicated for 90 min at 250 W. To prevent the Oxidation of exfoliated flakes, the temperature should be maintained less than 25 °C.	After 90 mins of probe sonication in pure ethanol, the dispersion is centrifuged to precipitate the unexfoliated flakes and the supernatant is collected by pipette. 5 µL of the supernatant is drop cast and spin coated on the electrode pattern of the sensor.	Spin coated sensors are annealed at different annealing temperatures under ambient air.		
CRITICAL PARAMETERS AND CONTROL OF PROCESS STEPS							
1. Surface tension energy of solvent; 2. Evaporation temperature of solvent.	1. Ball powder weight ratio; 2. Speed; 3. Ball milling time; 4. Energy.	1. Evaporation temperature.	1. Concentration of dispersion (mg. mL ⁻¹); 2. Sonication time; 3. Sonication power; 4. Sonication temperature.	Centrifugation: 1. Speed; 2. Time; 3. Temperature. Spin coating: 1. speed; 2. time.	1. Temperature; 2. Time; 3. Heating and cooling rate.		

5.1.1 Reagents Mixing, Milling and Evaporation



For preparation of exfoliated mono-few layers WS₂, 2 g of WS₂ commercial powder (Sigma-Aldrich 243639-50G) with 99% purity and average particle size of 2 μm were dispersed in 2 mL of acetonitrile (ACN - VWR 83639.320) and ball milled in a planetary milling machine at 400 rpm with 12 stainless steel balls ($D=12$ mm) and ball/powder weight ratio of 24 for 2 hours (steps of 15 min milling and 5 min idle to avoid excessive warming).

Low energy ball milling exfoliation mechanism and its associated forces is illustrated and discussed in section 2.7.1. Also, a schematic of exfoliation comprising low energy ball milling and the associated shear and compression forces from balls during ball milling is illustrated in Figure 5-1.

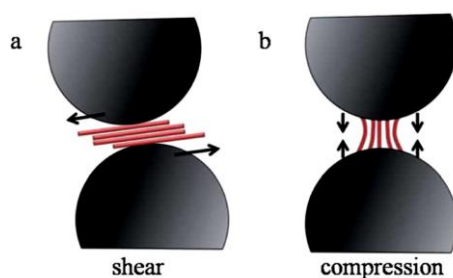


Figure 5-1- The illustration of the thinning and exfoliation effects of combined low-energy ball milling and sonication. (A) and (B) 2D nanosheet exfoliation by low-energy ball milling. (A) Shear force-induced exfoliation. (B) Compression force-induced exfoliation.

The ball milling machine utilized in this work for exfoliation was planetary type and is illustrated in Figure 5-2.

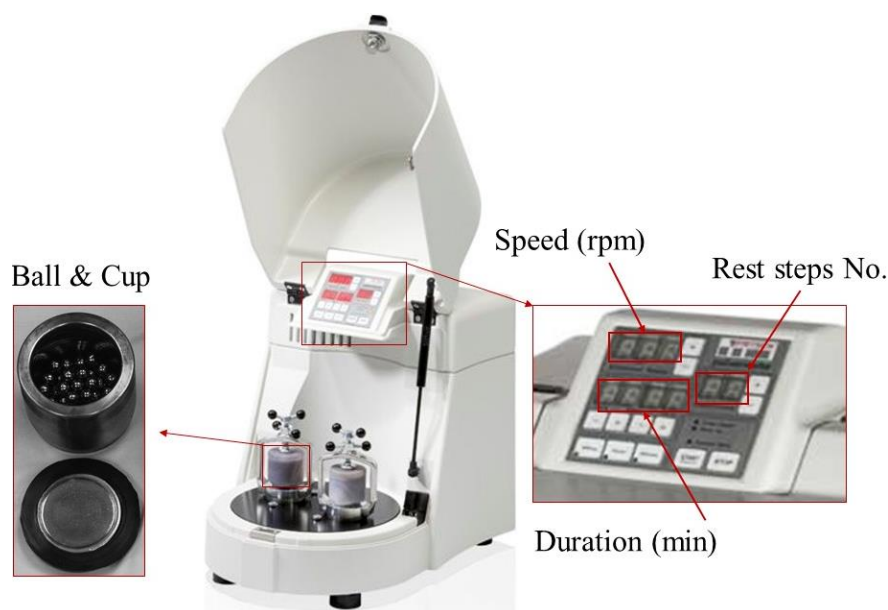


Figure 5-2- Palentary ball milling machine.

5.1.1.1 Operating principles of ball milling

Figure 5-3 shows the schematic of the ball milling operation, rotation directions and axes, and induced forces to the powder during milling procedure.

The powder is crushed and ground by induced forces from balls in a grinding bowl. The centrifugal forces from the rotation of the grinding bowls around their own axis and from the rotating support disc act on the contents of the grinding bowl which consists of powder and balls. The bowl and the support disc have opposite directions of rotation so that the centrifugal forces alternate in the same direction and in the opposite direction. The result is that the grinding balls run down the inside of the bowl's wall providing a friction effect and the grinding balls hit the opposite wall of the grinding bowl providing an impact effect. The impact effect is amplified by the impact of the grinding balls against each other.

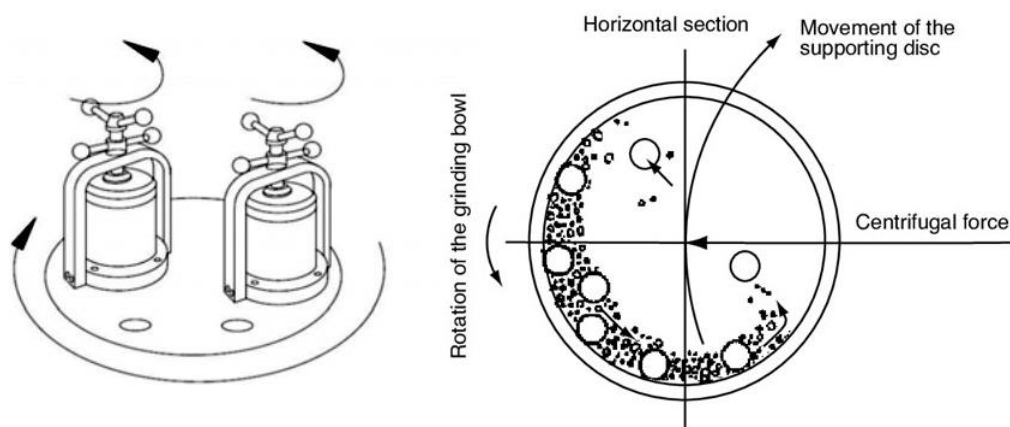


Figure 5-3- Schematic of the ball milling operation, rotation directions and associated forces

5.1.1.2 Ball milling: Influential Parameters

Ball-to-powder ratio effect

One of the milling parameters that directly changes the amount of induced forces and energies to the layered material is the weight of balls versus powder. The objective is to dominate the shear force due to the rolling of the balls and depress the impact forces of the balls. Ball weight ratio has shown significant influence on dominating these energies so that by increasing the ball weight ratio the shearing forces increase while the impact forces increase as well. This means that the adjacent layers are exfoliated while their lateral dimensions are decreasing too.

Deepika et al., showed that compared to the results from the ball-to-powder ratio of 10:1, a similar amount of BN nanosheets were produced when the ratio increased to 20:1. However, the 20:1 ratio produced more BN nanosheets less than 200 nm in diameter. When the 50:1 ratio was applied, many small particles instead of sheets were found. The formation of these particles is due to damage to the BN nanosheets. This indicates that the increase of ball-to-powder ratio can result in higher yields of sheets, but at the cost of more structural damage owing to higher chance of ball-to-vial or ball-to-ball collision and possibly stronger collision see.

They obtained the ball powder ratio of 10:1 for exfoliation of BN utilizing 1 mm stainless steel balls [125].

Milling speed effect

Studies have shown that the shear force during ball milling increases by increasing the ball milling speed, hence the exfoliation increases. Deepika et al., showed that increasing the milling speed from 600 rpm to 800 rpm results in more exfoliation and exfoliated nanosheets with higher aspect ratio [125].

Ball size effect

It is reported that the bigger balls provide larger surface area that increases the probability for ball to ball or ball to wall interaction and impact and thus more shearing forces. The other issue is the weight of balls of different sizes, the lighter weight of balls makes the shear forces gentler and minimize the crystal damage comprising from the impact force [125].

Milling Time

Milling time has been reported as the most significant processing parameter in several studies. It is shown that by increasing the milling time the induced power increases. Deng et al. [126], showed that the concentration of exfoliated graphite milled supernatant increases non-linearly with increasing the milling time. They showed that when the milling time is less than 10 hours the concentration of supernatant increases slowly but over 10 hours of ball milling the concentration significantly increases. They obtained 10 hours of ball milling as the turning point of ball milling where under this duration shear force is dominant. **Error! Reference source not found.** They concluded that up to the turning point (10 hours in their study) the initial large graphite bulk sheets are broken to smaller pieces under compression forces from balls, see Figure 5-4, and the size of graphite decreases and concentration of the supernatant increases slowly at the beginning, as shown in Figure 5-4 the gradient of the concentration up to 7 hours. After that, since smaller graphite flakes are easier to exfoliate as the collective van der Waals force between layers is lower in them, shear force becomes dominant up to the turning point. By exceeding the turning point the impact point becomes dominant and the exfoliated layers are broken on lateral dimensions [126].

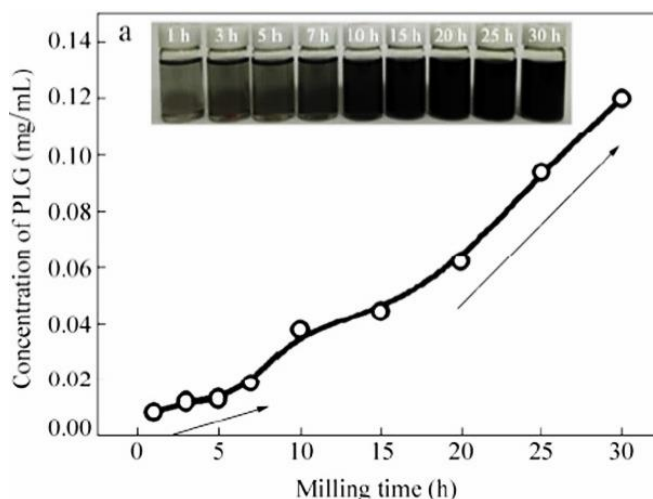


Figure 5-4- Concentration of FLG as a function of milling time (0.4 g of EG, milling speed: 500 r/min, centrifugation speed: 4000 r/min) [126].

Milling solvent

wet milling is widely used and studied to make sure that the shearing effect is dominant during ball milling. A good solvent for ball milling exfoliation of van der Waals layered materials is the one that has a matched surface energy for overcoming the van der Waals forces of adjacent flakes, such as DMF, NMP, tetramethylurea. Different kind of organic solvents with appropriate surface tension energy has been used in planetary milling machine to fabricate graphene and few layer TMDs. This scheme depends on milling time and rotational speed of milling to dominate the sheering force.

Besides, although organic solvents with appropriate range of surface tension energies have shown good solvents for ball milling exfoliation, their residuals usually remain on the surface of exfoliated flakes due to their high boiling point and do not evaporate even by mild annealing.

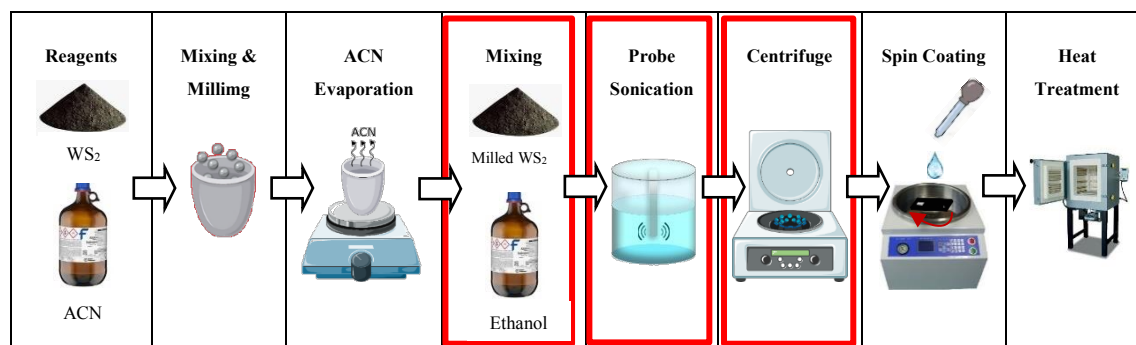
For these reasons an appropriate solvent for high yield ball milling exfoliation to obtain pristine mono-few layers flake is a kind of solvent with surface energy of 70-80 mJ.m⁻², or a surface tension energy of 40-50 mJ.m⁻² at room temperature and can be easily evaporated at low annealing temperature to prevent the oxidation and drawbacks due to elevating temperature [98, 127].

Considering the above mentioned influential parameters in ball milling process, Acetonitrile was chosen as milling solvent in this work, due to its low evaporation temperature to fabricate pristine exfoliated mono-few layers WS₂. Besides, ball size and

milling speed are kept constant and effect of milling time on exfoliation procedure is extensively studied that will be discussed after explaining the sonication process.

After ball milling of WS₂ to evaporate ACN residuals after milling, the collected slurry was left overnight at 23±2°C and 40±3% Relative Humidity (RH).

5.1.2 Mixing, Probe Sonication and Centrifugation



After ACN evaporation at room temperature, 0.05 g of the ball milled powder dispersed in 100 mL of pure ethanol and probe sonicated for 90 minutes in a cool bath ($T \leq 25^\circ\text{C}$). Finally, the sonicated dispersion was centrifuged at 2500 rpm for 40 min at 20°C and the supernatant collected, and spin coated on a Si₃N₄ substrate.

The mechanism of sonication assisted liquid-phase exfoliation method and its associated forces, as a large-scale production technique to fabricate mono-few layer TMDs from their bulk form was extensively discussed in section 2.7.1.

The sonicator machine used in this work is a simple probe sonicator machine that is a part of dynamic light scattering machine, Figure 5-5 (a). To control the temperature during the sonication process, WS₂ dispersion beaker was placed inside a bath comprising a cooled water circulating coil, Figure 5-5 (b), and the coil was connected to a lab chiller, Figure 5-5 (d).

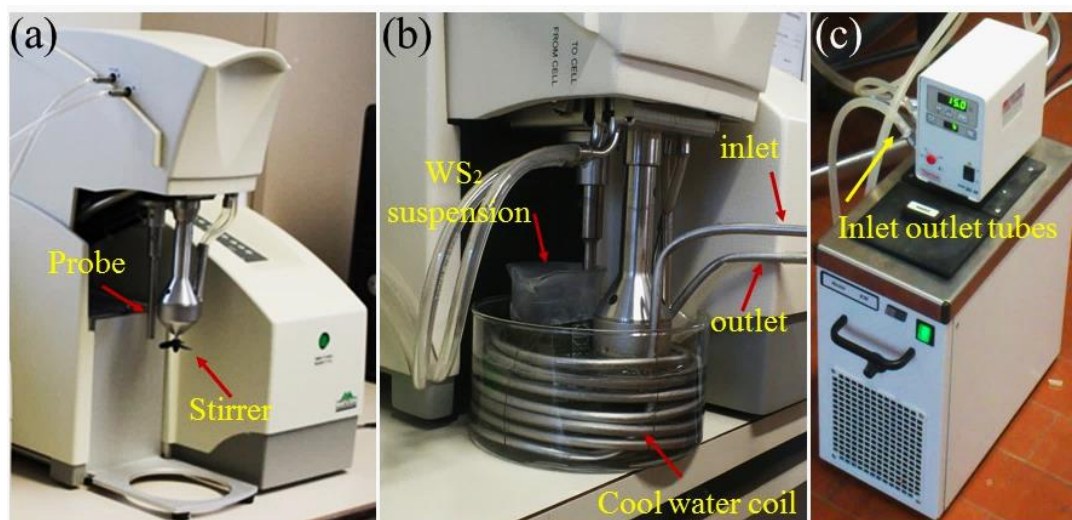


Figure 5-5- Sonication process set up; (a) probe sonicator, (b) water cooled coil and bath, (c) Chiller.

5.1.2.1 Sonication: Influential Parameters

Studies show that sonication conditions and parameters can critically influence on the exfoliation process and thickness, sizes and other properties of the mono-few layered TMDs formed from their bulk format.

When ultrasonic treatment occurs in a solvent, acoustic waves passing through the fluid create progressive compressions and decompressions in it, with rate depending on the frequency. If the intensity of ultrasound is high enough, the expansion cycle can create bubbles or voids in the liquid. Formation, growth, pulsation and collapse of bubbles in a liquid constitute the phenomenon of cavitation.

Based on the observations, two main consequences of MX₂ sonication are (i) exfoliation into MX₂ nanosheets, that means the detachment of layers from the bulk, that were only bonded by van der Waals forces (Figure 5-6 C); and (ii) scission into particles with smaller dimensions, down to nanoparticles, by breaking covalent MeQ bonds (Figure 5-6 D).

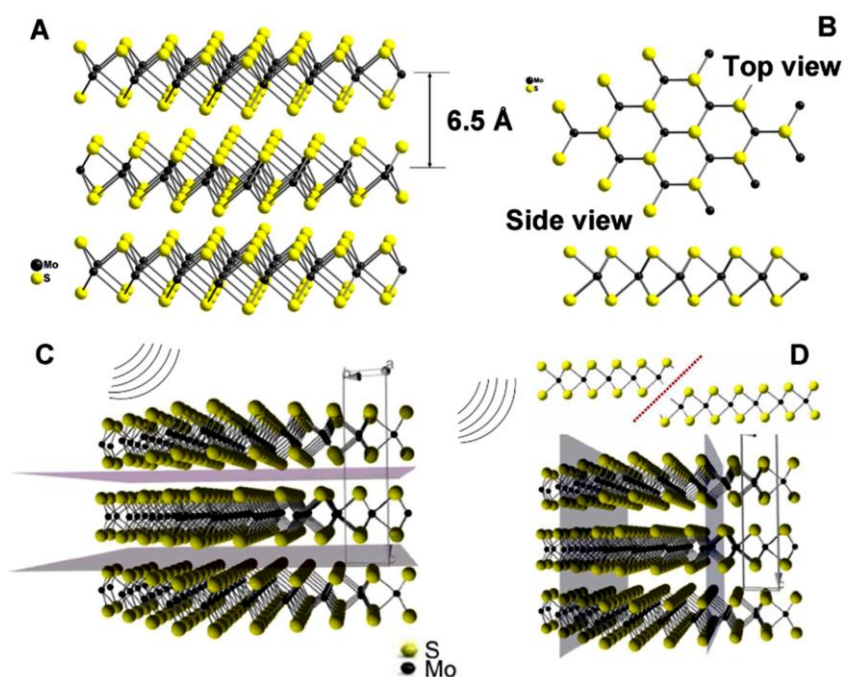


Figure 5-6- Structure of MoS₂ and effects of the strong sonication on MoS₂ flakes dispersed in a solvent. (A) Bulk MoS₂ crystal, where single layers are separated by a 6.5 Å distance (center to center); (B) MoS₂ monolayer: top and side views; (C) Exfoliation into nanosheets: breaking van der Waals bonds between layers; (D) Fragmentation of lamellae: breaking covalent bonds within layers. Yellow and black spheres correspond to sulfur and molybdenum, respectively. C and D.

Important parameters affecting the sonication assisted liquid exfoliation process are sonotrode shape, sonication time, pressure and temperature of the reaction, ultrasound intensity, solvent density etc.

Sonication power

One of the most effective parameters in sonication is the power of sonication. Authors studied the influence of the ultrasound power in the range of 100-500 W on the properties of the MoS₂ dispersions forming in NMP, chloroform and acetonitrile or in water/surfactant solutions. It was shown that increase in sonication power from 350 to 500 W decreased nanosheet lateral dimensions almost twice from 200 nm, while thicknesses of 6-12 nm stayed unchanged, and the yield of the dispersed product increased maximum up to 0.43 mg/mL. The expected rise in concentration with increasing ultrasound power was also noted in the paper for MoS₂ (WS₂)/water/ surfactant

combinations. In this work these effects were studied in more detail, and it was demonstrated that at first, the increase in the ultrasound power led to higher concentrations and lower lateral sizes, however, as the power exceeded 320 W, concentrations started to fall, while the nanosheets areas became somewhat larger. This phenomenon is due to the cavitation shielding effect. Two types of cavitation in liquids are discussed (Figure 5-7a). At lower acoustic fields, stable (no inertial) cavitation takes place, that is, the bubbles have a relatively long growth cycle and oscillate around an equilibrium position over many acoustic cycles. In contrast to stable cavitation, inertial cavitation takes over at higher ultrasound powers. During several acoustic wave cycles, oscillating bubbles or voids rapidly grow, reach their resonant sizes, expand and collapse abruptly, producing high speed liquid jets. When the power is within 100-200 W, stable cavitation is realized. In this case, stably oscillating bubbles colliding against MoS₂ basal planes are not able to break covalent S-Mo-S bonds but can easily overcome van der Waals bonds interlinking MoS₂ layers. Thus, in this range of powers, larger MoS₂ nanosheets are produced (150×75 nm, 3-7 nm thick, Figure 5-7b, E). When the transmitted power rises to about 320 W, inertial cavitation becomes effective. As a result, high-intensity bubble knocks cleave covalent MoS bonds and, thus, generate surface defects in MoS₂ basal planes, leading to nanosheet scission into numerous smaller parts (Figure 5-7d, Figure 5-7c). This effect is most pronounced at 200-250 W, giving smallest nanosheets with narrow size distributions (72 ×33 nm) and thicknesses of 1-5 nm (Figure 5-7b, e). However, at 285 W and, especially, at 400 W, ultrasonic cavitation shielding effect commences. This phenomenon consists in the accumulation of many bubbles around the sonotrode, which hinders the transmission of acoustic waves and development of inertial cavitation (Figure 5-7d). As a consequence, lateral sizes of the exfoliating sheets increase up to 207× 112 nm with thicknesses of 2-10 nm (Figure 5-7b, E) [128].

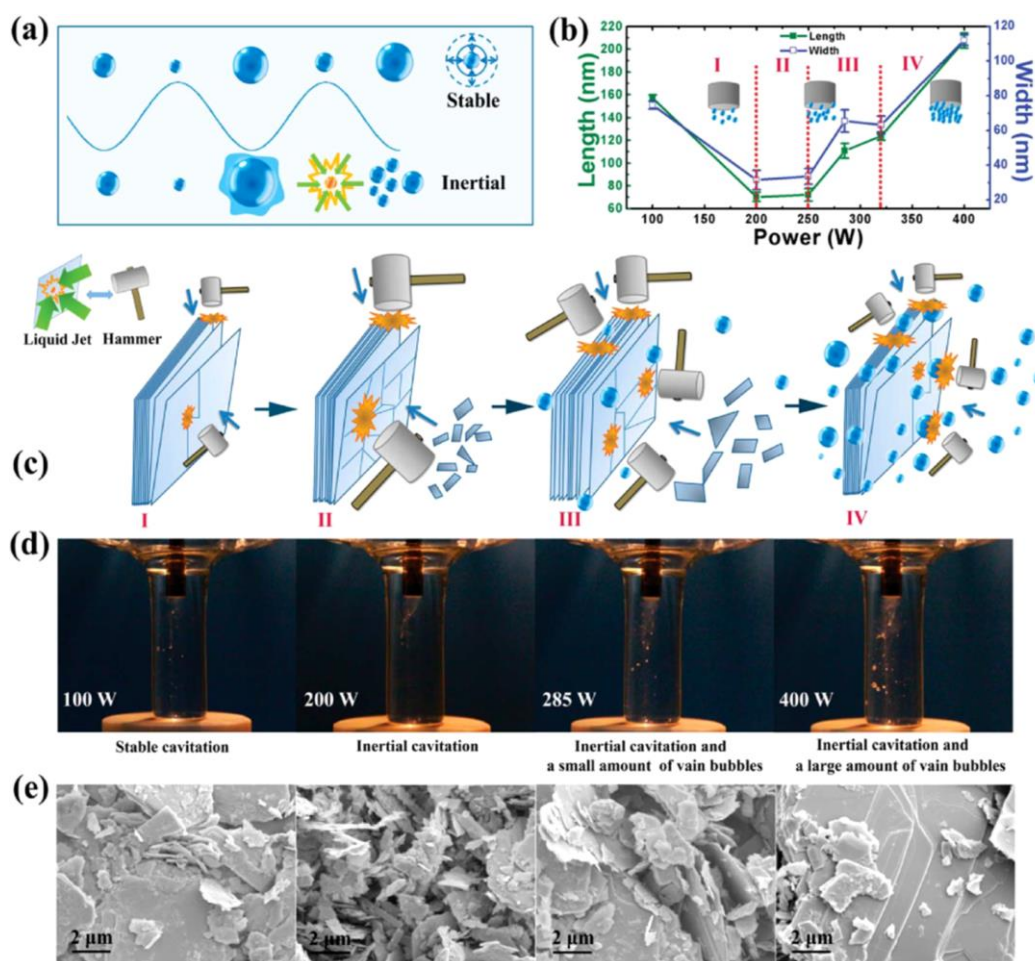


Figure 5-7- Illustration of the two types of cavitation mechanism; (B) Mean flake length and width (based on > 300 randomly selected nanoflakes for each sample) obtained at different ultrasonic power intensities; (C) Schematic representation of the exfoliation procedure to obtain MoS₂ nanoflakes in four distinct regions (I to IV); (D) Images of the acoustic cavitation bubbles in NMP solvent at different input powers; (E) SEM images of the sediment after centrifugation of 100, 200, 285 and 400 W samples.

Sonication solvent

Many studies have been done to investigate the effect of sonication solvent on exfoliation properties from various points of view.

On one hand, many studies consider intermolecular MX₂-solvent interactions, which may be strong enough to overcome interlayer attraction forces, but do not lead to the formation of covalent bonds. On the other hand, recent research shows that interactions of the solvents with MX₂ surfaces may be of a more complex chemical nature, which is due, in particular, to the ability of the solvents to form chemically active particles upon sonolysis.

Following, both aspects are discussed.

J. Coleman and co-authors as well as Ajayan and co-authors have symmetrically investigated the exfoliation of numerous dichalcogenides (MoS₂, WS₂, MoSe₂, MoTe₂, TaS₂, TaSe₂, NbSe₂, NiTe₂, Bi₂Te₃) in various solvents under ultrasonication.

Many of these works investigate the appropriateness of various solubility parameters, that is, quantitative characteristics of a solvent and MX₂ that should have similar values to minimize the exfoliation energy (enthalpy of mixing) and to form a colloidal dispersion. As such, solvent's surface energy was considered as a solubility parameter. It was noticed that all "successful" solvents had a common value of surface tension σ around 40 mJ.m⁻² which corresponds to the surface energies $\gamma \sim 70 \text{ mJ}\cdot\text{m}^{-2}$, as these parameters correlate as the equation 5-1;

$$\gamma = (\sigma + TS) \quad 5-1$$

where S is the surface entropy, and $TS \sim 29 \text{ mJ}\cdot\text{m}^{-2}$ for most liquids at room temperature. This value of surface energy is very close to that of the dichalcogenide nanosheets (75 mJ·m⁻², as measured by inverse gas chromatography). The best solvent for both MoS₂ and WS₂ were N-vinyl-pyrrolidone, DMSO, N-dodecyl-pyrrolidone, cyclohexyl-pyrrolidone, dimethyl-imidazolidinone and DMF. Highest concentrations achieved in NMP were 0.30 mg·mL⁻¹ for MoS₂ and 0.15 mg·mL⁻¹ for WS₂ (Figure 5-8) by optimizing sonication conditions and centrifugation time, J. Coleman's group succeeded in preparation of MoS₂/NMP colloids with very high concentrations of 40 mg·mL⁻¹ and yields reaching 40%.

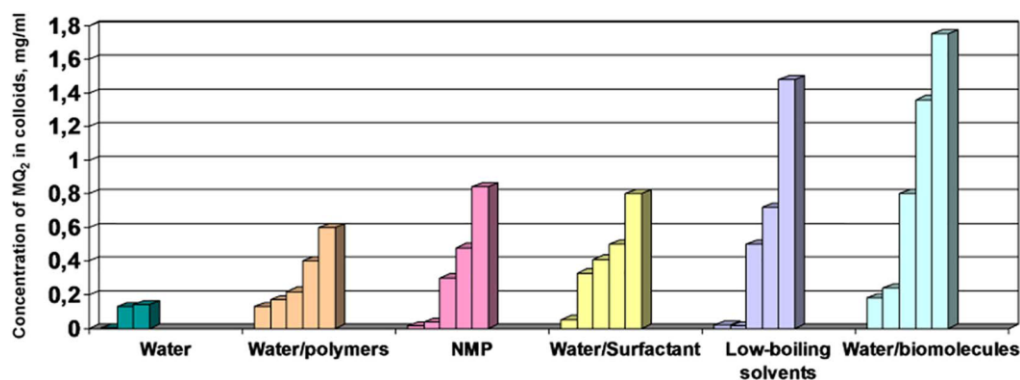


Figure 5-8- Concentrations of colloidal MX₂ nanosheets in different media, produced by direct

sonication, mg/mL (summarized from data reported by different authors). This chart gives a general impression of average achievable numbers, however, in some cases, much higher concentrations are reported: MoS₂/NMP after 140 h- long sonication: 40 mg/mL, MoS₂/ethanol/water derived from grinding-assisted process: 26 mg/mL; MoS₂/water/surfactant Pluronic P-123: 12 mg/mL. For comparison, intercalation-exfoliation methods often yield much more concentrated MX₂ colloids: MoS₂/organic solvents: 30-55 mg/mL; WS₂/DMF: 19 mg/mL; MoS₂/ethanol+ water: 1.6-2.2 mg/mL. It should be noted that (i) results may vary depending on the method used for estimation of the colloidal concentration (weighing method or UV data), and (ii) characteristics of the dispersions with similar concentrations may vary (thickness of the nanosheets, their lateral sizes, stability, etc.).

However, it is not rare that solvents with close surface tensions σ disperse MX₂ to different extents. For example, this happens with NMP and pyridine. The explanation may lie in the fact that σ describes interactions in general, while intermolecular interactions may have different nature. Full surface tension may be represented by two components accounting for polar (σ_p) and dispersion (σ_d) interactions. If one interaction differs strongly in solvent and MX₂, even at similar σ , then no colloid formation takes place. While precise values of those components for different solvents are not known, σ_p/σ_d ratio may be obtained by measuring contact angles of MX₂ with liquids. This method allowed the authors to identify different MX₂ dispersing media with matching values of σ_p/σ_d ratios by simply varying proportions of the solvents in their binary mixtures. Colloidal dispersions are produced in isopropanol/water mixtures (Table 5-1), acetone/water mixtures (3:2, $\sigma_p/\sigma_d = 0.479$) and THF/water (1:1, $\sigma_p/\sigma_d = 0.476$). As illustrated in Table 5-1, matching the ratio of surface tension components σ_p/σ_d of MX₂ and of a solvent mixture is even more important than matching their full surface tensions [128].

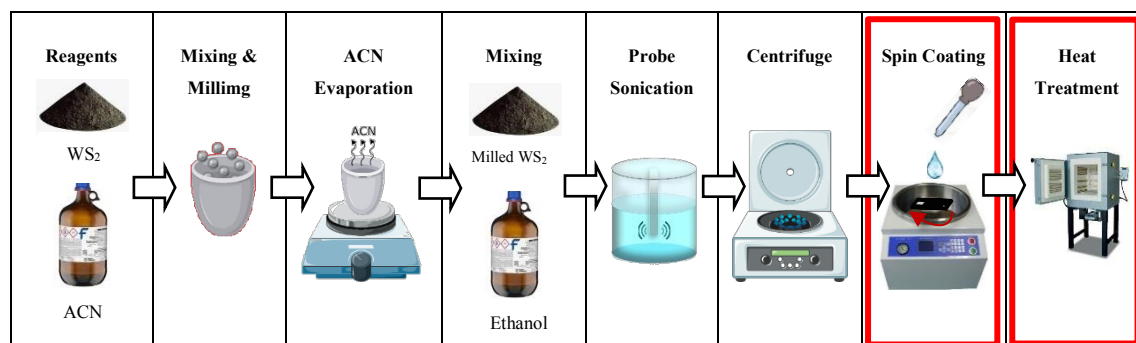
Material	σ , mJ.M ⁻²	σ^p/σ^d
MoS ₂	~ 40	0.449
Isopropanol: water (4:1)	23.4	0.450
WS ₂	~ 40	0.563
Isopropanol: water (1:1)	25.1	0.482

Table 5-1- Full surface tension σ and the ratio of its polar and dispersive components σ_p/σ_d for layered dichalcogenides MX₂ and water-isopropanol mixtures best suitable to stabilize MX₂ colloids.

Sonication time

Lengthening of the sonication time does not bring about any noticeable changes to hexagonal structures of dispersed MX₂ nanosheets, but lowers their lateral sizes due to cutting effects (Figure 5-6 d) and increases concentrations of the colloids.

5.1.3 Spin Coating and heat treatment



After probe sonication, the obtained dispersion will be centrifuged to precipitate non-exfoliated WS₂ flakes and collect the supernatant containing exfoliated mono-few layered WS₂. After obtaining the supernatant, one drop of it (5 μ L) will be spin coated on Si₃N₄ substrate for material characterization or on sensor substrate for gas sensing measurements. The spin coating is explained in the flow chart and Annex 2.

Considering the above mentioned influential parameters in ball milling assisted sonication process, WS₂ exfoliation parameters are presented in table Table 5-2.

After spin coating of WS₂ solution, the substrates will be annealed at 180°C.

Annealing and thermal analysis of few layered WS₂ flakes at elevated temperatures is extensively studied in Chapter 6.

Sample	Grinding parameters						Sonication parameters			Centrifugation parameters	
	WS ₂ -ACN	Speed [rpm]	Milling time [h]	Nbr. of balls	Weight of each ball [g]	Ball/Powder weight ratio	WS ₂ -EtOH	Duration [min]	Temperature [°C]	Duration [min]	Speed [rpm]
1	2 g- 2 mL	400	72	12	4	24	0.05 g- 100 mL	90	25	40	2500

2	2 g- 2 mL	400	24	12	4	24	0.05 g- 100 mL	90	25	40	2500
3	2 g- 2 mL	400	2	12	4	24	0.05 g- 100 mL	90	25	40	2500
4	2 g- 2 mL	400	2	12	4	24	0.05 g- 100 mL	120	25	40	2500

Table 5-2- Ball milling assisted sonication exfoliation parameters.

5.2 WS₂ microstructure and oxidation during exfoliation

Microstructure and surface oxidation of exfoliated WS₂ by milling and sonication are affected by a large number of variables, mainly: solvents, composition, grinding and sonication methods, duration times and operating temperatures. We found that the microstructural features of the exfoliated WS₂ are mostly affected by the duration of the milling and sonication steps, whereas surface oxidation depends on the combined action of sonication and temperature.

5.2.1 Microstructural properties of exfoliated WS₂

The evolution of the microstructure was investigated at each step of the exfoliation process as shown above. Regarding the ball milling process a key role is represented by the solvent. Considering that TMDs surface energies range between 70-80 mJ m⁻², solvents with surface tension values of 40-50 mJ m⁻² are suitable for exfoliation of layered materials [127, 129, 130]. Although solvents like N-Methyl Pyrolidone (NMP) and Dimethyl Formamide (DMF) with surface tension values of 40.8 mJ m⁻² and 37.1 mJ m⁻² respectively represent high yield exfoliation[131], their high boiling point and the remaining residues after drying, may restrict their applications when pure surfaces are needed. In our case acetonitrile (ACN) as a milling solvent, with surface tension of 29.5 mJ m⁻² [127, 130], has been selected as a trade-off between surface tension and moderate boiling point, enabling complete removal of the solvent at room temperature after grinding.

With the aim to maximize the “aspect ratio” of lateral dimension to the thickness of the stacked flakes, which may well represent the 2D character of an exfoliated structure, both influences of the grinding and sonication times were investigated. Several suspensions with constant WS₂/ACN ratio decreasing the duration from 72 h, to 24 h and 2 h while increasing the sonication time from 90 min to 120 min were prepared. All the preparation parameters are shown in Table 5-2.

Regarding the influence of the grinding time, particles’ size distribution of the starting WS₂ powder (blue plot), determined by DLS technique (see section 3.2.9) and shown in Figure 5-9a, downshifts towards smaller average sizes after 72 h grinding (red plot) and slightly further after 90 min sonication (green plot). The particle size distribution of the WS₂ starting powder displays an average particle size of $\approx 8\mu\text{m}$ (blue plot) whereas the 72 h ball milled shows a bimodal distribution (red plot), with larger aggregates centered at $\approx 20\mu\text{m}$ and smaller ones at $\approx 0.7\mu\text{m}$. After 90 min sonication the bimodal distribution of the ground powder disappears (green plot) and the average particle dimension places at $\approx 0.6\mu\text{m}$.

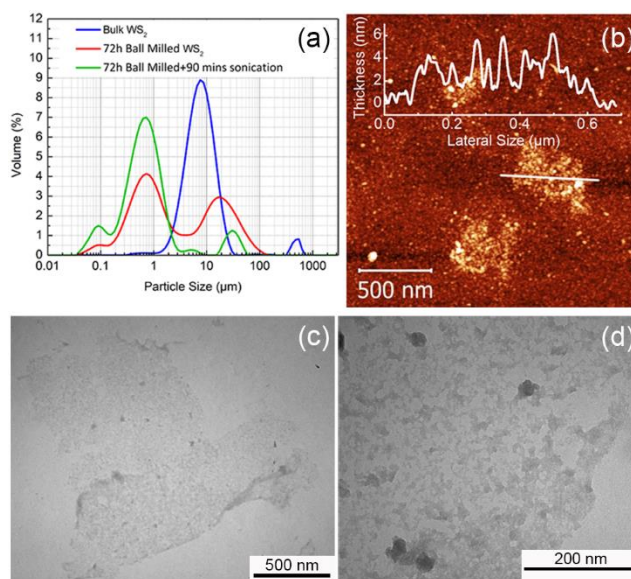


Figure 5-9- (a) Comparison of the particle size distribution of the starting WS₂ commercial powder (blue), 72 h ball milled (red) and 72 h ball milled and 90 min sonicated (green); (b) AFM picture of 72 h ball milled and 90 min sonicated and associated thickness profile along the white line; (c) low magnification and (d) high magnification TEM pictures of the 72 h ball milled and 90 min sonicated WS₂

It may be concluded, that grinding has an effective influence to reduce the particle size, while sonication, beside its effectiveness to suppress the bimodal distribution (presumably by separating agglomerated WS₂ particles), shows only minor effects to further decrease the particle size of the ground powder, confirming the dominant role of the milling step. Figure 5-9b shows the AFM image of the 72 h ball milled and 90 min sonicated WS₂ sample. The inset of this image depicts a rough thickness profile along the selected line, with an average height from the substrate of 2 nm. Low and high magnification TEM images illustrated in Figure 5-9c and Figure 5-9d respectively, show that long term ball milling for 72 h results in a fragmented structure, which eventually revealed to be amorphous by fast Fourier electron diffraction measurements. These features can be explained considering the two main forces induced by ball milling. As mentioned in sections 2.7.1 and 5.1.1.2, the primary force is the shear force provided by rolling of balls on the surface of layers, which causes the removal and the exfoliation of surface layers. The secondary force is the vertical impact from the balls which combined with longer grinding times can fragment the larger exfoliated sheets into smaller ones, eventually collapsing of the crystal structure [132].

With the aim to minimize the fragmentation effect, the ball milling duration time is gradually reduced from 72 to 2 hours, maintaining the sonication time at 90 min. By decreasing the milling time to 2 h, the flake's fragmentation sharply decreases as shown in Figure 5-10, enforcing the formation of well-defined terraced structures comprising stacked WS₂ flakes.

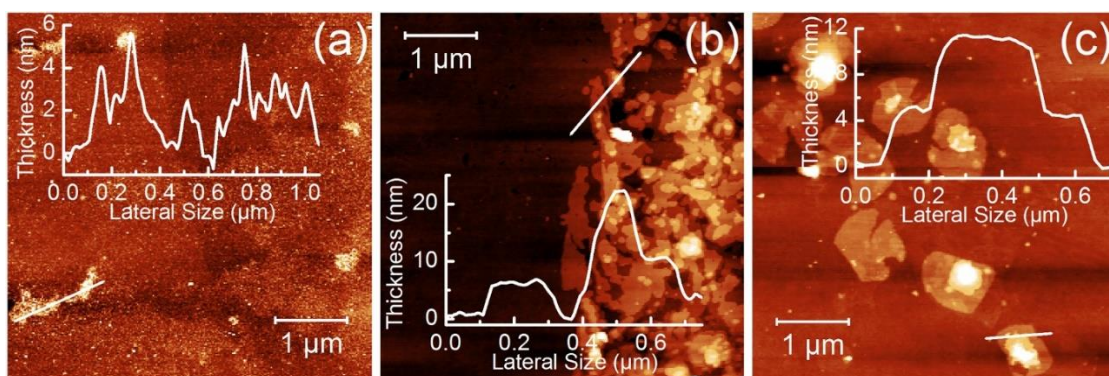


Figure 5-10- AFM pictures of exfoliated WS₂ flakes: (a) 72 h ball milled and 90 min sonicated; (b) 24 h ball milled and 90 min sonicated; (c) 2 h ball milled and 90 min sonicated. The inset of each picture shows the thickness profile along the white lines

Figure 5-11 shows the main microstructural features of the 2 h milled and 90 min sonicated WS₂ powders.

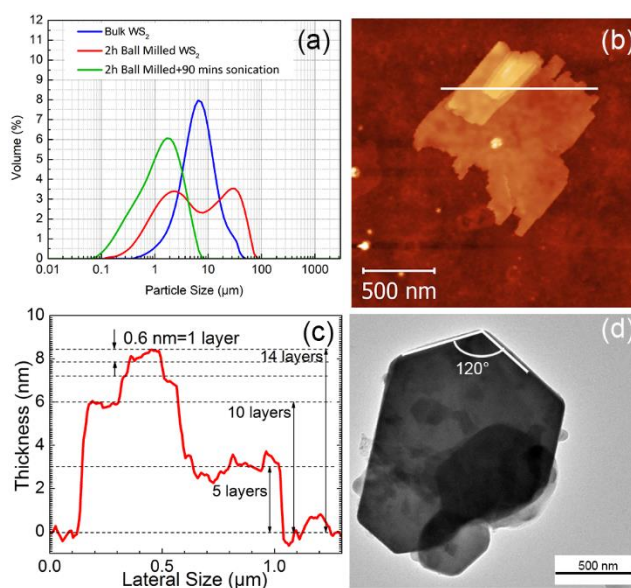


Figure 5-11- (a) comparison of the particle size distribution of the starting WS₂ commercial powder (blue), 2 h ball milled (red) and 2 h ball milled and 90 min sonicated (green); (b) AFM picture of 2 h ball milled and 90 min sonicated; (c) thickness profile of the stacked flake along the white line of Figure (b); (d) TEM picture of exfoliated WS₂ flakes.

Aside from particle size distribution of the starting WS₂ powder (Blue plot), Figure 5-11a shows, as in the previous case, the occurrence of a bimodal particle size distribution after 2 h grinding (red plot), but with larger average particles' with respect to the 72 h milled (i.e. $\approx 25 \mu\text{m}$ vs $\approx 20 \mu\text{m}$ and $\approx 2 \mu\text{m}$ vs $\approx 0.7 \mu\text{m}$), confirming the indirect relationship between the decrease of the grinding time and the increase of the lateral particles' dimension. Sonication for 90 min removes the bimodal distribution with no particular effect on decreasing particles' average size, which maintains at $\approx 2 \mu\text{m}$. Figure 5-11b shows, as opposite to Figure 5-9b, the formation of a well-shaped 2D-flake with a large flat surface of $1 \mu\text{m}$ length. The corresponding thickness profile drawn in Figure 5-11c highlights a clear formation of a stacked structure comprising a 3 nm thick basal plane, 6 nm thick secondary plane and a third one at the top. Considering that the slight step on top of the profile, 0.6 nm high, corresponds to 1-layer thickness WS₂ [133], it is shown that the first step is made of 5 layers and the second one of 10 layers respectively. The 2D character of the actual stacked structure shown in Figure 5-11b, as defined by the "aspect

ratio” is high, with an associated value of 250, attesting to the successful optimization of the grinding time for exfoliation. The TEM image depicted in Figure 5-11d illustrates also a well-shaped exfoliated flake with edge angles of 120°. Comparing Figure 5-9c with Figure 5-11d it is shown that by reducing the grinding time to 2 h, the crystalline hexagonal structure of the WS₂ nano-sheet is maintained with respect to the 72 h ground one.

Figure 5-12 and Figure 5-13 show HRTEM images of both edges and surfaces of the flakes. Figure 5-12b exhibits two layers with associated interlayer distance of ≈ 0.63 nm which is in good agreement with the AFM thickness measurements illustrated in Figure 5-11c. This interlayer displacement could be also observed at the flake’s edges depicted in Figure 5-12d and in Figure 5-13, where almost 11 layers can be clearly counted on the 7 nm thick edge. The atoms arrangement displayed in Figure 5-12b and Figure 5-13c exhibit the hexagonal atomic structure, with lattice spacing of 0.27 nm and 0.25 nm, that are characteristics of (100) and (101) crystal planes of 2H-WS₂ flakes, respectively [134]. Moreover, the Fast Fourier Transforms (FFTs) shown as the inset of Figure 5-12, further confirms the hexagonal crystalline structure of the flake.

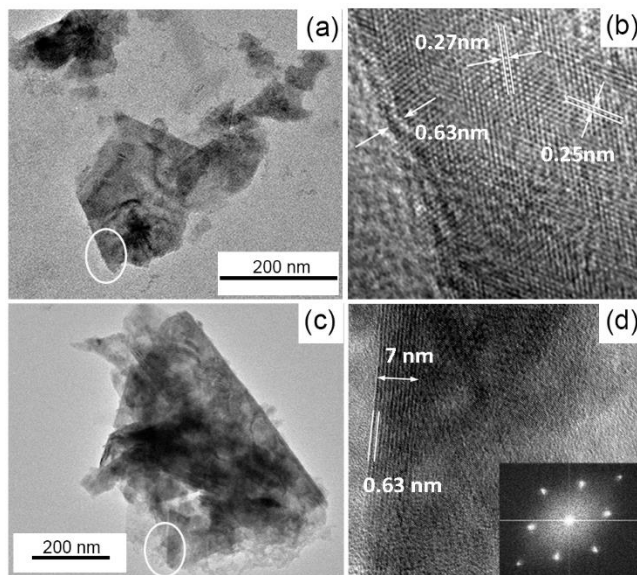


Figure 5-12- (a) & (c) TEM of 2 h ball milled and 90 min sonicated WS₂; (b) HRTEM corresponding to the circled area shown in Figure (a) with highlighted the interlayer distance (0.63 nm) and lattice spacing (0.27 nm and 0.25 nm), corresponding to (100) and (101) planes of WS₂ respectively; (d) HRTEM of the edge of the flake corresponding to the circled area shown in figure (c) with highlighted the 7 nm thick edge corresponding to 11 layers. The inset

show the Fast Fourier Transform of the flake.

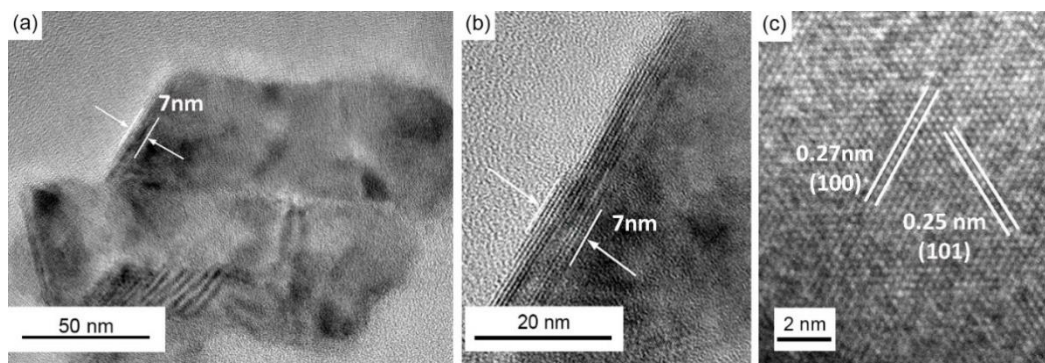


Figure 5-13- HRTEM pictures of (a) 2 h ball milled and 90 mins sonicated WS₂ flake; (b) Edge thickness and number of layers corresponding to the area shown in (a); (c) Lattice spacing and crystal planes of exfoliated WS₂.

To give a statistical insight of the reproducibility of the preparation, four different suspensions were prepared after 2 h milling and 90 min sonication and the corresponding centrifuged suspensions collected, and spin coated on Si₃N₄ substrates. Figure 5-14a-d shows the AFM images of each prepared sample covering an area of 10x10 μm² and corresponding to a total population of ≈220 flakes. Overall flakes' thickness follows a log-normal distribution as shown in Figure 5-14e, indicating that almost 30% of the flakes are ≤ 3.0 nm thick (i.e. ≈ 5 layers) and that about 75% are ≤ 6 nm (i.e. ≈ 10 layers). Moreover, as displayed in Figure 5-14f, average flake lateral dimensions are approximately ≈110 nm yielding a surface coverage of ≈6% as shown in Figure 5-14g. The overall calculated “aspect ratio” is 27.5, which is comparable to the ones previously reported for MoS₂ and WS₂, given the same preparation methodology [127, 130]. The reduced standard deviations shown in Figure 5-14f and Figure 5-14g attest to the high reproducibility of the exfoliation process.

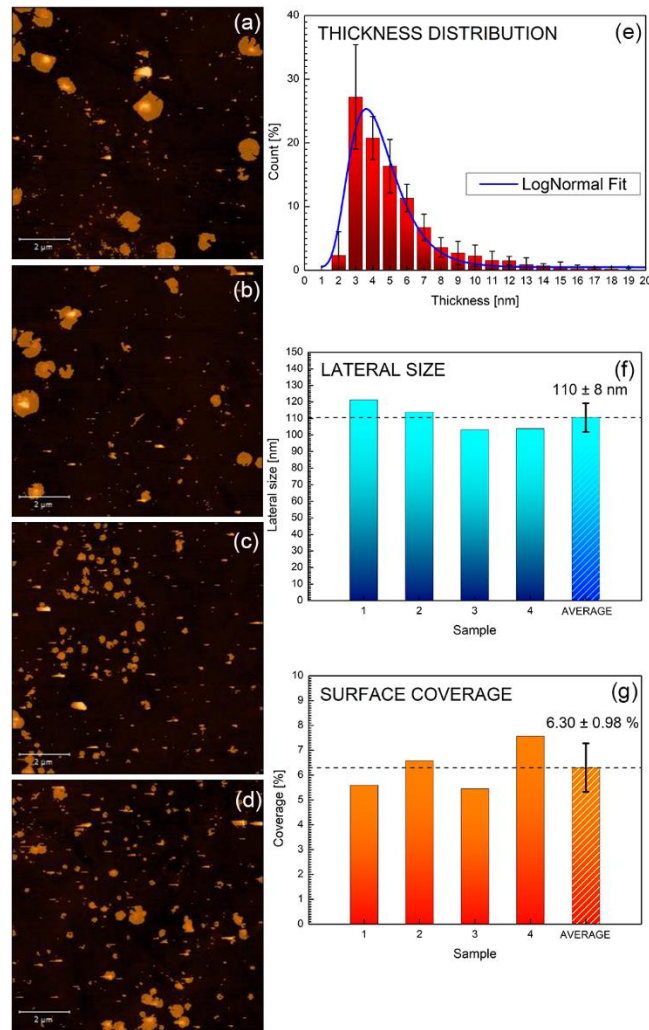


Figure 5-14- (a-d) AFM pictures of WS₂ exfoliated corresponding to four different samples prepared under the same conditions (i.e. 2 h ball milling and 90 min sonication). Statistical analysis corresponding to thickness distribution (e), Lateral dimensions (f) and surface area coverage (g).

Lastly, the influence of the sonication time on microstructure is investigated by increasing the duration from 90 min to 120 min, as shown in Figure 5-15. Comparing Figure 5-14 and Figure 5-15, it is shown that the percentage of flakes with thicknesses ≤ 3.0 nm and ≤ 6 nm increases to 55% and 90% respectively. By contrast, lateral flakes' dimensions drop from 110 nm to 64 nm, surface coverage decreases from 6.3% to 4.1% and the "aspect ratio" turns down from 27.5 to 21.2. Given these results and in light of its final application, 90 min sonication time which corresponds to both improved surface coverage and bigger lateral flake dimensions is selected, to enhance percolation paths of charge carriers between interconnected flakes.

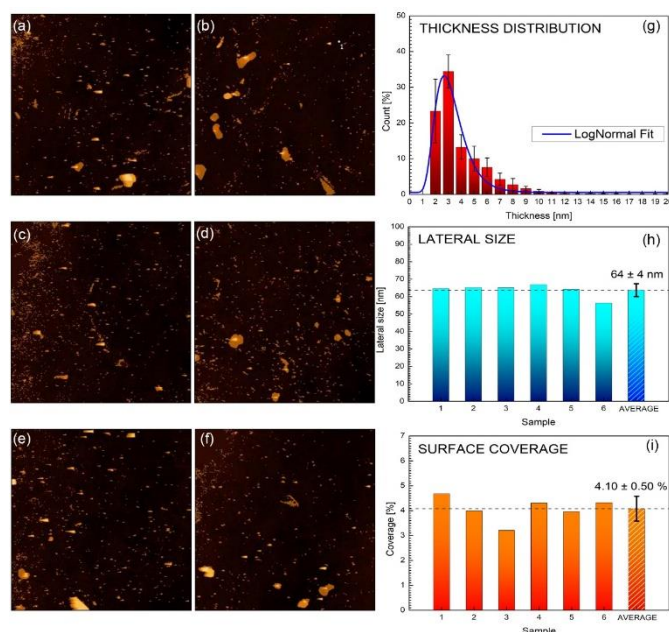


Figure 5-15- (a-f) AFM pictures of WS₂ exfoliated corresponding to six different samples prepared under the same conditions (i.e. 2 h ball milling and 120 min sonication). Statistical analysis corresponding to thickness distribution (g), Lateral dimensions (h) and surface area coverage (i).

5.2.2 Chemical composition of exfoliated WS₂

Chemical issues related to both the evolution of point defects and oxidation phenomena of TMDs highlight important challenges associated with the practical utilization of TMDs monolayers in electronic and optoelectronic devices. Sulphur vacancy is one of the most typical point defect in 2D MoS₂ and WS₂ monolayers [135], leading to active sites for gas adsorption. On the other hand, spontaneous oxidation of metal sulphides into their metal oxide counterparts [94], may result in poor reproducibility of the gas-sensing response over the long-term. In the discussion which follows we highlight possible strategies to control ambient oxidation of 2 h ground and 90 min sonicated WS₂, demonstrating the major role played by the combined action of sonication and temperature.

Figure 5-16a reports the W 4f core level XPS spectra of the pristine commercial WS₂ powder (PWD). The two doublets corresponding to 4f_{7/2} peaks are assigned, according

to literature, to WS₂ and WO₃ respectively [136]. Notably the pristine powder is already oxidized, with a WO₃ content of $\approx 18\%$.

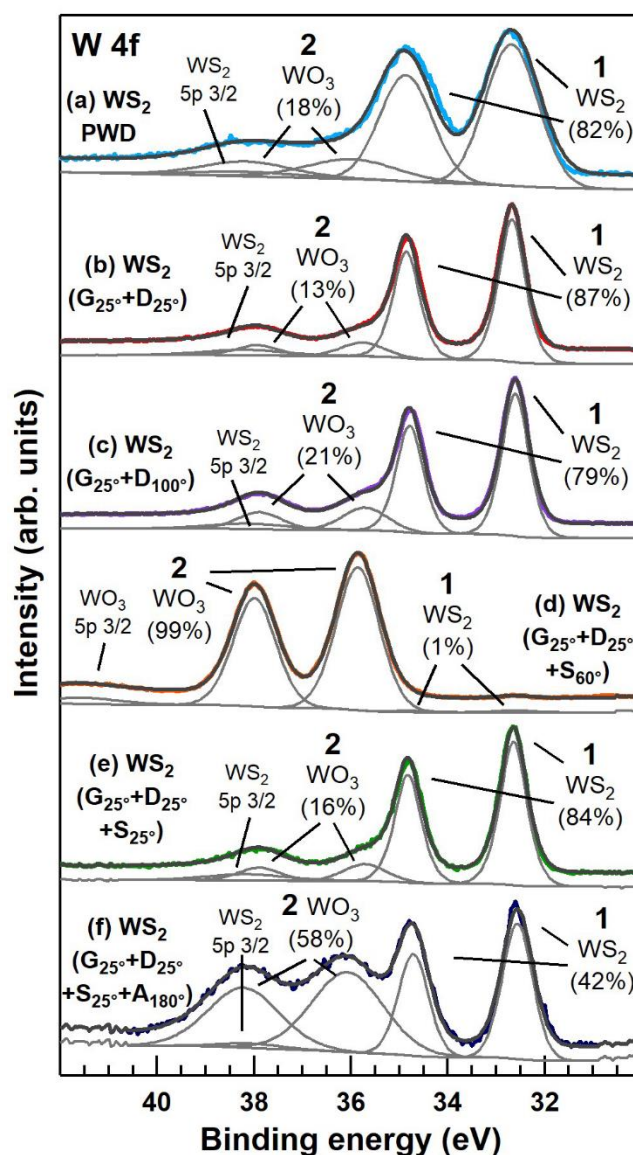


Figure 5-16- XPS spectra of W 4f core level acquired respectively on (a) pristine WS₂ commercial powder (WS₂ PWD); (b) ball milled and dried WS₂ at 25 °C (G₂₅+D₂₅); (c) ball milled at 25 °C and dried at 100 °C (G₂₅+D₁₀₀); (d) ball milled and dried at 25 °C, and sonicated at 60°C (G₂₅+D₂₅+ S₆₀); (e) ball milled, dried and sonicated at 25 °C, (G₂₅+D₂₅+ S₂₅); (f) ball milled, dried and sonicated at 25°C and post-annealed at 180°C (G₂₅+D₂₅+ S₂₅+ A₁₈₀). All the components and their relative atomic percentages are labeled in the figure.

This phenomenon, most likely due to a surface oxidation, as confirmed by the absence of WO₃ peaks in the Raman spectrum in Figure 5-17, is not surprising considering that

surface oxidation at room temperature after 6-12 months has been already reported in literature, demonstrating poor-long term stability of MoS₂ and WS₂ monolayers [124].

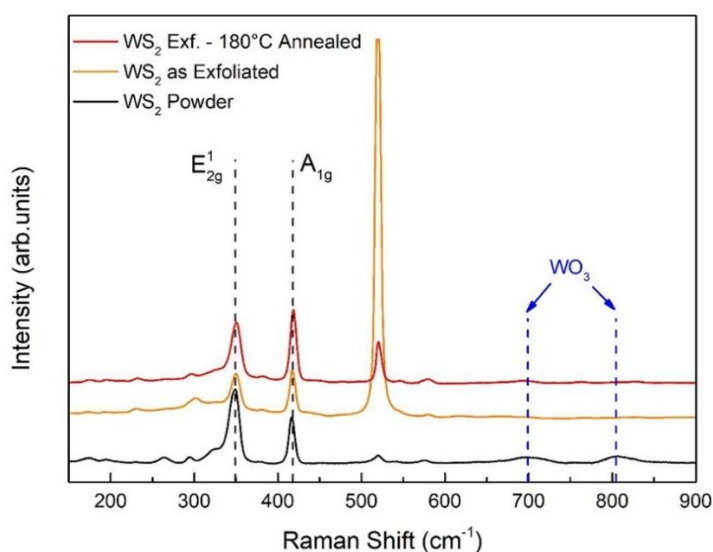


Figure 5-17- Raman spectra of WS₂ bulk powder, WS₂ as-exfoliated nanosheets and WS₂ flakes annealed at 180°C.

Figure 5-16b shows that after grinding at room temperature (G_{25°) and subsequent drying (D) to evaporate ACN solvent at 25°C, i.e. ($G_{25^\circ} + D_{25^\circ}$), the WO₃ content decreases to $\approx 13\%$. This could be reasonably explained considering that by grinding WS₂ powders, newly not-yet-oxidized surfaces are formed, resulting in a smaller content of WO₃ as evidenced by XPS measurements. Conversely, as shown in Figure 5-16c, by grinding at 25°C and drying at 100°C, i.e. ($G_{25^\circ} + D_{100^\circ}$), the WO₃ content increases to $\approx 21\%$. This result implies that, although the positive action of grinding leads to an increase in the WS₂ surface area, drying at 100°C moderately enhances the oxidation process. By grinding and drying at 25°C followed by 90 min sonication at 60°C, i.e. ($G_{25^\circ} + D_{25^\circ} + S_{60^\circ}$), as reported in Figure 5-16d, WS₂ is almost fully oxidized to $\approx 99\%$ WO₃. Conversely by grinding, drying and sonicating at 25°C, i.e. ($G_{25^\circ} + D_{25^\circ} + S_{25^\circ}$), only $\approx 16\%$ of WO₃ is formed, as shown in Figure 5-16e. This behaviour can be clarified considering the combined action of sonication and temperature on the oxidation kinetics of WS₂. Literature reports demonstrated that the oxidation of bulk TMDs comprises two parallel steps. Oxygen atoms rapidly exchange with surface sulphur forming an oxide layer, whilst WS₂ interlayer channels provide a path for inward-oxygen and backward-sulphur

diffusion, resulting in the formation of amorphous WO₃, which propagates over time into the TMD flakes [137, 138]. Sonication has the positive effect of exfoliating the ground WS₂, removing the coarser particles in the bimodal distribution of Figure 5-11a. Under these circumstances the oxygen/sulphur atoms counter diffusion mechanism between the layers can be excluded. The fast surface oxidation of WS₂ flakes of the early exfoliated samples is driven by temperature, which boosts the substitution of sulphur operated by oxygen atoms. The combined action of sonication and temperature is further confirmed considering the WO₃ content of the (G_{25°} + D_{100°}) and (G_{25°} + D_{25°} + S_{60°}). Despite a drying temperature of 100°C the final WO₃ content of the (G_{25°} + D_{100°}) is only ≈21% as compared to ≈99% of the (G_{25°} + D_{25°} + S_{60°}). Compared to sonicated samples, the ground samples are comprised of a microstructure of coarser, not yet fully-exfoliated aggregates. Under these circumstances the counter diffusion of S and O atoms between packed layers may be regarded as the controlling step of the whole oxidation process. It shows that surface oxidation is not enhanced by increasing the drying temperature to 100°C, except for a minor effect.

As discussed in the next paragraph, given the optimum operating temperature for gas sensing at 150°C, exfoliated WS₂ suspensions of (G_{25°} + D_{25°} + S_{25°}), were therefore drop cast and air annealed at 180°C for 1 h, i.e. (G_{25°} + D_{25°} + S_{25°} + A_{180°}) to stabilize the oxidation levels. As shown in Figure 5-16 the WO₃ content increased to ≈58%. Raman spectroscopy shown in Figure 5-17 displays the absence of WO₃ peaks at 180°C annealing, confirming that WO₃ forms on the surface of the exfoliated WS₂. The STEM image shown in Figure 5-18 highlights also that W, S and O atoms are homogeneously distributed within the 180°C annealed WS₂ flakes, and that no domains pertaining to secondary phases are detectable. Moreover, considering that the onset of the crystallization temperature of WO₃ is ≈250°C as previously determined by XRD analysis, it transpires that the formation of crystalline WO₃ at 180°C annealing can be excluded [124].

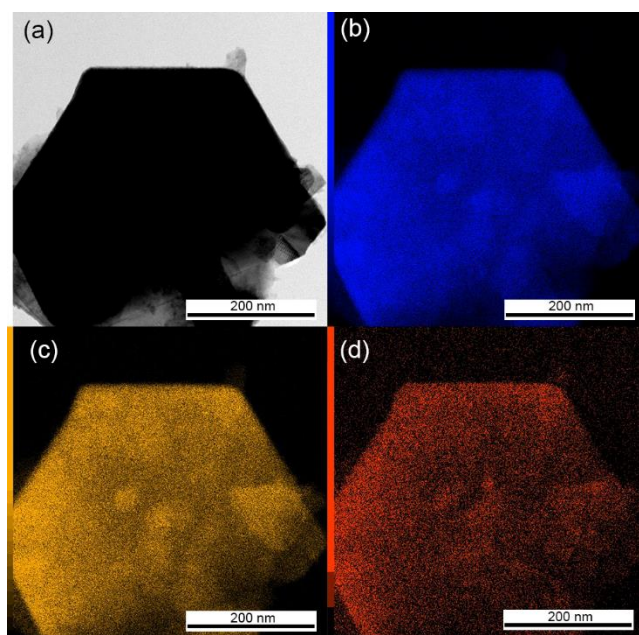


Figure 5-18- STEM pictures of an exfoliated WS₂ flake annealed at 180°C (a) and corresponding elemental mapping of (b) Tungsten, (c) Sulphur and (d) Oxygen.

Lastly, considering 1% the detection limit of the XPS measurement, we found no clear evidence of defects or sulfur vacancies related components (typically at binding energies of ≈ 36.1 eV) in the W 4f core level XPS spectra of Figure 5-16. The analysis of the S 2p core level XPS spectra, reported in Figure 5-19 is in line with the analysis reported for the W 4f. Notably the analysis of the S 2p spectra confirms the strong oxidative action produced by the combined action of sonication and temperature as previously discussed.

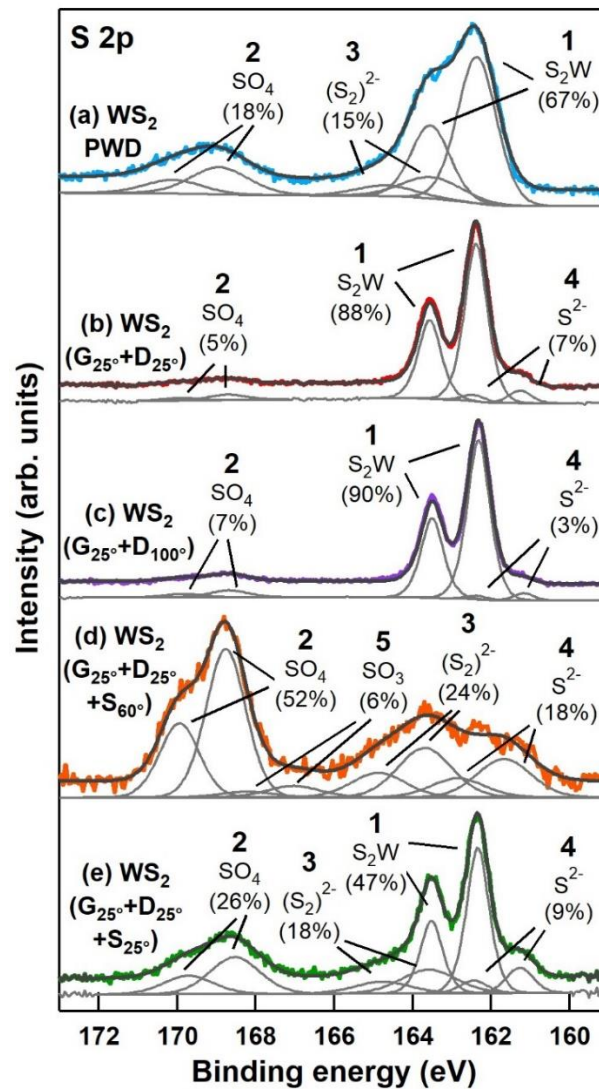


Figure 5-19- XPS spectra of S 2p core level acquired respectively on (a) pristine WS₂ commercial powder (WS₂ PWD); (b) ball milled and dried WS₂ at 25 °C (G₂₅+D₂₅); (c) ball milled at 25 °C and dried at 100 °C (G₂₅+D₁₀₀); (d) ball milled and dried at 25 °C, and sonicated at 60 °C (G₂₅+D₂₅+ S₆₀); (e) ball milled, dried and sonicated at 25 °C, (G₂₅+D₂₅+ S₂₅).

5.3 Gas sensing response

It has been reported that TMDs gas sensors operating at room temperature have shown remarkable limitations, largely related to irreversible desorption of the gas molecules, displaying incomplete recovery of the base line [139]. My research (presented in the next

chapter) demonstrated that by heating the films at 150°C operating temperature (OT), all the irreversible phenomena were eliminated [124]. In this work, to operate gas response at 150°C OT the films, previously drop casted on Si₃N₄ substrates (G_{25°} + D_{25°} + S_{25°}), were air annealed at 180°C, i.e. (G_{25°} + D_{25°} + S_{25°} + A_{180°}), to stabilize microstructure and WO₃ content. Figure 5-20 highlights a homogeneous distribution of annealed flakes, enabling current percolation paths between adjacent flakes, covering an area of 1.4x0.6 mm² over 30 μm spaced Pt interdigitated electrodes.

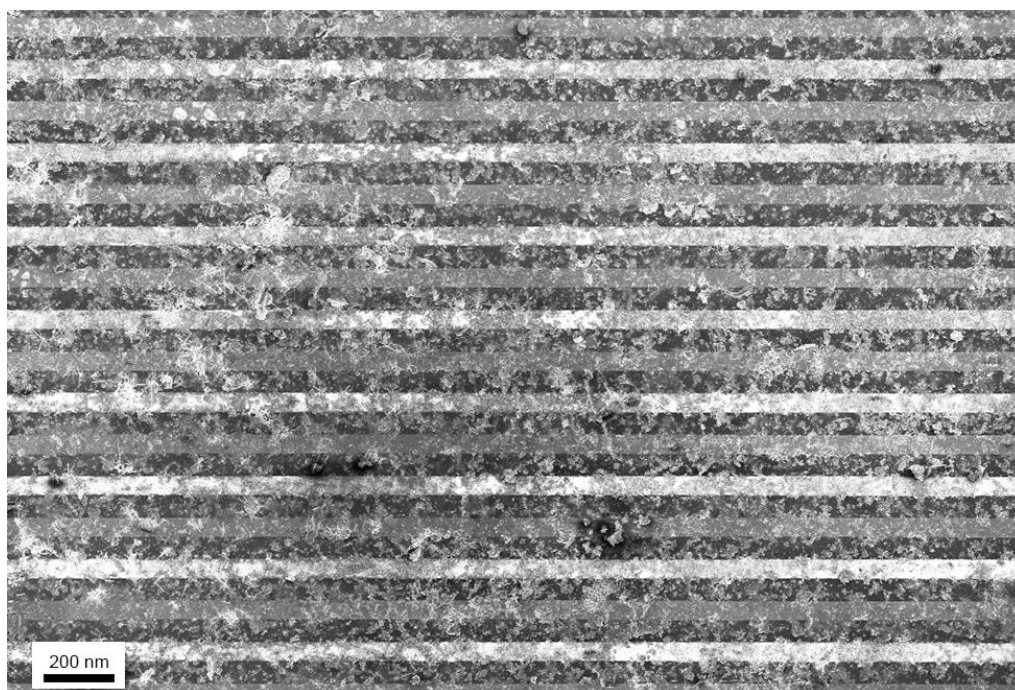


Figure 5-20- SEM picture of sensor obtained by drop casting exfoliated WS₂ and annealing at 180°C on Si₃N₄ substrate provided with Pt finger type electrodes.

Figure 5-21a shows the normalized dynamic resistance changes of (G_{25°} + D_{25°} + S_{25°} + A_{180°}) thin films to NO₂ and H₂ in the 100 ppb–10 ppm and 1 ppm–500 ppm gas concentration ranges and 150°C OT. WS₂ films respond as *n*-type semiconductors with decreasing/increasing resistance upon exposure to H₂/NO₂ respectively. Degassing with dry air at 150°C OT, the base line resistance (BLR), as indicated by the black dotted line

in the figure, is almost recovered. WS₂ flakes are more sensitive to NO₂ than H₂ gas, with associated detection limits of 200 ppb and 5 ppm respectively, confirming what has been previously reported in literature.

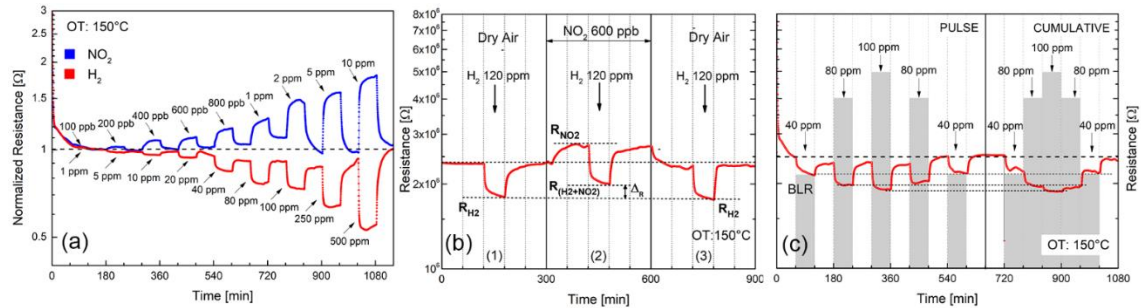


Figure 5-21- Electrical responses of (G_{25°}+D_{25°}+ S_{25°}+ A_{180°}) exfoliated WS₂ at 150°C operating temperature in dry air. (a) Comparison of the normalized dynamic response to NO₂ (100 ppb-10 ppm) and H₂ (1-500 ppm); (b) NO₂ cross sensitivity to H₂: first panel the response to 120 ppm H₂ in dry air, second panel response to 120 ppm H₂ with 600 ppb NO₂, third panel response to 120 ppm H₂ (as to first panel) for comparison; (c) Reproducibility and base line recovery by exposing the film to both pulse and cumulative H₂ concentrations in the range 40–100 ppm. H₂ concentrations highlighted in the figure by grey shadowed rectangular plots.

Discussing a possible gas response mechanism two routes are here outlined to explain the change of the electrical resistance of *n*-type TMDs sensors interacting with gaseous molecules.

As presented in the next chapter, to speculate on the strong gas sensitivity to sub-ppm NO₂ of WS₂ thin films prepared by drop casting WS₂ commercial flakes, as a possible mechanism, the adsorption of NO₂ gas is assumed to be on sulphur vacancies, claiming a similar mechanism as to the NO₂ adsorption on oxygen vacancies in oxygen-deficient metal oxide sensors [124, 140]. Considering that the exfoliated WS₂ thin films have been air-annealed at 180°C, it is likely that ambient oxygen quickly passivates sulphur defects. This reasoning can be sustained in light of XPS measurements shown in Figure 5-16, demonstrating a sulphur vacancy content of less than 1%. Under these circumstances a

response gas mechanism promoted by the presence of sulphur vacancies as active sites for gas adsorption is not straightforward.

In a second mechanism, the variation of the electrical resistance is explained by physisorption of NO₂ and H₂ molecules on passivated WS₂ surface. It was recently demonstrated by first-principles calculations on single MoS₂ sulphur-defective layer that O₂ irreversibly chemisorbs on sulphur vacancies and that the “heal” of these defects by substitutional O atoms is thermodynamically favourable [11, 140]. It shows that even at room temperature, oxygen may replace sulphur atoms, confirming the slow “aging” due to spontaneous oxidation of WS₂ and MoS₂ flakes previously reported [96, 141]. Moreover, in the case of direct NO₂ molecules interaction with sulphur defective MoS₂, a dissociative adsorption of NO₂, leading to O atoms passivating the vacancies, and NO molecules physisorbed on the MoS₂ surface, was also discussed [140, 142]. We hypothesize that both O₂ and NO₂ suppress sulphur vacancies, supporting a gas response mechanism based on physisorption of NO₂ and H₂ molecules on passivated WS₂ surface. This hypothesis is sustained by theoretical studies on the adsorption of NO₂, H₂, O₂, H₂O, NH₃ and CO gases on defect-free single layer MoS₂ and WS₂ [143]. Indeed, a key question to be resolved, is how WO₃ which is homogeneously distributed on the surface of the WS₂ flakes as shown in Figure 5-18, may or may not contribute to the overall gas sensing mechanism. A possible answer is that the as formed WO₃ is in its amorphous state, thus unlikely contribute to the modulation of the electrical signal.

According to the above mentioned physisorption model, the size and sign of the resistance changes, when exposing few-flakes of WS₂ to oxidizing (NO₂) and reducing (H₂) gases, depend on the number of exchanged carriers (i.e. electrons) and their direction. NO₂ being more electronegative than H₂ induces a large electron withdrawal, whereas H₂ results in weak electron injection, explaining the increase/decrease of electrical resistance in *n*-type

WS₂, and the smaller detection limit to H₂ (i.e. 5 ppm) as compared to NO₂ (200 ppb). The ability of WS₂ to detect H₂ in the presence of NO₂ interfering gas has been evaluated by a “cross sensitivity test” as shown in Figure 5-21b. Panel (1) of Figure 5-21b shows the WS₂ response of the (G_{25°} + D_{25°} + S_{25°} + A_{180°}) sample to H₂ alone in dry air carrier at 150°C OT. The “cross sensitivity” produced by interfering NO₂ to the measure of H₂ is displayed in panel (2) of Figure 5-21b. By exposing to 600 ppb NO₂, sensor resistance initially increases, yielding at equilibrium the resistance value R_{NO₂}. As soon as 120 ppm H₂ is introduced, the resistance decreases yielding the equilibrium value shown as R_(H₂+NO₂). The cross-sensitivity effect is displayed in the picture as (Δ_R), to indicate the gap between the electrical resistance to 120 ppm H₂ alone (i.e. R_{H₂}) and that—in the presence of 120 ppm H₂ and 600 ppb NO₂ (i.e. R_(H₂+NO₂)). These results imply that the response to H₂ (120 ppm) is largely affected by the presence of a small amount of NO₂ interfering gas (600 ppb), confirming the stronger affinity of WS₂ to NO₂ compared with H₂.

The reproducibility of the electrical response to dynamic and cumulative adsorption of H₂ gas is shown in Figure 5-21c, demonstrating outstanding response characteristics to H₂. Under pulse mode conditions, the base line resistance fully regains its initial value after completion of each desorption cycle in air. Under cumulative stepwise adsorption/desorption mode, the H₂ gas resistance increases/decreases steadily matching almost the same H₂ resistances at saturation (black lines at saturation corresponding to 40, 80 and 100 ppm H₂). These responses represent clear evidence that annealing the films at 180°C to stabilize microstructure and control oxidation, the desorption kinetics largely improves at 150°C OT, leading to high reproducible responses in the short run.

5.4 Chapter summary and conclusion

In conclusion, it is demonstrated that the microstructure of exfoliated WS₂ commercial powders produced by an enhanced ball milling and sonication process is mostly affected by the duration of the milling steps, whereas surface oxidation depends on the combined action of sonication and temperature. Specifically, the optimization of the grinding and sonication process followed by drop casting the centrifuged exfoliated suspension leads to the deposition of thin films of well packed and interconnected WS₂ flakes with controlled and reproducible microstructure over large areas, thus representing a fast, simple and scalable method, compatible with standard microelectronic fabrication techniques. The influence of the combined action of sonication and temperature upon oxidation of WS₂ demonstrating the formation of amorphous WO₃ is investigated which resulted in homogeneously distributed over the WS₂ flakes, thus addressing the crucial role of surface oxidation upon the long-term response of TMDs monolayers in electronic applications. Lastly, it is demonstrated that by pre-annealing the films at 180°C, reproducible gas sensing responses to NO₂ and H₂ at 150°C operating temperature are achieved, thus highlighting a possible strategy to control the spontaneous ageing of these devices by thermal induced oxidation.

***6 Chapter 6: Thermal stability of
WS₂ flakes for gas sensing
applications***

6.1 Introduction

Two-dimensional (2D) materials like graphene, graphene oxide, phosphorene and more recently transition metal dichalcogenides (TMDs) have attracted tremendous interest for gas sensing applications considering their high surface to volume ratio, wide range of chemical compositions and their unique thickness-dependent physical and chemical properties [118]. Graphene, despite its zero bandgap, by virtue of its fast electron transport kinetic and low electronic noise has shown NO₂ gas detection limits down to few ppm [144]. Reduced graphene oxide, on the other hand, has been used to construct high performance gas sensors with high sensitivity and reduced humidity cross-interference [145]. More recently new layered materials were tested for gas sensing applications. Among them few and mono layers of black phosphorous, usually referred as phosphorene, demonstrated room temperature gas sensing properties to both NO₂ oxidizing and NH₃ reducing gases [146]. As explained in detail in previous chapters TMDs [51], chemically represented by the MX₂ formula where M is a transition metal of group VI (i.e. Mo, W) and X is a chalcogen (i.e. S, Se, Te), can be easily exfoliated to mono or few layers by different routes yielding ultra-high surface-to-volume ratio structures with controlled number of layers. MX₂ exhibits peculiar properties like versatile chemistry, wide range of catalytic properties and layer-dependent tunable electrical response ranging from semiconducting to metallic [129] [64]. In the rich family of 2D materials MoS₂ and WS₂ sulphides represent, so far, the most widely investigated TMDs for gas sensing applications, mainly because their semiconducting properties with bandgaps typically in the 1–2 eV range. Although the exfoliation procedure of MoS₂ powders by lithium ion intercalation dates back to the eighties [147], only in 1996 the first H₂ response of Pt loaded few-layers MoS₂ was firstly reported [148]. More recently MoS₂ exfoliated thin films, single or few-layers field effect transistors (FET) and metal nano particles functionalized MoS₂, have been proposed as room temperature NH₃, NO₂, H₂ and organic vapors sensors [149]. Analogous to MoS₂, WS₂ was firstly exfoliated in 1988 for catalytic applications [150] and its applications as gas sensor is rapidly growing. WS₂ sensors in the form of thin films, multilayer photoresponsive FET, Pd-loaded nanosheets and metallic 1T-WS₂ have been recently tested as room temperature NH₃, H₂ [28], and different vapors gas sensors [151]. Indeed, in view of their practical use, TMDs gas

sensors operating at room temperature, show remarkable limitations largely related to incomplete desorption of the gas molecules, showing poor recovery of the base line in chemoresistive devices and adsorption-induced hysteresis phenomena in mono and few-layers MoS₂ FETs [152]. These drawbacks, as in the case of metal oxide sensors (MOX), might be successfully solved by heating the TMD sensors at mild temperatures ($\approx 100^\circ\text{C}$), eventually in combination with visible light radiating source, to improve their self-cleaning capabilities, as recently reported for WO₃ nanowires [4]. Thermal stability of TMDs in the 100–150°C operating temperature (OT) range represents, therefore, a key issue worth of further investigation, in light of the spontaneous oxidation of metal sulphides into their metal oxide counterparts. Drawing from previous works it is already demonstrated that few layers MoS₂-TMDs become partially oxidized in air to MoO₃ at temperatures ranging from 150°C to 250°C [96]. In line with our research it was also recently reported that WS₂ flakes undergo grain boundaries oxidation and that even at room temperature in air WS₂ and MoS₂ are hardly stable over a period of one year [94] [153]. These preliminary results imply that the oxidation process of WS₂ leads to the formation of a composite WS₂/WO₃ structures, comprising metal-sulphide/metal-oxide surfaces both susceptible to react with gaseous molecules. In conclusion, the “ageing effects” due to spontaneous oxidation may represents the “Achilles’ heel” of these 2D-TMDs for gas sensing applications. Slow oxidation of TMDs sensors working at mild operating temperatures may be eventually responsible for long-term signal-drift phenomena, representing, so far, the major drawback to the exploitation of TMDs materials as chemoresistive sensors. This PhD thesis reports about a practical and high-sensitive H₂, NH₃ and NO₂ chemoresistive thin film sensor, obtained by drop deposition of a commercial solution of dispersed few-layers WS₂ flakes and annealing the films at 150, 250 and 350°C in air. The oxidation mechanism of annealed WS₂ films and annealed WS₂ commercial powders has been investigated by X-ray photo-emission spectroscopy (XPS), scanning electron microscopy (SEM), X-ray diffraction (XRD) and by simultaneous thermal analysis (STA) techniques. The devices at 150°C OT in dry air carrier, display higher sensitivities to reducing (H₂ and NH₃) than (NO₂) oxidizing gases, with low detection limit (LDL) of 1 ppm to H₂, which is the smallest ever measured to date for WS₂-based TMDs. The analysis of the cross sensitivity to water vapor at 60% relative humidity (R.H.) for H₂ and NH₃ shows that such effects are negligible. Both the oxidation and gas response mechanisms are discussed in light of the annealing conditions

and by discriminating the single contribution of each phase of the WS₂/WO₃ composite to the overall gas response. The long-term stability of the electrical properties of the WS₂/WO₃ composite, considering the “ageing” of WS₂ at operating temperatures higher than 150°C, is still under investigation.

6.2 Materials and sensor fabrication

WS₂ thin films were prepared by drop casting commercial WS₂ nano-flakes dispersed in ethanol/water solution purchased from Graphene Laboratory inc (www.graphene-supemarket.com). The purity and the concentration of the solution were 99% and 26 mgL⁻¹ respectively. The lateral size of WS₂ flakes (1–4 monolayers) was 50–150 nm. Thin films samples, investigated by XPS and SEM techniques, were prepared by drop casting the solution on 500 nm Si₃N₄ thick substrate grown on Si, and oven-annealed in static air for 1 h in the temperature range 25–450°C, using a heating and cooling rate of 5°C.min⁻¹. The WS₂ sensors were prepared by drop casting the solution on Si₃N₄ substrates. The as-deposited thin films were oven-annealed in static air for 1 h within the temperature range 150–350°C using a heating and cooling rate of 5°C.min⁻¹. Before use, the substrates and the sensors substrates were cleaned with a 1:1 propanol: acetone solution, then dried on a hot plate at 200°C for 5 min and finally cooled down at room temperature.

6.3 Thermal stability of WS₂ flakes

Thermal stability of WS₂ films were investigated by XPS and by SEM techniques by annealing WS₂ samples at different temperatures in static air. Figure 6-1(a) and (b) show the evolution of the W 4f and the S 2p core level photo emission spectra as a function of the annealing temperature respectively.

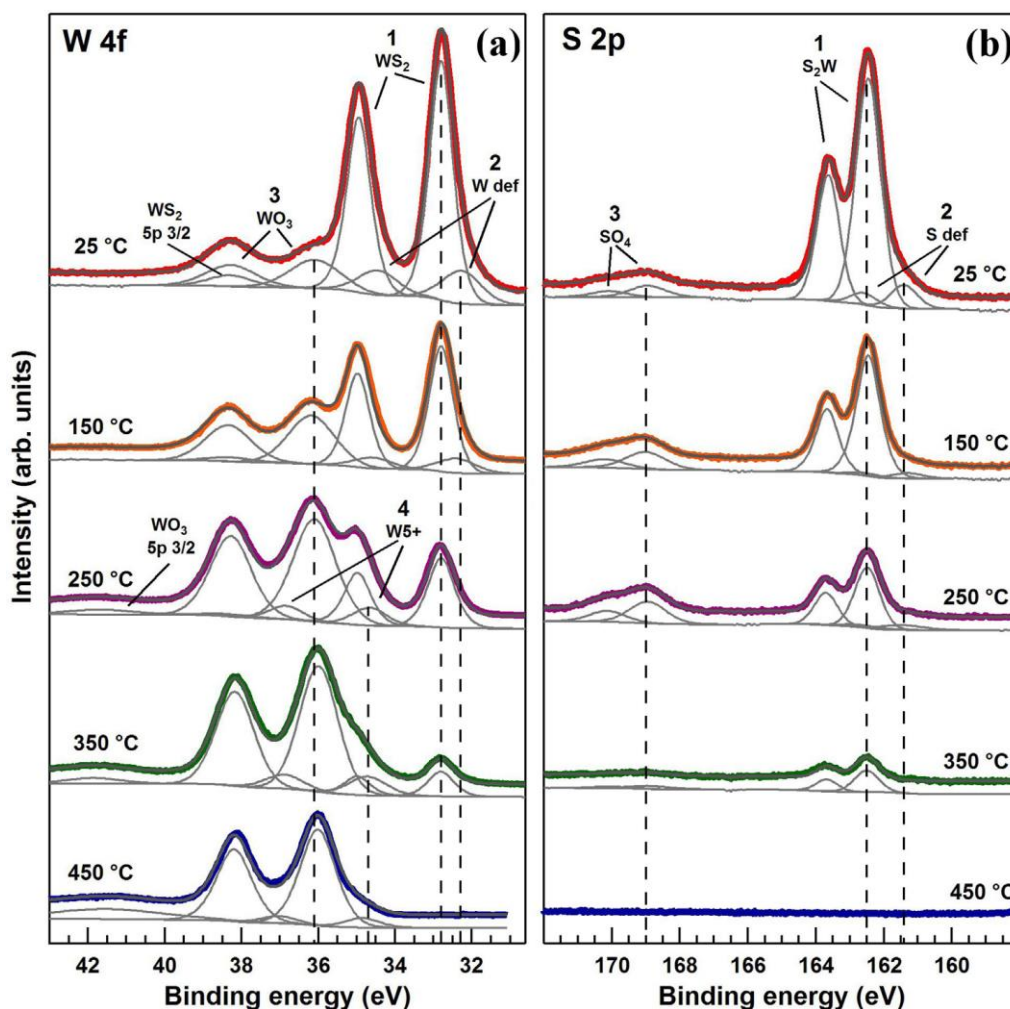


Figure 6-1- W 4f and the S 2p core level photo emission spectra acquired on WS₂ thin films before (25 °C) and after annealing in air at 150 °C, 250 °C, 350 °C and 450 °C. All the W4f (S 2p) components are composed by the 4f_{7/2} (2p_{3/2}) and 4f_{5/2} (2p_{1/2}) shifted peaks.

The XPS spectra were acquired on as-deposited WS₂ thin film (labeled with 25 °C in the figure) and on 150 °C, 250 °C, 350 °C and 450 °C annealed WS₂ thin films. As shown in Figure 6-1(a) the W 4f core level spectra are characterized by four chemically shifted components, each of which composed by the W 4f_{7/2} and the W 4f_{5/2} doublet (shifted by 2.18 eV) and the W 5p_{3/2} (shifted by 5.5 eV respect the 4f_{7/2} peak). The binding energy of the W 4f_{7/2} peaks of each components is respectively 32.8 eV (1), 32.3 eV (2), 36.1 eV (3) and 34.7 eV (4). The components, labeled in Figure 6-1(a), are assigned to W belonging to hexagonal WS₂ (1 WS₂) and to defective WS₂ (2 W def), and to W fully coordinated (3 WO₃) and partially coordinated (4 W5+) in WO₃. According to Figure 6-1(b) the S 2p core level spectra are characterized by three components, each composed

by the S 2p_{3/2} and the S₂p_{1/2} (shifted by 1.18 eV). The binding energy of the S 2p_{3/2} peaks are respectively 162.5 eV (1), 161.4 eV (2) and 169 eV (3). The components of the S 2p spectra are assigned to S belonging to hexagonal WS₂ (1 S₂W) and to defective WS₂ (2 S def), and to S belonging to SO₄²⁻ anions (3 SO₄). The assignment of WS₂, WO₃ and SO₄ components (i.e. all the peaks with the exception of the labeled “2” peaks) is straightforward and in good agreement with the literature [136]. Literature reports that the components at lower binding energy with respect to those relative to the hexagonal WS₂ semiconducting phase, are usually assigned to the 1T-WS₂ metallic phase [154], or to sulphur vacancies in the crystal structure [96]. In this case the assignment of the components labeled as “2” to defects [155] is made considering that: 1) the position of the 2 W def peaks are shifted at lower binding energy by only 0.5 eV from the 1 WS₂ peaks and not 1 eV, as expected for the 1T-WS₂; 2) the stoichiometric ratio between the 2 S def and the 2 W def components is ~1 and not 2, as expected for both the 1T-WS₂ and vacancies [96, 154]. The results of the quantitative analysis calculated from the fitting of the XPS spectra are summarized in Table 6-1.

T (°C)	W-S ₂ (%)	W-S ₂ def (%)	W-O ₃ (%)	W-5+ (%)	S ₂ -W (%)	S-O ₄ (%)	S ₂ -W def (%)	S ₂ -W/W- S ₂
25	68	15	17	0	84	7	9	2.0
150	53	9	38	0	78	18	4	2.0
250	28	0	63	9	60	32	8	2.0
350	11	0	77	12	81	19	0	1.8
450	0	0	91	9	0	0	0	-

Table 6-1- Summary of the stoichiometric analysis obtained from the fitting of the XPS spectra reported in Figure 6-1. The table is divided in four sections. The second and the third section shows respectively the percentages of the W 4f and of the S 2p components. In the last section it is reported the ratio between the 1 S₂W and the 1 WS₂ components.

The main effect of the annealing in air is the progressive oxidation of the WS₂ flakes as shown by the relative percentages of the W4f components reported in the second section of Table 6-1. The WS₂ components decrease from 68% in the pristine (25°C) film to 0% in the annealed film at 450°C, while the WO₃ component increase from 17% to 91% in the same samples. The oxidation is confirmed by the overall intensity reduction of the S 2p spectra.

The S/W ratios calculated from the 1 S₂W and the 1 WS₂ components, reported in the last section of Table 6-1 is in good agreement with the expected value of 2. The presence of defects both in the WS₂ and WO₃ crystal (the 2 W def and the 4 W 5+ components) is consistent with the chemical exfoliation procedure. To confirm this, the comparison between the XPS spectra acquired on the powder and on the thin film are shown in Figure 6-2, where the spectra are identical with the exception of the defects related peaks.

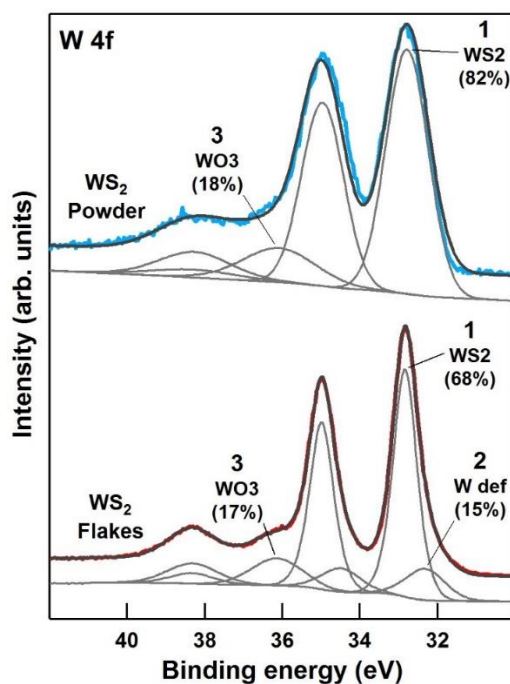


Figure 6-2- W 4f core level photoemission spectra of WS₂ commercial powder and flakes respectively. The assignment and the relative percentage of each component are reported near the W 4f_{7/2} peaks.

The presence of defects in the WS₂ flakes is supposed to play a major role in the gas sensing mechanism of the prepared devices as it will be discussed in electrical measurements section. Figure 6-3 shows the morphological changes of the WS₂ thin films after annealing in air at 150°C (panels a–b), 250°C (panels c–d), 350°C (panels e–f) and 450°C (panels g–h).

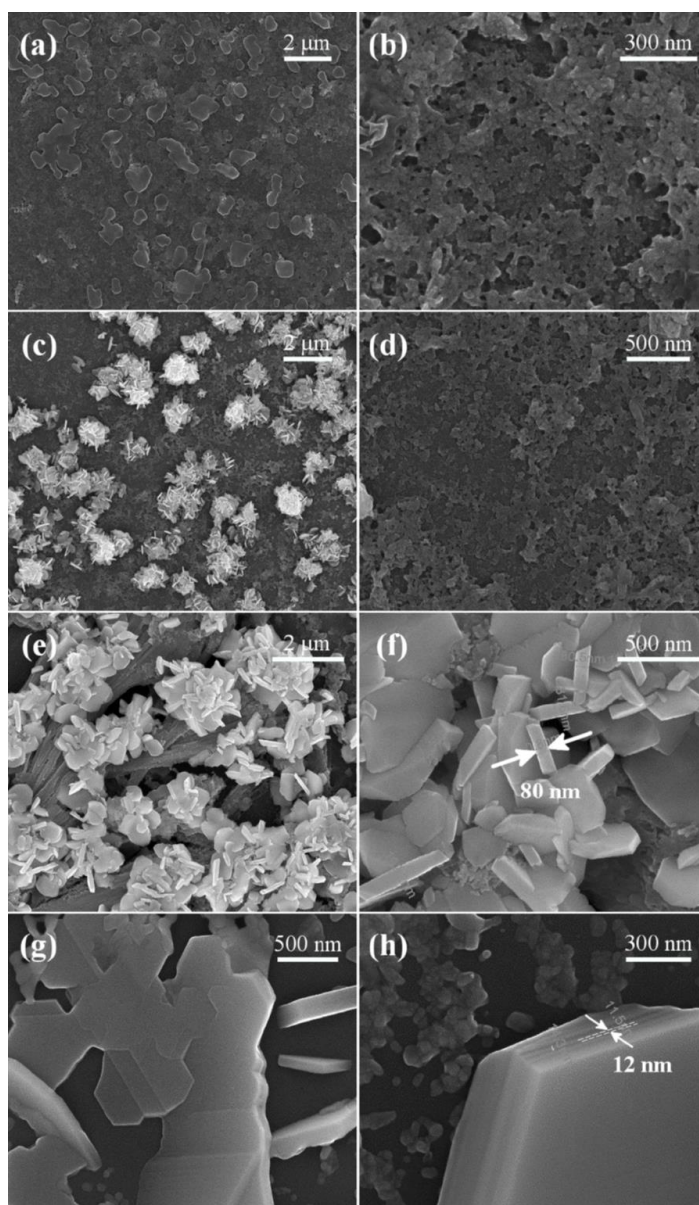


Figure 6-3- SEM images of WS₂/WO₃ thin films annealed at 150°C (a), 250°C (c), 350°C (e) and 450°C (g). In panels (b), (d), (f), (h) are reported the corresponding magnified images.

SEM characterization shows the appearance of 3D-lamellar structures at 250°C (panel c) on a uniform and porous underlying film (panels a-b and d). These 3D structures, which are usually associated with the formation of orthorhombic transition metal oxide crystals [156, 157], increase their size with increasing of the annealing temperature as shown in (panels e-h).

From the observation of each SEM picture and from the comparison with the XPS results it is possible to understand the effects of the annealing on the morphology of the WS₂

films. The 150°C annealed film (Figure 6-3(a) and (b)) is composed of micrometric (1–2 μm length) flat-shaped 2D-WO₃ amorphous structures (Figure 6-3(a)) laid on a porous and homogenous background of WS₂ (Figure 6-3(b)). These assignments can be made considering that the lateral dimensions of the flat-shaped structures are one order of magnitude larger than the dimensions of the WS₂ flakes, which are in the range of 50-150 nm, and taking into account both XPS and XRD results, as it will be further discussed in the next paragraph.

The 250°C annealed film (Figure 6-3(c) and (d)) is composed of micrometric lamellar structures of crystalline 3D-WO₃, grown on the flat-shaped 2D-WO₃ amorphous structures (Figure 6-3(a)) and by a porous and homogenous background of WS₂. The size and thickness of the 3D-WO₃ lamellar structures increase in the 350°C annealed film (Figure 6-3(e) and (f)), while the porous WS₂ background is replaced by a flat and terraced background. The magnification (Figure 6-3(f)) shows that the thickness of these 3D-WO₃ structures is ~80 nm. At 450°C annealing (Figure 6-3(g) and (h)) the 3D-WO₃ crystal growth continues and the transition from WS₂ to 3D-WO₃ is completed. At this temperature, as shown in (Figure 6-3(h)), terraces of ~12 nm thickness stack together to form thick WO₃ lamellar structures. To better understand the thermal induced oxidation of WS₂ we have also investigated the oxidation of WS₂ commercial powder by XRD and STA techniques, under the same experimental heating conditions. The comparative study between the commercial WS₂ powder and WS₂ flakes has been previously successfully tested for consistency by comparing the XPS spectra of W 4f as reported in Figure 6-2. Figure 6-4 compares the XRD diffraction spectra in the 10°–28° 2θ region of commercial WS₂ powder annealed in air for 1 h in the temperature range 25°C–400°C.

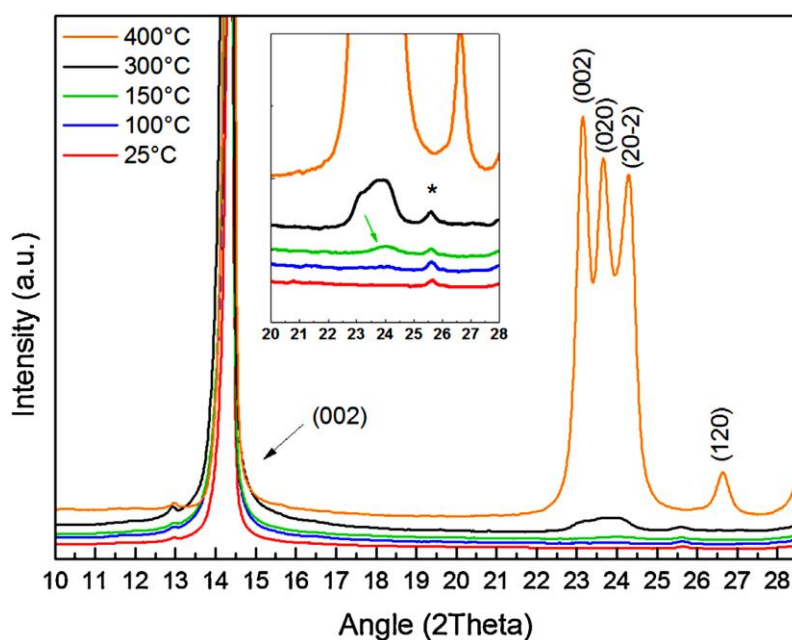


Figure 6-4- XRD plots of WS₂ commercial powders annealed at 5 C.min⁻¹ to different temperatures for 1 h. The inset shows the close up of the XRD signals in the 2 θ region of the characteristic main peaks of WO₃.

The XRD maximum at 14.32° corresponds to the basal plane (002) of hexagonal WS₂ (ICSD card 98-008-4181). The crystallization process of WO₃ starts at 150 °C, as displayed by the occurrence of a reflection at around 23.98° 2 θ (green arrow in the close up of Figure 6-4). With increasing annealing temperature, the XRD reflections related to WO₃ become more intense. At 300°C annealing temperature a broad signal represented by the convolution of 23.07° (002), 23.62° (020) and 24.12° (20-2) peaks of monoclinic WO₃ is clearly evident. At 400°C the characteristic diffraction peaks at 23.12° (002), 23.66° (020) and 24.26° (202) of monoclinic WO₃ (ICSD card 98-001-7003) are fully developed with a slightly preferential growth along the (002) plane. The peak at 25.63° (111) (as * in the inset of Figure 6-4) has been assigned to orthorhombic tungstite (WO₃·H₂O) (ICDS card 98-020- 1806), which represents one of the possible hydrated forms of WO₃. Notably this peak disappears at 400°C annealing due to the transformation of metastable orthorhombic tungstite into monoclinic WO₃ [158]. The entire oxidation process of WS₂ into monoclinic WO₃ is completed at temperatures greater than 500°C as shown in Figure 6-5.

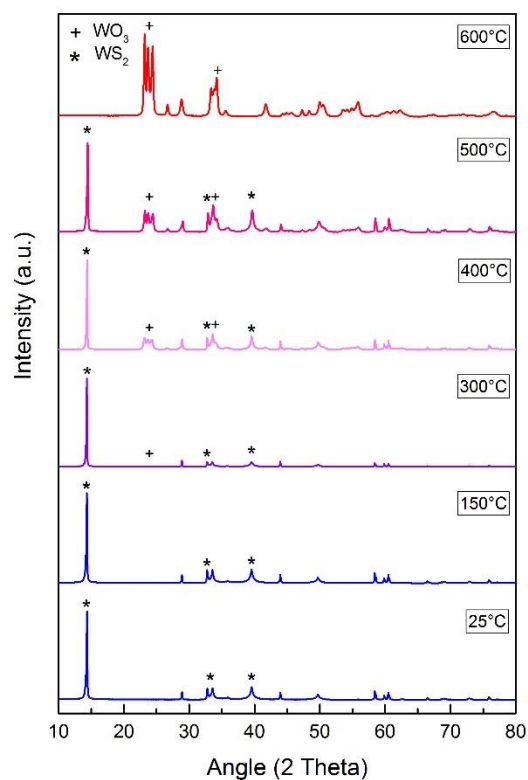


Figure 6-5- XRD patterns of the commercial WS₂ powder annealed at 5°C.min⁻¹ for 1 hour up to 600°C.

Figure 6-6 shows the thermo-gravimetric (TG) plot of the WS₂ powder heated at 5°C/min from 25°C to 800°C in static air.

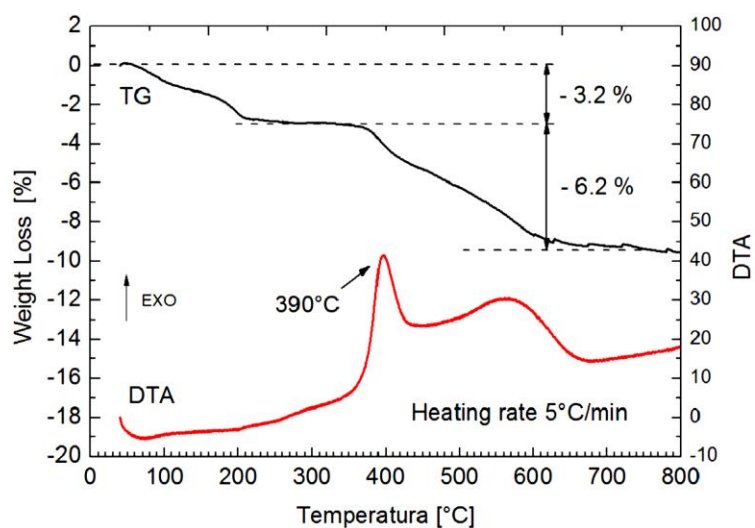
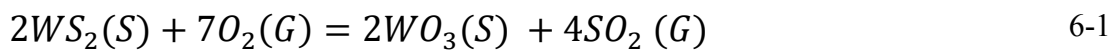


Figure 6-6- Comparison of the thermogravimetric and differential thermal analysis plots of WS₂ commercial powder heated at 5°C.min⁻¹ to 800°C in static air.

A cumulative weight loss of 9.4% is shown in the whole temperature investigated range, comprising a primary loss of around 3.2%(25–200°C range) and a secondary of 6.2% (380–630°C range). The first weight loss may be ascribed to the evaporation of chemisorbed water, the second one to the oxidation of WS₂, leading to the formation of WO₃ oxides. According to literature [159] the oxidation of WS₂ to WO₃ is confirmed by both the evolution of a strong exothermic peak around 390°C, as shown by the differential thermal analysis (DTA) plot, and by the occurrence of a weight loss of approximately - 6.2%, as displayed by the TG signal, which is reasonably close to the theoretical weight loss expected for the oxidation of WS₂ to WO₃ (6.4%). Notably, at temperatures higher than 600°C no further weight loss is shown, attesting the complete oxidation of WS₂. This evidence is in full agreement with the disappearance of the characteristic WS₂ peak in the XRD spectra, corresponding to the annealing temperature of 600°C as shown in Figure 6-5.

6.4 WS₂/WO₃ composite growth mechanism

The formation of WS₂/WO₃ composite has been divided into different steps, each of them related to the annealing temperature and discussed in light of the XPS, SEM, XRD and STA analysis and published works. As a first issue, thermodynamic calculations [160] reveal favorable conditions (i.e. $G < 0$) for direct oxidation of WS₂ in air, as to reaction 6-1, for all the investigated annealing temperatures.



$$\Delta G_{150^\circ C}(S) = -1642.8 \text{ kJ/mol} \quad 6$$

$$\Delta G_{250^\circ C}(S) = -1447 \text{ kJ/mol} \quad 6$$

$$\Delta G_{350^\circ C}(S) = -1246 \text{ kJ/mol}$$

Beside these preliminary thermodynamic computations, kinetics issues involving diffusion phenomena within the layers, direct sulphide atoms replacement by air oxygen,

nucleation and growth of new crystalline structures, play a major role. As a first consideration density functional theory (DFT) simulations on MoS₂ single layer demonstrated that the substitution of an S atom by an O atom is energetically favorable, even at room temperature, suggesting a high susceptibility of MoS₂ defective layers to be oxidized [143]. By heating in the temperature range 25-150°C in ambient air (45% ± 5 relative humidity) oxygen atoms rapidly exchange with sulphur as to reaction 6-1, forming an oxide layer, possibly located, on defective edge planes of WS₂ flakes. WS₂ interlayer channels provide a path for inward-oxygen and backward-sulphur diffusion, resulting in the formation of amorphous WO₃, which propagates over time into the TMD flakes. This mechanism is likely to occur considering, as previously reported, the oxidation kinetic of mono-layer WS₂ in ambient air [94], and the reverse sulphidization process of bulk WO₃ to yield inorganic fullerene-like WS₂ nano-tubes [137].

At 25°C the as received WS₂ commercial flakes are yet partially oxidized displaying the occurrence of around 17% of WO₃ phase (see column four of Table 6-1) as shown by the XPS. The spontaneous oxidation in air of WS₂ is in line with latest literature [94]. At 150°C annealing temperature the micrometric flat-shaped 2D-WO₃ structures, shown in Figure 6-3a, are in their amorphous state, at last in their very early crystallization stage, as shown by the presence of a shallow crystallization peak in the XRD spectra on the 150°C annealed powders (see inset of Figure 6-4). At 150°C annealing, these structures are characterized by a growing number of surface defects, reasonably attributed to oxygen vacancies, as revealed by XPS analysis (see column five of Table 6-1). WS₂ pristine flakes, partially oxidized by the formation of a skin-growing amorphous WO₃ layer, maintain their structure as shown by SEM (Figure 6-3(b)). At 250°C the nucleation and crystallization of a 3D-WO₃ crystalline phase takes place as shown in Figure 6-3(b). Considering that the basal area of the crystalline platelet 3D-WO₃ structures reported in Figure 6-3(c) has approximately the same extension of the area of the flat-shaped WO₃ amorphous structures reported in Figure 6-3(a), it is reasonable that these structures provide an underlying interface for a heterogeneous nucleation and crystallization of lamellar 3D-WO₃. At 350°C annealing temperature, as shown by SEM (Figure 6-3(e) and (f)) and XRD (Figure 6-4), the crystallization of monoclinic WO₃ secondary-phase is fully accomplished. We assign the platelet-like structure reported in Figure 6-3(f) to monoclinic WO₃, in light of its morphological resemblance with atomically thin 3D-WO₃ sheets from hydrated tungsten trioxide [161] and flower-like 3D-WO₃ architectures [119].

With the proceeding of the 3D-WO₃ crystallization, the thickness of the underlying WS₂ film decreases, enabling the formation of a hierarchical structure represented by thick slabs of 3D-WO₃ grown on WS₂ layers. By extending the annealing process up to 450°C a further growth of the monoclinic 3D-WO₃ structures is shown according to Figure 6-3(h) and Figure 6-3. WO₃ terraces, of ~12 nm thickness, stacks together yielding wider and thicker 3D-WO₃ structures. At this temperature the WS₂ film surface is completely oxidized as demonstrated by the disappearance of the sulphur signal in the XPS analysis in Figure 6-1.

It may be concluded that the formation of a composite WS₂/WO₃ hierarchical structure is accomplished by a two-step oxidation and crystallization process in the 150–350°C annealing temperature range. The whole oxidation process accounts for an initial substitution of sulphur by oxygen atoms in the primary WS₂ phase, followed by a heterogeneous nucleation and growth of crystalline 3D-WO₃ secondary phase at temperature higher than 250°C. The influence of this composite structure and the role played by edges and terraces adsorption sites on gas sensing properties is discussed in the next section.

6.5 Electrical response of WS₂ films- Results

Gas response to both reducing (H₂ and NH₃) and oxidizing (NO₂) gases of the annealed WS₂ sensors has been analyzed in the OT range 25–150°C utilizing dry air as carrier gas. The maximum OT was set at 150°C in order to not exceed the annealing temperature of the film. Figure 6-7(a), (b) and Figure 6-8 show the resistive responses of the 150°C annealed WS₂ film to 500 ppm H₂, 2 ppm NO₂ and 180 ppm NH₃ at different OTs respectively.

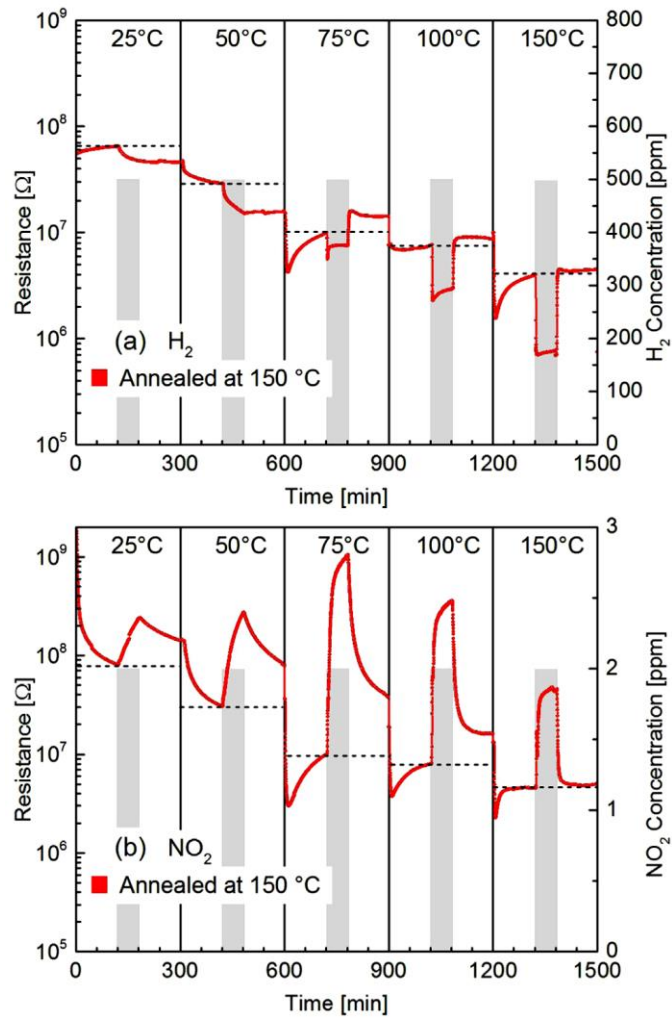


Figure 6-7- The electrical response of the 150°C annealed WS₂ film to H₂ and NO₂. Panel(a): resistive responses to 500 ppm H₂ in dry air as a function of the OT; Panel (b): resistive responses to 2 ppm NO₂ in dry air as a function of the OT. Horizontal black dot lines mark the base line resistances. H₂ and NO₂ pulses are represented by the grey shaded rectangular plots. The time scale of the experiment consists of 2 h conditioning in dry air and 1-h exposure to H₂ and NO₂ gases respectively.

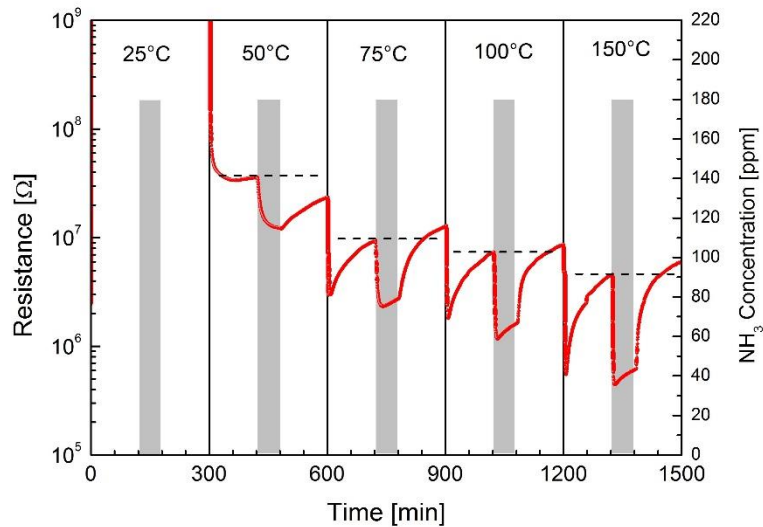


Figure 6-8- Resistive responses to 180 ppm NH₃ in dry air as a function of OT of the 150°C annealed WS₂ film. Horizontal black dot lines mark the base line resistance in air. NH₃ ppm pulses are represented by grey shaded rectangular plots.

Horizontal black dot lines mark the base line resistances (BLR) in air while grey shadowed rectangular shapes represent the H₂, NO₂ and NH₃ pulses respectively. WS₂ films annealed at 250°C and 350°C respond to H₂, NH₃ and NO₂ gases in a similar way as the one annealed at 150°C. Both Figure 6-7(a) and (b) show a monotonic decrease of the BLR (i.e. the resistance in dry air) with increasing the OT, suggesting a semiconducting behavior. All the annealed WS₂ films respond as n-type semiconductor with decreasing/increasing the resistance upon exposure to H₂/NO₂ respectively. In the temperature range 25–50°C, as displayed in Figure 6-7(a), the 150°C annealed WS₂ film shows a negligible RR to 500 ppm reducing H₂ and almost no recovery of the BLR after 2 h of dry air purge. With increasing the OT both RRs and desorption kinetic improve. The BLR is fully regained starting from 100°C OT while the highest RR is achieved at 150°C. Gas response of the 150°C annealed WS₂ film to 2 ppm oxidizing NO₂ reported in Figure 6-7(b), shows an increase of the electrical resistance with a maximum of the RR located at 75°C OT. As in the previous case gas desorption kinetic improves with increasing the OTs enabling full recovery of the BLR starting from 150°C OT. Comparing H₂ and NO₂ gas responses at 100°C and 150°C OTs, we observe that H₂ desorption at 100°C OT in air is both faster and reversible compared to NO₂, as shown by the square-shape of the adsorption/desorption curves, and by the occurrence of a reversible and

complete recovery of the BLR after 2 h dry air conditioning. At 150°C OT both H₂ and NO₂ BLRs are completely regained after 5 min and 12 min respectively. H₂ RR increases from 2.8 (@ 100°C OT) to 5.3 (@ 150°C OT), whereas NO₂ decreases from 44.6 (@ 100°C OT) to 10.1 (@ 150°C OT). The 250°C and 350°C annealed WS₂ films show similar adsorption/desorption features as respect to the one annealed at 150°C, but reduced RRs to H₂ and NH₃ in the whole 25–150°C OT range. It can be concluded that at 150°C OT, the 150°C annealed WS₂ film, is the one which better accomplishes faster and reversible BLR recovery and enhanced gas response. Figure 6-9 shows the dynamic gas response of all the annealed WS₂ films to increasing H₂ concentrations from 1 ppm to 10 ppm at 150°C OT in dry air carrier.

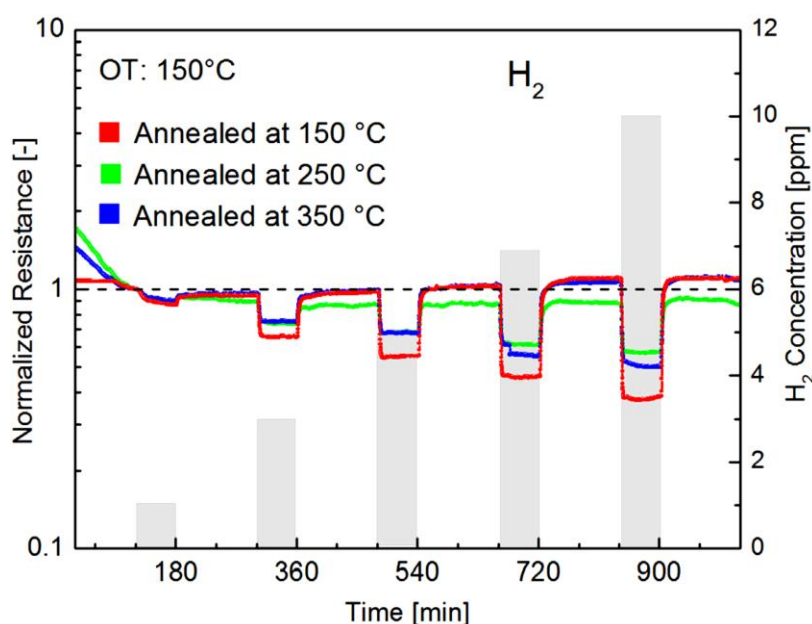


Figure 6-9- Dynamic gas responses to increasing H₂ gas concentrations (1–10 ppm) in dry air carrier and 150°C OT of the WS₂ films annealed at 150°C, 250°C and 350°C.

The NH₃ response of the 150°C annealed WS₂ film, under the same experimental conditions, is shown for comparison in Figure 6-10.

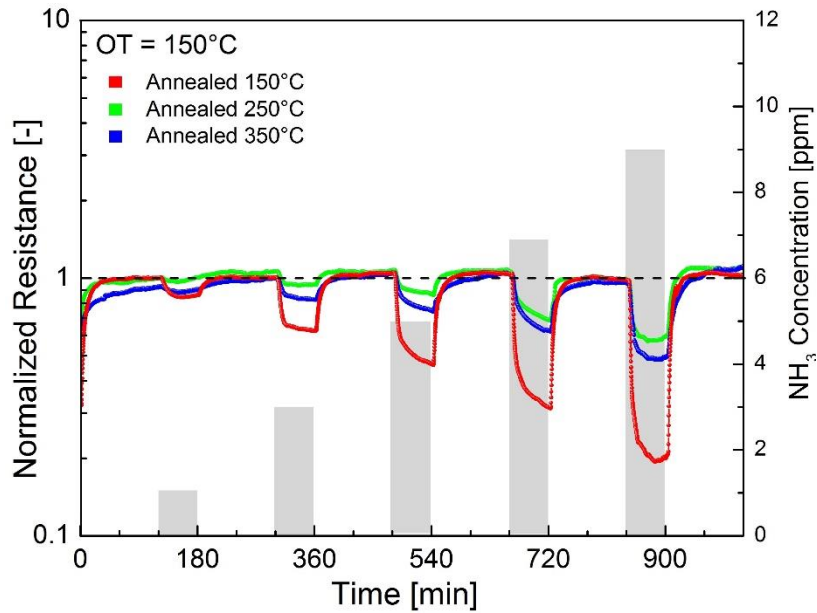


Figure 6-10- Electrical resistance variations to NH₃ of the 150°C, 250°C and 350°C annealed WS₂ films.

Increasing the annealing temperature, the RRs for a given H₂ gas concentration decrease. This behavior is clearly depicted in Figure 6-9 comparing the 150°C annealed WS₂ as respect to both the 250°C and 350°C annealed. WS₂ films annealed at 250°C and 350°C show comparable H₂ sensing properties, with the anomaly represented by a slightly better response of the 350°C as respect to the 250°C annealed. Numerical figures show that at 10 ppm H₂ the 150°C annealed WS₂ film yields RR = 2.9 compared to RR = 1.5 and RR = 1.9 of the 250°C and 350°C respectively. Under the same experimental conditions, similar responses have been obtained exposing all the annealed films to NH₃, as shown in Figure 6-10. Table 6-2 provides also numerical computations of both the RRs and adsorption/desorption times, enabling full comparison of the gas responses to H₂ and NH₃ at 150°C OT of all the annealed films.

WS ₂ Annealed at	Gas conc. H ₂ /NH ₃ [ppm]	RR=R _A /R _G [-]		τ _{ads} [min]		τ _{des} [min]	
		H ₂	NH ₃	H ₂	NH ₃	H ₂	NH ₃
150°C	1	1,15	1,16	/	/	/	/
	3	1,44	1,60	5,9	15	27,2	28,9
	5	1,76	2,24	5	25,3	12,4	27,9
	7	2,24	3,29	5,2	20,6	18,9	21,8
	10	2,87	4,93	5	13,1	9,6	23
250°C	1	1,15	0,99	/	/	/	/
	3	1,22	1,12	5,5	13,5	30,6	32,8
	5	1,28	1,23	5,2	35,7	6,8	31
	7	1,43	1,55	5,8	40,1	12,1	14,1
	10	1,53	1,68	5,4	13,7	6,6	27,3
350°C	1	1,10	1,01	/	/	/	/
	3	1,28	1,22	5,7	29,9	36,8	83,6
	5	1,46	1,39	5,3	35,3	22,6	76,3
	7	1,71	1,65	5,6	36,1	17	42,6
	10	1,94	1,96	5,6	16,3	10,5	65,5

Table 6-2- Comparison at 150°C operating temperature of the Relative Responses (RRs) and response times to H₂ and NH₃ of the 150°C, 250°C and 350°C annealed WS₂ films.

Figure 6-11 shows the electrical responses of the 150°C annealed WS₂ film at 150°C OT, exposing the film to same concentrations of reducing H₂ and NH₃ gases in dry air carrier.

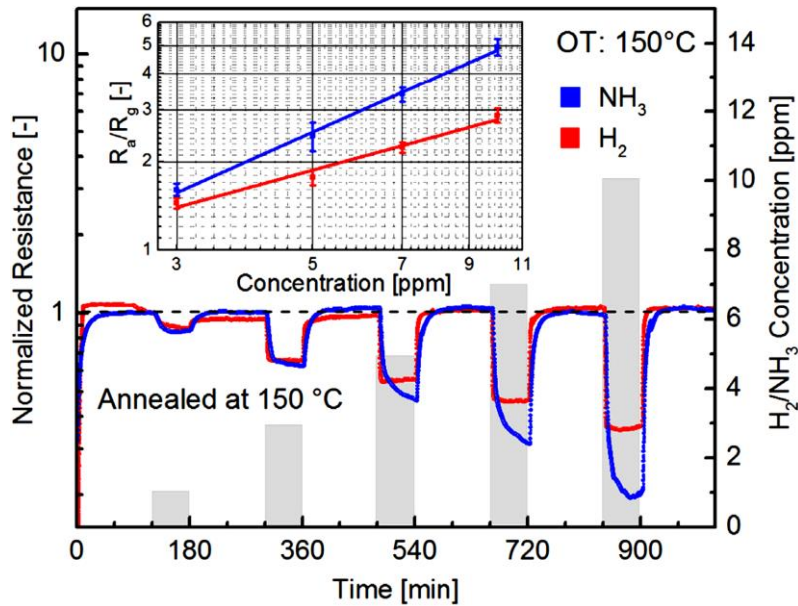


Figure 6-11- Electrical responses of the 150°C annealed WS₂ film at 150°C OT, exposing the film to identical concentration of H₂ and NH₃ (1–10 ppm) in dry air carrier. The inset shows the calibrating lines to NH₃ and H₂ respectively. The bars in the inset represent the standard deviation calculated over a set of 5 measurements performed for each gas concentration.

Some features differentiate the H₂ compared to the NH₃ gas response. As a first consideration a LDL of 1 ppm H₂ and 1 ppm NH₃ are clearly displayed in Figure 6-11. The 150°C annealed film always shows bigger RRs to NH₃ as compared to H₂. According to Table 6-2 and the inset of Figure 6-11 at 10 ppm gases concentration, RRs are 2.9 and 4.9 to H₂ and NH₃ gases respectively. NH₃ gas sensitivity, as represented by the slope of the regression line of the log–log plot shown in the inset of Figure 6-11, is higher than H₂. Adsorption and desorption response times to NH₃ are always significantly higher as compared to H₂ as reported in Table 6-2. Figure 6-12 shows the dynamic gas response of all the annealed WS₂ films to increasing NO₂ concentrations from 40 ppb to 1 ppm at 150°C OT in dry air carrier.

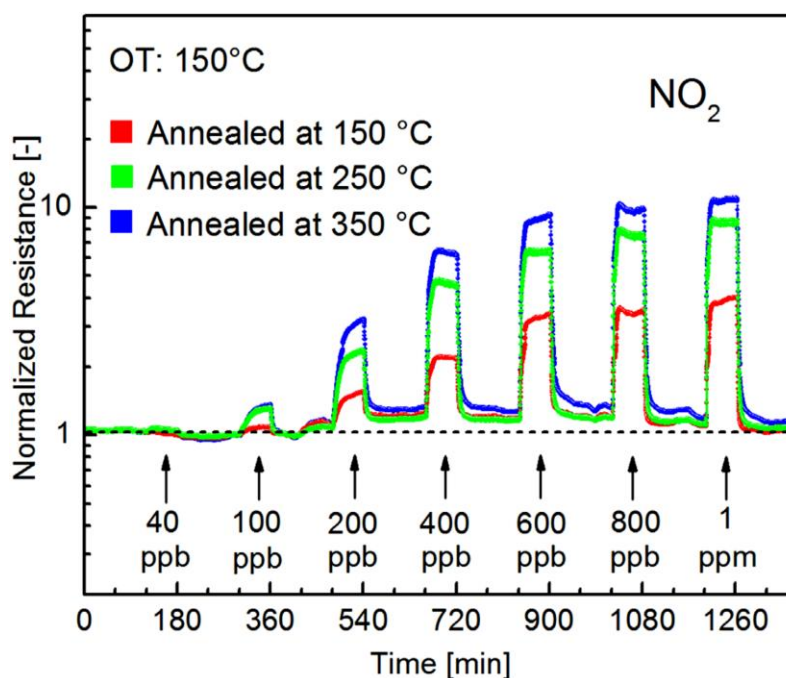


Figure 6-12- Dynamic gas responses to increasing NO₂ gas concentrations (40 ppb–1 ppm) in dry air carrier at 150°C OT of the WS₂ films annealed at 150°C, 250°C and 350°C.

NO₂ oxidizing gas increases films resistances according to the n-type nature of both WS₂ and WO₃. The NO₂ response clearly starts at 100 ppb though at 40 ppb a small increase of the electrical resistance may not be excluded. Notably, with increasing the annealing temperature, the NO₂ gas RR increases. At 400 ppb, the NO₂ RR increases from 2.0 (WS₂ annealed @150°C) to 4.2 (WS₂ annealed @250 °C) to reach 4.9 (WS₂ annealed @350°C). This behavior is exactly the opposite as the one reported in Figure 6-9 and Figure 6-10, which display a RRs decrease to H₂ and NH₃, with increasing the annealing temperature. NO₂ adsorption and desorption times are much higher than the one recorded for H₂, but comparable with those of NH₃. One of the most important feature of a gas sensors is represented by its ability to recover, within the time scale of the experimental procedure, its BLR. This behavior demonstrates the absence of irreversible gas adsorption, which conversely, would strongly restricts its practical utilization. The reproducibility of the gas response to H₂ and the base line recovery features of the 150°C annealed, by conditioning the sensor to both dynamic and cumulative H₂ and NH₃ exposures are shown in Figure 6-13 and Figure 6-14 respectively.

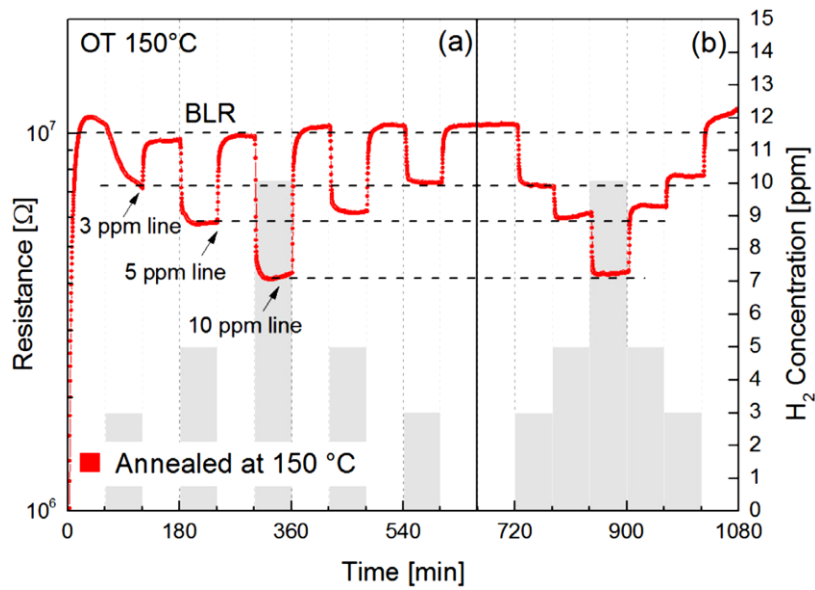


Figure 6-13- Reproducibility and base line recovery features of the 150°C WS₂ annealed at 150°C OT by exposing the film to both dynamic and cumulative H₂ concentrations in the range 3–10 ppm. Panel (a): dynamic responses to repeated on/off runs; panel (b): cumulative adsorption/desorption runs by stepwise increase and decrease of the H₂ concentration.

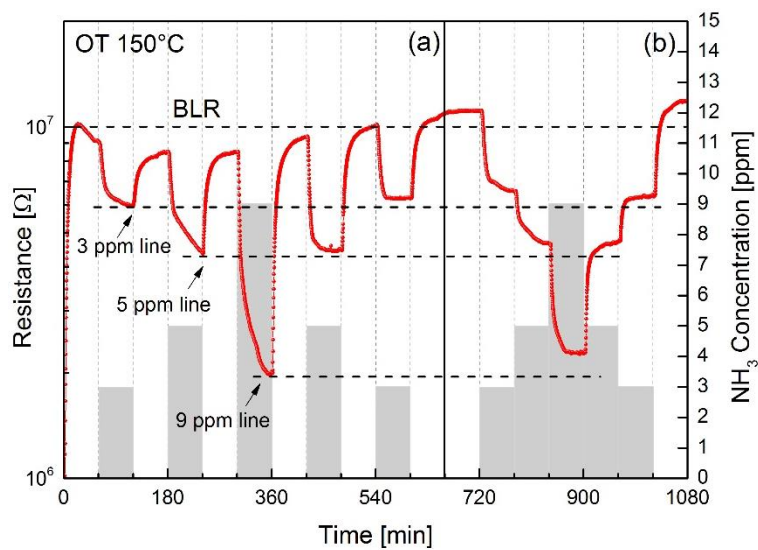


Figure 6-14- Reproducibility and base line recovery features of the 150°C WS₂ at 150°C OT, by exposing the film to both dynamic and cumulative NH₃ concentrations in the range 3-9 ppm. Panel (a) shows the dynamic responses to repeated on/off runs by increasing/decreasing the NH₃ concentration; panel (b) shows the cumulative adsorption/desorption runs by stepwise increase and decrease the NH₃ concentration.

The 150°C annealed WS₂ film shows outstanding dynamic and cumulative responses to H₂. Figure 6-13(a) displays the electrical signal under forward and backward dynamic pulses to H₂ in the concentration range 3–10 ppm. BLR fully regains its initial value after completion of each cycle. Under cumulative step wise adsorption/desorption mode, as shown in Figure 6-13(b), the H₂ gas resistance increases/decreases steadily matching almost the same H₂ resistances at saturation (black lines at saturation corresponding to 3, 5 and 10 ppm H₂). The NH₃ response of the 150°C annealed under the same experimental conditions, as reported in Figure 6-14, shows the occurrence of adsorption induced hysteresis phenomena, within the time scale of 1 h, reasonably due to the longer response times of NH₃ as respect to H₂.

Another aspect we investigated, is represented by the ability of WS₂ to detect H₂ and NH₃ while water vapor is present. These features can be evaluated by “cross sensitivity” test, as shown in Figure 6-15 (H₂O H₂) and in Figure 6-16 (H₂O NH₃).

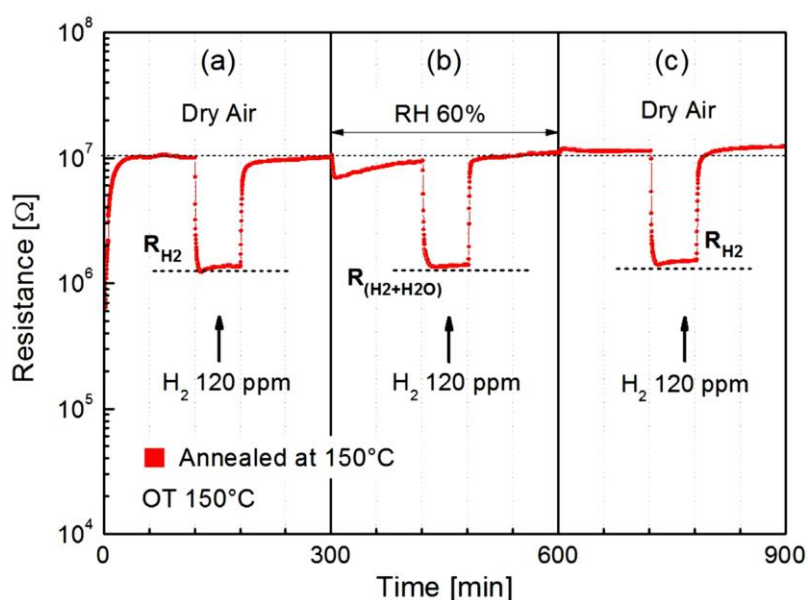


Figure 6-15- Relative Humidity cross sensitivity to H₂ of the 150°C annealed WS₂ film at 150°C operating temperature. (a) response to 120 ppm H₂ in dry air. (b) response to 120 ppm H₂ in 60% R.H. (c) response to 120 ppm H₂ in dry air.

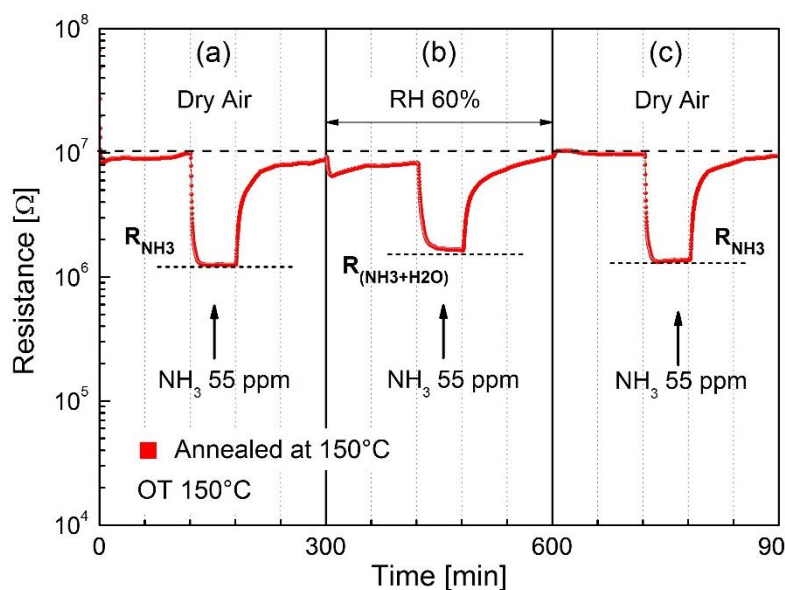


Figure 6-16- Relative Humidity (R.H.) cross sensitivity to NH₃ of the 150°C annealed WS₂ at 150°C operating temperature. (a) response to 55 ppm NH₃ in dry air; (b) response to 55 ppm NH₃ in 60% R.H.; (c) response to 55 ppm NH₃ in dry air.

In Figure 6-15 H₂ is considered as the target gas (at 120 ppm) and water as the interfering one (at 60% R.H., measured at room temperature). Panel (a) of Figure 6-15 shows the 150°C annealed WS₂ film response to H₂ in dry air carrier at 150°C OT. After exposure to 120 ppm H₂ the electrical resistance decreases as respect to the base line resistance, yielding at equilibrium the resistance value highlighted in the picture as R_{H₂}. The “cross sensitivity” produced by interfering water to the measure of H₂ is displayed in panel (b). By preliminary exposing to 60% R.H., sensor resistance after an initial decrease, steadily increases, almost recovering the same base line resistance as in dry air. Subsequently, as 120 ppm H₂ was introduced, the resistance decreases yielding the equilibrium value shown as R_(H₂+H₂O). The comparison between R_{H₂} and R_(H₂+H₂O) shows no substantial humidity cross sensitivity effects. The electrical response to 120 ppm H₂ in dry air has been repeated after the “cross test” as shown in panel (c). The electrical response of panel (c) is almost the same as the one previously shown in panel (a), highlighting a good reproducibility in the short time of the electrical response. Similar behavior of the humidity cross sensitivity to the NH₃ are shown in Figure 6-16. Regarding the long-term stability properties of the electrical response of the WS₂ annealed films to H₂ and NH₃ gases, tests, lasting one year, are running now following the same methodology as previously reported for pure WO₃ thin films [105]. Beside long-term stability response, which may represent a crucial limitation, yet under investigation, it may be concluded

that WS₂ transition metal dichalcogenide has shown potential advantages in terms of the reported low detection limits of 1 ppm H₂, 1 ppm NH₃, as respect to most popular metal oxide sensors (MOS).

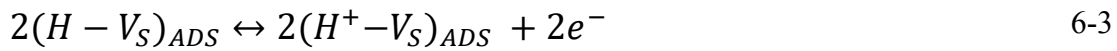
6.6 Electrical response of WS₂ films– discussion

Discussing the electrical response to both reducing and oxidizing gases a large number of factors (mainly related to the microstructure, chemical composition, phases distribution, amorphous to crystalline transitions phenomena) play a significant role. This is a complex issue, and still under study to clarify the specific sensing mechanism. As a first consideration both WS₂ and WO₃ single phases, given their n-type semiconductor response, contribute with the same sign, yet to different extends, to the electrical changes when exposed to reducing (H₂ and NH₃) and oxidizing (NO₂) gases. The role of WS₂ and WO₃ single phases to the overall gas response can be rationalized in the way which follows.

6.6.1 H₂ gas

No literature so far reported the H₂ sensing properties of pure WS₂, with the exception of Pd-nanoparticles loaded WS₂ and MoS₂ films, which demonstrated room temperature H₂ response and associated LDL of 500 ppm [139, 162]. Pure WO₃, on the other hand, is reported to respond to H₂ with associated LDL, at best, of 5 ppm and 150°C OT [163]. Considering that a LDL of 1 ppm to H₂ has never been reported in literature for pure WO₃, bearing in mind from XPS and XRD measurements that crystalline WS₂ is the prevailing phase at 150°C annealing temperature, taking into account that the as formed WO₃ is almost in its amorphous state (inset of Figure 6-4) and thus unlikely contributing to the gas response, we assign the H₂ gas response in the 1–10 ppm concentration range to WS₂. The smaller H₂ RRs, with increasing the annealing temperature to 250°C and 350°C, as shown in Figure 6-9, can be explained, consequently, by the formation of crystalline WO₃, which decreases the amount of the WS₂ phase, eventually reducing the H₂ response. A possible mechanism supporting the WS₂ reactivity to H₂ starts with the assumption that the catalytic dissociative chemisorption of hydrogen molecules, by a spill over

mechanism, does not occur on WS₂ and WO₃ surfaces, unless activated by Pt/Pd nanoparticles, as previously reported [139, 164]. Recent studies on the electrocatalytic hydrogen evolution reaction (HER) highlighted that H₂ easily evolves on defective edges of exfoliated MoS₂ and WS₂ as respect to surface sites [119], and that the HER can be largely improved, preparing films with vertically aligned layers, exposing all their edge sites to H₂ molecular adsorption [165]. DFT studies confirmed the experimental evidence, demonstrating that edges of layered WS₂ are truly active sites for hydrogen adsorption, being energetically favorable respect to surface sites [166]. To this extend a reaction mechanism is here suggested considering the circumstance for a reverse HER, as shown by reactions 6-2 and 6-3. In a first step 6-2 H₂ gas molecules adsorbs on the active edge-sites of WS₂, here assigned to sulphur vacancies (VS). This assumption is based on previous research, demonstrating the role played by edge sulphur vacancies to enhance heterogeneous catalysis on single layer layer MoS₂ [167]. In a second step 6-3 the ionization of the adsorbed H takes place leading to electrons release.



The decrease of the WS₂ edge sites concentration with increasing the annealing temperature, and the formation of crystalline WO₃, explain also the reduction of the H₂ gas sensitivity of the 250°C and 350°C annealed films in the 1–10 ppm H₂ concentration range. Under these circumstances, it could be worth of future investigations to find new preparation routes aimed to maximize the number of exposed edges, extending the well-known paradigm from surface to volume, to length (of exposed edges) to volume ratio.

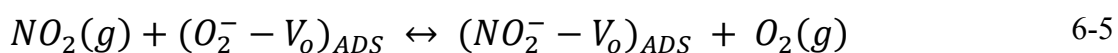
6.6.2 NH₃ gas

The response mechanism of the WS₂/WO₃ composite to NH₃ is not this straightforward. Previous reports demonstrated that WS₂ and MoS₂ thin films show NH₃ room temperature response in nitrogen gas, with LDL of 1.4 ppm and 300 ppb respectively [168]. By contrast, WO₃ nanowire sensors displayed, at best, LDL of 10 ppm to NH₃ in dry air at 200°C OT [169]. Taking into account that a LDL of 1.4 ppm to NH₃ has been reported for pure WS₂ utilizing nitrogen as carrier gas [168], we have demonstrated in Figure 6-11

and Figure 6-10 that the 150°C annealed is able to detect NH₃ in dry air carrier, with comparable LDL, and improved recovery of the BLR. Considering that we achieved a LDL of 1 ppm, which is ten times smaller than the one ever measured with WO₃ sensors, we assign to WS₂ the NH₃ gas response at concentrations smaller than 10 ppm. Moreover, it is the reduction of the WS₂ phase with increasing the annealing temperature that explains the reduction of the NH₃ response of the 250°C and 350°C annealed films as shown in Figure 6-10.

6.6.3 NO₂ gas

No literature, to the best of our knowledge, reported so far, the NO₂ response of bulk or exfoliated WS₂. By contrast, single or few-layer MoS₂ show room temperature NO₂ sensing, with associated LDL of 20 ppb [170]. WO₃, on the other hand, is well known to have a quite high sensitivity to NO₂ with LDL of around 40 ppb in air [171]. Noticeably, as reported in Figure 6-12, one peculiar feature drives our attention. NO₂ gas sensitivity increases with increasing the annealing temperature, showing an opposite behavior if compared to H₂ and NH₃ gas responses (Figure 6-9 and Figure 6-10). A possible explanation of this phenomenon, considers that when the annealing temperature is 250°C and 350°C, increases both the amount of crystalline WO₃ and the concentration of oxygen vacancies as displayed by XRD and XPS analysis respectively. Under these conditions a standard reaction mechanism as to reaction 6-4 and 6-5 accounts for the WO₃ contribution to the overall NO₂ gas response. In a first step O₂ gas adsorbs primarily on defective WO₃ oxygen vacancies as to reaction 6-4. In a second step adsorbed oxygen is replaced by NO₂ molecules yielding NO₂⁻ adsorbates. The increase of the electrical resistance is due to the stronger electronegative force of NO₂ as respect to O₂ to withdraw electrons from the conduction band of crystalline WO₃.



Reactions 6-4 and 6-5 fully describe the role played by the oxygen-defective WO₃

crystalline phase to detect NO₂ in the 250°C and 350°C annealed films. Reactions 6-4 and 6-5, indeed, do not support the WS₂ response to NO₂, considering the lack of oxygen vacancies in TMDs. A question to be resolved, therefore, is why and how the 150°C annealed responds to NO₂. The presence of an oxygen-defective WO₃ phase in the 150°C annealed, as demonstrated by XPS analysis, which may contribute to the gas response according to reactions 6-4 and 6-5, can be excluded, taking into account that at 150°C annealing the as formed WO₃ is in its amorphous state. On the other hand, if we focus on the presence of sulphur vacancies in the 150°C annealed crystalline WS₂, it is more reasonable that, in the same fashion as for metal oxide sensors, the WS₂ contribution to the overall NO₂ gas response is rationalized by simply substituting oxygen (V_O) with sulphur (V_S) vacancies in reactions 6-4 and 6-5.

6.7 Chapter summary and conclusion

To summarize, in this chapter a comprehensive and systematic study about the oxidation in air of commercial WS₂ flakes and their gas sensing properties to reducing (H₂ and NH₃) and oxidizing (NO₂) gases was reported. The oxidation process begins at room temperature with the substitution of sulphur by oxygen atoms in the primary WS₂ phase, yielding amorphous WO₃ which increases up to 150°C annealing. A heterogeneous nucleation and crystallization process, leading to the formation of crystalline WO₃ secondary phase, takes place at annealing temperatures of 250°C. The heating of WS₂ flakes in the 150–350°C annealing temperature range results in the formation of a WS₂/WO₃ composite hierarchical structures. WS₂/WO₃ composite films show excellent gas sensing properties to reducing H₂ and NH₃ gases in the 1–10 ppm gases concentration range, and 150°C OT. In this work, the LDL of 1 ppm to H₂, 1 ppm NH₃ and 100 ppm NO₂ in dry air carrier, are found as the smallest so far ever measured utilizing WS₂ flakes. These outstanding gas sensing properties have been demonstrated by annealing the WS₂ films at 150°C, thus precluding the formation of crystalline WO₃. Outstanding reproducibility responses, by exposing the 150°C annealed sensor to dynamic and cumulative gas pulses were obtained utilizing H₂ gas. No substantial cross sensitivity effects due to water at 60% R.H. have been found to both H₂ and NH₃ gases response. Tests, lasting one year, are running now to assess the long-term stability properties of the

electrical response of the WS₂/WO₃ composite annealed films to H₂ and NH₃ gases.

7 References

References

1. Seiyama, T., et al., *A new detector for gaseous components using semiconductive thin films*. Analytical Chemistry, 1962. **34**(11): p. 1502-1503.
2. Raguse, B., et al., *Gold nanoparticle chemiresistor sensors: direct sensing of organics in aqueous electrolyte solution*. Analytical chemistry, 2007. **79**(19): p. 7333-7339.
3. Liu, Y., et al., *Solid-state gas sensors for high temperature applications—a review*. Journal of Materials Chemistry A, 2014. **2**(26): p. 9919-9943.
4. Giancaterini, L., et al., *The influence of thermal and visible light activation modes on the NO₂ response of WO₃ nanofibers prepared by electrospinning*. Sensors and Actuators B: Chemical, 2016. **229**: p. 387-395.
5. Wang, C., et al., *Metal oxide gas sensors: sensitivity and influencing factors*. Sensors, 2010. **10**(3): p. 2088-2106.
6. Lang, I. and Y.A. Firsov, *Kinetic theory of semiconductors with low mobility*. Sov. Phys. JETP, 1963. **16**(5): p. 1301.
7. Franke, M.E., T.J. Koplín, and U. Simon, *Metal and metal oxide nanoparticles in chemiresistors: does the nanoscale matter?* Small, 2006. **2**(1): p. 36-50.
8. Barsan, N., M. Schweizer-Berberich, and W. Göpel, *Fundamental and practical aspects in the design of nanoscaled SnO₂ gas sensors: a status report*. Fresenius' journal of analytical chemistry, 1999. **365**(4): p. 287-304.
9. Liu, X., et al., *A survey on gas sensing technology*. Sensors, 2012. **12**(7): p. 9635-9665.
10. Yamazoe, N., G. Sakai, and K. Shimanoe, *Oxide semiconductor gas sensors. Catalysis Surveys from Asia*, 2003. **7**(1): p. 63-75.
11. Barsan, N. and U. Weimar, *Conduction model of metal oxide gas sensors*. Journal of Electroceramics, 2001. **7**(3): p. 143-167.
12. Samson, S. and C. Fonstad, *Defect structure and electronic donor levels in stannic oxide crystals*. Journal of Applied Physics, 1973. **44**(10): p. 4618-4621.
13. Jarzebski, Z. and J. Marton, *Physical properties of SnO₂ materials II. Electrical properties*. Journal of the electrochemical Society, 1976. **123**(9): p. 299C-310C.
14. Maier, J. and W. Göpel, *Investigations of the bulk defect chemistry of polycrystalline tin (IV) oxide*. Journal of solid state chemistry, 1988. **72**(2): p. 293-302.
15. Göpel, W. and K.D. Schierbaum, *SnO₂ sensors: current status and future prospects*. Sensors and Actuators B: Chemical, 1995. **26**(1-3): p. 1-12.
16. Madou, M.J. and S.R. Morrison, *Chemical sensing with solid state devices*. 2012: Elsevier.
17. Lenaerts, S., et al., *In situ infrared and electrical characterization of tin dioxide gas sensors in nitrogen/oxygen mixtures at temperatures up to 720 K*. Sensors and Actuators B: Chemical, 1994. **19**(1-3): p. 478-482.
18. Schierbaum, K., et al., *Conductance, work function and catalytic activity of SnO₂-based gas sensors*. Sensors and Actuators B: Chemical, 1991. **3**(3): p. 205-214.
19. Bochenkov, V. and G. Sergeev, *Preparation and chemiresistive properties of nanostructured materials*. Advances in colloid and interface science, 2005. **116**(1): p. 245-254.
20. Xu, C., et al., *Grain size effects on gas sensitivity of porous SnO₂-based elements*. Sensors and Actuators B: Chemical, 1991. **3**(2): p. 147-155.
21. Xu, C., et al., *Correlation between gas sensitivity and crystallite size in porous SnO₂-*

- based sensors*. Chemistry Letters, 1990. **19**(3): p. 441-444.
22. Sakai, G., et al., *Theory of gas-diffusion controlled sensitivity for thin film semiconductor gas sensor*. Sensors and Actuators B: Chemical, 2001. **80**(2): p. 125-131.
 23. Matsunaga, N., et al., *Formulation of gas diffusion dynamics for thin film semiconductor gas sensor based on simple reaction-diffusion equation*. Sensors and Actuators B: Chemical, 2003. **96**(1): p. 226-233.
 24. Vuong, D.D., et al., *Preparation of grain size-controlled tin oxide sols by hydrothermal treatment for thin film sensor application*. Sensors and Actuators B: Chemical, 2004. **103**(1): p. 386-391.
 25. Vuong, D.D., et al., *Hydrogen sulfide gas sensing properties of thin films derived from SnO₂ sols different in grain size*. Sensors and Actuators B: Chemical, 2005. **105**(2): p. 437-442.
 26. Pagnier, T., et al., *Reactivity of SnO₂-CuO nanocrystalline materials with H₂S: a coupled electrical and Raman spectroscopic study*. Sensors and Actuators B: Chemical, 2000. **71**(1): p. 134-139.
 27. Korotcenkov, G., *Gas response control through structural and chemical modification of metal oxide films: state of the art and approaches*. Sensors and Actuators B: Chemical, 2005. **107**(1): p. 209-232.
 28. Kim, Y.T., et al., *Electrochemical Synthesis of CdSe Quantum-Dot Arrays on a Graphene Basal Plane Using Mesoporous Silica Thin-Film Templates*. Advanced Materials, 2010. **22**(4): p. 515-518.
 29. Buffat, P. and J.P. Borel, *Size effect on the melting temperature of gold particles*. Physical review A, 1976. **13**(6): p. 2287.
 30. Kim, W.Y., Y.C. Choi, and K.S. Kim, *Understanding structures and electronic/spintronic properties of single molecules, nanowires, nanotubes, and nanoribbons towards the design of nanodevices*. Journal of Materials Chemistry, 2008. **18**(38): p. 4510-4521.
 31. Tiwari, J.N., R.N. Tiwari, and K.S. Kim, *Zero-dimensional, one-dimensional, two-dimensional and three-dimensional nanostructured materials for advanced electrochemical energy devices*. Progress in Materials Science, 2012. **57**(4): p. 724-803.
 32. Iijima, S., *Helical microtubules of graphitic carbon*. nature, 1991. **354**(6348): p. 56-58.
 33. Dresselhaus, M.S., G. Dresselhaus, and P.C. Eklund, *Science of fullerenes and carbon nanotubes: their properties and applications*. 1996: Academic press.
 34. Wang, C., et al., *A Review on the Electrospun Oxide Nanofibers for Anode Electrodes in Lithium-Ion Batteries*. Current Nanoscience, 2017. **13**(4): p. 394-409.
 35. Sen, S., et al., *Growth of SnO₂/W₁₈O₄₉ nanowire hierarchical heterostructure and their application as chemical sensor*. Sensors and Actuators B: Chemical, 2010. **147**(2): p. 453-460.
 36. Wagner, R.S., *Vapor-liquid-solid crystal growth technique*. 1970, Google Patents.
 37. Ding, B., et al., *Gas sensors based on electrospun nanofibers*. Sensors, 2009. **9**(3): p. 1609-1624.
 38. Rabouw, F.T. and C. de Mello Donega, *Excited-State Dynamics in Colloidal Semiconductor Nanocrystals*. Topics in Current Chemistry, 2016. **374**(5): p. 58.
 39. Sun, Y.-F., et al., *Metal oxide nanostructures and their gas sensing properties: a review*. Sensors, 2012. **12**(3): p. 2610-2631.

40. Patil, J.V., et al., *Electrospinning: A versatile technique for making of 1D growth of nanostructured nanofibers and its applications: an experimental approach*. Applied Surface Science, 2017.
41. Khalil, A., et al., *Electrospun metallic nanowires: Synthesis, characterization, and applications*. Journal of Applied Physics, 2013. **114**(17): p. 12_1.
42. Ke, P., et al., *From macro to micro: structural biomimetic materials by electrospinning*. RSC Advances, 2014. **4**(75): p. 39704-39724.
43. Elahi, F., et al., *Core-shell fibers for biomedical applications-a review*. Bioeng. Biomed. Sci. J, 2013. **3**(01): p. 1-14.
44. Yu, M., K.H. Ahn, and S.J. Lee, *Design optimization of ink in electrohydrodynamic jet printing: Effect of viscoelasticity on the formation of Taylor cone jet*. Materials & Design, 2016. **89**: p. 109-115.
45. Buer, A., S. Ugbolue, and S. Warner, *Electrospinning and properties of some nanofibers*. Textile Research Journal, 2001. **71**(4): p. 323-328.
46. Reneker, D.H. and A.L. Yarin, *Electrospinning jets and polymer nanofibers*. Polymer, 2008. **49**(10): p. 2387-2425.
47. Brinker, C.J., *GW Scherer Sol-Gel Science. The Physics and Chemistry of Sol-Gel Processing*, Academic, San Diego, CA, 1990.
48. Yue, Q., et al., *Adsorption of gas molecules on monolayer MoS₂ and effect of applied electric field*. Nanoscale research letters, 2013. **8**(1): p. 425.
49. Tongay, S., et al., *Broad-range modulation of light emission in two-dimensional semiconductors by molecular physisorption gating*. Nano letters, 2013. **13**(6): p. 2831-2836.
50. Loh, K.P., et al., *Graphene oxide as a chemically tunable platform for optical applications*. Nature chemistry, 2010. **2**(12): p. 1015-1024.
51. Chhowalla, M., et al., *The chemistry of two-dimensional layered transition metal dichalcogenide nanosheets*. Nature chemistry, 2013. **5**(4): p. 263-275.
52. Meyer, J.C., et al., *The structure of suspended graphene sheets*. Nature, 2007. **446**(7131): p. 60-63.
53. Bertolazzi, S., J. Brivio, and A. Kis, *Stretching and breaking of ultrathin MoS₂*. ACS nano, 2011. **5**(12): p. 9703-9709.
54. Eda, G., et al., *Coherent atomic and electronic heterostructures of single-layer MoS₂*. Acs Nano, 2012. **6**(8): p. 7311-7317.
55. Wilson, J. and A. Yoffe, *The transition metal dichalcogenides discussion and interpretation of the observed optical, electrical and structural properties*. Advances in Physics, 1969. **18**(73): p. 193-335.
56. Bissessur, R., et al., *Encapsulation of polymers into MoS₂ and metal to insulator transition in metastable MoS₂*. Journal of the Chemical Society, Chemical Communications, 1993(20): p. 1582-1585.
57. Frindt, R. and A. Yoffe. *Physical properties of layer structures: optical properties and photoconductivity of thin crystals of molybdenum disulphide*. in *Proceedings of the Royal Society of London A: Mathematical, Physical and Engineering Sciences*. 1963. The Royal Society.
58. Py, M. and R. Haering, *Structural destabilization induced by lithium intercalation in MoS₂ and related compounds*. Canadian Journal of Physics, 1983. **61**(1): p. 76-84.
59. Ganal, P., et al., *Soft chemistry induced host metal coordination change from octahedral*

- to trigonal prismatic in 1T-TaS₂. *Solid State Ionics*, 1993. **59**(3-4): p. 313-319.
60. Eda, G., et al., *Photoluminescence from chemically exfoliated MoS₂*. *Nano letters*, 2011. **11**(12): p. 5111-5116.
 61. Lorenz, T., et al., *Theoretical study of the mechanical behavior of individual TiS₂ and MoS₂ nanotubes*. *The Journal of Physical Chemistry C*, 2012. **116**(21): p. 11714-11721.
 62. Neto, A.C., *Charge density wave, superconductivity, and anomalous metallic behavior in 2D transition metal dichalcogenides*. *Physical review letters*, 2001. **86**(19): p. 4382.
 63. Heising, J. and M.G. Kanatzidis, *Exfoliated and restacked MoS₂ and WS₂: Ionic or neutral species? Encapsulation and ordering of hard electropositive cations*. *Journal of the American Chemical Society*, 1999. **121**(50): p. 11720-11732.
 64. Wang, Q.H., et al., *Electronics and optoelectronics of two-dimensional transition metal dichalcogenides*. *Nature nanotechnology*, 2012. **7**(11): p. 699-712.
 65. Splendiani, A., et al., *Emerging photoluminescence in monolayer MoS₂*. *Nano letters*, 2010. **10**(4): p. 1271-1275.
 66. Mak, K.F., et al., *Atomically thin MoS₂: a new direct-gap semiconductor*. *Physical review letters*, 2010. **105**(13): p. 136805.
 67. Tongay, S., et al., *Thermally driven crossover from indirect toward direct bandgap in 2D semiconductors: MoSe₂ versus MoS₂*. *Nano letters*, 2012. **12**(11): p. 5576-5580.
 68. Zhao, W., et al., *Evolution of electronic structure in atomically thin sheets of WS₂ and WSe₂*. *ACS nano*, 2012. **7**(1): p. 791-797.
 69. Xiao, D., et al., *Coupled spin and valley physics in monolayers of MoS₂ and other group-VI dichalcogenides*. *Physical Review Letters*, 2012. **108**(19): p. 196802.
 70. Voiry, D., A. Mohite, and M. Chhowalla, *Phase engineering of transition metal dichalcogenides*. *Chemical Society Reviews*, 2015. **44**(9): p. 2702-2712.
 71. Seifert, G., et al., *Structure and electronic properties of MoS₂ nanotubes*. *Physical Review Letters*, 2000. **85**(1): p. 146.
 72. Gong, Y., et al., *Vertical and in-plane heterostructures from WS₂/MoS₂ monolayers*. *Nature materials*, 2014. **13**(12): p. 1135-1142.
 73. Miró, P., M. Ghorbani-Asl, and T. Heine, *Transition Metal Monolayers: Spontaneous Ripple Formation in MoS₂ Monolayers: Electronic Structure and Transport Effects (Adv. Mater. 38/2013)*. *Advanced Materials*, 2013. **25**(38): p. 5366-5366.
 74. Podila, R., et al., *Raman spectroscopy of folded and scrolled graphene*. *ACS nano*, 2012. **6**(7): p. 5784-5790.
 75. Terrones, H., F. López-Urías, and M. Terrones, *Novel hetero-layered materials with tunable direct band gaps by sandwiching different metal disulfides and diselenides*. *Scientific reports*, 2013. **3**: p. 1549.
 76. Zhou, W., et al., *Intrinsic structural defects in monolayer molybdenum disulfide*. *Nano letters*, 2013. **13**(6): p. 2615-2622.
 77. Komsa, H.-P. and A.V. Krasheninnikov, *Native defects in bulk and monolayer MoS₂ from first principles*. *Physical Review B*, 2015. **91**(12): p. 125304.
 78. Chen, Y., et al., *Tunable band gap photoluminescence from atomically thin transition-metal dichalcogenide alloys*. *Acs Nano*, 2013. **7**(5): p. 4610-4616.
 79. Cheng, Y., et al., *Prediction of two-dimensional diluted magnetic semiconductors: doped monolayer MoS₂ systems*. *Physical Review B*, 2013. **87**(10): p. 100401.
 80. Zhang, K., et al., *Manganese doping of monolayer MoS₂: the substrate is critical*. *Nano*

- Lett, 2015. **15**(10): p. 6586-6591.
81. Komsa, H.-P., et al., *From point to extended defects in two-dimensional MoS₂: evolution of atomic structure under electron irradiation*. Physical Review B, 2013. **88**(3): p. 035301.
 82. Han, Y., et al., *Stabilities and electronic properties of monolayer MoS₂ with one or two sulfur line vacancy defects*. Physical Chemistry Chemical Physics, 2015. **17**(5): p. 3813-3819.
 83. Lin, J., S.T. Pantelides, and W. Zhou, *Vacancy-induced formation and growth of inversion domains in transition-metal dichalcogenide monolayer*. ACS nano, 2015. **9**(5): p. 5189-5197.
 84. Schweiger, H., et al., *Shape and edge sites modifications of MoS₂ catalytic nanoparticles induced by working conditions: a theoretical study*. Journal of Catalysis, 2002. **207**(1): p. 76-87.
 85. Azizi, A., et al., *Dislocation motion and grain boundary migration in two-dimensional tungsten disulphide*. Nature communications, 2014. **5**: p. 4867.
 86. Crowne, F.J., et al., *Blueshift of the A-exciton peak in folded monolayer 1 H-MoS₂*. Physical Review B, 2013. **88**(23): p. 235302.
 87. Hsu, W.-T., et al., *Second harmonic generation from artificially stacked transition metal dichalcogenide twisted bilayers*. ACS nano, 2014. **8**(3): p. 2951-2958.
 88. Miró, P., M. Ghorbani-Asl, and T. Heine, *Spontaneous ripple formation in MoS₂ monolayers: electronic structure and transport effects*. Advanced Materials, 2013. **25**(38): p. 5473-5475.
 89. Liu, H. and D. Chi, *Dispersive growth and laser-induced rippling of large-area single-layer MoS₂ nanosheets by CVD on c-plane sapphire substrate*. Scientific reports, 2015. **5**: p. 11756.
 90. Geim, A.K. and I.V. Grigorieva, *Van der Waals heterostructures*. Nature, 2013. **499**(7459): p. 419-425.
 91. Lin, Y.-C., et al., *Direct synthesis of van der Waals solids*. ACS Nano, 2014. **8**(4): p. 3715-3723.
 92. Terrones, H. and M. Terrones, *Electronic and vibrational properties of defective transition metal dichalcogenide Haeckelites: new 2D semi-metallic systems*. 2D Materials, 2014. **1**(1): p. 011003.
 93. Azizi, A., et al., *Freestanding van der Waals heterostructures of graphene and transition metal dichalcogenides*. ACS nano, 2015. **9**(5): p. 4882-4890.
 94. Gao, J., et al., *Aging of transition metal dichalcogenide monolayers*. ACS nano, 2016. **10**(2): p. 2628-2635.
 95. Yang, S., C. Jiang, and S.-h. Wei, *Gas sensing in 2D materials*. Applied Physics Reviews, 2017. **4**(2): p. 021304.
 96. Donarelli, M., et al., *Response to NO₂ and other gases of resistive chemically exfoliated MoS₂-based gas sensors*. Sensors and Actuators B: Chemical, 2015. **207**: p. 602-613.
 97. Li, B.L., et al., *Low-Dimensional Transition Metal Dichalcogenide Nanostructures Based Sensors*. Advanced Functional Materials, 2016. **26**(39): p. 7034-7056.
 98. Yi, M. and Z. Shen, *A review on mechanical exfoliation for the scalable production of graphene*. Journal of Materials Chemistry A, 2015. **3**(22): p. 11700-11715.
 99. Wetchakun, K., et al., *Semiconducting metal oxides as sensors for environmentally hazardous gases*. Sensors and Actuators B: Chemical, 2011. **160**(1): p. 580-591.

100. Hsueh, T.-J., et al., *Laterally grown ZnO nanowire ethanol gas sensors*. Sensors and Actuators B: Chemical, 2007. **126**(2): p. 473-477.
101. Gurlo, A., et al., *In 2 O 3 and MoO 3–In 2 O 3 thin film semiconductor sensors: interaction with NO 2 and O 3*. Sensors and Actuators B: Chemical, 1998. **47**(1): p. 92-99.
102. Agarwal, S., A. Greiner, and J.H. Wendorff, *Functional materials by electrospinning of polymers*. Progress in Polymer Science, 2013. **38**(6): p. 963-991.
103. Badilescu, S. and P. Ashrit, *Study of sol–gel prepared nanostructured WO 3 thin films and composites for electrochromic applications*. Solid State Ionics, 2003. **158**(1): p. 187-197.
104. Prabhu, N., et al., *EFFECT OF TEMPERATURE ON THE STRUCTURAL AND OPTICAL PROPERTIES OF WO 3 NANOPARTICLES PREPARED BY SOLVO THERMAL METHOD*. Digest Journal of Nanomaterials & Biostructures (DJNB), 2013. **8**(4).
105. Cantalini, C., et al., *The comparative effect of two different annealing temperatures and times on the sensitivity and long-term stability of WO₃ thin films for detecting NO₂*. IEEE Sensors Journal, 2003. **3**(2): p. 171-179.
106. De Marcellis, A., et al., *WO_3 Hydrogen Resistive Gas Sensor and Its Wide-Range Current-Mode Electronic Read-Out Circuit*. IEEE Sensors Journal, 2013. **13**(7): p. 2792-2798.
107. Nagy, Z.K., et al., *Comparison of electrospun and extruded soluplus®-based solid dosage forms of improved dissolution*. Journal of pharmaceutical sciences, 2012. **101**(1): p. 322-332.
108. Enke, C., *Nonstoichiometry, diffusion, and electrical conductivity in binary metal oxides*. (Wiley series on the science and technology of materials). P. Kofstad. 160 Abb. 11 Tab. XI, 382 S. Ca. 1060 Schrifttumshinweise. Format 15.5× 23 cm. Wiley Interscience (J. Wiley & Sons, Inc.) New York-London-Sydney-Toronto, 1972. Gebunden ca. DM 52,-. Materials and Corrosion, 1974. **25**(10): p. 801-802.
109. Chang, S.C., *Oxygen chemisorption on tin oxide: correlation between electrical conductivity and EPR measurements*. Journal of Vacuum Science and Technology, 1980. **17**(1): p. 366-369.
110. Giberti, A., C. Malagù, and V. Guidi, *WO 3 sensing properties enhanced by UV illumination: an evidence of surface effect*. Sensors and Actuators B: Chemical, 2012. **165**(1): p. 59-61.
111. Zhang, C., et al., *Room temperature responses of visible-light illuminated WO 3 sensors to NO 2 in sub-ppm range*. Sensors and Actuators B: Chemical, 2013. **181**: p. 395-401.
112. Deng, L., et al., *Visible-light activate mesoporous WO 3 sensors with enhanced formaldehyde-sensing property at room temperature*. Sensors and Actuators B: Chemical, 2012. **163**(1): p. 260-266.
113. González-Borrero, P., et al., *Optical band-gap determination of nanostructured WO 3 film*. Applied Physics Letters, 2010. **96**(6): p. 061909.
114. Fan, S.-W., A.K. Srivastava, and V.P. Dravid, *UV-activated room-temperature gas sensing mechanism of polycrystalline ZnO*. Applied Physics Letters, 2009. **95**(14): p. 142106.
115. Geng, Q., et al., *Gas sensing property of ZnO under visible light irradiation at room*

- temperature*. Sensors and Actuators B: Chemical, 2013. **188**: p. 293-297.
116. Maiti, A., et al., *SnO₂ nanoribbons as NO₂ sensors: insights from first principles calculations*. Nano Letters, 2003. **3**(8): p. 1025-1028.
117. Prades, J.D., et al., *Ab initio study of NO_x compounds adsorption on SnO₂ surface*. Sensors and Actuators B: Chemical, 2007. **126**(1): p. 62-67.
118. Yang, W., et al., *Two-dimensional layered nanomaterials for gas-sensing applications*. Inorganic Chemistry Frontiers, 2016. **3**(4): p. 433-451.
119. Voiry, D., et al., *Enhanced catalytic activity in strained chemically exfoliated WS₂ nanosheets for hydrogen evolution*. Nature materials, 2013. **12**(9): p. 850-855.
120. Mak, K.F. and J. Shan, *Photonics and optoelectronics of 2D semiconductor transition metal dichalcogenides*. Nature Photonics, 2016. **10**(4): p. 216-226.
121. Pumera, M., Z. Sofer, and A. Ambrosi, *Layered transition metal dichalcogenides for electrochemical energy generation and storage*. Journal of Materials Chemistry A, 2014. **2**(24): p. 8981-8987.
122. Abdelkader, A. and I. Kinloch, *Mechanochemical exfoliation of 2D crystals in deep eutectic solvents*. ACS Sustainable Chemistry & Engineering, 2016. **4**(8): p. 4465-4472.
123. Jawaid, A., et al., *Mechanism for liquid phase exfoliation of MoS₂*. Chemistry of Materials, 2015. **28**(1): p. 337-348.
124. Perrozzi, F., et al., *Thermal stability of WS₂ flakes and gas sensing properties of WS₂/WO₃ composite to H₂, NH₃ and NO₂*. Sensors and Actuators B: Chemical, 2017. **243**: p. 812-822.
125. Li, L.H., et al., *High-efficient production of boron nitride nanosheets via an optimized ball milling process for lubrication in oil*. Scientific reports, 2014. **4**: p. 7288.
126. Deng, S., et al., *A facile way to large-scale production of few-layered graphene via planetary ball mill*. Chinese Journal of Polymer Science, 2016. **34**(10): p. 1270-1280.
127. Nguyen, E.P., et al., *Investigation of two-solvent grinding-assisted liquid phase exfoliation of layered MoS₂*. Chemistry of Materials, 2014. **27**(1): p. 53-59.
128. Grayfer, E.D., M.N. Kozlova, and V.E. Fedorov, *Colloidal 2D nanosheets of MoS₂ and other transition metal dichalcogenides through liquid-phase exfoliation*. Advances in Colloid and Interface Science, 2017.
129. Nicolosi, V., et al., *Liquid exfoliation of layered materials*. Science, 2013. **340**(6139): p. 1226419.
130. Carey, B.J., et al., *Two solvent grinding sonication method for the synthesis of two-dimensional tungsten disulphide flakes*. Chemical Communications, 2015. **51**(18): p. 3770-3773.
131. Ghorai, A., et al., *Exfoliation of WS₂ in the semiconducting phase using a group of lithium halides: a new method of Li intercalation*. Dalton Transactions, 2016. **45**(38): p. 14979-14987.
132. Xing, T., et al., *Gas protection of two-dimensional nanomaterials from high-energy impacts*. Scientific reports, 2016. **6**: p. 35532.
133. Gutiérrez, H.R., et al., *Extraordinary room-temperature photoluminescence in triangular WS₂ monolayers*. Nano letters, 2012. **13**(8): p. 3447-3454.
134. Zhou, P., et al., *Fabrication of Two-Dimensional Lateral Heterostructures of WS₂/WO₃·H₂O Through Selective Oxidation of Monolayer WS₂*. Angewandte Chemie International Edition, 2015. **54**(50): p. 15226-15230.

135. Hong, J., et al., *Exploring atomic defects in molybdenum disulphide monolayers*. Nature communications, 2015. **6**.
136. Di Paola, A., et al., *Coupled semiconductor systems for photocatalysis. Preparation and characterization of polycrystalline mixed WO₃/WS₂ powders*. The Journal of Physical Chemistry B, 1999. **103**(39): p. 8236-8244.
137. Feldman, Y., et al., *Bulk synthesis of inorganic fullerene-like MS₂ (M= Mo, W) from the respective trioxides and the reaction mechanism*. Journal of the American Chemical Society, 1996. **118**(23): p. 5362-5367.
138. Margolin, A., et al., *Study of the growth mechanism of WS₂ nanotubes produced by a fluidized bed reactor*. Journal of Materials Chemistry, 2004. **14**(4): p. 617-624.
139. Kuru, C., et al., *High-performance flexible hydrogen sensor made of WS₂ nanosheet–Pd nanoparticle composite film*. Nanotechnology, 2016. **27**(19): p. 195501.
140. Long, H., et al., *High surface area MoS₂/graphene hybrid aerogel for ultrasensitive NO₂ detection*. Advanced Functional Materials, 2016. **26**(28): p. 5158-5165.
141. Burman, D., et al., *Role of vacancy sites and UV-ozone treatment on few layered MoS₂ nanoflakes for toxic gas detection*. Nanotechnology, 2017. **28**(43): p. 435502.
142. Ma, D., et al., *Repairing sulfur vacancies in the MoS₂ monolayer by using CO, NO and NO₂ molecules*. Journal of Materials Chemistry C, 2016. **4**(29): p. 7093-7101.
143. KC, S., et al., *Surface oxidation energetics and kinetics on MoS₂ monolayer*. Journal of Applied Physics, 2015. **117**(13): p. 135301.
144. Nomani, M.W., et al., *Highly sensitive and selective detection of NO₂ using epitaxial graphene on 6H-SiC*. Sensors and Actuators B: Chemical, 2010. **150**(1): p. 301-307.
145. Kim, Y.H., et al., *Self-activated transparent all-graphene gas sensor with endurance to humidity and mechanical bending*. ACS nano, 2015. **9**(10): p. 10453-10460.
146. Donarelli, M., et al., *Exfoliated black phosphorus gas sensing properties at room temperature*. 2D Materials, 2016. **3**(2): p. 025002.
147. Miremadi, B.K., T. Cowan, and S.R. Morrison, *New structures from exfoliated MoS₂*. Journal of applied physics, 1991. **69**(9): p. 6373-6379.
148. Miremadi, B.K., et al., *A highly sensitive and selective hydrogen gas sensor from thick oriented films of MoS₂*. Applied Physics A: Materials Science & Processing, 1996. **63**(3): p. 271-275.
149. Lee, K., et al., *High-performance sensors based on molybdenum disulfide thin films*. Advanced materials, 2013. **25**(46): p. 6699-6702.
150. Miremadi, B. and S. Morrison, *The intercalation and exfoliation of tungsten disulfide*. Journal of applied physics, 1988. **63**(10): p. 4970-4974.
151. Mayorga-Martinez, C.C., et al., *Metallic 1T-WS₂ for Selective Impedimetric Vapor Sensing*. Advanced Functional Materials, 2015. **25**(35): p. 5611-5616.
152. Perkins, F.K., et al., *Chemical vapor sensing with monolayer MoS₂*. Nano letters, 2013. **13**(2): p. 668-673.
153. Rong, Y., et al., *Controlled preferential oxidation of grain boundaries in monolayer tungsten disulfide for direct optical imaging*. ACS nano, 2015. **9**(4): p. 3695-3703.
154. Ambrosi, A., Z. Sofer, and M. Pumera, *2H → 1T phase transition and hydrogen evolution activity of MoS₂, MoSe₂, WS₂ and WSe₂ strongly depends on the MX₂ composition*. Chemical Communications, 2015. **51**(40): p. 8450-8453.
155. Shpak, A., et al., *XPS studies of the surface of nanocrystalline tungsten disulfide*. Journal of Electron Spectroscopy and Related Phenomena, 2010. **181**(2): p. 234-

- 238.
156. Kida, T., et al., *Highly sensitive NO₂ sensors using lamellar-structured WO₃ particles prepared by an acidification method*. *Sensors and Actuators B: Chemical*, 2009. **135**(2): p. 568-574.
157. Golozar, M., K. Chien, and T.W. Coyle, *Orthorhombic α -MoO₃ coatings with lath-shaped morphology developed by SPPS: applications to super-capacitors*. *Journal of thermal spray technology*, 2012. **21**(3-4): p. 469-479.
158. Kuti, L.M., S.S. Bhella, and V. Thangadurai, *Revisiting Tungsten Trioxide Hydrates (TTHs) Synthesis-Is There Anything New?* *Inorganic chemistry*, 2009. **48**(14): p. 6804-6811.
159. Li, Y.-H., et al., *Novel Route to WO_x Nanorods and WS₂ Nanotubes from WS₂ Inorganic Fullerenes*. *The Journal of Physical Chemistry B*, 2006. **110**(37): p. 18191-18195.
160. O'hare, P., et al., *Calorimetric measurements of the low-temperature heat capacity, standard molar enthalpy of formation at 298.15 K, and high-temperature molar enthalpy increments relative to 298.15 K of tungsten disulfide (WS₂), and the thermodynamic properties to 1500 K*. *The Journal of Chemical Thermodynamics*, 1984. **16**(1): p. 45-59.
161. Laursen, A.B., et al., *Molybdenum sulfides—efficient and viable materials for electro- and photoelectrocatalytic hydrogen evolution*. *Energy & Environmental Science*, 2012. **5**(2): p. 5577-5591.
162. Kuru, C., et al., *MoS₂ nanosheet–Pd nanoparticle composite for highly sensitive room temperature detection of hydrogen*. *Advanced Science*, 2015. **2**(4).
163. Calavia, R., et al., *Fabrication of WO₃ nanodot-based microsensors highly sensitive to hydrogen*. *Sensors and Actuators B: Chemical*, 2010. **149**(2): p. 352-361.
164. Boudiba, A., et al., *Sensitive and rapid hydrogen sensors based on Pd–WO₃ thick films with different morphologies*. *international journal of hydrogen energy*, 2013. **38**(5): p. 2565-2577.
165. Kong, D., et al., *Synthesis of MoS₂ and MoSe₂ films with vertically aligned layers*. *Nano letters*, 2013. **13**(3): p. 1341-1347.
166. Jaramillo, T.F., et al., *Identification of active edge sites for electrochemical H₂ evolution from MoS₂ nanocatalysts*. *science*, 2007. **317**(5834): p. 100-102.
167. Tuxen, A., et al., *Size threshold in the dibenzothiophene adsorption on MoS₂ nanoclusters*. *ACS nano*, 2010. **4**(8): p. 4677-4682.
168. O'Brien, M., et al., *Plasma assisted synthesis of WS₂ for gas sensing applications*. *Chemical Physics Letters*, 2014. **615**: p. 6-10.
169. Vuong, N.M., D. Kim, and H. Kim, *Surface gas sensing kinetics of a WO₃ nanowire sensor: Part 2—Reducing gases*. *Sensors and Actuators B: Chemical*, 2016. **224**: p. 425-433.
170. Cho, B., et al., *Bifunctional sensing characteristics of chemical vapor deposition synthesized atomic-layered MoS₂*. *ACS applied materials & interfaces*, 2015. **7**(4): p. 2952-2959.
171. Wang, C., et al., *Nanosheets assembled hierarchical flower-like WO₃ nanostructures: synthesis, characterization, and their gas sensing properties*. *Sensors and Actuators B: Chemical*, 2015. **210**: p. 75-81.

8 Annexes

8.1 A1: Operating instructions: material preparations

Preparation of solutions for electrospinning					IOP 1
Purpose					
The purpose of the following IOP is to describe the preparation process of the precursor and polymer solutions. It represents the initial step of nanofiber electrospinning fabrication process.					
Materials					
A precise amount of precursor powder is combined with a precise quantity of solvent in the following proportions:					
Precursor solution			Solution polymer		
Precursor	Powder	Solvent	Solvent	Polymer	
WO₃	Tungsten(IV) Chloride	Ethanol	Dimethylformamide (DMF)	polyvinylpyrrolidone (PVP)	
	SIGMA ALDRICH purity $\geq 99\%$	SIGMA ALDRICH purity $\geq 99.8\%$	SIGMA ALDRICH purity $\geq 99.8\%$	SIGMA ALDRICH MW ≈ 1300000 g/mol	
	0.4 g	5.0 ml	1.0 ml	0.17 g	
Tungsten chloride powder was dissolved in ethanol and refluxed under nitrogen. Polymer powder was dissolved in solvent under stirring. The final precursor was prepared by drop by drop addition of polymer solution in precursor under stirring in nitrogen environment. After mixing polymer and precursor solutions, the final precursor was left under stirring for few hours to obtain a homogenous precursor.					

Preparation of exfoliated mono-few layer WS₂				IOP 2
Purpose				
The purpose of the following IOP is to describe the preparation process of the exfoliated mono-few layer WS ₂ nanosheets. It represents the ball milling assisted sonication exfoliation process.				
Materials				
A precise amount of powder is combined with a precise quantity of solvent in the following proportions:				
Mono-few layer WS₂ suspension				
Suspension	Powder	Solvent	Powder	Ethanol
WS₂	Tungsten disulfide	Acetonitrile	Ball milled Tungsten Disulfide	Ethanol
	SIGMA ALDRICH purity \geq 99%	SIGMA ALDRICH purity \geq 99.8 %	SIGMA ALDRICH purity \geq 99%	SIGMA ALDRICH purity \geq 99.8 %
	2.0 g	2.0 ml	0.05 g	0.17 g
Tungsten disulfide was dispersed in acetonitrile and ball milled. After acetonitrile evaporation, ball milled powder was dispersed in pure ethanol and probe sonicated.				
The final dispersion was centrifuged after probe sonication and the supernatant containing exfoliated mono-few layer tungsten disulfide was collected.				

8.2 A2: Operating instructions: preparation processes

Electrospinning deposition process		IOP 3			
Purpose					
The purpose of the following IOP is to describe the parameters used for electrospinning deposition.					
Methodology					
<p>The solution is inserted into a 5 mL syringe driven by the dosing pump.</p> <p>The syringe is connected to the needle via a small tube that allows the solution to be transported from the syringe barrel to the needle.</p> <p>The needle, in turn, is connected to the positive electrode of a high voltage potential generator via a metal clamp. The substrate is instead placed on the grounded manifold.</p> <p>From the drop at the end of the needle, it is possible to observe the formation of a cone, known as Taylor's cone, with consequent formation of the nanofiber.</p> <p>When the jet travels in the air, its diameter decreases due to the simultaneous effect of the elongation of the jet and the evaporation of the solvent.</p> <p>The fibers impact and settle on the collector connected to the ground, the charges carried by the jet thus complete the electrical circuit.</p> <p>The experimental conditions used for electrospinning of tungsten trioxide nanofibers are as follows:</p>					
	Distance Needle/collector (cm)	Solution Flow Rate (μL/min)	Applied Voltage (kV)	Relative Humidity (%)	Temperature ($^{\circ}$C)
WO₃ nanofiber	10	1	14	4.5% \pm 2%	21

Exfoliation process						IOP 4			
Purpose									
The purpose of the following IOP is to describe the parameters used for exfoliation fabrication process for fabrication of mono-few layer tungsten disulfide.									
Metodology									
2 g of WS ₂ commercial powder with 99% purity and average particle size of 2μm is dispersed in 2 mL of acetonitrile and ball milled in a planetary milling machine (steps of 15 min milling and 5 min idle to avoid excessive warming).									
The ACN residuals were then evaporated overnight (i.e. drying) at room temperature.									
After ACN evaporation, 0.05 g of the ball milled powder dispersed in 100 mL of pure ethanol and probe sonicated (d) for 90 minutes in a cool bath (T=25°C).									
Finally, the sonicated dispersion was centrifuged at 20°C and the supernatant was collected and spin coated (for spin coatig parameters see IOP5).									
The experimental conditions used for exfoliation process of tungsten disulfide are as follows:									
	Grinding parameters					Sonication parameters		Centrifugation parameters	
	Speed [rpm]	duration [h]	Nbr. of balls	Weight of each ball [g]	Ball/Powder weight ratio	Duration [min]	Temperature [°C]	Duration [min]	Speed [rpm]
WS₂	400	72	12	4	24	90	25	40	2500

Spin coating process	IOP 5						
Purpose							
The purpose of the following IOP is to describe the parameters used for spin coating of mono-few layer exfoliated WS ₂							
Metodology							
The supernatant obtained by means of exfoliation process explained in IOP 4, is deposited on the Si ₃ N ₄ substrate placed on the rotating plate of the spin coater by means of a micro pipette, having the foresight that the drop (30-40 µL) completely covers the surface of the substrate. At this point the rotating plate is covered with the appropriate cover and the rotation starts with the following parameters:							
<table border="1" data-bbox="459 864 1211 958"> <thead> <tr> <th data-bbox="459 864 651 909"></th> <th data-bbox="651 864 927 909">Duration</th> <th data-bbox="927 864 1211 909">Rpm</th> </tr> </thead> <tbody> <tr> <td data-bbox="459 909 651 958" style="text-align: center;">step</td> <td data-bbox="651 909 927 958" style="text-align: center;">30 s</td> <td data-bbox="927 909 1211 958" style="text-align: center;">1000 rpm</td> </tr> </tbody> </table>			Duration	Rpm	step	30 s	1000 rpm
	Duration	Rpm					
step	30 s	1000 rpm					

8.3 A3: Interdigitated substrate: technical specifications and characterization

Geometric and constructive characteristics

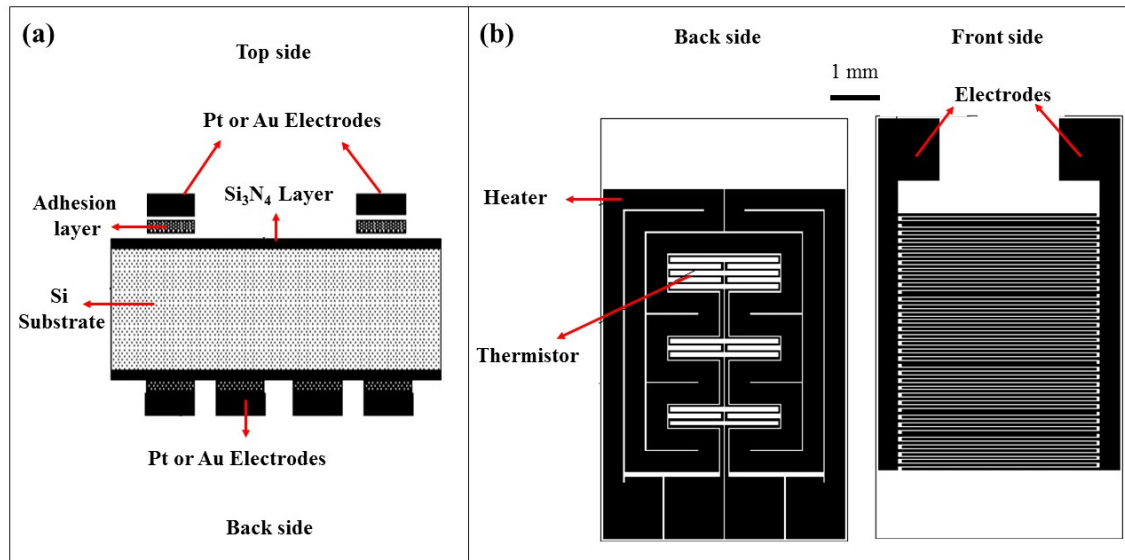


Figure 8-1- Figure 1: On the left: section of the substrate used; on the right: substrate structure: "Back" side and "Front" side.

The "Front side", of the sensor, where the sensing material is deposited on, has comb electrodes. The dimensions and the main technological features are shown in the table Table 8-1.

Front side	
Finger" electrode configuration	
Thickness of electrodes	Ta 100 Å + Pt 500 Å
Thickness of electrodes on welding pads	Pt 4000 Å
Track width 30 Microns	Step 30 Microns

BACK SIDE	
Length of the heater circuit	43.4 mm
Thickness of the heater	Ta 200 Å / Pt 2800 Å
Width of the heater	310 μm
Section of the heater	93 μm ²

Table 8-1- The dimensions and the main technological features of sensor substrate

An AFM survey carried out on the sensor, made it possible to estimate the thickness of the electrodes on the front side. Figure 8-2 shows this result. The electrode thickness is about 400 Å.

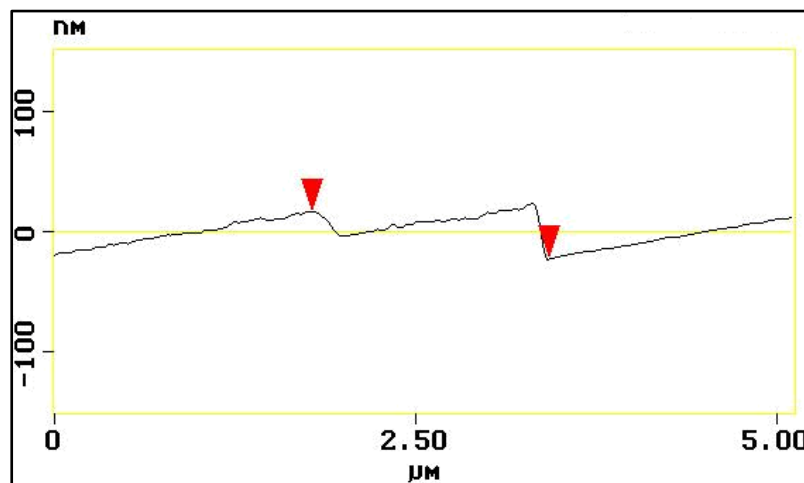


Figure 8-2- Platinum electrode thickness profile. Distance between the two arrows in the figure is approximately 40 nm.

The electrodes are made of platinum, but they adhere to the support through another material, tantalum, which makes better the adhesion of platinum on silicon nitride. The choice of materials has been conditioned by the high temperatures and by potentially aggressive environments, in which the sensor works.

Microstructural characteristics

The substrates were characterized from a microstructural point of view by AFM (Atomic Force Microscopy).

This characterization was used to obtain information on the superficial morphological characteristics of the substrates, as well as being used to measure the average roughness of the substrates. The results of this characterization are shown in Figure 8-3.

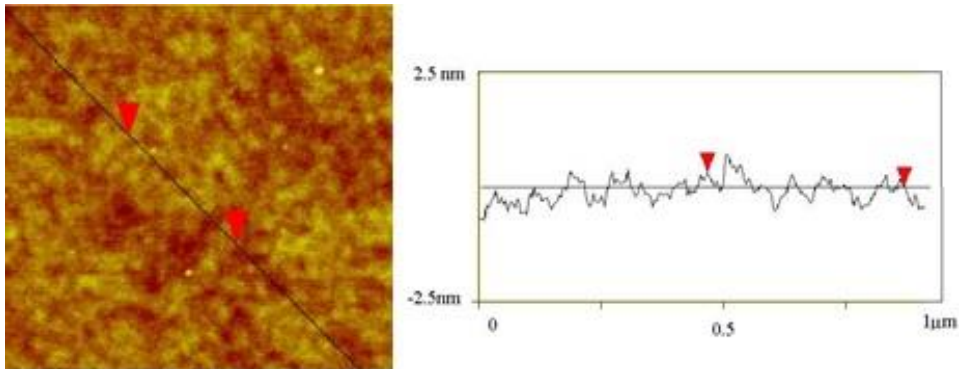


Figure 8-3- Microstructural characterization of substrates with AFM technique. Left: top photo of Si / Si₃N₄ substrate. On the right: proof of roughness of this substrate automatically calculated by the instrument in correspondence of the black line of the figure on the left.

Thermal characterization

The substrates were characterized from the thermal point of view by feeding the current heating circuit and measuring the temperature reached on the substrate surface by means of an infrared camera (Figure 8-4).

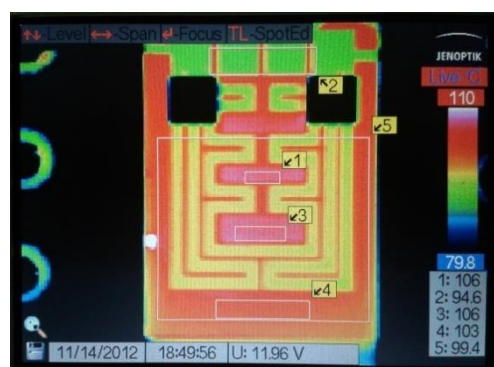


Figure 8-4- Image generated by the IR thermal camera during thermal calibration of the substrate

A calibration curve has been obtained where it is possible to identify the operating

temperature based on the electric power supplied to the heating circuit (Figure 8-5).

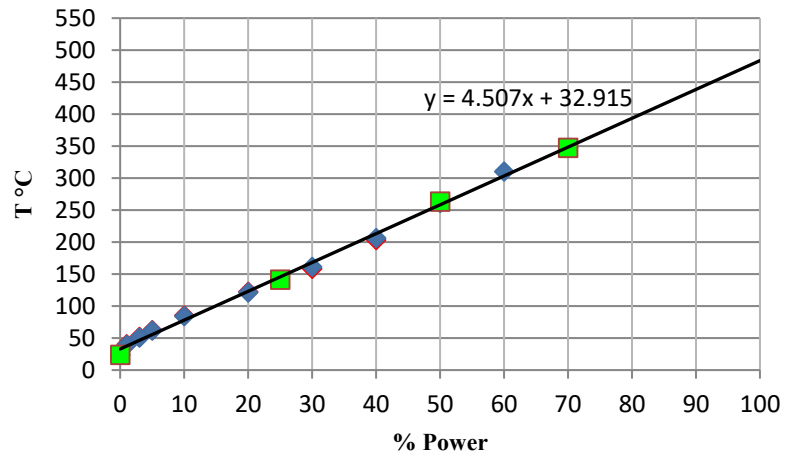


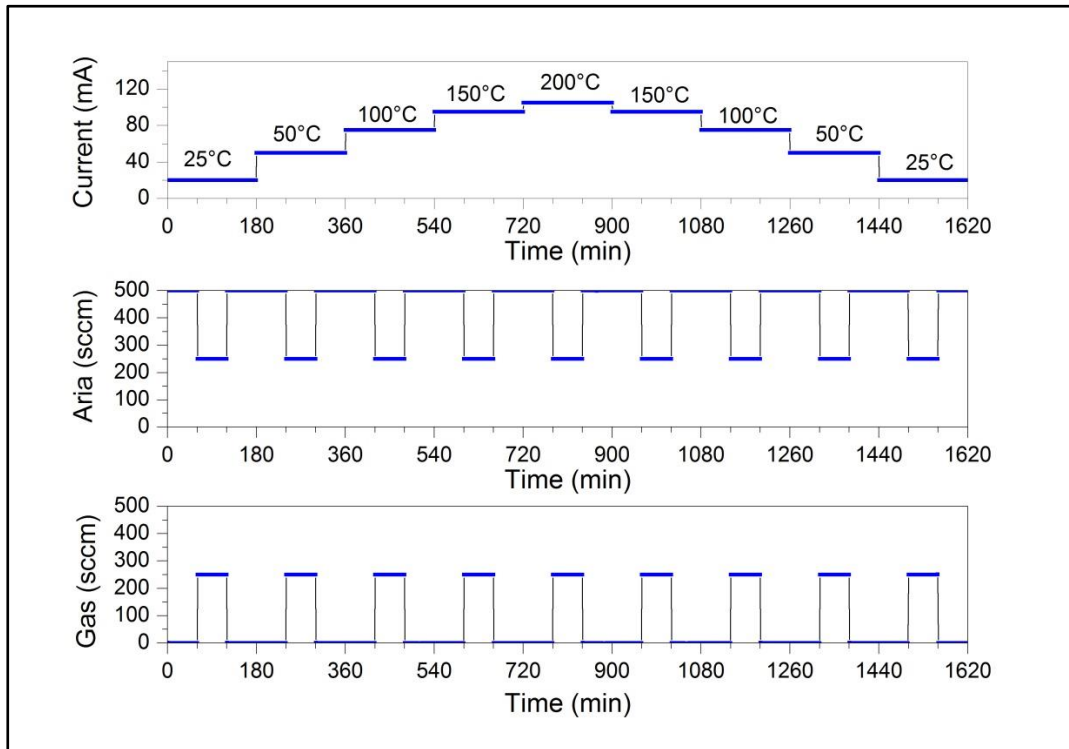
Figure 8-5- Thermal calibration curve of the used substrate.

8.4 A4: Characteristic parameters for a semiconductor oxide sensor

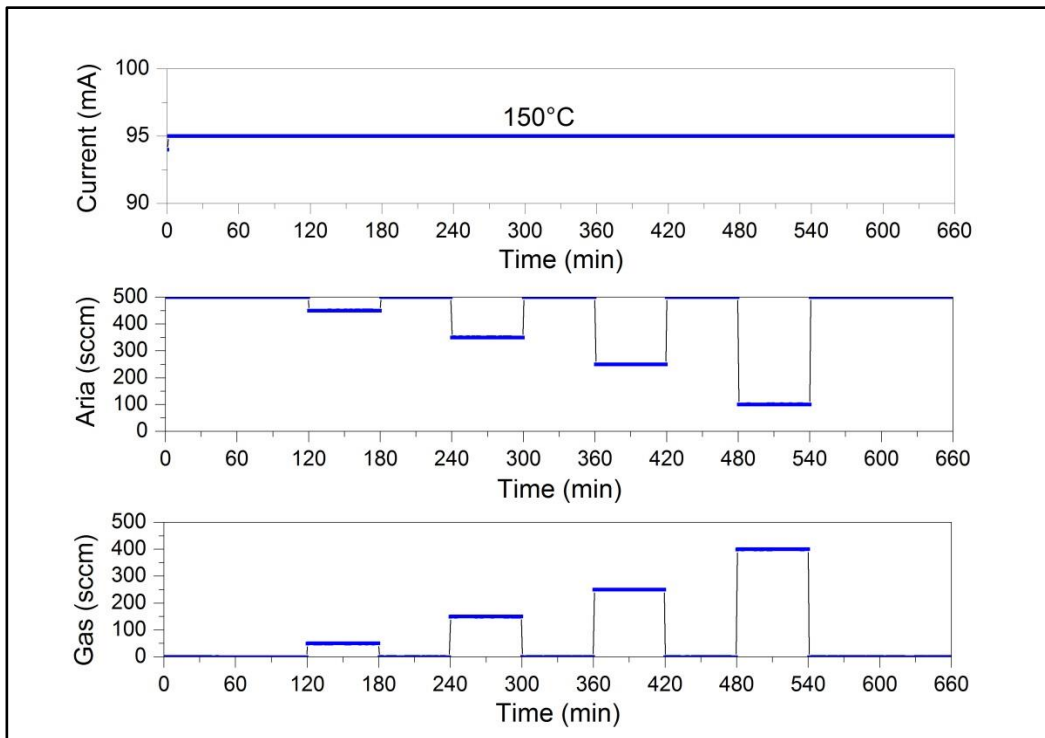
Parameters	Definitions	Equations
Relative response (RR)	Relative response is defined as the change of resistance of the material in the presence or absence of the target gas.	$S = \frac{ R_a - R_g }{R_a}$ $S = \frac{R_g}{R_a}$ <p>Where: R_a = Resistance in air R_g = Resistance in gas</p>
Sensitivity	Sensitivity is defined as the relationship between the variation of the sensor response and the variation of the gas concentration. Mathematically, it is expressed as the derivative of the sensor response curve	$S = \frac{\Delta R}{\Delta C}$ <p>Where: ΔR = Resistance Variation ΔC = Concentration variation</p>
Stability	It is the sensor's ability to maintain its operating characteristics unaltered for a relatively long time.	
Selectivity	It is the sensor's ability to maintain its operating characteristics unaltered for a relatively long time.	
Selectivity	It is the ability of the sensing material to respond to a specific target gas in the presence of an interfering gas	
Response time $\tau_{90\%}$	It is the time taken by the sensor to reach 90% of the total in the presence of the target gas response.	
Recovery time $\tau_{90\%}$	It is the time taken by the sensor to recover 90% of the base value after exposure to the target gas.	

8.5 A5: Testing protocol for electrical tests

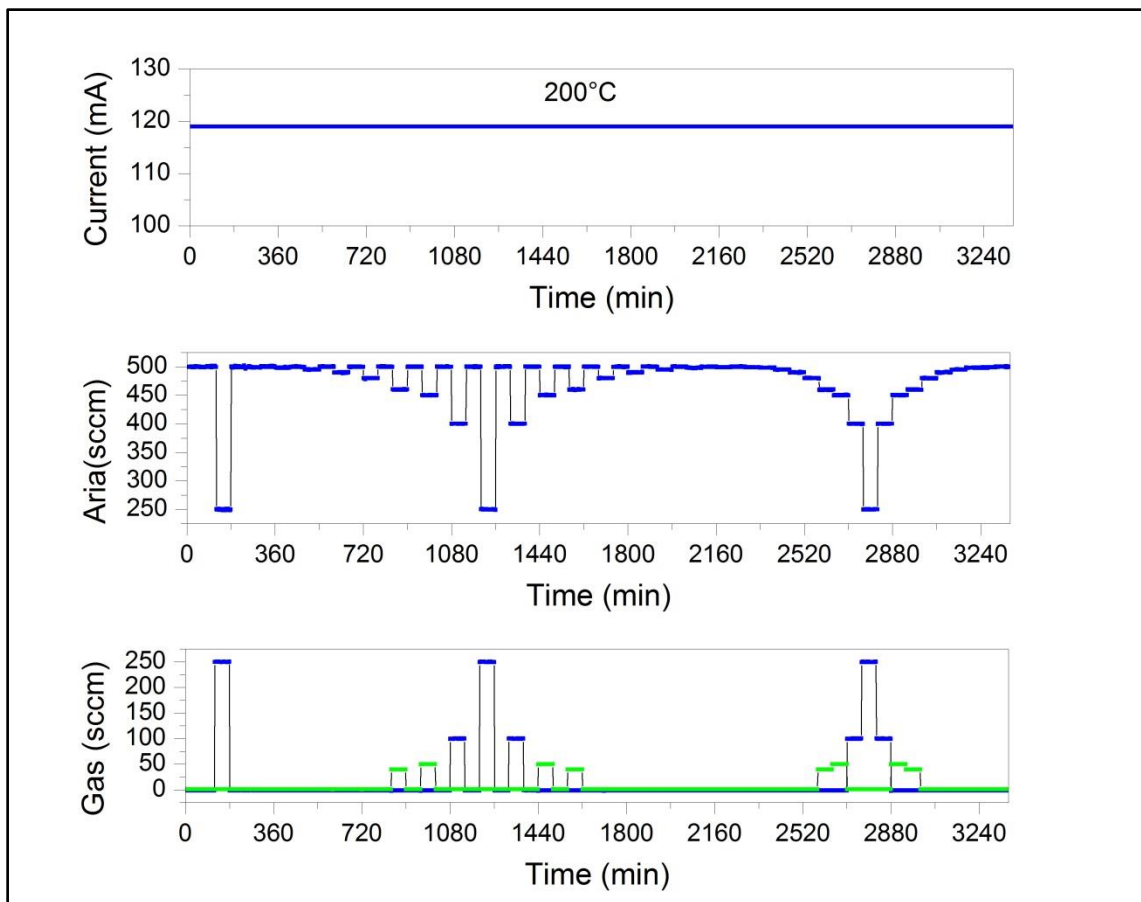
Test at different temperatures with target gas step



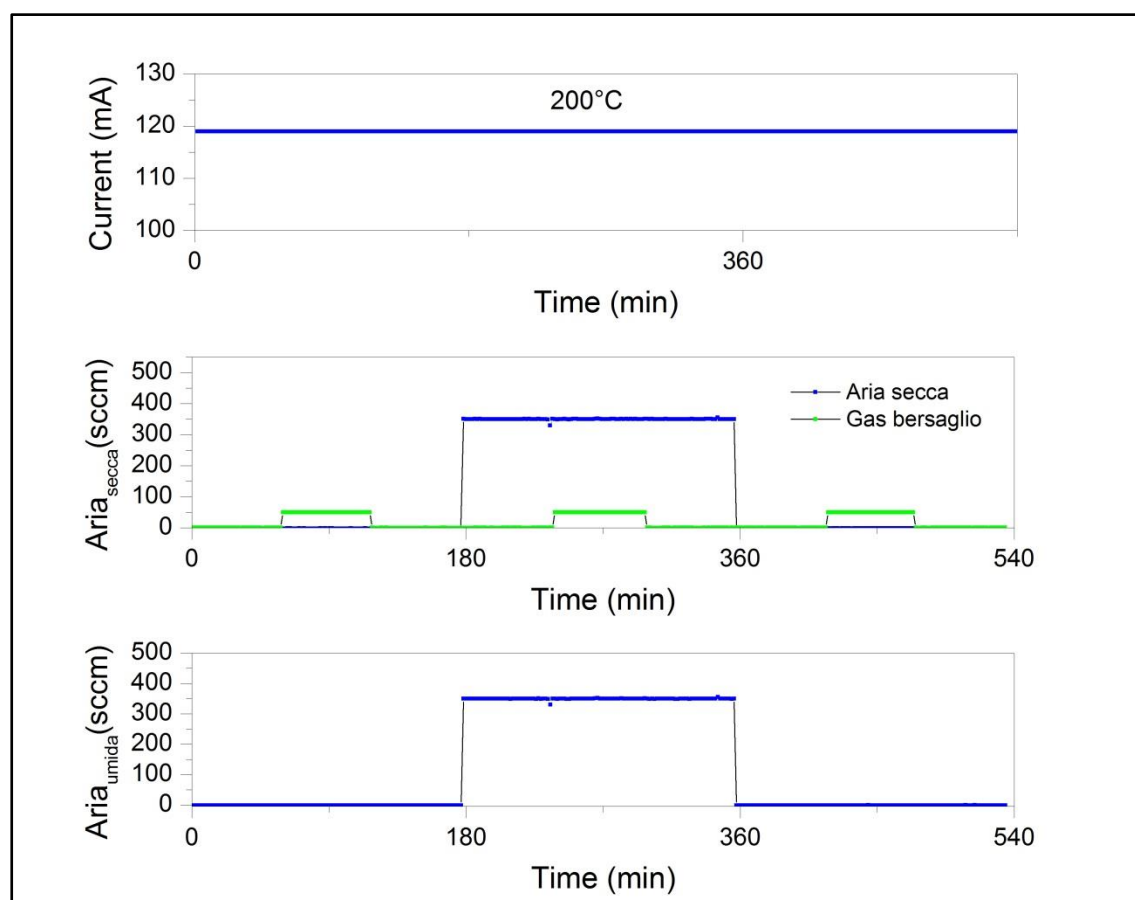
Test description: Response to different operating temperatures: each step has a duration of 3 h; for each temperature, dry air is insufflated for 1 h, a gas stream is sent at a given concentration for 1 h and finally dry air for 1 h. All possible operating temperatures are investigated.

Try different concentrations of target gas

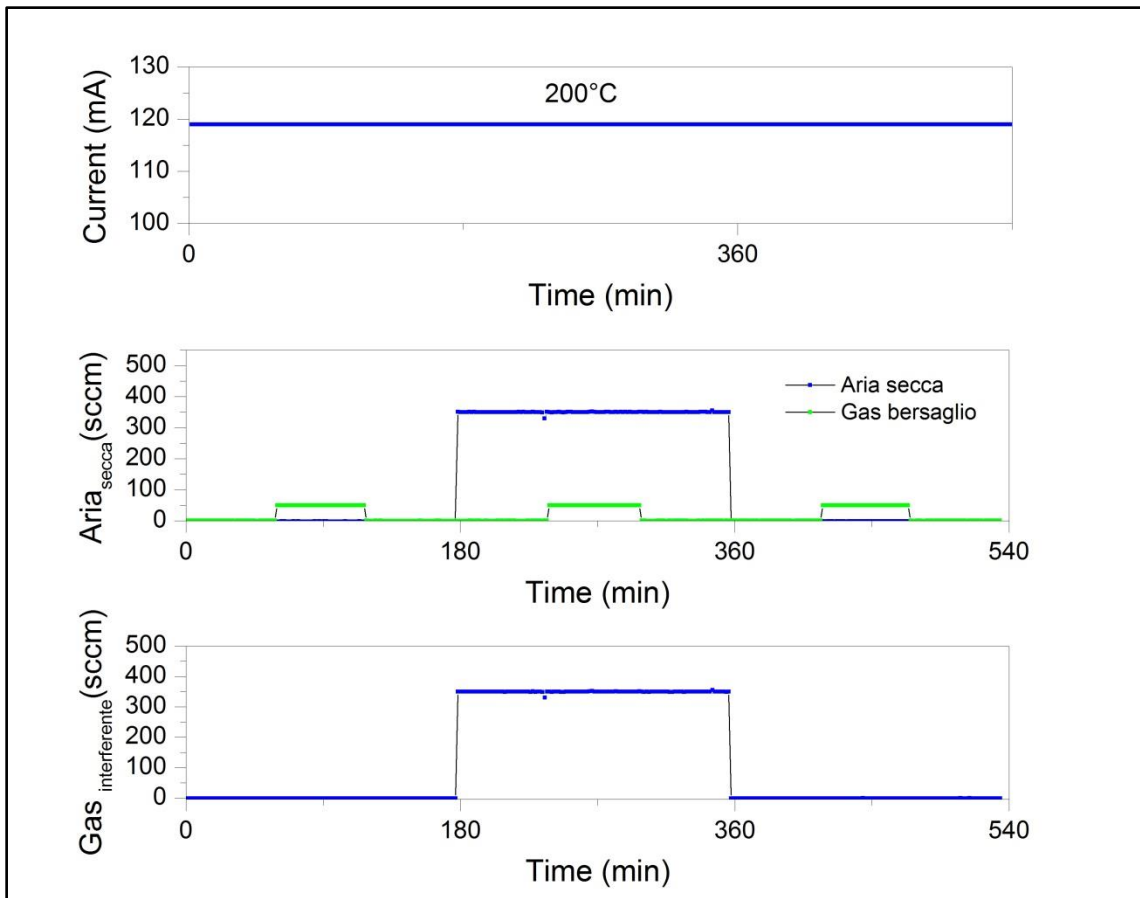
Test description: Response to various concentrations of target gas at constant temperature: each step has a duration of 2 h, at constant temperature a ramp of concentrations is carried out (depending on the range to be investigated). During each step, dry air is insufflated for 1 h and then a target concentration gas stream set for 1 h.

Test at different concentrations of target gas - cumulative test

Test description: Response to various concentrations of target gas - cumulative test at constant temperature: adsorption and desorption cycle at increasing concentrations of target gas, from the minimum to the maximum of the concentrations investigated. Afterwards, the sensor is again exposed to increasing and decreasing concentrations of gas like NO₂ (at the same concentrations), but eliminating the desorption step.

Cross sensitivity (Target gas - Humidity)

Test description: First step: standard response to target gas in dry air. Second Step: for the duration of the central step, moist air is insufflated at a known percentage and a concentration of the target gas is sent simultaneously. Third Step: standard response to target gas in dry air.

Cross sensitivity (Target gas - Interfering gas)

Test description: First step: standard response to target gas in dry air. Second Step: for the duration of the central step a known concentration of an interfering gas is insufflated and a concentration of the target gas is sent simultaneously in the central step. Third Step: standard response to target gas in dry air.